Self-organized Structures and Excitations in Dipolar Quantum Fluids

Von der Fakultät Mathematik und Physik der Universität Stuttgart
zur Erlangung der Würde eines Doktors der
Naturwissenschaften (Dr. rer. nat.) genehmigte Abhandlung

Vorgelegt von

Jens Hertkorn

aus Stuttgart

Hauptberichter	Prof. Dr. Tilman Pfau
Mitberichter	Prof. Dr. Sebastian Loth
Prüfungsvorsitzender	Prof. Dr. Hans Peter Büchler
Tag der mündlichen Prüfung	18. Juli 2024

5. Physikalisches Institut
Universität Stuttgart
2024

Ehrenwörtliche Erklärung

Hiermit erkläre ich, dass ich diese Arbeit selbständig verfasst und keine anderen als die von mir angegebenen Quellen und Hilfsmittel verwendet habe.

Stuttgart, 12. Juni 2024

_____

Jens Hertkorn

Abstract

Quantum many-body phenomena at a macroscopic scale, such as superfluidity and superconductivity, are rooted in the interplay between microscopic particles, governed by the laws of quantum mechanics. Exploring how this interplay leads to quantum behavior at a large scale allows us to gain a deeper understanding of nature and to discover new quantum phases. An elusive quantum phase in which the frictionless flow of superfluids and the crystal structure of solids coexists – the supersolid – was recently realized with quantum droplets in dipolar Bose-Einstein condensates.

In this thesis we investigate self-organized structures, their formation mechanism, and excitations in dipolar quantum fluids created from such Bose-Einstein condensates. We show that the supersolid formation mechanism is driven by density fluctuations due to low-energy roton excitations, leading to a crystal structure of quantum droplets that are immersed in a superfluid background. These roton excitations split into a Goldstone mode and a Higgs amplitude mode, associated to the broken translational symmetry in the supersolid. We investigate the symmetry breaking of dipolar quantum fluids in a range of confinement geometries and establish a comprehensive description of elementary excitations across the superfluid to supersolid droplet phase transition. The droplets are stabilized by an interplay between interactions and the presence of quantum fluctuations. We show how this interplay can be used to find regimes where droplets are immersed in a high superfluid background, allowing for frictionless flow throughout the crystal. Moreover we show that towards higher densities beyond the quantum droplet phase, this interplay leads to several new self-organized structures in the phase diagram of dipolar quantum fluids. We theoretically predict new supersolid honeycomb, amorphous labyrinth, and other phases in oblate dipolar quantum fluids. Finally, we present a new experimental setup for the exploration of self-organized phases in dipolar quantum fluids and which also lays the foundation for the implementation of a quantum gas microscope.

The results of this thesis present a complete framework for understanding and creating exotic phases in dipolar quantum fluids. The versatile structure formation, governed by a competition of controllable interactions and the presence of quantum fluctuations, positions dipolar quantum fluids as a model system for exploring self-organized equilibrium in weakly-interacting quantum many-body systems.

List of Publications

1. **J. Hertkorn**, P. Stürmer, K. Mukherjee, K. Ng, P. Uerlings, F. Hellstern, L. Lavoine, S. Reimann, T. Pfau, and R. Klemt, "Decoupled sound and amplitude modes in trapped dipolar supersolids", arXiv:2404.12384 (submitted for peer review) (2024).
2. **J. Hertkorn**, J.-N. Schmidt, M. Guo, F. Böttcher, K. S. H. Ng, S. D. Graham, P. Uerlings, H. P. Büchler, T. Langen, M. Zwierlein, and T. Pfau, "Supersolidity in Two-Dimensional Trapped Dipolar Droplet Arrays", Phys. Rev. Lett. **127**, 155301 (2021).
3. **J. Hertkorn**, J.-N. Schmidt, M. Guo, F. Böttcher, K. S. H. Ng, S. D. Graham, P. Uerlings, T. Langen, M. Zwierlein, and T. Pfau, "Pattern formation in quantum ferrofluids: From supersolids to superglasses", Phys. Rev. Res. **3**, 033125 (2021).
4. J.-N. Schmidt*, **J. Hertkorn***, M. Guo, F. Böttcher, M. Schmidt, K. S. H. Ng, S. D. Graham, T. Langen, M. Zwierlein, and T. Pfau, "Roton Excitations in an Oblate Dipolar Quantum Gas", Phys. Rev. Lett. **126**, 193002 (2021).
5. **J. Hertkorn***, J.-N. Schmidt*, F. Böttcher, M. Guo, M. Schmidt, K. S. H. Ng, S. D. Graham, H. P. Büchler, T. Langen, M. Zwierlein, and T. Pfau, "Density Fluctuations across the Superfluid-Supersolid Phase Transition in a Dipolar Quantum Gas", Phys. Rev. X **11**, 011037 (2021).
6. F. Böttcher, J.-N. Schmidt, **J. Hertkorn**, K. S. H. Ng, S. D. Graham, M. Guo, T. Langen, and T. Pfau, "New states of matter with fine-tuned interactions: quantum droplets and dipolar supersolids", Rep. Prog. Phys. **84**, 012403 (2021).
7. **J. Hertkorn**, F. Böttcher, M. Guo, J. N. Schmidt, T. Langen, H. P. Büchler, and T. Pfau, "Fate of the Amplitude Mode in a Trapped Dipolar Supersolid", Phys. Rev. Lett. **123**, 193002 (2019).
8. M. Guo*, F. Böttcher*, **J. Hertkorn***, J.-N. Schmidt, M. Wenzel, H. P. Büchler, T. Langen, and T. Pfau, "The low-energy Goldstone mode in a trapped dipolar supersolid", Nature (London) **574**, 386 (2019).

*These authors contributed equally.

9. F. Böttcher, J.-N. Schmidt, M. Wenzel, **J. Hertkorn**, M. Guo, T. Langen, and T. Pfau, "Transient supersolid properties in an array of dipolar quantum droplets", Phys. Rev. X **9**, 011051 (2019).

Other publications

1. **J. Hertkorn**, and M. Fyta, "Electronic features of vacancy, nitrogen, and phosphorus defects in nanodiamonds", Electronic Structure **1**, 025002 (2019).
2. **J. Hertkorn**, J. Wrachtrup, and M. Fyta, "Vacancy defect centers in diamond: influence of surface termination", The European Physical Journal Special Topics **227**, 1591 (2019).
3. F. A. L. Souza, G. Sivaraman, **J. Hertkorn**, R. G. Amorim, M. Fyta, and W. L. Scopel, "Hybrid 2D nanodevices (graphene/h-BN): selecting NO_x gas through the device interface", J. Mater. Chem. A **7**, 8905 (2019).

Acknowledgment

I take this opportunity to thank everyone who contributed to the projects over the years and the people outside the projects who shaped what enabled me to write this thesis.

I am deeply grateful to my PhD advisor Tilman Pfau. Tilman created for my doctoral studies an environment that was challenging, full of support, and inspiring. Apart from physics, I can only hope to have learned from Tilman how a creative mind can flourish in the good times while using the bad times to become more powerful.

I thank Sebastian Loth for taking the co-reporter role for this thesis and for the flexibility in the arrangements.

To Hans Peter Büchler my gratitude goes for invaluable theory support before and during this thesis. Just before beginning undergraduate school in a brief conversation Hans Peter had a first chance to bias the route that I will be taking. I am grateful for the bias. I also thank Hans Peter for being the chairman for this thesis.

Sincere gratitude goes to Tim Langen. Starting from an excellent lecture by Tim, I learned that I wanted to learn more about the ultracold. Before and during this PhD, from Tim I have received nothing but support, advice, and I was never refused an opinion.

I thank Martin Zwierlein for the persistent questions and the creative suggestions brought into our group meetings at the beginning of my PhD. To my astonishment I learned then that some computer stuff I was fooling around with could be of interest to a wider range of people. Talking with Martin about something interesting is like testing one's' own body's aerodynamics in a wind tunnel and I am deeply grateful for reliving this chance towards the end of my doctoral research.

I thank the Vector foundation for generous support. Being selected as a principal investigator of a MINT-Innovationen ("STEM innovations") project simultaneous to my PhD completely changed my perspective, my independence, and my responsibilities during this time, for which I am deeply grateful.

I thank Mingyang Guo, Jan-Niklas Schmidt, Fabian Böttcher, and Matthias Wenzel. Mingyang was an important pillar for me in the transition time from old experimental setup to new one, presenting an example of accuracy and efficiency, and that not everything will be lost in relativism. I value greatly that Jan-Niklas engaged in mental combat with me already before I was part of the group. Without Jan-Niklas neither the early design of the new experimental setup nor our analysis of density fluctuations would have been possible. I thank Fabian Böttcher for being an advisor before and at the start of my PhD

and for taking me seriously whenever I had a question. I am grateful to Matthias Wenzel for leaving an impression in me of someone who is razor-sharp and relaxed at the same time and for motivating me the way he did, whether he wanted it or not.

I thank the "new-machine-team" including Kevin Ng, Paul Uerlings, Sean Graham, Ralf Klemt, Lucas Lavoine, and Fiona Hellstern. You all contributed significantly to our ever-evolving new experimental setup. With Kevin, Paul, and Sean together, I enjoyed metal-to-metal both as a sport and as a philosophical point of discussion. I am grateful to Ralf and Lucas for joining the new machine, adapting quickly, and being voices of experience and reason. I thank Fiona for diving in just as quickly and I look forward to how you together with the team control the new machine before it controls the team. Kevin, I thank you for engaging in sensible as well as nonsensical discussions with me at times when neither of them seemed sensible.

I thank the students that completed their projects in or with our team. In particular I thank Matthias Schmidt, Ninaad Adhvaryu, and Akshay Shankar for trusting in me to some extent with their thesis projects. Thanks to you I was challenged to see a subject from another point of view and I hope I have as a supervisor contributed positively to your success.

I thank the entire institute for the useful and sustainable atmosphere. In particular, I thank the IT team consisting of Harald Kübler, Fabian Munkes, Matthias Schmidt, Christian Hölzl, and Achim Scholz among others. Special thanks go to Harald Kübler and Fabian Munkes for being helpful and tolerant with my sometimes unusual needs in storage and computational tools. Also I want to thank the administration team Karin Otter, Murielle Naud-Barthelmeß, and Anne-Katrin Kriesch for keeping administrative burdens manageable. It happened that Anne-Katrin was bombarded by me with a statistically unlikely amount of mountains of extra paperwork, which was sorted out with professionalism at breathtaking speed and I am deeply grateful for the help.

I thank my family. I am certain that emerging from my background significantly influenced who I am today, and I am grateful for it.

Di, I thank you eternally.

List of Abbreviations

AOD acousto-optical deflector

AOM acousto-optical modulator

BdG Bogoliubov de-Gennes

BEC Bose-Einstein condensate

cMOT compressed magneto-optical trap

cODT crossed optical dipole trap

COM center of mass

eGPE extended Gross-Pitaevskii equation

GPE Gross-Pitaevskii equation

ML machine learning

MOT magneto-optical trap

ODT optical dipole trap

TC transversal cooling

TOF time of flight

ZS Zeeman slower

Zusammenfassung

Spontane Symmetriebrechung liegt vielen Aspekten unseres aktuellen Verständnisses der Natur zugrunde, von der Entstehung elementarer Teilchen bis zur Charakterisierung von Phasenübergängen in kondensierter Materie [10, 11]. Eine Symmetrie wird spontan gebrochen wenn die Gesetze, welche das Verhalten eines Systems bestimmen, eine bestimme Symmetrie aufweisen und ein Zustand entsteht welcher die Symmetrie mit diesen Gesetzen nicht teilt. Dieser Prozess ist gleichermaßen fundamental wie auch üblich in der Natur: Wenn ein ausreichend dichtes und wechselwirkendes Fluid (Gas oder Flüssigkeit) abgekühlt wird friert es schließlich und geht in einen Festkörper über, in welchem die Translationssymmetrie spontan gebrochen wurde. Die Unterscheidung verschiedener Phasen basierend auf deren Symmetrie geht auf L. Landau zurück [12]. Auch wenn nur ein externer Parameter, die Temperatur, geändert wurde um einen Festkörper aus einem Fluid zu erhalten, verhalten sich diese beiden Phasen drastisch unterschiedlich. Wenn diese in einem Behälter platziert werden nehmen Fluide die Form des Behälters an, während Festkörper steif bleiben und sich weniger leicht deformieren. Dieser emergente qualitative Unterschied hat mit dem Wettbewerb von Wechselwirkungen im System zu tun. In einem Festkörper ist das Verhalten seiner Bestandteile durch Wechselwirkungen zwischen Teilchen dominiert. In Gasen dominiert die kinetische Energie über Wechselwirkungen zwischen Teilchen und in Flüssigkeiten ist keine der beiden Energiebeiträge vernachlässigbar.

Der Wettbewerb von Wechselwirkungen zwischen Teilchen treibt nicht nur die Selbstorganisation der klassischen Phasen bei endlicher Temperatur. Alan Turing hat 1952 einen Satz an Reaktionsdiffusionsgleichungen vorgeschlagen, um den Ursprung von Musterbildung in der Entwicklungsbiologie, basierend auf dem Wettbewerb chemischer Reaktanten, zu erklären [13]. Die dynamisch selbstorganisierten Strukturen, welche als Lösungen aus diesen Gleichungen hervorgehen, sind seitdem als Turing Muster bekannt. Turing Muster sind allgegenwärtig in der Natur [14], von chemischen Mischungen [15, 16] über biologische Pigmentierungen [17] bis hin zu Vegetationsmustern [18–20]. Solche Muster sind in einem möglicherweise noch einfacheren und formalen System wieder auffindbar – einem Aktivator-Inhibitor zellularen Automaten [21]. Dieser besteht aus einem Gitter an Feldern, welche entweder aus oder an (tot oder lebendig), basierend auf ihrer direkten Umgebung, sind [22]. Diese Beispiele illustrieren, dass komplexes Verhalten aus relativ einfachen Bestandteilen hervorgehen kann, wie beispielsweise aus dem Wettbewerb zwischen eines aktivierenden und eines hemmenden Mechanismus für Selbstorganisation und dass die gleichen Muster in

weitgehend unterschiedlichen Systemen auftreten, unabhängig von ihren mikroskopischen Bestandteilen. Die hervorgehenden Phasen benötigen oft neue Gesetze, Konzepte, und Verallgemeinerungen um ihr Verhalten zu Beschreiben [10].

Bei niedrigen Temperaturen wird die Quantenmechanik entscheidend um emergentes Verhalten zu verstehen. Während die Temperatur erniedrigt wird, verringert sich die kinetische Energie und thermische Fluktuationen, welche klassische Phasenübergänge treiben, werden abgeschwächt. Die Wichtigkeit der relativen Wechselwirkungsstärken und der Quantenfluktuationen steigt. Deren Wechselwirkung treibt, am Temperaturnullpunkt, Quantenphasenübergänge zwischen Quantenphasen. Suprafluidität, der reibungsfreie Fluss von Teilchen, und Supraleitung, der Stromfluss ohne Widerstand, sind Grundpfeiler der faszinierenden Verhaltensweisen von Quantenphasen. Die erste Supraflüssigkeit wurde von K. Onnes in 1908 erzeugt indem er verflüssigtes Helium-4 unter den Lambda-Punkt $T_\lambda = 2.2\,\mathrm{K}$ abkühlte ohne von dessen supraflüssigen Eigenschaften zu wissen. Er benutzte es im Jahre 1911 um Quecksilber auf die Temperatur $T_c = 4.2\,\mathrm{K}$ zu bringen und stellte fest, dass der Widerstand auf nicht messbare Werte absank, womit er den ersten Supraleiter herstellte [23]. Kapitza [24], Allen und Misener [25] entdeckten den reibungsfreien Fluss von Helium-4 im Jahre 1938 und schlugen den Namen Supraflüssigkeit in Analogie zum supraleitenden Zustand vor [26]. Es dauerte mehrere Jahrzehnte um herauszufinden, dass diese beiden Phänomene ihren Ursprung in Bose-Einstein Kondensation haben [26–28]. Bose-Einstein-Kondensate (BEKs) wurden für lange Zeit als ein theoretisches Konstrukt angesehen, erstmals durch Bose und Einstein beschrieben [29–31] als eine makroskopische Besetzung des Quantenmechanischen Grundzustands eines bosonischen Mehrteilchensystem aufgrund von bosonischer Quantenstatistik. Die erfolgreichen phänomenologischen Zwei-Fluid Modelle der Supraflüssigkeiten und Tieftemperatur-Supraleitern, welche einen thermischen und einen weiteren Komponenten beschreiben, konnten trotzdem miteinander verbunden werden indem die nicht-thermische Komponente beschrieben wurde als BEK von bosonischen Teilchen für Supraflüssigkeiten und als BEK von Fermion-Paaren (Cooper-Paare) für Supraleiter nach Bardeen, Cooper und Schrieffer (BCS) Theorie [32].

Laserkühlungstechniken hin zu ultrakalten atomaren Gasen [33] und kontrollierbare Wechselwirkungen mit Feshbach Resonanzen [34, 35] haben ultrakalte Atome als Modellsysteme für Quanten-Vielteilchen Phänomene etabliert. Ein fundamentaler Durchbruch ist im Jahre 1995 gelungen durch die Realisierung von BEKs mit ultrakalten und ultraverdünnten atomaren Gasen in den Gruppen von C. Wieman & E. Cornell und W. Ketterle [36, 37]. Durch die Verwendung von ultrakalten Gasen mit Temperaturen unter $1\,\mu\mathrm{K}$ und Dichten

von $10^{20}\,\mathrm{m}^{-3}$ (acht Größenordnungen niedriger als die Dichte von Helium-4 bei T_λ) wurde eine Modellsystem für Studien von reinen BEKs realisiert. Atome bei ultrakalten Temperaturen entwickeln eine de-Broglie Wellenlänge auf der Größenordnung des Teilchenabstands und überlappen durch die Abkühlung der Atome zunehmend. Das BEK ist dann durch eine makroskopische Wellenfunktion beschrieben, welche das kollektive Verhalten der Atome als Ganzes beschreibt. Die Atome erwerben eine gemeinsame konstante globale Phase, was die $U(1)$ Symmetrie bricht. Das kollektive Verhalten des BEKs ist genau durch eine Molekularfeldtheorie beschrieben wobei Quantenfluktuationen und starke Korrelationen vernachlässigbar sind [27]. Die supraflüssigkeit von BEKs mit endlichen Wechselwirkungsstärken wurde bemerkenswert durch das Auftreten von Vortices demonstriert als das BEK in rotation gebracht wurde [38–40].

Modellsysteme spielen eine wichtige Rolle für das Verstehen und Vorhersagen von komplexen Vielteilchenphänomenen in heutiger Physik. Um R. Feynman's Vorschlag [41] von Quantensimulation – gut kontrollierbare Quanten-Vielteilchensysteme zu verwenden um das Verhalten von weniger gut kontrollierbaren Quanten-Vielteilchensystemen zu simulieren – zu realisieren ist die Komplexität vieler Plattformen mit ulrakalten Atomen gestiegen. Experimente wurden entwickelt zur Realisierung des BEK zu BCS Crossovers [28, 42], des Übergangs von Supraflüssigkeit zu Mott-Isolator [43, 44] und topologischer Zustände [45–47] in optischen Gittern, von Quantencomputern mit Dutzenden logischen Qubits [48–50] und von Hubbard-Modellen zur Quantensimulation von Festkörpern [44, 51–53]. Zum Beispiel erlaubt das unitäre Fermigas die Zustandsgleichung für das Suprafluid, welches im Kern von Neutronensternen vermutet wird, zu beschränken [54, 55] und es wird vermutet, dass das Fermi-Hubbard Modell wichtig für den Mechanismus der Hochtemperatursupraleitung [56–59] ist, wie zum Beispiel realisiert durch die Cuprate [60]. Um eine Größenordnung an Komplexität wie in ungewöhnlichen Supraleitern zu verstehen wurde ein interessanter Ansatz im Feld der kondensierten Materie mit dem Aufstieg der Twistronik verfolgt [61, 62]. Verglichen mit Verbindungen wie Cupraten erscheinen Materialien wie verdrehtes zweilagiges Graphen weniger strukturell komplex [61–63]. Dennoch etablierten diese Materialien ein Modellsystem für stark korrelierte Vielteilchenzustände in kondensierter Materie. Mit der Realisierung von verdrehtem zweilagigem Graphen und verdrehten mehrlagigen Strukturen [61, 62, 64] wurden einstellbare unkonventionelle Supraleitung [61, 62, 65], der fraktionale Quanten-Hall-Effekt und der fraktionale anomale Quanten-Hall-Effekt beobachtet [66, 67].

Ein exotischer Materiezustand, welcher vor über 60 Jahren im Kontext von flüssigem Helium vorhergesagt wurde, ist der Suprafestkörper [68–77]. In diesem Materiezustand

sind reibungsfreier Fluss einer Supraflüssigkeit und die Kristallstruktur eines Festkörpers gleichzeitig vorhanden [78]. Intensive und frühe theoretische Arbeit etablierte, dass ein Suprafestkörper möglich ist [75, 78–89], aber eindeutige experimentelle Beobachtungen eines Suprafestkörpers mit Helium konnten bis heute nicht festgemacht werden [83, 90–92]. Suprafestkörper wurden zuerst realisiert im Kontext von ultrakalten Gasen mit BEKs mit Spin-Orbit Kopplung [93, 94], in mehrmodigen optischen Resonatoren [95] und vor kurzem in dipolaren Quantengasen [9, 96, 97]. Diese Suprafestkörper erlauben Phonon-Anregungen weil die Kristallstruktur durch Wechselwirkungen bestimmt ist und nicht extern eingeprägt wird wie in Experimenten welche Atome in optischen Gittern gefangen halten [43, 51, 98–100].

Die Suche nach dem Suprafestkörper in dipolaren Quantengasen wurde ursprünglich Motiviert durch die Präsenz eines rotonischen Anregungsspektrums wenn diese Gase gefangen sind. Das rotonische Anregungsspektrum ist charakterisiert durch ein Minimum bei einem endlichen Wellenvektor, welcher eine charakteristische Längenskala für Selbstorganisation darstellt. Rotonische Anregungsspektra sind auch vorhanden in flüssigem Helium [101–105] und in klassischen Ferrofluiden [106–108]. Diese klassischen Ferrofluide, welche aus feinen magnetischen Partikeln, suspendiert in einer Flüssigkeit, bestehen, werden als ein Modellsystem für selbstorganisierte Musterbildung im Gleichgewicht betrachtet [106, 109–111]. Daher spielen sie eine vergleichbare Rolle wie das Aktivator-Inhibitor System, welches Turing für dynamische Musterbildung vorschlug. In dipolaren Quantengasen können die Wechselwirkungen so kontrolliert werden, dass das Roton-Minimum nahezu Null Anregungsenergie kostet. Wenn in einem BEK mit einer endlichen Wechselwirkungsstärke, welches eine gut kontrollierbare Supraflüssigkeit ist, spontan die Translationssymmetrie gebrochen werden würde und sich eine Kristallstruktur selbstorganisieren würde, dann wäre der Zustand ein Kandidat für einen Suprafestkörper.

Dipolare Quantengase wurden zuerst mit bosonischem Chromium [112], später mit bosonischem und fermionischem Dysprosium [113, 114] und Erbium [115, 116], und zuletzt mit Europium [117] realisiert. Diese atomaren Spezies außer Chromium sind Lanthanoide welche Größenordnungen höhere dipolare Wechselwirkungsstärken für dipolare BEKs bieten. Dysprosium, mit Terbium zusammen, hat die stärkste dipolare Wechselwirkung. Studien dipolarer Quantengase haben sich in ein eigenständiges Feld entwickelt seit der Kondensation von Chromium. Diese Studien beinhalten unter anderem Beobachtungen des d-Wellen Kollapses [118, 119] und Spinor-Physik in Chromium [120, 121], und mit Lanthanoiden wurden chaotische Streuung, erweiterte Bose-Hubbard Physik [51, 100],

Quanten-Hall Systeme [122, 123], und die rotonische Dispersionsrelation untersucht [4, 5, 104, 124–129]. Wenn die Wechselwirkungen in den Bereich kontrolliert wurden in welchem Chromium einen *d*-Wellen Kollaps unterging [118, 119], welcher sich gut durch eine Molekularfeldtheorie beschreiben lässt, ist das Dysprosium BEK anstatt dessen in mehrere, individuell stabilisierte Quantentröpfchen aufgebrochen [130]. Diese Beobachtung konnte nicht mit derselben Molekularfeldtheorie erklärt werden. Die Stabilisierung der Tröpfchen war derzeit nicht klar bis Experimente [131, 132] zeigten, dass Korrekturen über Molekularfeldtheorie hinausgehend wichtig sind [133–136]. Der Wettbewerb zwischen Wechselwirkungen beim Beginn der Tröpfchenbildung führt dazu, dass sich die Molekularfeldtheorie-Terme nahezu aufheben und machen die Korrekturen wichtig. Es wurde gezeigt, dass die Tröpfchen Quantenflüssige Eigenschaften besitzen [133, 137–139] und dass sie selbstgebunden sind, womit keine Notwendigkeit für ein Fallenpotential für ihre Stabilität besteht. Die Tröpfchen wurden darauffolgend hin als eine neue Art schwach wechselwirkende Quantenflüssigkeit studiert [140–145]. Erste Studien, welche mögliche Suprafestkörper-Eigenschaften in Tröpfchenanordnungen entlang einer Dimension untersuchten, fanden keine globale Phasenkohärenz über die Anordnung hinweg [146]. Diese Kohärenz ist eine Voraussetzung für supraflüssigkeit über die Anordnung hinweg ist. Eine theoretische Arbeit schlug einen Parameterbereich vor, in welchem diese Tröpfchenanordnungen in einem supraflüssigen Hintergrund liegend auftreten sollen [147]. Schnell konnten unsere und ähnliche Experimente zeigen, dass eine globale Phasenkohärenz in einem kleinen Wechselwirkungsstärkebereich aufrechterhalten werden kann [9, 96, 97]. Diese Beobachtungen haben den Ausgangspunkt für weitere Untersuchungen der phasenkohärenten Tröpfchenanordnungen markiert und die supraflüssigkeit des Systems konnte bewiesen werden indem die Existenz eines energetisch niedrig liegenden Goldstone Phonons [8], welches reibungsfreien Fluss von Teilchen durch den Tröpfchenkristall voraussetzt, gezeigt wurde. Zudem wurden höhere Kompressionsmoden beobachtet [96, 148]. Die Realisierung der dipolaren Suprafestkörper wurde somit in unserer Gruppe mit Dysprosium [9] und in zwei Gruppen in Pisa und Innsbruck mit Dysprosium und Erbium [96, 97] direkt vor dem Beginn dieser Dissertation erreicht.

In dieser Dissertation untersuchen wir selbstorganisierte Strukturen in dipolaren Quantenfluiden, indem wir stark dipolare BEKs in Bereichen betrachten in welchen der Wettbewerb zwischen Wechselwirkungen und Quantenfluktuationen Suprafestkörper und andere exotische Quantenphasen hervorbringen. Zuerst betrachten wir eindimensionale Anordnungen an Tröpfchen-Suprafestkörpern und untersuchen ihr Anregungssprektrum, welches

Goldstone-Moden und Higgs-Amplitudenmoden beinhaltet, und wir untersuchen den Strukturbildungsmechanismus. Wir schlagen theoretisch einen Suprafestkörper in einer Torusfalle vor, in welcher Anregungen entkoppelt sind und Ähnlichkeiten zu unendlich großen Suprafestkörpern und Analogien zu den Anregungen in Helium hervorgehen. Zweitens diskutieren wir den Strukturbildungsmechanismus in oblaten Fallengeometrien, in welchen die Tröpfchenkristallstrukturen in zwei Dimensionen auftreten. Wir zeigen, dass die dominanten Fluktuationen, welche den Übergang treiben, Roton-Anregungen mit einer winkelabhängigen Struktur entsprechen. Unsere theoretische Erweiterung dieser Studie zeigt welche Parameter angepasst werden müssen um einen Suprafestkörper mit einer zweidimensionalen Kristallstruktur zu erhalten. Wir diskutieren den dynamischen Formationsprozess des Suprafestkörpers sowie die Goldstone-Mode und Higgs-Amplitudenmode in zweidimensionalen Suprafestkörpern. Diese Studien und die meisten vorhergehende Studien zu dipolaren Suprafestkörpern haben sich auf den Fall konzentriert, bei dem die Kristallgitterplätze Quantentröpfchen entsprechen, welche sich in einer Kristallstruktur selbstorganisieren. Wir zeigen, dass andere Suprafestkörper und amorphe Zustände mit dipolaren Quantenfluiden bei größeren Dichten möglich sind. Diese Zustände selbstorganisieren eine Bienenwabenstruktur, Labyrinthstruktur, und weitere räumliche Strukturen, welche bisher nicht mit dipolaren Quantenfluiden experimentell beobachtet wurden. Gleichzeitig zu diesen Untersuchungen haben wir einen neues Quantengasexperiment entworfen und konstruiert, welches auf die Anspruchsvollen Dichten der neuen selbstorganisierten Phasen abzielt und mit modernen Ansätzen zur Experimentsteuerung ausgerüstet ist.

Die Ergebnisse und Techniken, welche in dieser Dissertation präsentiert sind, legen den Grundstein für das Verständis und die Erzeugung exotischer Phasen in dipolaren Quantenfluiden. Unsere Untersuchungen etablieren die Vielseitigkeit des stark dipolaren BEKs um mehrere selbstorganisierte Muster im ultrakalten und ultraverdünnten Regime zu bilden, was eine Quanten-Version des klassischen Ferrofluids darstellt – ein Modellsystem für selbstorganisiertes Gleichgewicht in schwach wechselwirkenden Quanten-Vielteilchen Systemen.

Contents

"More is different."

– Philip Anderson

Chapter 1

Introduction

Spontaneous symmetry breaking underlies many aspects of our current understanding of nature, from the emergence of elementary particles to the characterization of *phase transitions* in condensed matter [10, 11]. A symmetry is spontaneously broken when the laws governing a system exhibit a certain symmetry and a state arises that does not share that symmetry with those laws. The process is as fundamental as it is common throughout nature: When a sufficiently dense and interacting fluid (gas or liquid) is cooled, eventually it freezes into a solid in which translational symmetry has been spontaneously broken. The distinction of different phases of matter based on their symmetry goes back to Landau [12]. Although only one external parameter, the temperature, has been changed to obtain a solid out of a fluid, the two phases have drastically different behavior. When they are placed in a container, fluids acquire the shape of the container while solids remain rigid and do not deform as easily. This emergent qualitative difference relates to the competition of interactions in the system. In a solid, interparticle interactions dominate the constituents' behavior and the kinetic energy is negligible. In gases, the kinetic energy dominates over the interparticle interaction and in liquids neither energy contribution is negligible.

This theme of competing interactions giving rise to self-organized structures is not limited to the classical phases at finite temperature. In 1952 A. Turing suggested a set of reaction-diffusion equations to explain the *origin of patterns* observed in developmental biology based on the competition of chemical reactants [13]. The dynamical *self-organized spatial patterns* emerging as solutions to these equations have since become known as Turing patterns which are ubiquitous throughout nature [14] from chemical mixtures [15, 16] and biological pigmentations [17] to vegetation patterns [18–20]. Such patterns can be recreated in an arguably even simpler and formal system, which is an *activator-inhibitor* cellular automaton [21], consisting of a grid of fields that are either off or on (dead or

alive) depending on their immediate environment [22]. These examples illustrate that complex behavior can emerge from relatively simple components, like the competition between activation and inhibition mechanisms of self-organizing systems and that the same patterns occur in vastly different systems irrespective of their microscopic constituents. The emergent phases often require new laws, concepts, and generalizations for a description of their behavior [10].

At low temperature, quantum mechanics is key for understanding emergent behavior. As the temperature is lowered, the kinetic energy decreases and thermal fluctuations, which drive classical phase transitions, are diminished. The importance of the *relative interaction strength* and *quantum fluctuations* then increases. Their competition drives, at zero temperature, *quantum phase transitions* between *quantum phases*. *Superfluidity*, that is the frictionless flow of particles, and superconductivity, that is the flow of current without resistance, are cornerstones of the fascinating emergent behaviors of quantum phases. The first superfluid was produced by K. Onnes in 1908 by cooling liquefied helium-4 below the lambda point $T_\lambda = 2.2\,\mathrm{K}$ whilst not knowing of its superfluid properties at the time. He used it as a coolant to bring mercury to the temperature $T_c = 4.2\,\mathrm{K}$ in 1911, noting that the resistivity drops to non-measurable values, and thus the first superconductor was created [23]. Kapitza [24], Allen and Misener [25] discovered the frictionless flow of helium-4 in 1938 and suggested the name superfluid in analogy to the superconducting state [26]. It took several decades to discover that these two phenomena are rooted in *Bose-Einstein condensation* [26–28]. For a long time, Bose-Einstein condensates (BECs) were a theoretical construct initially described by Bose and Einstein [29–31] as a macroscopic occupation of the quantum mechanical ground state of a bosonic many-body system due to its bosonic quantum statistics. The successful phenomenological two-fluid models describing a thermal and a non-thermal component of superfluids and low-temperature superconductors could nonetheless be related by describing the non-thermal components as a BEC of bosonic particles for superfluids and as a BEC of fermion pairs (Cooper pairs) for superconductors described by Bardeen-Cooper-Schrieffer (BCS) theory [32].

Ultracold atoms were established via laser cooling techniques [33] and pristine control over their interactions using Feshbach resonances [34, 35] as *model systems* for studying quantum-many body phenomena. A fundamental breakthrough occurred in 1995 with the realization of BECs with ultracold and ultradilute atomic gases in the groups of C. Wieman & E. Cornell, and W. Ketterle [36, 37]. Using ultracold gases at temperatures below 1 µK and densities of $10^{20}\,\mathrm{m}^{-3}$ (eight orders of magnitude lower than the density of helium-4 at T_λ), a

model system for studies of pure BECs on their own terms was realized. Atoms at ultracold temperature develop a de-Broglie wavelength comparable to the interparticle spacing, leading to increasing overlap as the atoms are cooled. The BEC is then characterized by a macroscopic wavefunction that governs the collective behavior of the atoms as a whole. The atoms acquire a common constant global phase, spontaneously breaking the $U(1)$ symmetry. The collective behavior of the BEC is accurately described within a *mean-field* theory where quantum fluctuations and strong correlations are neglected [27]. The superfluidity of BECs with finite interaction strengths was remarkably demonstrated by the appearance of vortices when the BEC is stirred, signaling irrotational flow [38–40].

Model systems play a crucial role in understanding and predicting complex many-body phenomena in contemporary physics. In the spirit of R. Feynman's proposal [41] of *quantum simulation* – using well-controlled quantum many-body systems to simulate the behavior of less well-controllable and -measurable quantum-many body systems – many ultracold atom platforms are increasing in complexity for studying many-body correlations starting with individual atoms. Experiments have been devised to achieve the BEC to BCS crossover [28, 42], to explore the superfluid to Mott insulator transition [43, 44] and topological states [45–47] in optical lattices. Additionally, quantum computers with tens of logical qubits [48–50] and Hubbard models for the quantum simulation of solids [44, 51–53] were realized. The unitary Fermi gas allows to constrain the equation of state for the superfluid that is believed to be hosted in the core of neutron stars [54, 55] and the Fermi-Hubbard model is believed to be important for the mechanism of unconventional high-temperature superconductors [56–59] as realized for example with the cuprates [60]. To understand a level of complexity as observed with unconventional superconductors, an interesting approach was taken in the field of condensed matter with the rise of twistronics [61, 62]. Compared to compounds like cuprates, materials like twisted bilayer graphene [61–63] appear less complex structurally. Yet these materials have established a model system for the study of strongly correlated many-body states in condensed matter. Using twisted bilayer graphene and twisted multilayered structures [61, 62, 64], tunable unconventional superconductivity [61, 62, 65], the fractional quantum Hall effect, and the fractional anomalous quantum Hall effect have been observed [66, 67].

An exotic state of matter predicted over 60 years ago in the context of liquid helium is the *supersolid* [68–77], which combines the frictionless flow of a superfluid and the crystalline structure of a solid [78]. Intense and early theoretical work established that the supersolid is a possibility [75, 78–89]. Yet, experimental observations of the supersolid in liquid helium

have remained elusive to this day [83, 90–92]. Supersolids have been realized in ultracold gases using BECs with spin-orbit coupling [93, 94], in multimode optical cavities [95], as well as most recently in dipolar quantum gases [9, 96, 97]. These supersolids host *phonon excitations* since the crystal structure is predominantly determined by interactions and is not externally imposed like in experiments considering atoms in optical lattices [43, 51, 98–100].

The motivation for realizing supersolids with dipolar quantum gases originated from the *rotonic excitation spectrum* which develops when these gases are trapped. The roton excitation spectrum is characterized by a minimum at a finite wave vector, providing a characteristic length scale for self-organization. Rotonic excitation spectra are also present in liquid helium [101–105] and classical ferrofluids [106–108]. These classical ferrofluids, consisting of fine magnetic particles suspended in a fluid, are considered a *model system for self-organized equilibrium* [106, 109–111], similar to the dynamical activator-inhibitor system Turing suggested for dynamical pattern formation. In dipolar quantum gases, the interactions can be tuned such that the roton minimum approaches zero excitation energy. A supersolid could potentially form if spontaneous translational symmetry breaking occurs in this process and the interacting BEC, which forms a well-controlled superfluid, self-organizes into a crystal structure.

Dipolar quantum gases were first realized with bosonic chromium [112, 149], later with bosonic and fermionic *dysprosium* [113, 114] and erbium [115, 116] and most recently with europium [117]. The latter three atomic species are lanthanides, offering orders of magnitude stronger dipolar interaction for BECs than alkali atoms. Dysprosium has the strongest dipolar interaction in the periodic table, matched only by terbium. The study of dipolar quantum gases has advanced into a distinct field ever since the condensation of chromium. These studies include but are not limited to observations of a d-wave collapse [118, 119] and spinor physics [120, 121] in chromium, chaotic scattering in lanthanides [150, 151], extended Bose-Hubbard physics [51, 100], quantum Hall systems [122, 123], and the roton dispersion relation [4, 5, 104, 124–129]. When the interactions were tuned into a regime where chromium BECs underwent the d-wave collapse [118, 119] that is accurately described at a mean-field level, the dysprosium BEC instead fractured into an array of individually stable *dipolar quantum droplets* [130]. This observation could not be explained by a standard mean-field theory. The stabilization mechanism of these droplets was not clear at the time until experiments [131, 132] have demonstrated that quantum fluctuations beyond the mean-field have to be taken into account [133–136]. The competing interactions

at the onset of the droplet formation leads to a near-cancellation of the mean-field terms and make the quantum fluctuation correction important. The droplets were shown to exhibit *quantum liquid* properties [133, 137–139] and that they can be self-bound with no need of an external confinement to stabilize them. The droplets were subsequently investigated as a new form of weakly-interacting quantum liquids [140–145]. First studies investigating potential supersolid properties in dipolar quantum droplet arrays arranged along one dimension found no global *phase coherence* across the droplet array [146], a prerequisite for superfluidity throughout the array. A theoretical study suggested a parameter range in which these quantum droplets would be found in a superfluid background [147] and rapidly our and related experiments showed that a global phase coherence can be maintained in a narrow interaction regime [9, 96, 97]. The superfluidity of the system was proved by showing the existence of a low-energy Goldstone phonon [8], which requires the superfluid flow of particles throughout the droplet crystal, and higher-lying compressional modes related were observed [96, 148]. The realization of the dipolar supersolids in our group with dysprosium [9] and two groups in Pisa and Innsbruck with dysprosium and erbium [96, 97] occurred right before the start of this thesis.

In this thesis, we investigate self-organized structures and excitations in dipolar quantum fluids by considering strongly dipolar BECs of dysprosium in regimes where the competition between interactions and quantum fluctuations gives rise to supersolids and other exotic quantum phases. First, we consider one-dimensional supersolid arrays of quantum droplets and investigate their excitation spectrum, including Goldstone and Higgs amplitude modes, as well as the their structure formation mechanism. We propose theoretically a supersolid in a toroidal trap, in which excitations are decoupled, similarities to infinite dipolar supersolids arise, and analogies to excitations in helium are emerging. Second, we discuss the structure formation mechanism in oblate trapping geometries, where crystal structures of droplets arrange in two dimensions. We show that the dominant fluctuations driving the transition correspond to roton excitations with an angular structure. Our theoretical extension of this work shows how parameters need to be adjusted to establish a supersolid with a two-dimensional crystal structure and we discuss the supersolid dynamical formation process as well as the Goldstone and Higgs amplitude modes in two-dimensional supersolids. These studies and most previous studies on dipolar supersolids have focused on the case where the crystal sites correspond to individual quantum droplets that self-organize in a crystal structure. We further show that other supersolid and amorphous states are possible in dipolar quantum fluids towards higher densities. These states self-organize in honeycomb,

labyrinthine, and other spatial patterns, which have so far not been observed with dipolar quantum fluids. Simultaneously to these investigations we have designed and constructed a new quantum gas experimental setup for dysprosium that is geared towards the challenging density regimes required for the observation of the new predicted self-organized phases and is equipped with modern approaches to experimental control.

The results and techniques presented in this thesis lay the foundation for understanding and creating exotic phases in dipolar quantum fluids. Our work establishes the versatility of the strongly dipolar BEC to realize several self-organized patterns in the ultracold and ultradilute regime, suggesting it as a quantum version of the classical ferrofluid – a model system for self-organized equilibrium in weakly interacting quantum many-body systems.

Outline of the thesis

This thesis contains both theoretical and experimental results. Chapters 3-4 report on experimental results from our previous dysprosium setup combined with theoretical studies while chapter 5 focuses on the design, construction, and results of our new experimental setup. Therefore we focus in chapters 3-4 on the physics starting from dipolar BECs while the setup has been described in previous theses [152] including the last changes on this machine [129, 153] before its deconstruction.

- Chapter 2 introduces theoretical background, concepts, and intuition useful for understanding the following chapters and puts them into a theoretical framework. Additionally, numerical methods are introduced in this chapter which are employed throughout the subsequent chapters.

- Chapter 3 focuses on supersolids created by the self-organization of dipolar quantum droplets in one direction. We discuss the ground state phase diagram, the excitations, and the density fluctuations leading to the supersolid formation in this chapter.

- Chapter 4 focuses on structures that form in oblate trapping geometries. We discuss the crystal structure formation mechanism of two-dimensional arrays of quantum droplets by considering the elementary excitations of dipolar quantum fluids. We explain theoretically how parameters are adapted to realize supersolids with two-dimensional crystal structures and discuss the modifications of the excitation spectrum as well as the supersolid formation dynamics. We also show the emergence

of supersolid honeycomb and amorphous labyrinthine states in these trapping geometries, discuss their properties and the relevance of these structures for future experiments with dipolar quantum fluids.

- Chapter 5 details the design and construction of a dysprosium quantum gas experimental setup and first results. A vacuum system was assembled that overcomes limitations of the previous experimental setup, a new experimental control software was devised, and we achieved magneto-optical traps (MOTs) and BECs of dysprosium with the new setup.

- Chapter 6 concludes this thesis and gives an outlook regarding the new self-organized quantum phases and experimental setup.

"If I have seen further it is by standing on the shoulders of giants."

– Isaac Newton

Chapter 2

Theoretical background

Chapter Contents

This chapter introduces the theoretical background used to understand and model self-organized structures and excitations in dipolar quantum fluids. Due to the breadth of topics involved we refer to several references for further discussion. The purpose of this chapter is to comprehensively assemble essential concepts underlying the rest of this thesis.

2.1. Phases and symmetry

Here we introduce a minimal model of Ginzburg-Landau theory and review non-exhaustively the connections between spontaneous symmetry breaking, ordered phases, the order parameter, and the emergence of Goldstone and Higgs amplitude modes. The supersolid phase, which is a major focus in this thesis, is highlighted in this context.

2.1.1. Ginzburg-Landau theory

Ordered phases[1] are distinguished by their symmetry [10, 154]. Established by Landau [12] this viewpoint describes phases as classes of distinct symmetry which states of matter can be grouped into. Consequently at a phase transition the symmetry of a physical system changes. For example sufficiently dense fluids, including gases and liquids, have no periodic spatial order and eventually undergo a phase transition to a solid when they are cooled to lower temperatures [155]. The continuous translational symmetry of the fluid is broken and a crystal with discrete translational symmetry or an amorphous solid emerges.

Such a classification of phases entails an intimate connection to the concept of spontaneous symmetry breaking [156] describing the situation where the Hamiltonian of a system is invariant with respect to a symmetry operation while the ground state is not [157]. As the symmetry is spontaneously broken, the newly emerged state has a higher degree of order and correspondingly lower symmetry. The appearance of the order is described by an order parameter that is zero in the disordered (higher symmetry) phase and acquires a finite value in the ordered (lower symmetry) phase. With these concepts in mind a general understanding of phase transitions can be gained by considering the free energy of the system and expanding the energy in terms of its order parameter. To illustrate the generality we consider the generic Ginzburg-Landau free energy functional

$$\begin{aligned} F[\Phi] &= \alpha(\lambda)|\Phi|^2 + \beta(\lambda)|\Phi|^4, \\ \hookrightarrow F(A,\varphi) &= \alpha(\lambda)A^2 + \beta(\lambda)A^4, \end{aligned} \tag{2.1}$$

where terms of higher order in $A = |\Phi|$ of the order parameter $\Phi = Ae^{i\varphi}$ are neglected and $\beta > 0$. This expansion is valid near the phase transition point where the order parameter is small. The control parameter λ and the choice of the order parameter depends on the

[1] Or symmetry broken phases, as opposed to phases with no broken symmetry characterized by topological order or other symmetry constraints [154].

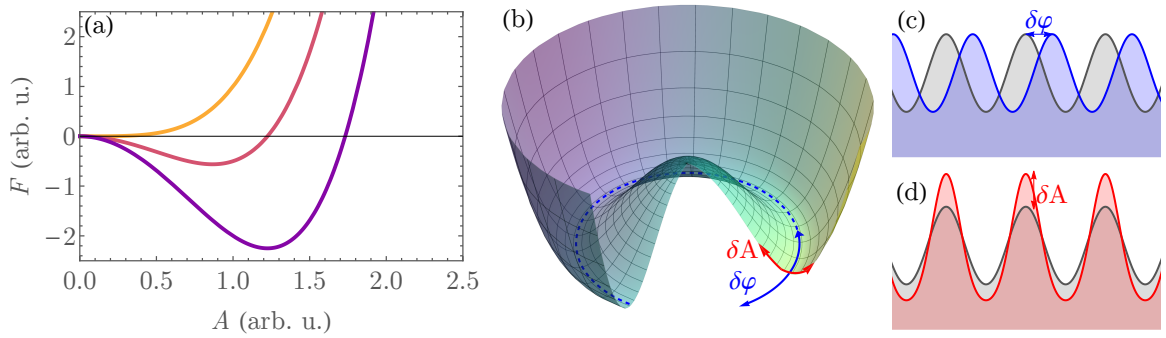

Figure 2.1.: **Sombrero potential and excitations.** (a) Free energy F (Eq. (2.1)) across a second order phase transition controlled by λ for $\alpha/\beta = 0,\ -1.5,\ -3$ from yellow to purple. Across the transition the order parameter minimizing the energy continuously grows, attaining a finite value in the ordered phase. (b) The free energy in the ordered phase as a function of (A, φ) has the shape of a sombrero hat, allowing for gapless (zero-energy) phase excitations $\delta\varphi$ along the brim of the hat and gapped (finite-energy) excitations δA along the curved direction orthogonal to ϕ corresponding to gapless Goldstone and gapped Higgs modes, respectively. (c)-(d) Schematic of a supersolid ground state density (grey) as a function of position and schematic of possible gapless Goldstone (c) and gapped Higgs (d) excitations.

physical system. For example in superconductors described by Bardeen-Cooper-Schrieffer theory [32, 158] $|\Phi|^2$ and φ correspond to the superconducting density and phase of the wavefunction, respectively, and the control parameter corresponds to the temperature. The terms appearing in the expansion Eq. (2.1) inform about the symmetry of the system. The absence of a term $\propto A^3$ implies that the energy is independent of the sign of the order parameter which we assume here for the discussion. When the control parameter λ is tuned in such a way that α becomes negative, Eq. (2.1) is minimized at a finite order parameter modulus $A = A_0 = \sqrt{-\alpha/2\beta}$ with $F(A_0, \varphi) = -\alpha^2/4\beta$ for any φ (Fig. 2.1(a)). The ground state acquires some φ, spontaneously breaking the symmetry in the emergent phase. Time dependent Ginzburg-Landau theory [11, 153, 159, 160] extends the expansion in Eq. (2.1) with time dependent fluctuations of the order parameter, allowing to study excitations of the ground state. We focus on a main result from this extension, namely that the symmetry broken state has two new characteristic excitations known as Goldstone [161–163] and Higgs modes (Fig. 2.1(b)).

The Goldstone mode corresponds to a gapless[2] phase excitation of the order parameter along the brim of the hat and the Higgs mode is an amplitude excitation of the order

[2] Except for the case where the symmetry is explicitly broken or when the matter is charged, which pushes the Goldstone energy to the plasma frequency [11, 164].

parameter and gapped away from the transition point. The Higgs mode we discuss here is a collective excitation as discussed in the context of condensed matter [11, 164] and distinct from the Higgs boson in elementary particle physics [165]. Due to the generality of the form for the energy (2.1) the Goldstone mode and Higgs amplitude modes appear in several systems. Goldstone modes arise necessarily when a symmetry is spontaneously broken [166] but a distinct Higgs amplitude requires the underlying theory giving rise to Eq. (2.1) to have equal orders in space and time derivatives (Lorentz invariance) [11, 164]. Galilean invariant theories such as the Gross-Pitaevskii theory for homogeneous superfluids have no Goldstone and Higgs modes with a distinct dispersion [11, 153, 159]. If the Galilean invariance is broken, for example through translational symmetry breaking, the existence of a stable Higgs mode cannot be ruled out [7, 167–169]. As these modes are excitations of the order parameter in a generic situation of spontaneous symmetry breaking, investigating the Higgs mode plays a central role in understanding the phase transition to various ordered phases. For example the Higgs amplitude mode has been discussed in a supersolid formed by mode populations in a crossed optical cavity [170] where the order parameter is a combination of the cavity field populations, in superconductors [171, 172], with quantum gases in optical lattices for the superfluid to Mott insulator transition [173] and in strongly interacting quantum gases [174, 175]. In these cases the Higgs mode is either stabilized by particle-hole symmetry giving rise to effective Lorentz invariance [11, 159] or a damped Higgs mode could be observed. Another stabilization mechanism was discussed for a confined Fermi system [176] where the confinement decouples the Higgs mode from other excitations.

We have shown the existence of a Higgs amplitude mode in harmonically trapped dipolar supersolids which is decoupled from other modes due to a finite trapping potential in a narrow range of interaction strengths [7]. This Higgs amplitude mode together with the corresponding Goldstone mode will be discussed as part of section 3.2 and these collective supersolid excitations play a role throughout chapters 3-4.

2.1.2. Supersolid

In this section the supersolid as part of the self-organized phases we study in this thesis will be put into the context of the concepts introduced in the previous section.

Supersolids are characterized by the simultaneous presence of the frictionless flow of superfluids and the crystal structure of solids. Formally this corresponds to the simultaneous

presence of off-diagonal and diagonal order in the system's density matrix [78]. The supersolids we consider throughout this thesis arise from interacting BECs which self-organize into states of matter that exhibit crystal or other spatial structures. Interacting BECs are superfluids with a broken $U(1)$ symmetry and as their density self-organizes into specific shapes, the translational or rotational symmetry is broken. In Fig. 2.1(c)-(d) this situation is schematically shown for a broken translational symmetry along one direction, where the Goldstone mode (Higgs amplitude mode) represents a phase shift (amplitude modulation) of the density modulation. This density modulation is the order parameter Φ of the supersolid and is directly connected to the superfluid fraction (section 3.1). The supersolids are described at zero temperature in a Gross-Pitaevskii framework (section 2.4) whose mean-field energy functional density corresponds to the free energy [177, 178] introduced in the last section and contains higher-order and nonlocal terms in Φ.

2.2. Bose-Einstein condensation

Bose-Einstein statistics were the basis for an alternative derivation of Planck's law for photons provided by S. Bose in 1924 [29]. Einstein generalized Bose's results to particles with finite mass M [30] and predicted that below a critical temperature T_c, a macroscopic fraction of bosons would occupy the same quantum state [31]. This quantum state is now known as Bose-Einstein condensate (BEC).

In the absence of interactions the phase transition from thermal gas to BEC is dictated only by quantum statistics. The state j with single-particle energy ϵ_j is occupied by non-interacting bosons at a temperature T on average by

$$\langle n_j \rangle = \frac{1}{\exp(\beta(\epsilon_j - \mu)) - 1} \tag{2.2}$$

particles, which is determined by $\beta = 1/k_{\mathrm{B}}T$ with the Boltzmann constant k_{B}, the chemical potential μ, and the total atom number $N = \sum_j \langle n_j \rangle$. For a given T the ground state occupancy $N_0 = \langle n_0 \rangle$ at the lowest energy ϵ_0 grows at a higher rate with μ than all higher occupancies $\langle n_{j>0} \rangle$ individually. For large particle numbers μ approaches ϵ_0 and the ground state becomes macroscopically occupied, which means that N_0 becomes on the order of N [27]. The condensate fraction N_0/N then depends on T. Qualitatively T_c can be estimated using the density n related to the mean inter-particle spacing $d = n^{-1/3}$, and the thermal

de-Broglie wavelength

$$\lambda_T = \sqrt{\frac{2\pi\hbar^2}{Mk_BT}} \tag{2.3}$$

describing the spatial extent of the individual particle's wavefunction with the reduced Planck constant $\hbar$. Quantum effects become important when d and λ_T become comparable $n\lambda_T^3 \approx 1$ and one estimates[3]

$$k_\mathrm{B}T_c \approx \frac{2\pi\hbar^2 n^{2/3}}{M}. \tag{2.4}$$

This estimate is closely connected to the notion that a condensate can be described by a single, macroscopic, coherent matter wave as λ_T increases and bosons enter a single quantum state.

The density and critical temperature of a Bose gas confined in an external potential depend on the shape of the confinement. We consider now the case of a trapped Bose gas in a spherical harmonic potential $V_\mathrm{ext}(\boldsymbol{r}) = M\omega^2|\boldsymbol{r}|^2/2$ where M is the atomic mass, $\boldsymbol{r}$ the position, and ω is the trap frequency. This situation arises often in experiments with atoms trapped in optical potentials created by laser light [181]. At zero temperature the ground state of the particle exchange symmetric many-body wavefunction in this harmonic confinement is

$$\psi(\boldsymbol{r}_1, \boldsymbol{r}_2, \ldots, \boldsymbol{r}_N) = \prod_j \phi_0(\boldsymbol{r}_j) \tag{2.5}$$

with the single-particle ground state wavefunction $\phi_0(\boldsymbol{r}) = \exp(-r^2/2x_0^2)/\pi^{3/4}x_0^{3/2}$ and the harmonic oscillator length $x_0 = \sqrt{\hbar/M\omega}$, resulting in a density of $n(\boldsymbol{r}) = N|\phi_0(\boldsymbol{r})|^2$. Taking into account the shape of the density allows to calculate the condensate fraction[4]

$$\frac{N_0}{N} = 1 - \left(\frac{T}{T_c}\right)^3 \tag{2.6}$$

and the critical temperature

$$k_\mathrm{B}T_c \approx 0.94\hbar\omega N^{1/3} \tag{2.7}$$

in a harmonic trap [27, 182]. Typical experimental conditions result in critical temperatures $T_c \lesssim 1\,\mu\mathrm{K}$ and at half the critical temperature the condensate fraction is about 90 %.

Interactions between particles yield further quantitative corrections to the critical

[3] An exact calculation shows $k_\mathrm{B}T_c = \zeta(3/2)^{-2/3}2\pi\hbar^2n^{2/3}/M$ with $\zeta(3/2)^{-2/3} \approx 0.53$ for a homogeneous Bose gas in a box, where ζ is the Riemann-Zeta function [179, 180]

[4] The exponent in Eq. (2.6)-(2.7) is characteristic of the harmonic confinement and depends on the density of states [182].

temperature [183–185] of trapped BECs but also qualitatively change their fundamental properties and behavior. For example BECs without atomic interactions have a vanishing Landau critical velocity while a finite interaction strength lifts the critical velocity to a finite value, which is the superfluid speed of sound of BECs [27, 180]. Further, interactions provide the basis for self-organization of structures in BECs that we study in later chapters. In the presence of interactions the many-body wavefunction does not factorize into a product of single-particle states as in Eq. (2.5) and a formal definition of BECs is desirable. The density matrix formalism addresses this demand [180]. In this formalism the bosonic[5] field operators $\hat{\psi}(\boldsymbol{r})^\dagger$ ($\hat{\psi}(\boldsymbol{r})$) creating (annihilating) a particle at point $\boldsymbol{r}$ define with their expectation value the one-body density matrix

$$n^{(1)}(\boldsymbol{r},\boldsymbol{r'}) = \langle \hat{\psi}^\dagger(\boldsymbol{r})\hat{\psi}(\boldsymbol{r'})\rangle \,. \tag{2.8}$$

The diagonal components correspond to the density distribution $n(\boldsymbol{r}) = n^{(1)}(\boldsymbol{r},\boldsymbol{r})$. The coherence properties of the condensate are investigated using the off-diagonal components by introducing the relative coordinate $s = |\boldsymbol{r} - \boldsymbol{r'}|$. For homogeneous BECs $\lim_{s\to\infty} n^{(1)}(\boldsymbol{r},\boldsymbol{r'}) = n_0$ tends to a finite value, which is the density in the zero momentum or condensate state, and describes the existence of off-diagonal long range order [27]. Considering the case of a trapped condensate [180] the density matrix

$$n^{(1)}(\boldsymbol{r},\boldsymbol{r'}) = N_0\chi_0(\boldsymbol{r})^*\chi_0(\boldsymbol{r'}) + \sum_{j\neq 0} n_j\chi_j(\boldsymbol{r})^*\chi_j(\boldsymbol{r'}) \tag{2.9}$$

is expanded in its eigenfunctions χ_j where n_j are the eigenvalues of the one-body density matrix. This expression for the one-body density matrix characterizes BEC as a state where N_0 becomes of order N and as $s \to \infty$, the contribution $\propto N_0$ remains finite due to the condensate coherence while the sum over other momentum states tends to zero due to destructive interference. The coherence property of the condensate has been observed experimentally [186, 187].

An order parameter for the condensate can be defined by separating the field operator

$$\hat{\psi}(\boldsymbol{r}) = \chi_0(\boldsymbol{r})\hat{a}_0 + \sum_{j\neq 0}\chi_j(\boldsymbol{r})\hat{a}_j \tag{2.10}$$

[5] Bosonic field operators obey the commutation relations $[\hat{\psi}(\boldsymbol{r}),\hat{\psi}^\dagger(\boldsymbol{r})] = \delta(\boldsymbol{r}-\boldsymbol{r'})$ and $[\hat{\psi}(\boldsymbol{r}),\hat{\psi}(\boldsymbol{r})] = [\hat{\psi}^\dagger(\boldsymbol{r}),\hat{\psi}^\dagger(\boldsymbol{r})] = 0$.

into condensate and other components, where $\hat{a}_j$ ($\hat{a}_j^\dagger$) are the bosonic[6] annihilation (creation) operators of a particle in state χ_j. For a macroscopic ground state occupation $N_0 = \langle \hat{a}_0^\dagger \hat{a}_0 \rangle \gg 1$, Eq. (2.10) is the starting point for the Bogoliubov approximation which allows to describe the condensate as a combination of a classical field and quantum fluctuations. In this approximation $\hat{a}_0$ and $\hat{a}_0^\dagger$ are replaced by $\sqrt{N_0}$ and their commutator being unity is neglected. One obtains

$$\hat{\psi}(\boldsymbol{r}) = \psi(\boldsymbol{r}) + \delta\hat{\psi}(\boldsymbol{r}), \tag{2.11}$$

where we have defined the condensate wavefunction

$$\psi(\boldsymbol{r}) = \sqrt{N_0}\chi_0(\boldsymbol{r}) = \sqrt{N_0}|\chi_0(\boldsymbol{r})|e^{i\phi(\boldsymbol{r})} \tag{2.12}$$

and the fluctuation operator for the non-condensed component

$$\delta\hat{\psi}(\boldsymbol{r}) = \sum_{k\neq 0} \chi_j(\boldsymbol{r}) a_j. \tag{2.13}$$

The condensate wavefunction Eq. (2.12) plays the role of an order parameter for the BEC and encapsulates the coherence property of the condensate by the global phase ϕ. The condensate wavefunction can be multiplied by $e^{i\alpha}$ with any constant global phase factor α without changing any physical quantity ($U(1)$ symmetry). This reflects the gauge symmetry of all equations describing the condensate wavefunction. The bosons entering the condensate acquire a common global phase, corresponding to the spontaneous symmetry breaking of the $U(1)$ symmetry [157, 188–191].

Equations (2.11)-(2.13) lay the foundation for developing the extended Gross-Pitaeskii (eGPE) theory discussed in section 2.4. The field operator for the condensate is replaced by a classical field $\psi = \langle\hat{\psi}\rangle$ in Eq. (2.12) yielding a mean-field Gross-Pitaevskii equation and Eq. (2.13) describes beyond mean-field quantum fluctuations of particles out of the condensate even at zero temperature.

[6] Bosonic operators obey the commutation relations $[\hat{a}_i, \hat{a}_j^\dagger] = \delta_{ij}$ and $[\hat{a}_i, \hat{a}_j] = [\hat{a}_i^\dagger, \hat{a}_j^\dagger] = 0$.

2.3. Interactions in ultracold dipolar quantum fluids

In this thesis we focus on dipolar BECs made of dysprosium. These BECs have typical densities of 10^{19}–$10^{21}\,\mathrm{m}^{-3}$ and critical temperatures on the order of $T_c \simeq 100\,\mathrm{nK}$, which is ultradilute and ultracold in comparison to many other systems. For example an ideal gas at room temperature has a density of $10^{25}\,\mathrm{m}^{-3}$ and liquid ^{4}He at its superfluid transition temperature $T_\lambda = 2.2\,\mathrm{K}$ has a density of $10^{28}\,\mathrm{m}^{-3}$ [129, 192].

The low density and temperature of dipolar BECs allows to describe them accurately using a zero-temperature mean-field theory based on Eq. (2.11). Interestingly the competition of interactions in dipolar BECs makes the first order quantum fluctuation correction to this mean-field theory relevant, and allows dipolar BECs to behave as a quantum liquid for certain interaction strengths and as a quantum gas for others. The description for these regimes is introduced in section 2.4 within an extended mean-field theory. Remarkably this theory relies only on the use of pseudopotentials which encapsulate microscopic details between individual scattering events of atoms in analytic expressions that recover the low-energy scattering behavior of the true potential.

In this section we introduce the contact and dipolar interactions present in dipolar BECs and focus on the pseudopotenials relevant for the extended mean-field description. We briefly mention the underlying scattering phenomena but refer to a more detailed description within the framework of scattering theory to Refs. [180, 193, 194] and previous theses [107, 146, 152, 195–197].

2.3.1. Contact interaction

The interaction potential between atoms features a repulsive behavior at very short distances due to electrostatic repulsion and an attractive long-range behavior scaling as $-r^{-6}$ due to van der Waals interactions[7]. The typical inter-particle interaction range r_0 defined by this potential is much smaller than the inter-particle spacing at low densities $r_0 \ll n^{-1/3} = d$ and reduces the probability for three-body and higher order interactions. The low temperature limits the momentum $p = \hbar k = 2\pi\hbar/\lambda_T$ to low collisional energies with $kr_0 \ll 1$. The atoms are typically prepared in internal states that do not scatter inelastically but only elastically. High angular momentum states ($l > 0$) in the scattering process are suppressed at low temperatures due to the centrifugal barrier in the center

[7] The Lennard-Jones potential is a pseudopotential incorporating these properties.

of mass (COM) frame of the two-body problem and only spherically symmetric s-wave scattering processes occur for bosons [193, 196]. The low-energy behavior of the scattering process depends on a single parameter, which is the s-wave scattering length a_s [180, 193]. The effect on the outgoing s-wave at large interparticle distance is a phase shift proportional to a_s.

The pseudopotential describing this low-energy scattering process is the contact interaction [27, 180, 193]

$$V_s(\boldsymbol{r}) = g_s \delta(\boldsymbol{r}) \tag{2.14}$$

where

$$g_s = \frac{4\pi\hbar^2 a_s}{M} \tag{2.15}$$

is the contact interaction strength. This is the typical interaction also present in weakly or non-dipolar condensates as realized for example with alkali atoms [188]. The contact interaction strength is experimentally tunable using Feshbach resonances [34, 35, 198]. This resonance phenomenon occurs when the energy of a bound molecular state in the molecular potential of a closed channel between two atoms approaches the energy of the scattering state in the open channel [35]. The relative energy between the bound state and the scattering state can be brought into resonance using light or magnetic shifts. In the latter case the dependence between a_s and the magnetic field B for a Feshbach resonance can be expressed in the form

$$a_s(B) = a_{\mathrm{bg}} \left(1 - \frac{\Delta}{B - B_0}\right) \tag{2.16}$$

where Δ (B_0) describes the width (position) of the resonance and a_{bg} is the background scattering length far from resonances. The Feshbach resonances of dysprosium are briefly discussed in section 5.1. Feshbach resonances allow to tune the interaction in Eq. (2.14) from attractive ($a_s < 0$) to zero and to repulsive ($a_s > 0$). We consider the case $a_s > 0$ in this thesis since the dipolar interaction provides an attractive contribution to the total interaction energy and it is the competition between repulsive and attractive interactions that leads to the self-organization of phases we are most interested in. Magnetic fields at Feshbach resonances and negative scattering lengths lead to three-body recombination and atom loss [138, 152].

2.3.2. Dipolar interaction

To create a dipolar BEC, atoms are trapped in an external confinement and are cooled to quantum degeneracy in the presence of a magnetic field $\boldsymbol{B}$ that polarizes the atoms with magnetic moment $\boldsymbol{\mu}_m \parallel \boldsymbol{B}$. The interaction between two particles separated by a distance $|\boldsymbol{r}|$ and polarized along the magnetic field direction is given by

$$V_{\mathrm{dd}}(\boldsymbol{r}) = \frac{3g_{\mathrm{dd}}}{4\pi} U_{\mathrm{dd}}(\boldsymbol{r}) = \frac{3g_{\mathrm{dd}}}{4\pi} \frac{1 - 3\cos^2(\theta)}{|\boldsymbol{r}|^3}, \tag{2.17}$$

where $\theta \sphericalangle(\boldsymbol{\mu}_m, \boldsymbol{r})$ is the angle between the spin polarization direction and the relative position $\boldsymbol{r}$ and we introduced the dipolar interaction strength

$$g_{\mathrm{dd}} = \frac{4\pi\hbar^2 a_{\mathrm{dd}}}{M} \tag{2.18}$$

with the dipolar length

$$a_{\mathrm{dd}} = \frac{\mu_0 \mu_m^2 M}{12\pi\hbar^2} \tag{2.19}$$

for convenience in later notation. Here μ_0 is the magnetic constant.

The dipolar interaction is long range[8] and anisotropic. The angle dependence introduces anisotropy (Fig. 2.2). Particles in a side-by-side (head-to-tail) configuration repel (attract) each other and the interaction vanishes at the magic angle $\theta_{\mathrm{m}} = \arccos\left(1/\sqrt{3}\right) \approx 54.7°$. The relevant interaction strength in the presence of both contact and dipolar interaction is the relative dipolar strength

$$\epsilon_{\mathrm{dd}} = \frac{g_{\mathrm{dd}}}{g_s} = \frac{a_{\mathrm{dd}}}{a_s}, \tag{2.20}$$

comparing dipolar to contact interaction strength. The dipolar length determines the overall dipolar interaction strength $a_{\mathrm{dd}} \propto M\mu_m^2$ which reaches the highest value $a_{\mathrm{dd}} \simeq 130\, a_0$ with $\mu_m \simeq 10\, \mu_B$ (a_0 is the Bohr radius and μ_B the Bohr magneton) in the periodic table for dysprosium (see section 5.1).

In general all partial waves $l > 0$ contribute to the scattering process for dipolar particles and the question arises which pseudopotential reproduces the low-energy scattering behavior of the potential including all partial waves [199, 200]. It was shown that for low collisional energies compared to the dipolar interaction energy the scattering processes involve only s-wave channels [199, 201–203]. This regime is reached for dysprosium at collisional energies

[8] An interaction described by a r^{-n} potential is considered as long-range in d dimensions if $\int_{r_c}^{\infty} r^{-n} \mathrm{d}^d r$ diverges with a small cut-off r_c, yielding the condition $n \leq d$ [190, 197].

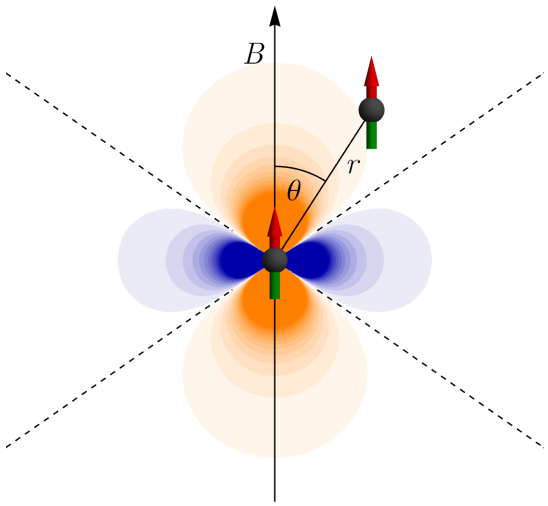

Figure 2.2.: **Dipolar interaction.** Two particles polarized along the magnetic field direction $\boldsymbol{B}$ at a distance $r = |\boldsymbol{r}|$ with an angle θ between the relative position and the polarization direction interact with the dipolar potential Eq. (2.17). The orange (blue) color indicates an attractive (repulsive) interaction $V_{\mathrm{dd}} < 0$ ($V_{\mathrm{dd}} > 0$) for a head-to-tail (side-by-side) configuration and the interaction vanishes $V_{\mathrm{dd}} = 0$ at the magic angle $\theta = \theta_m \approx 54.7°$ shown as dashed lines. The dipolar interaction is anisotropic due to the θ-dependence and long-ranged due to the radial r^{-3} decay.

on the order of 10 µK [197] such that dipolar BECs of dysprosium fall into the regime where contact and dipolar scattering amplitudes can be added. The total effective potential is

$$\begin{aligned} V(\boldsymbol{r}) &= V_s(\boldsymbol{r}) + V_{\mathrm{dd}}(\boldsymbol{r}) \\ &= g_s \delta(\boldsymbol{r}) + \frac{3g_{\mathrm{dd}}}{4\pi} \frac{1 - 3\cos^2(\theta)}{|\boldsymbol{r}|^3}. \end{aligned} \tag{2.21}$$

The Fourier transform of the dipolar potential

$$\tilde{V}_{\mathrm{dd}}(\boldsymbol{k}) = g_{\mathrm{dd}} \left(3\cos^2(\alpha) - 1\right) \tag{2.22}$$

is obtained after regularizing it at the origin [200, 204, 205] and is used in later sections for the Bogoliubov excitation spectrum of homogeneous dipolar quantum gases, the quantum fluctuation corrections, and the numerical simulations. Here α is the angle between the magnetic moment $\boldsymbol{\mu}_m \parallel \boldsymbol{B}$ and the wave vector $\boldsymbol{k}$ in momentum space.

In conclusion the total effective interaction of dipolar quantum gases can be described

by Eq. 2.21 and in momentum space by

$$\tilde{V}(\boldsymbol{k}) = g_s + g_{\mathrm{dd}} \left(3\cos^2(\alpha) - 1\right). \tag{2.23}$$

2.4. Gross-Pitaevskii framework

In this section we introduce an extended mean-field description for dipolar quantum fluids. The mean-field description for trapped quantum gases of section 2.4.1 is extended to include a beyond-mean field correction in section 2.4.2. This extended Gross-Pitaevskii equation is the main theoretical basis and the basis for the numerical description of the self-organized phases described in chapters 3-4. The extended Gross-Pitaevskii framework in dimensionless units reveals useful scaling relations, presented in section 2.4.3. A framework to investigate excitations and fluctutations of dipolar quantum fluids building on this extended Gross-Pitaevskii equation is introduced in section 2.4.4.

2.4.1. Gross-Pitaevskii equation

In the framework of second quantization [27, 206, 207], the Hamiltonian H of an interacting system of N particles[9] in an external potential V_{ext} can be written as

$$\begin{aligned} H = &\int \mathrm{d}^3 r \left[\hat{\psi}^\dagger(\boldsymbol{r}) \left(-\frac{\hbar^2\nabla^2}{2M} + V_{\mathrm{ext}}(\boldsymbol{r})\right) \hat{\psi}(\boldsymbol{r})\right] \\ &+ \frac{1}{2}\int \mathrm{d}^3 r\, \mathrm{d}^3 r'\ \hat{\psi}^\dagger(\boldsymbol{r})\hat{\psi}^\dagger(\boldsymbol{r}')V(\boldsymbol{r},\boldsymbol{r}')\hat{\psi}(\boldsymbol{r}')\hat{\psi}(\boldsymbol{r}) \end{aligned} \tag{2.24}$$

where $V(\boldsymbol{r},\boldsymbol{r}')$ is the potential of the two-body interaction and $\hat{\psi}^\dagger(\boldsymbol{r})$, $\hat{\psi}(\boldsymbol{r})$ are the field operators introduced in section 2.2. The time dependence of the field operator is given in the Heisenberg picture by $\partial_t\hat{\psi}(\boldsymbol{r},t) = \frac{i}{\hbar}[H,\hat{\psi}(\boldsymbol{r},t)]$ and results in the field equation of motion [206]

$$\begin{aligned} i\hbar\partial_t\hat{\psi}(\boldsymbol{r},t) = &\left(-\frac{\hbar^2\nabla^2}{2M} + V_{\mathrm{ext}}(\boldsymbol{r})\right)\hat{\psi}(\boldsymbol{r},t) \\ &+ \left(\int \mathrm{d}^3 r'\, \hat{\psi}^\dagger(\boldsymbol{r}',t)V(\boldsymbol{r},\boldsymbol{r}')\hat{\psi}(\boldsymbol{r}',t)\right)\hat{\psi}(\boldsymbol{r},t). \end{aligned} \tag{2.25}$$

[9] We restrict ourselves to two-body interactions and neglect three-body interactions or more generally, terms that contain more than two field operators. As we outlined in the previous section this is justified for dilute and ultracold BECs.

To move to a mean-field description we use the Bogoliubov approximation and Eq. (2.11) where we first keep the classical field $\hat{\psi} \approx \langle\hat{\psi}\rangle = \psi(\boldsymbol{r}, t)$ and neglect quantum fluctuations (2.13). We use the two-body interaction potential described in section 2.3 and obtain the dipolar Gross-Pitaevskii equation (dGPE)

$$i\hbar\partial_t\psi = \left(-\frac{\hbar^2\nabla^2}{2M} + V_{\text{ext}} + g_s|\psi|^2 + g_{\text{dd}}\int \mathrm{d}^3r' U_{\text{dd}}(\boldsymbol{r}-\boldsymbol{r}')|\psi(\boldsymbol{r}',t)|^2\right)\psi. \tag{2.26}$$

The dynamics of the condensate wavefunction is described by this nonlocal nonlinear integro-differential equation [133, 208, 209]. Without the dipolar interaction term, this equation reduces to the Gross-Pitaevskii or nonlinear Schrödinger equation which appears in various fields from nondipolar BECs to nonlinear optics [210] to pure mathematics [211].

Early experiments with dysprosium condensates showed that below a critical scattering length the condensate fractures into quantum droplets which are themselves smaller individual condensates and live up to hundreds of milliseconds [130]. These observations could not be explained with Eq. (2.26) as this theory predicts the dipolar collapse observed with more weakly dipolar chromium[10] condensates [119, 200]. It was found that the description of strongly dipolar condensates using Eq. (2.26) is incomplete and that the droplet stabilization is explained by taking beyond mean-field quantum fluctuations $\delta\hat{\psi}$ into account [131, 133].

2.4.2. Extended Gross-Pitaevskii equation

Here we introduce the first order correction to the dGPE, leading to an extended mean-field description that forms the basis of the numerical results in this thesis.

The starting point is to take the quantum fluctuation operator Eq. (2.13) into account. The first order correction is obtained by applying Bogoliubov theory to a homogeneous gas at zero temperature with density $n = N/V$ and expand the field operator $\hat{\psi} = V^{-1/2}\sum_{\boldsymbol{k}} \hat{a}_{\boldsymbol{k}} e^{i\boldsymbol{k}\boldsymbol{r}}$ [27, 197], keeping terms up to quadratic order of the operators $\hat{a}_{\boldsymbol{k}}$ in the Hamiltonian. The Hamiltonian is diagonalized using a Bogoliubov transformation [206, 212] and one obtains [206, 213, 214]

$$H = E_0 + \sum_{\boldsymbol{k}\neq 0} \hbar\omega_{\boldsymbol{k}}\hat{\alpha}^\dagger_{\boldsymbol{k}}\hat{\alpha}_{\boldsymbol{k}} \tag{2.27}$$

[10] ^{52}Cr has a magnetic moment of $\mu_{\text{m}} = 6\,\mu_{\text{B}}$ and a dipolar length of $a_{\text{dd}} \simeq 15\,a_0$. See also section 5.1.

where E_0 is the ground state energy,

$$\hbar\omega_{\boldsymbol{k}} = \sqrt{\tau_{\boldsymbol{k}}^2 + 2\tau_{\boldsymbol{k}} n \tilde{V}(\boldsymbol{k})} \tag{2.28}$$

is the Bogoliubov excitation spectrum, and $\hat{\alpha}_{\boldsymbol{k}}$ are related to $\hat{a}_{\boldsymbol{k}}$ by the Bogoliubov transformation. Here $\tilde{V}(\boldsymbol{k})$ is the two-body potential in momentum space and $\tau_{\boldsymbol{k}} = \hbar^2\boldsymbol{k}^2/2M$ is the free particle kinetic energy. The Hamiltonian including two-body interactions has been split up into a ground state energy and a set of non-interacting quasiparticles with creation and annihiliation operators $\hat{\alpha}_{\boldsymbol{k}}^\dagger$, $\hat{\alpha}_{\boldsymbol{k}}$ and the dispersion relation in Eq. (2.28). Due to interactions there is a finite population in the excited quasiparticle states. These particles are removed from the ground state, which leads to a quantum depletion Δn of the ground state density. The change in density is connected to a shift of the ground state energy and the chemical potential $\mu = \partial_N E_0$ is modified. These modifications are known as Lee-Huang-Yang (LHY) corrections

$$\frac{\Delta n}{n} = \frac{8}{3\sqrt{\pi}}\sqrt{n a_s^3} \tag{2.29a}$$

$$\Delta\mu = \frac{32}{3\sqrt{\pi}} g_s n \sqrt{n a_s^3} \tag{2.29b}$$

first derived by Lee, Huang, and Yang in 1957 [215] for a contact-interacting gas. A next order correction $\mu \propto n a_s^3 \ln(n a_s^3)$ considering three-particle interactions is known for contact-interacting gases, derived by Wu in 1959 [216].

The gas parameter $\eta = n a_s^3$ quantifies weakly interacting systems with $\eta \ll 1$ [27] corresponding to small quantum depletions (2.29a). At a typical scattering length of $a_s = 100\, a_0$ even the highest densities on the order of $10^{21}\,\mathrm{m}^{-3}$ for quantum droplets and other structures we investigate in this thesis fall into the regime $\eta < 10^{-3}$ with quantum depletion $\Delta n/n < 5\,\%$. By tuning the scattering length near a Feshbach resonance the effect of a finite quantum depletion due to quantum fluctuations could be observed with an alkali gas in a box potential [217]. In comparison, strong interactions in ^{4}He result in a high quantum depletion leaving less than $10\,\%$ condensate fraction [218, 219]. These values underline that the mean-field Gross-Pitaevskii framework is suitable for the weakly interacting bose gases while strong correlations in systems such as ^{4}He require quantum Monte Carlo techniques for an accurate description [218–220].

The results (2.29) have been generalized for homogeneous systems with dipolar interac-

tions [134–136, 221] to

$$\frac{\Delta n}{n} = \frac{8}{3\sqrt{\pi}}\sqrt{n a_s^3} Q_3(\epsilon_{\mathrm{dd}}) \tag{2.30a}$$

$$\Delta\mu = \frac{32}{3\sqrt{\pi}} g_s n \sqrt{n a_s^3} Q_5(\epsilon_{\mathrm{dd}}) \tag{2.30b}$$

with $Q_l(\epsilon_{\mathrm{dd}}) = \frac{1}{2}\int_0^\pi \mathrm{d}\alpha \sin(\alpha)\left[1+\epsilon_{\mathrm{dd}}(3\cos^2(\alpha)-1)\right]^{l/2}$. Q_3 and Q_5 develop a small imaginary part for $\epsilon_{\mathrm{dd}} > 1$ which is an artifact due to the use of the local density approximation in the derivation of Eq. (2.30) as a three-dimensional dipolar gas exhibits a phonon instability at $\epsilon_{\mathrm{dd}} > 1$ [169, 222]. The imaginary parts are negligible for the regimes investigated in this thesis and the series expansion for the relevant function $Q_5(\epsilon_{\mathrm{dd}}) \approx 1 + 3\epsilon_{\mathrm{dd}}^2/2$ is an excellent approximation [136, 144, 223]. Nonetheless the artifact indicates that quantum fluctuation corrections of inhomogeneous dipolar BECs are desirable [222]. In lack of such a theory the state-of-the art description for quantum fluctuations in weakly-interacting dipolar BECs is given by Eq. (2.30).

We incorporate these results into the dGPE within the the local density approximation [130, 136] where n is identified with $|\psi(\boldsymbol{r})|^2$. The chemical potential shift $\Delta\mu(\boldsymbol{r}) = g_{\mathrm{qf}}|\psi(\boldsymbol{r})|^3$ for the dGPE leads to the extended dipolar Gross-Pitaevskii equation (eGPE)

$$i\hbar\partial_t\psi = \left(-\frac{\hbar^2\nabla^2}{2M} + V_{\mathrm{ext}} + g_s|\psi|^2 + g_{\mathrm{dd}}\int \mathrm{d}^3r' U_{\mathrm{dd}}(\boldsymbol{r}-\boldsymbol{r}')|\psi(\boldsymbol{r}',t)|^2 + g_{\mathrm{qf}}|\psi|^3\right)\psi, \tag{2.31}$$

with

$$g_{\mathrm{qf}} = \frac{32}{3\sqrt{\pi}} g_s a_s^{3/2}\left(1+\frac{3}{2}\epsilon_{\mathrm{dd}}^2\right). \tag{2.32}$$

Importantly compared to the dGPE, the eGPE includes the cubic quantum fluctuation term $\propto g_{\mathrm{qf}}|\psi|^3$ which has a stronger density scaling compared to the quadratic mean-field terms $\propto |\psi|^2$. The quantum fluctuation term is positive, providing a repulsive contribution which prevents dipolar collapse and allows for the stabilization of quantum droplets [130, 131, 133]. The validity of the extended mean-field description to describe such droplets stabilized by quantum fluctuations was shown using a path-integral Monte Carlo method [224]. The adaptation of the beyond mean-field corrections to different dimensions [169, 225, 226] and developing more accurate density functionals [227] are subjects of active research.

We define the operator

$$H_{\mathrm{GP}}[\psi] = -\frac{\hbar^2\nabla^2}{2M} + V_{\mathrm{ext}} + g_s|\psi|^2 + g_{\mathrm{dd}}U_{\mathrm{dd}} * |\psi|^2 + g_{\mathrm{qf}}|\psi|^3 \tag{2.33}$$

with the dipolar mean-field potential

$$\begin{aligned}\Phi(\boldsymbol{r},t) &= g_{\mathrm{dd}}\int \mathrm{d}^3r' U_{\mathrm{dd}}(\boldsymbol{r}-\boldsymbol{r}')|\psi(\boldsymbol{r}',t)|^2 \\ &= g_{\mathrm{dd}}U_{\mathrm{dd}} * |\psi|^2,\end{aligned} \tag{2.34}$$

where $*$ indicates convolution. Then the eGPE can be cast in the form

$$i\hbar\partial_t\psi = H_{\mathrm{GP}}[\psi]\psi. \tag{2.35}$$

The wavefunction[11] is normalized to the atom number $N = \langle\psi|\psi\rangle$. The dynamics of the dipolar quantum fluids we describe in this thesis are described by Eq. (2.35) and their ground states $\psi_0(\boldsymbol{r})$ correspond to the stationary solutions of Eq. (2.35). The chemical potential for a ground state is given by $\mu = \langle\psi_0|H_{\mathrm{GP}}[\psi_0]\psi_0\rangle \,/\, \langle\psi_0|\psi_0\rangle$.

A useful formulation of the eGPE is to consider it as the solution to the variational equation $i\hbar\partial_t\psi = \delta E/\delta\psi^*$ [147, 178, 180, 191, 207] where $\delta E/\delta\psi^*$ is the functional derivative [228–230] of the energy functional

$$E[\psi] = \int \mathrm{d}^3r \left(\frac{\hbar^2}{2M}|\nabla\psi|^2 + V_{\mathrm{ext}}|\psi|^2 + \frac{1}{2}g_s|\psi|^4 + \frac{1}{2}g_{\mathrm{dd}}|\psi|^2(U_{\mathrm{dd}} * |\psi|^2) + \frac{2}{5}g_{\mathrm{qf}}|\psi|^5\right). \tag{2.36}$$

Functions ψ minimizing the functional[12] (2.36) are stationary solutions of Eq. (2.35) [228]. In general analytic solutions for the ground states are unavailable and numerical techniques have to be used to solve Eq. (2.35) [234–236]. We have implemented several such methods, including imaginary time evolution for Eq. (2.35) as well as a conjugate gradient algorithm for Eq. (2.36) that we outline in section 2.6.

[11] We define the inner product (Dirac notation) $\langle\psi_1|\psi_2\rangle = \int \mathrm{d}^3r\ \psi_1^*(\boldsymbol{r})\psi_2(\boldsymbol{r})$ and $\langle\psi_1|A|\psi_2\rangle = \langle\psi_1|A\psi_2\rangle$ with an operator A.

[12] The energy functional is closely related to the chemical potential via virial relations [231–233].

2.4.3. Scaling relations

In this section we provide general scaling relations based directly on the eGPE in dimensionless units.

The ground state solution of the eGPE is determined by the energy functional in Eq. (2.36) and is specified by the external potential parameters and the interaction parameters (a_s, a_{dd}, N). In most cases of this thesis, the external potential parameters correspond to the trap frequencies of the harmonic confinement, but may be left general in case of other external potentials. We nondimensionalize Eq. (2.36) by introducing the rescaled variables $\tilde{t} = t\omega_0, \tilde{\boldsymbol{r}} = \boldsymbol{r}/x_s, \tilde{\psi} = \psi\sqrt{x_s^3/N}$ [2, 3, 236–238], with an arbitrary unit of length x_s on which we base the unit of time $\omega_0^{-1} = Mx_s^2/\hbar$ and energy $\epsilon = \hbar\omega_0$ and define the dimensionless energy functional per particle $\tilde{E} = E/N\epsilon$. After omitting the tildes the wavefunction is normalized to unity and we obtain $E = \int \mathrm{d}^3r\,(\mathcal{E}_0 + \mathcal{E}_{\mathrm{nl}})$ with $\mathcal{E}_0 = |\nabla\psi|^2/2 + (V_{\mathrm{ext}}/\hbar\omega_0)|\psi|^2$ and the nonlinear and nonlocal dimensionless energy density

$$\mathcal{E}_{\mathrm{nl}}(C, D, Q) = \frac{1}{2}C|\psi|^4 + \frac{1}{2}D|\psi|^2(U_{\mathrm{dd}} * |\psi|^2) + \frac{2}{5}Q|\psi|^5. \tag{2.37}$$

The dimensionless interaction strengths are given by

$$C = \frac{4\pi a_s N}{x_s}, \tag{2.38a}$$

$$D = \frac{4\pi a_{\mathrm{dd}} N}{x_s}, \tag{2.38b}$$

$$Q = \frac{4}{3\pi^2}\frac{C^{5/2}}{N}\left(1 + \frac{3}{2}\epsilon_{\mathrm{dd}}^2\right), \tag{2.38c}$$

where $\epsilon_{\mathrm{dd}} = D/C$. In this formulation, the dimensionless numbers (C, D, Q), or equivalently (C, D, N), in addition to the external trapping parameters specify distinct points in the parameter space of the eGPE framework. The corresponding operator for Eq. (2.33) in dimensionless units is

$$\tilde{H}_{\mathrm{GP}}[\psi] = -\nabla^2/2 + V_{\mathrm{ext}}/\hbar\omega_0 + C|\psi|^2 + DU_{\mathrm{dd}} * |\psi|^2 + Q|\psi|^3. \tag{2.39}$$

We find the most general way to reason about similarities between ground states at different physical parameters is by thinking a patch of the ground state phase diagram in the coordinate system (C, D, Q) that is subject to a geometric transform as a physical parameter is changed.

Both C and D are proportional to the linear density N/x_s. Consequently the solutions of the eGPE are the same along contours with $N/x_s = \text{const}$ in parameter space if quantum fluctuations are negligible [237, 239–241]. If quantum fluctuations are not negligible their effective strength is tunable along these contours. Let $(N, x_s) \to (N/s, x_s/s)$ for some scale s, then $(C, D, Q) \to (C, D, sQ)$. A concrete application of this scaling property for a harmonic external trap is revealed when basing the length scale $x_s = \sqrt{\hbar/M\omega_\alpha}$ ($\alpha = x, y,$ or z) on one of the trap frequencies ω_α. Then $N/x_s \propto N\sqrt{\omega_\alpha}$ and areas in parameter space (C, D) at (N, ω_α) are similar to those at $(N/s, \omega_\alpha s^2)$ but with larger (smaller) Q towards lower (higher) particle numbers and tighter (looser) traps. Similar scaling properties have also proven useful for BECs interacting with an induced gravity-like interaction [242, 243] and one-dimensional systems [244, 245], where they enabled the reduction of the parameter space dimension by one.

In a fixed trapping geometry there are only two independent parameters describing the phase diagram. With $x_s = 4\pi a_{\text{dd}}$ one has $(C, D) = (\epsilon_{\text{dd}}^{-1} N, N)$ [233]. In this case (C, D, Q) depend explicitly only on ϵ_{dd} and N. At a given particle number only different ratios ϵ_{dd} will lead to different solutions of the eGPE.

For atomic gases where the dipolar length is fixed, the two ways to explore the phase diagram towards higher particle numbers (higher densities) are to increase the bare atom number or to tighten the trap. All dimensionless interaction parameters (C, D, Q) increase monotonically in this direction. For molecular gases in the future [246, 247] the tunability of a_{dd} in addition to a_s allows to achieve higher (C, D, Q) at lower N by increasing both a_{dd} and a_s, probing regimes of dipolar quantum gases that are challenging to reach using dipolar atoms. Considering $(a_s, a_{\text{dd}}, N) \to (sa_s, sa_{\text{dd}}, N/s)$ leads to $(C, D, Q) \to (C, D, sQ)$, which is the same geometric transformation on (C, D, Q) as for $(N, x_s) \to (N/s, x_s/s)$ discussed above. Larger a_s and a_{dd} result in the same effective interaction parameter change as if one were to tighten the trap at lower a_{dd}. Ground states at lower molecular density and higher a_{dd} are expected to be similar to higher atomic density and lower a_{dd}. A lower density all other things being equal is favorable for lower three-body loss.

2.4.4. Bogoliubov-de Gennes equations and the structure factor

To describe the collective excitations of the ground states of trapped dipolar quantum fluids, the Bogoliubov-de Gennes (BdG) equations [177, 240, 248] have emerged as an important tool, especially recently for dipolar quantum droplets and supersolids [7, 125,

147, 205, 223]. We focus here on an outline of the derivation of the BdG equations while we provided additional details in Ref. [205] and refer for to Refs. [177, 240, 248] for further mathematical details.

Once a ground state $\psi_0(\boldsymbol{r})$ and its chemical potential μ of Eq. (2.35) is known we are interested in studying the oscillations of the wavefunction

$$\psi(\boldsymbol{r},t) = \left[\psi_0(\boldsymbol{r}) + \sum_j \lambda_j \left(u_j(\boldsymbol{r})e^{-i\omega_j t} + v_j^*(\boldsymbol{r})e^{i\omega_j t}\right)\right] e^{-i\mu t/\hbar} \tag{2.40}$$

around its equilibrium value ψ_0 with the Bogoliubov amplitudes u_j and v_j for small excitation amplitudes λ_i. The Bogoliubov amplitudes are normalized by $\int \mathrm{d}^3r\, u_i^*(\boldsymbol{r})u_j(\boldsymbol{r}) - v_i^*(\boldsymbol{r})v_j(\boldsymbol{r}) = \delta_{ij}$ [248] and after substituting Eq. (2.40) into the eGPE and keeping linear terms in λ_j we obtain the BdG equations

$$\begin{pmatrix} H_{\mathrm{GP}}[\psi_0] - \mu + \hat{X} & \hat{X} \\ -\hat{X} & -\left(H_{\mathrm{GP}}[\psi_0] - \mu + \hat{X}\right) \end{pmatrix} \begin{pmatrix} u_j \\ v_j \end{pmatrix} = \hbar\omega_j \begin{pmatrix} u_j \\ v_j \end{pmatrix} \tag{2.41}$$

with the coupling operator

$$\hat{X}\chi(\boldsymbol{r}) = \psi_0(\boldsymbol{r}) \int \mathrm{d}^3r' [V_{\mathrm{dd}}(\boldsymbol{r}-\boldsymbol{r}') + g_s\delta(\boldsymbol{r}-\boldsymbol{r}')]\psi_0^*(\boldsymbol{r}')\chi(\boldsymbol{r}') + \frac{3}{2}g_{\mathrm{qf}}|\psi_0(\boldsymbol{r})|^3\chi(\boldsymbol{r}) \tag{2.42}$$

defined[13] by its action on the functions $\chi = u_j,\ v_j$. Introducing

$$f_j = u_j + v_j \tag{2.43a}$$

$$g_j = v_j - u_j \tag{2.43b}$$

the BdG equations further simplify [240] to

$$\begin{pmatrix} 0 & H_{\mathrm{GP}}[\psi_0] - \mu \\ H_{\mathrm{GP}}[\psi_0] - \mu + 2\hat{X} & 0 \end{pmatrix} \begin{pmatrix} f_j \\ g_j \end{pmatrix} = \hbar\omega_j \begin{pmatrix} f_j \\ g_j \end{pmatrix}. \tag{2.44}$$

Applying the matrix in Eq. (2.44) again to Eq. (2.44) results in two decoupled equations

[13] In Eq. (2.41) we considered real-valued functions $\psi_0 = \psi_0^*$ and $\hat{X}^* = \hat{X}$ which applies for stationary frames of references, such as with Eq. (2.35). For rotating or translating frames of references, the wavefunction is complex and the BdG equations become complex [249, 250].

[177, 240]

$$(H_{\mathrm{GP}}[\psi_0] - \mu)(H_{\mathrm{GP}}[\psi_0] - \mu + 2\hat{X})f_j = \hbar^2\omega_j^2 f_j, \tag{2.45a}$$

$$(H_{\mathrm{GP}}[\psi_0] - \mu + 2\hat{X})(H_{\mathrm{GP}}[\psi_0] - \mu)g_j = \hbar^2\omega_j^2 g_j. \tag{2.45b}$$

It is sufficient to solve the eigenvalue problem for one of the two functions f_j, g_j since the other can be obtained using Eq. (2.44). We solve Eq. (2.45a) for f_j and obtain g_j for $\omega_j \neq 0$ from Eq. (2.44) as $g_j = (\hbar\omega_j)^{-1}(H_{\mathrm{GP}}[\psi_0] - \mu + 2\hat{X})f_j$. With f_j and g_j, u_j and v_j can be recovered[14] by inverting Eq. (2.43). Equations (2.45) host what is known as the neutral mode with $g_j = \psi_0$ and $\omega = 0$. Its origin is a choice for the phase of the ground state (in practice zero) in Eq. (2.40) and is not a physical degree of freedom [157]. For $g_j = \psi_0$ the expression $(H_{\mathrm{GP}}[\psi_0] - \mu)g_j = 0$ simply means that the ground state fulfills the eGPE. Equation (2.45a) also has a neutral mode [177].

Fluctuations and the structure factor

The BdG equations closely relate to linear response theory [27]. Equation (2.40) provides the linear response of the wavefunction for a given mode j once the BdG functions f_j, g_j have been obtained. This response is related[15] to the density and phase fluctuations

$$\delta n_j = f_j\psi_0, \tag{2.46a}$$

$$\delta\varphi_j = g_j/\psi_0, \tag{2.46b}$$

respectively. The linearized time evolution of the density $n_j(\boldsymbol{r}, t) = |\psi(\boldsymbol{r}, t)|^2$ for a given mode j is then given by

$$n_j(\boldsymbol{r}, t) = n_0(\boldsymbol{r}) + 2\lambda_j\delta n_j(\boldsymbol{r})\cos(\omega_j t) \tag{2.47}$$

with the ground state density $n_0(\boldsymbol{r})$. The total spatial power spectrum of the density fluctuations added to the wavefunction in Eq. (2.40) is known as the dynamic structure factor

$$S(\boldsymbol{k}, \omega) = \sum_j |\delta n_j(\boldsymbol{k})|^2 \, \delta(\hbar\omega - \hbar\omega_j) \tag{2.48}$$

[14] We also orthogonalize u_j, v_j to the condensate ψ_0 [248, 251, 252].

[15] In quantum hydrodynamics [205, 253, 254] the response of the wavefunction to density fluctuations δn and phase fluctuations $\delta\varphi$ can be written as $\psi = e^{i\delta\varphi_j}\sqrt{n_0 + \delta n} \approx \sqrt{n_0} + \delta n/2\sqrt{n_0} + i\sqrt{n_0}\delta\varphi$ keeping only linear order in the fluctuations.

with

$$\delta n_j(\boldsymbol{k}) = \int \mathrm{d}^3 r \, \delta n_j^*(\boldsymbol{r}) e^{i\boldsymbol{k}\cdot\boldsymbol{r}}. \tag{2.49}$$

The dynamic structure factor (2.48) has proven indispensable in understanding the discrete excitation spectrum [7, 8, 125, 128, 148] of trapped dipolar quantum fluids providing evidence of the roton dispersion relation [125, 128] and describing a discretized version of the band structure of supersolids [7, 8, 148]. The dynamic structure factor is connected with sum rules [255, 256] that found application to describe the compressibility and the scissors mode frequency[16] in dipolar gases [197, 256–258], and the superfluid fraction [257, 259]. These sum rules make use of the moments

$$m_p(\boldsymbol{k}) = \hbar^{p+1} \int_{-\infty}^{\infty} \omega^p S(\boldsymbol{k}, \omega) \, \mathrm{d}\omega. \tag{2.50}$$

In particular the static structure factor

$$S(\boldsymbol{k}) = \frac{1}{N} m_0(\boldsymbol{k}) = \frac{1}{N} \sum_j |\delta n_j(\boldsymbol{k})|^2 \tag{2.51}$$

is given by the zeroth moment. This relationship has been used to measure the density fluctuations in ultracold gases [260–262]. We apply this relationship between the structure factor, density fluctuations, and the excitation spectrum in sections 3.2.3, 4.1.2 to trapped dipolar quantum fluids [4, 5] where the structure factor measured from density fluctuations corresponds to a volume-integrated version of the two-body pair correlation function [129, 263]. Such pair-correlation functions have been measured in the Mott insulator state [264].

The dynamic structure factor (2.48) can be generalized to finite temperatures [27, 252, 265]

$$S(\boldsymbol{k}, \omega, T) = \sum_j |\delta n_j(\boldsymbol{k})|^2 \left[(\bar{n}(\omega_j, T) + 1) \delta(\hbar\omega - \hbar\omega_j) + \bar{n}(\omega_j, T) \delta(\hbar\omega + \hbar\omega_j) \right] \tag{2.52}$$

by taking into account the Bose occupation $\bar{n}(\omega, T) = (\exp(\hbar\omega / k_\mathrm{B} T) - 1)^{-1}$. The generalization is valid for $T \ll T_c$ where the condensate fraction is near unity [27]. As a result

[16] Using linear response of the angular momentum operator instead of the density fluctuations.

the static structure factor at low temperature becomes[17]

$$S(\boldsymbol{k},T)=\frac{1}{N}\sum_j|\delta n_j(\boldsymbol{k})|^2\coth\left(\frac{\hbar\omega_j}{2k_\mathrm{B}T}\right). \tag{2.53}$$

The above equations can be used in a fully trapped system including the beyond mean-field corrections by solving the BdG equations (2.45) numerically, providing discrete modes indexed by j and a discretized version of the excitation spectrum $\hbar\omega_j$ and related quantities like the structure factor components $\propto|\delta n_j(\boldsymbol{k})|^2$. In homogeneous systems or when the discretized modes approximate a continuous function like the Bogoliubov spectrum $\epsilon(\boldsymbol{k})=\hbar\omega(\boldsymbol{k})$ further useful relations are obtained [266, 267]. In a single-mode approximation where the main contribution to $S(\boldsymbol{k},\omega,T)$ occurs due to a single mode the general inequality $\varepsilon(\boldsymbol{k})\leq\sqrt{m_1(\boldsymbol{k})/m_{-1}(\boldsymbol{k})}$ becomes saturated, leading to [27, 267, 268]

$$S(\boldsymbol{k},T)=\frac{\hbar^2k^2}{2M\varepsilon(\boldsymbol{k})}\coth\left(\frac{\varepsilon(\boldsymbol{k})}{2k_\mathrm{B}T}\right) \tag{2.54}$$

which is a generalized version of the Feynman-Bijl equation [103]

$$S(\boldsymbol{k})=S(\boldsymbol{k},T=0)=\frac{\hbar^2k^2}{2M\varepsilon(\boldsymbol{k})}. \tag{2.55}$$

The single mode approximation is well-fulfilled for weakly-interacting systems ($\eta\ll1$) and breaks down at large momenta for $k\gg1/a_\mathrm{s}$ [269]. For more strongly interacting superfluids like helium the Feynman-Bijl equation becomes less accurate [27, 270]. The fluctuation-disspation theorem [27] also relates the structure factor to thermometric methods in ultracold gases [271, 272].

Equation (2.54) illustrates that low-energy modes cause peaks in the structure factor corresponding to enhanced fluctuations. In the case of dipolar quantum fluids, this is particularly important since the spectrum can have a minimum at a finite wave vector as we discuss in the next section. These low-energy modes with $\varepsilon(\boldsymbol{k})\ll k_\mathrm{B}T$ can cause further enhancement of fluctuations by small but finite temperatures. Then[18]

$$S(\boldsymbol{k},T)\simeq S(\boldsymbol{k},0)\frac{2k_\mathrm{B}T}{\varepsilon(\boldsymbol{k})}=\frac{\hbar^2k^2k_\mathrm{B}T}{M\varepsilon(\boldsymbol{k})^2} \tag{2.56}$$

[17] Using $\coth(x/2)=(e^x+1)/(e^x-1)=(1-e^{-x})^{-1}-(1-e^x)^{-1}$.
[18] Using $\coth(x)\approx1/x$ for $x\ll1$.

shows that the associated peak in the structure factor at finite temperature is enhanced by a factor of $\simeq 2k_{\mathrm{B}}T/\Delta_{\mathrm{rot}}$ and scales as $\propto T/\Delta_{\mathrm{rot}}^2$. Here Δ_{rot} is the excitation energy of the lowest modes at a finite wave vector, which is the roton gap for sufficiently dipolar or dense systems (section 2.5.1).

2.5. Self-organization in dipolar quantum fluids

In this section we clarify the mechanisms at the core of self-organization and pattern formation in dipolar quantum fluids. The contact interaction is short-ranged (local) and repulsive. The competition with the dipolar long-ranged (nonlocal) interaction leads to a mechanism for instability at the mean-field level where quantum fluctuatiuons are neglegted. This mechanism is understood by considering the Bogoliubov excitation spectrum of trapped dipolar quantum fluids which features a minimum at a finite wave vector that can reach zero excitation energy if the system is sufficiently dipolar or dense. Once exited at this wave vector, these so called roton modes lead to a local and spatially periodic increase in density which is a positive feedback mechanism for further population of roton modes (section 2.5.1). An indefinite increase in density is prevented by including the effect of beyond mean-field quantum fluctuations which add negative feedback (section 2.5.2).

With the combination of positive and negative feedback mechanisms to self-organization, dipolar quantum fluids have the key components present in mathematical models of pattern formation [111, 273] as proposed in 1952 by A. Turing [13] in the context of reaction-diffusion systems [274] but also present in the Swift-Hohenberg model [14, 275, 276] and in activator-inhibitor cellular automata [21, 22]. The attractive contribution to the dipolar interaction provides an activating mechanism while the contact interaction and quantum fluctuations provide an inhibiting mechanism to local density increase.

We focus here on specific regimes that can be investigated analytically, which helps to understand the mechanisms intuitively.

2.5.1. Roton excitations and fluctuations

For a three-dimensional (3D) homogeneous dipolar gas with density n the Bogoliubov dispersion (2.28) becomes

$$\hbar\omega_{3\mathrm{D}}(\boldsymbol{k}) = \hbar k\sqrt{\left(\frac{\hbar k}{2M}\right)^2 + \frac{ng_s}{M}\left[1+\epsilon_{\mathrm{dd}}(3\cos^2\alpha-1)\right]} \tag{2.57}$$

where $k = |\boldsymbol{k}|$ and we have used the interaction potential in momentum space (2.23). For an interacting system the Bogoliubov dispersion relation (2.57) behaves linear at small k and at large k quadratic with a shift due to the mean interaction strength ng_s and other interaction parameters. Phonons are sound modes with a linear dispersion relation. The phonon speed of sound is defined in general as $c_s = \lim_{k\to 0}\hbar\omega(\boldsymbol{k})/k$. For the dipolar gas the speed of sound $c_s(\alpha) = c_s^{(0)}\sqrt{1+\epsilon_{\mathrm{dd}}(3\cos^2\alpha-1)}$ is anisotropic in contrast to a purely contact interacting gas with speed of sound $c_s^{(0)} = \sqrt{ng_s/M}$. The homogeneous three-dimensional dipolar gas with $\epsilon_{\mathrm{dd}} > 1$ exhibits a phonon instability where $c_s(\alpha)$ becomes imaginary [169, 222]. The speed of sound is closely related to the Landau critical velocity [277] $v_c = \min_{\boldsymbol{k}}\hbar\omega(\boldsymbol{k})/(\hat{\boldsymbol{v}}\cdot\boldsymbol{k})$ proposed first by Landau [101, 102] to describe the superfluidity of liquid helium [24]. The critical velocity describes the lowest velocity $v > v_c$ at which an impurity moving through a superfluid along $\boldsymbol{v} = v\hat{\boldsymbol{v}}$ causes dissipation in the superfluid. Fluids with $v_c \neq 0$ are superfluids. Contact interacting BECs ($g_s > 0, \epsilon_{\mathrm{dd}} = 0$) are superfluids where the speed of sound is the critical velocity $c_s^{(0)} = v_c$ and dipolar BECs ($g_s > 0, \epsilon_{\mathrm{dd}} > 0$) are superfluids where the critical velocity is generally angle dependent [146, 277, 278]. In contrast, noninteracting BECs ($g_s = \epsilon_{\mathrm{dd}} = 0$) have a free particle dispersion relation $\hbar\omega = \hbar^2k^2/2M$ with $v_c = 0$ and are not superfluid.

A trapped dipolar BEC exhibits a strongly modified excitation spectrum [104, 241, 279, 280]. To investigate these modifications we consider a dipolar gas trapped harmonically $V_{\mathrm{ext}} = \frac{1}{2}M\omega_z^2z^2$ along the magnetic field direction z and free in the x–y-plane. The quasi two-dimensional (2D) regime is reached for strong confinements in comparison to the chemical potential $\hbar\omega_z \gg \mu$ where the density distribution along the z direction assumes the form of the harmonic oscillator ground state which is Gaussian $n(\boldsymbol{r}) = n(x,y)\exp(-z^2/l_z^2)/\sqrt{\pi}l_z$ with the harmonic oscillator length $l_z = \sqrt{\hbar/M\omega_z}$ [197, 241, 280]. In this case the z direction of the mean-field dipolar interaction (2.36) integrates out [104, 197, 200, 280]

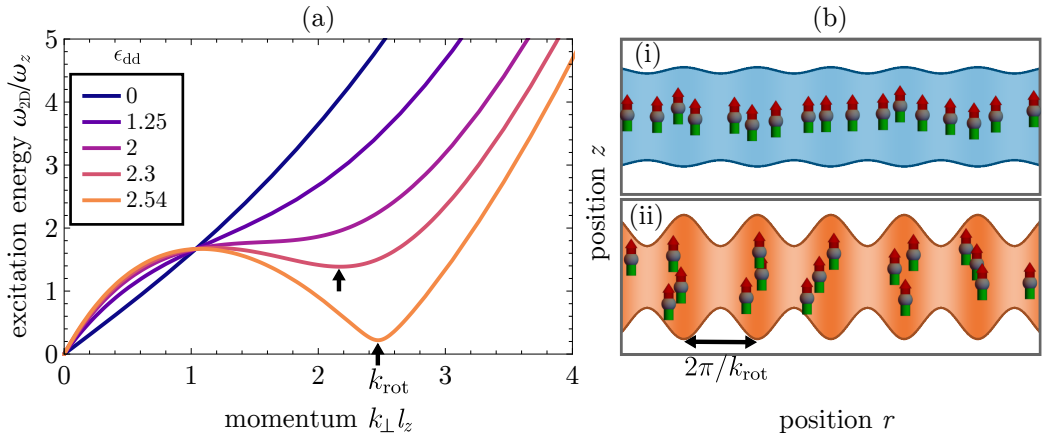

Figure 2.3.: **Roton excitation spectrum.** (a) Excitation spectrum (2.58) develops a roton-maxon structure for sufficiently high densities or relative dipolar interaction strengths $\epsilon_{\rm dd}$. The roton minimum at the roton momentum $k_{\rm rot}$ marked with arrows decreases (softens) towards higher $\epsilon_{\rm dd}$ reaching values close to zero. For these parameters roton modes can be excited at nearly no energy cost, providing a length scale $2\pi/k_{\rm rot}$ for self-organization. (b) Schematic illustration of density fluctuations induced by roton mode excitations. From low $\epsilon_{\rm dd}$ (i) to higher values (ii) roton modes are more easily populated and lead to a density wave where higher density regions provide additional attraction of further particles. Figure inspired by Refs. [125, 129]. Parameters for (a) are $n_0 = 10^{20}\,\mathrm{m}^{-3}$ and $\omega_z/2\pi = 250\,\mathrm{Hz}$ ($l_z \simeq 0.5\,\mu\mathrm{m}$).

and one obtains in total the spectrum of a quasi 2D dipolar gas

$$\hbar\omega_{\rm 2D}(k_\perp) = \hbar k_\perp \sqrt{\left(\frac{\hbar k_\perp}{2M}\right)^2 + \frac{n_0 g_s}{M}\left[1 + \epsilon_{\rm dd}\, F_\perp\left(\frac{k_\perp l_z}{\sqrt{2}}\right)\right]}. \tag{2.58}$$

Here $k_\perp$ is the in-plane momentum and $F_\perp(x) = 2 - 3\sqrt{\pi}\, x\, e^{x^2}\,\mathrm{erfc}(x)$ is a monotonously decreasing function from $F_\perp(0) = 2$ to $\lim_{x\to\infty} F_\perp(x) = -1$, with the complementary error function $\mathrm{erfc}(x)$ and $n_0 = n_{\rm 2D}/\sqrt{2\pi} l_z$ is the peak density defined by the in-plane density $n_{\rm 2D}$. The spectrum remains real-valued for $k_\perp \to 0$ if $1 + 2\epsilon_{\rm dd} > 0$ showing that the dipolar interaction prevents the phonon instability by being predominantly repulsive in-plane.

At larger momenta the spectrum develops a minimum that decreases or softens for higher densities n_0 and relative dipolar strengths $\epsilon_{\rm dd}$ (Fig. 2.3(a)). This minimum is known as the roton minimum and the momentum at which it occurs is the roton momentum $k_{\rm rot}$. At intermediate momenta a maximum remains, known as maxon. This roton-maxon spectrum is known from liquid helium [101–105]. The quasiparticle excitation at the roton momentum is known as roton, termed by Landau [101] and nowadays interpreted as a precursor to crystallization [281]. In liquid helium the interpretation of this excitation was complicated

due to its high density and the presence of strong correlations where the rotonic dispersion relation is fixed with the intrinsic interactions of helium. In quantum gas experiments the dispersion relation is tunable by changing the scattering length. The spectrum for weakly interacting gases also allows for a straightforward interpretation of the roton as a precursor to crystallization (Fig. 2.3(b)). At low relative dipolar interaction strengths ϵ_{dd} (i) the system is in equilibrium with a uniform in-plane density and excitations at finite momenta are energetically costly. Towards higher ϵ_{dd} (ii) as the roton minimum approaches zero excitation energy, at nearly no energy cost the excitations modulate the ground state density with a wave vector k_{rot} corresponding to the roton wavelength $\lambda_{\mathrm{rot}} = 2\pi/k_{\mathrm{rot}}$. In the absence of a stabilization mechanism the spectrum becomes imaginary for sufficiently high ϵ_{dd}, the magnetic particles accumulate in the high density regions (ii) and the system would undergo a roton instability mediated collapse. What was observed instead with dysprosium is the fracturing into individually stable quantum droplets [130, 282]. As explained in the next section the stabilization mechanism is the increase in quantum fluctuations towards higher densities. Several early theoretical and experimental studies have reported evidence of the rotonic dispersion relation in trapped three-dimensional dipolar gases by applying Bogoliubov theory [124, 126, 283], using scattering length quenches [125] or Bragg spectroscopy [128]. The interplay between rotonic dispersion relations and stabilization through quantum fluctuations is a main concept throughout chapters 3-4.

The mechanism of a low-energy excitation at a finite wave vector for structure formation is not limited to dipolar quantum fluids but a general occurrence in self-organizing systems [13, 14, 273, 284]. A direct analogy to the roton instability of dipolar quantum fluids is the Rosensweig instability in ferrofluids where the energy of a surface wave decreases with an externally applied magnetic field strength [106, 107, 285, 286]. As we outlined in section 2.4.4 softening excitations are generally connected to enhanced fluctuations within the framework of linear stability analysis [27, 273]. In essence this connection is encapsulated by the Feynman-Bijl relation $S(\boldsymbol{k}) = \hbar k^2/2M\omega(\boldsymbol{k})$ where the structure factor S is a measure for the density fluctuation strength. A roton minimum results in a structure factor peak at the roton momentum [267].

2.5.2. Density limitation, liquefaction, and quantum ferrofluids

To gain an intuitive understanding of the ground state behavior of dipolar quantum fluids we follow a variational approach [201, 287–290]. Variational methods in short assume a

trial wavefunction for the ground state depending on a set of parameters. The wavefunction is substituted into the energy functional Eq. (2.36) which then becomes dependent on these parameters and can be more directly minimized and understood than an arbitrary three-dimensional wavefunction. For our purpose here the variational approach offers the advantage that analytic expressions for the energy contributions can be obtained and analyzed.

We consider a cylindrically symmetric harmonic trapping potential $V_{\text{ext}} = \frac{1}{2}M(\omega_r^2\, r^2 + \omega_z^2\, z^2)$ with radial and transverse trap frequencies ω_r and ω_z, respectively. We substitute the Gaussian trial wavefunction

$$\psi(r,z) = \sqrt{\frac{N}{\pi^{3/2}\sigma_r^2\sigma_z}}\ \exp\left(-\frac{r^2}{2\sigma_r^2} - \frac{z^2}{2\sigma_z^2}\right) \tag{2.59}$$

with the two variational parameters $\sigma_r,\ \sigma_z$ for the width along radial and transversal directions in Eq. (2.36) and obtain

$$\begin{aligned} E(\sigma_r,\sigma_z) = {} & \frac{1}{4}N\frac{\hbar^2}{M}\left(2\sigma_r^{-2} + \sigma_z^{-2}\right) + \frac{1}{4}NM\left(2\omega_r^2\sigma_r^2 + \omega_z^2\sigma_z^2\right) \\ & + \frac{1}{2(2\pi)^{3/2}}\frac{g_s N^2}{\sigma_r^2\sigma_z}\left[1 - \varepsilon_{\text{dd}}\, f\!\left(\frac{\sigma_r}{\sigma_z}\right)\right] + \frac{2^{5/2}}{5^{5/2}\pi^{9/4}}\frac{g_{\text{qf}}N^{5/2}}{(\sigma_r^2\sigma_z)^{3/2}} \end{aligned} \tag{2.60}$$

for the total energy of the system [139, 141, 146]. From left to right the terms correspond to kinetic energy (quantum pressure), confinement energy, contact and dipolar interaction mean-field energies, and beyond mean-field quantum fluctuation energy. The anisotropy of the dipolar interaction is included in the function

$$f(\kappa) = \frac{1+2\kappa^2}{1-\kappa^2} - \frac{3\kappa^2\,\text{arctanh}\left(\sqrt{1-\kappa^2}\right)}{(1-\kappa^2)^{3/2}} \tag{2.61}$$

that depends on the density aspect ratio[19] $\kappa = \sigma_r/\sigma_z$. Despite the simple assumption of the wavefunction several phenomena of dipolar quantum fluids can be qualitatively understood with this approach. By minimizing this function for $\sigma_r,\ \sigma_z$, the tendency of dipolar BECs to elongate along the magnetic field direction (magnetostriction) [291, 292], the geometry dependent stability diagram, and the formation of a self-bound quantum droplet and its excitations can be understood [139, 141]. The energy minimization and above phenomena have been explained in depth in previous publications [139, 141, 197] and theses [129, 130,

[19] The dipolar interaction is mainly attractive (repulsive) for $\lim_{\kappa\to 0} f(\kappa) = 1$ ($\lim_{\kappa\to 0} f(\kappa) = -2$).

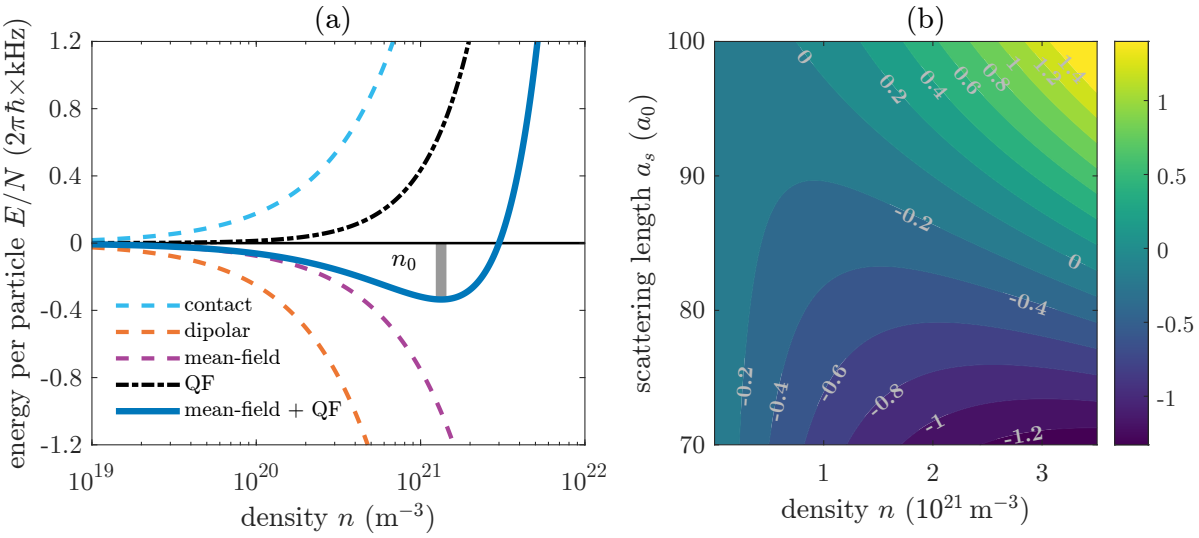

Figure 2.4.: **Energy contributions of dipolar quantum fluids.** (a) Towards high densities in dipolar quantum fluids elongated along the magnetic field direction the competition between repulsive contact and predominantly attractive dipolar interaction leads to an attractive mean-field (contact+dipolar) interaction. The repulsive quantum fluctuations (QF) with a steeper density scaling stabilize the system at a finite density $n_0 \simeq 10^{21}\,\mathrm{m}^{-3}$. The values $a_s = 85\,a_0$, $\sigma_z = 10\,\sigma_r$ and $\sigma_r = 0.3\,\mu\mathrm{m}$ and corresponding terms in Eq. (2.60) have been used. (b) The mean-field+QF energy per particle landscape for the same parameters of (a) as a function of a_s and n shows that towards smaller a_s the equilibrium density increases and saturates due to a large increase in quantum fluctuation for n on the order of n_0. The contours of a_s rise at small n and fall with n above n_0 indicating that quantum fluctuations take over the predominant stabilization role for densities of a few n_0.

152, 153, 197]. The Ansatz has also been extended to describe arrays of quantum droplets [143, 146, 293] and quantum mixtures [294].

To understand the interplay between interactions and quantum fluctuations we primarily focus on the scaling of the interaction terms. If we consider a dipolar gas and reduce a_s the repulsion of the contact interaction strength becomes smaller and the system becomes relatively more dipolar (larger ϵ_{dd}). The magnetic dipoles arrange increasingly in head-to-tail configuration, attract further atoms, and lead to an increase in the local density as shown in section 2.5.1. Eventually an elongated shape of a quantum droplet forms that has typically $\sigma_z \gtrsim 10\,\sigma_r$ [153, 197, 246]. If this runaway process would not be stopped the density would continue indefinitely towards an infinitely thin cigar-shaped cloud [119] that is precluded in the presence of three-body losses at high density leading to the d-wave collapse observed with ^{52}Cr atoms [118]. The dipolar length of dysprosium $a_{\mathrm{dd}} \simeq 8.6 a_{\mathrm{dd}}^{\mathrm{Cr}}$ is significantly larger than that of chromium $a_{\mathrm{dd}}^{\mathrm{Cr}} \simeq 15\,a_0$ leading to enhanced quantum

fluctuations (2.32). The interaction energy and quantum fluctuation contributions for the case of a typical dysprosium quantum droplet with and an elongated density with $\sigma_z = 10\,\sigma_r$ and $\sigma_r = 0.3\,\mu\text{m}$ are shown in Fig. 2.4(a) for $a_s = 85\,a_0$. Contact and dipolar interaction counteract one another and the indefinitely decreasing mean-field sum would lead to dipolar collapse as the density $n = N/\sigma_r^2\sigma_z$ increases. The mean-field scaling $\propto n$ for the energy per particle E/N is eventually overcome by the stronger scaling $\propto n^{3/2}$ of the quantum fluctuation term. The system is stabilized by the combination of mean-field and beyond mean-field effects at a finite density generally on the order of $n_0 \simeq 10^{21}\,\text{m}^{-3}$ [5, 246] allowing for stabilized quantum droplets, supersolids, and other structures that we investigate in this thesis. The kinetic energy at these high densities can be neglected, which is also known as the Thomas-Fermi approximation [200, 295]. In the presence of an external trap along the z-direction there is an energy penalty for the elongation of the quantum droplet. The dipolar interaction is sufficiently attractive at these densities for quantum droplets to be self-bound [133, 137, 296, 297] and the trap is not necessary for their stability. A steep increase of the total energy with n of a few n_0 limits the density of quantum droplets at which they become density saturated. Analogous to classical liquids, these droplets are incompressible and adding particles to the system leads to a growth in volume at fixed saturation density. These properties are similar to helium droplets at orders of magnitude higher density [192, 298, 299] which are described as quantum liquids [27]. In this sense the phases of dipolar quantum fluids near a saturation density we describe in this thesis are weakly-interacting dilute quantum liquids in comparison to liquid helium. Due to the emergence of quantum liquid properties and the analogy to classical ferrofluids, dipolar quantum fluids can be considered quantum ferrofluids [3, 107, 130, 292]. Interestingly dipolar BECs can be tuned from its 'gaseous' form at low density to the 'liquid' form near the density saturation by tuning the scattering length. A contour plot of the energy as a function of a_s and n (Fig. 2.4(b)) helps with an intuitive understanding of phase diagrams in dipolar quantum fluids presented in chapters 3-4. At low density the contours a_s of constant energy rise with n up to n_0 at which point the contours begin to decrease. Additionally the lowest energy shifts to higher density for smaller a_s. Such contours present candidates for critical scattering lengths separating one phase from another in dipolar quantum fluids (sections 3.1, 4.3).

The variational approach is limited for quantitative statements in several situations such as intermediate density regimes where the Thomas-Fermi approximation is not accurate and for states that do not assume the Gaussian shape enforced by the trial wavefunction

in Eq. (2.59). These situations where an interplay of multiple quantum droplets and states with no continuous cylinder symmetry give rise to supersolids and other self-organized structures are common in this thesis, and numerical methods supplementing the analytical intuition developed in this section are key.

2.6. Numerical simulations

In general the nonlinear and nonlocal properties of the eGPE (2.31) complicate an analytic understanding of its solutions. Approximations and the variational approach are limited to specific scenarios and the form of the variational wavefunction. For these reasons numerical simulations, allowing for the exact solution of the eGPE up to numerical errors, are an important tool in understanding dipolar quantum fluids. Especially since the observation of droplet arrays [130] characterized by an intricate spatial structure, dynamics, and collective excitations, numerical methods have become indispensable in accompanying experimental efforts and making theoretical predictions for further experiments.

Numerical simulations have played a crucial role in all our publications in this field [1–9] both in understanding experimental observations and in theoretical proposals. Moreover the toolbox we developed during the course of this thesis became more accessible to other team members and contributed to significant results in previous PhD theses [129, 153] and was a tool used in Master's projects [300, 301] fostering further progress in the closely related field of polar molecules [246]. The toolbox has proven useful to contribute to theoretical [302] and experimental [117] observations external to our group and enabled a theory collaboration with the group of S. Reimann [1].

This section outlines the methods used to solve the dynamics of the eGPE, to search for ground states by directly minimizing the eGPE energy functional, and to solve the BdG equations. The implementation details of the eGPE dynamics have been described in several reviews [235, 236] and we focus on motivating the methods as well as providing an understanding of them in section 2.6.1. The energy functional minimization is less standard and has played a significant role in accelerating the exploration of self-organized structures with minute energy differences (section 4.3). Therefore we provide a more detailed view of this method in section 2.6.2. We conclude with a short description of the solution of the BdG equations in section 2.6.3.

A starting point for the new numerical toolbox overall was a `C/C++` code initially developed by M. Wenzel [197, 205]. Our new toolbox is based on `matlab` [303] after

extending the `C/C++` code itself and porting parts of it to multiple programming languages for comparisons in performance and other criteria. Appendix A provides more comments on this initial phase.

All methods involving the solution of the eGPE and related equations that we describe here are based on a wavefunction discretized on a three-dimensional cartesian grid[20]. Fourier transforms are used to evaluate spatial derivatives and the dipolar interaction potential, which become local in momentum space. A spherical cutoff for the dipolar interaction in momentum space is used to avoid interaction with periodic images [197, 200, 233, 240], with the cutoff radius set to the box length [266]. This setup is a standard starting point for the development of numerical methods for dipolar quantum fluids [197, 240, 304].

2.6.1. Real and imaginary time evolution

The time evolution of the eGPE (2.35) is computed using the split-step Fourier[21] method [234, 236, 305]. Fourier methods to evaluate spatial derivatives as opposed to finite difference methods have been shown to converge significantly (in typical simulation setups orders of magnitude) better to exact solutions as a function of the spatial discretization and also orders of magnitude faster[22] in computational time [235, 308]. We have implemented both Lie and Strang splitting for the time evolution [309] and use Strang splitting in practice due to its higher order accuracy in time at negligible computational overhead. The split-step method is based on splitting the operator $H_{\mathrm{GP}} = H_\nabla + H_I$ into an operator containing all derivatives H_∇ and a second one containing all other terms H_I. In the limit of small time steps the two corresponding Schrödinger equations can be solved independently, of which the equation for H_I can be integrated in time exactly and then they are combined using the Lie or Strang expressions for the splitting [235, 309]. The split-step method also allows to include further derivative terms in the operator H_∇ corresponding to translating or rotating frames of references [234].

[20] Depending on the application with between 96^3 to 256^3 points. A typical example would be to get a fast solution for a range of parameters at a rougher grid size to get a qualitative understanding and then perform numerical checks with finer grids.

[21] We use the discrete Fourier transform as implemented in `matlab` with the `fftn` function using the `fftw3` library. The discrete sine transform has been proposed as a competitive alternative [234–236] in terms of spectral accuracy, although this implementation is less standard [305–307].

[22] We have compared our `matlab` to the previous `C/C++` implementation and found a speedup of a factor of two to three for the same numerical settings. Additionally due to the use of a spectral rather than finite difference method, the spatial grid resolution can be reduced for the same accuracy [235, 308].

In this framework a method to search for the ground state is obtained by changing time to imaginary time $t \to -it$, which is known as imaginary time evolution or gradient flow [235, 307]. If one considers the wavefunction at time t to be composed of a superposition of several functions, then components with higher energy decay faster in time leading to a convergence to the ground state over time [235, 307]. In imaginary time the wavefunction is renormalized at each step to the particle number such that it remains constant in the ground state while higher energy components continue to decay. The convergence to the ground state in imaginary time is monitored by tracking several quantities related to the ground state over imaginary time and stopping the search when a specified tolerance is reached[23].

2.6.2. Energy functional minimization

Imaginary time evolution runs into limitations in convergence time when investigating parameter regimes where many low-energy states are near-degenerate. In these cases the decay of metastable near-degenerate excited states slows down the convergence and eventually an exponentially long time is needed to extinguish these components from the wavefunction ψ in the convergence to the ground state ψ_0.

In such numerically challenging regimes applying conjugate gradient (CG) methods have proven successful, for example in the context of rotating or strongly dipolar BEC [240, 310–312]. We base our implementation on the works by X. Antoine et al. [313, 314], which provide a mathematically detailed description of the CG algorithm for nonlinear energy functionals.

For the CG algorithm we normalize the wavefunction temporarily to unity and use the dimensionless units introduced in section 2.4.3. We expand the wavefunction

$$\psi = \phi_{j+1}(\boldsymbol{r}) = \cos(\theta_j)\phi_j(\boldsymbol{r}) + \sin(\theta_j)\gamma_j p_j(\boldsymbol{r}) \tag{2.62}$$

with a function p_j to be determined during the iteration j of the CG algorithm and $\gamma_j = 1/||p_j|| = 1/\sqrt{\langle p_j|p_j\rangle}$. Before we explain how p_j is defined we first motivate the expansion (2.62) from a viewpoint we have considered in section 2.5.2, namely the variational approach. One can consider (2.62) a trial wavefunction for an energy functional (like

[23] The quantities for imaginary time evolution are chemical potential, all energy contributions in units of $\hbar\omega_0 = 2\pi\hbar \times 100\,\mathrm{Hz}$ and the peak density in units of $10^{-19}\,\mathrm{m}^{-3}$. The tolerance is typically 10^{-13} and the time step is typically set to $0.5\text{–}1 \times 10^{-3}/\omega_0$.

Eq. (2.36)) given an arbitrary function p_j. The goal of the CG algorithm is to minimize the energy and find ϕ_{j+1} such that $E[\phi_{j+1}] < E[\phi_j]$. Given p_j, in general this amounts to finding $\theta_j = \arg\min_\theta E[\phi_{j+1}]$.

A number of strategies to find θ_j exist [313]. The simplest method is to choose a constant and small θ_j that gives monotonically decreasing energies throughout the steps j. The downside of this approach is that it is unknown prior to running the CG algorithm which θ_j is sufficiently small and requires restart of the simulation until such a θ_j has been found. The most general method is to consider θ_j a one-dimensional minimization problem, also known as line search within the context of CG algorithms [240, 313]. For some energy functionals (like (2.36)), all terms of $E[\phi_{j+1}]$ can be computed analytically and many of the terms independent of θ_j can be numerically precomputed [312]. For local energy densities, the first and second order changes are found by the first and second order derivatives of the energy density and for nonlocal energy densities, these changes are related more formally to the first and second order functional derivatives of the energy density functional [313]. This general method requires the ability to evaluate these functional derivatives analytically and to implement them symbolically in the numerical minimization procedure. For energy functionals that are polynomial in the wavefunction (2.36) this can be done [227, 312]. Recently proposed extensions of the energy functional for finite temperature [315–317] involve general functions of the wavefunction where the most general approach can become cumbersome.

The strategy in intermediate complexity we choose in the following relies on a Taylor expansion of the energy functional up to second order [313, 314]. We find that this method is adequate up to all terms we have included in the energy functional, including quantum fluctuations[24]. Substituting (2.62) into (2.36) in dimensionless units one obtains

$$\begin{aligned} E(\theta_j) &= E[\phi_{j+1}] \\ &= E[\phi_j] + 2\gamma_j \operatorname{Re}\langle p_j|\tilde{H}_{\mathrm{GP}}[\phi_j]\phi_j\rangle\,\theta_j - \left[\mu_j - \gamma_j^2\left(\langle p_j|\tilde{H}_{\mathrm{GP}}[\phi_j]p_j\rangle + \operatorname{Re}\langle g_j|p_j\rangle\right)\right]\theta_j^2 \end{aligned} \tag{2.63}$$

up to second order in θ_j where $g_j = 2(C\rho^j_{p\phi} + DU_{\mathrm{dd}} * \rho^j_{p\phi} + (3/2)Q|\phi_j|\rho^j_{p\phi})\phi_j$ with $\rho^j_{p\phi} = \mathrm{Re}(\phi_j p_j^*)$. These expressions generalize the results obtained in Ref. [314] to include quantum

[24] Incidentally also including the thermal energy functional proposed by Refs. [315–317] which we will not consider further in the framework of this thesis.

fluctuations. Minimizing Eq. (2.63) yields the optimal angle

$$\theta_j^{\mathrm{opt}} = \frac{\gamma_j \,\mathrm{Re}\,\langle p_j|\tilde{H}_{\mathrm{GP}}[\phi_j]\phi_j\rangle}{\mu_j - \gamma_j^2\left(\langle p_j|\tilde{H}_{\mathrm{GP}}[\phi_j]p_j\rangle + \mathrm{Re}\,\langle g_j|p_j\rangle\right)}. \tag{2.64}$$

Now we return to the definition of p_j which depends on the choice of the step size available in the general context of CG algorithms. In our case we have

$$p_j = d_j - \mathrm{Re}\,\langle d_j|\phi_j\rangle\,\phi_j, \tag{2.65a}$$

$$d_j = -Pr_j + \beta_j p_{j-1}, \tag{2.65b}$$

$$\beta_j = \max\left(\mathrm{Re}\,\frac{\langle r_j - r_{j-1}|Pr_j\rangle}{\langle r_{j-1}|Pr_{j-1}\rangle}, 0\right), \tag{2.65c}$$

$$r_j = \tilde{H}_{\mathrm{GP}}[\phi_j]\phi_j - \mu_j\phi_j, \tag{2.65d}$$

$$\mu_j = \langle\phi_j|\tilde{H}_{\mathrm{GP}}[\phi_j]\phi_j\rangle\,. \tag{2.65e}$$

Geometrically p_j corresponds to the vector rejection of d_j from ϕ_j, and d_j is the conjugate gradient descent direction. The step size β_j corresponds to the Polak-Ribière choice with an automatic direction reset [313, 314, 318]. P is a preconditioner that in general can be tuned to improve convergence properties [312–314] but we do not employ preconditioning here and P is the identity operator. The nonlinear residual r_j and chemical potential μ_j are obtained readily from the wavefunction ϕ_j. The choices for the CG quantities in Eq. (2.65) lead to a negative first order coefficient for the energy correction for sufficiently small θ_j [313, 314] and to a move in the steepest energy descent direction. By checking that the coefficient for the second order correction is positive it can be ensured that the neighborhood of the energy landscape in that direction is a minimum and if not, a smaller θ_j is chosen. For $j = 0$ the algorithm begins with an initial state and one iteration is composed of computing Eq. (2.65e) through Eq. (2.65a), evaluating Eq. (2.64), and updating the new state with Eq. (2.62). After convergence the wavefunction can be renormalized to the atom number.

The convergence to the ground state is monitored by tracking the energies throughout the iterations and stopping when a specified tolerance is reached[25]. In comparison to imaginary time evolution we find with the same numerical settings convergence to the same ground state faster by a factor of three (for a simple BEC state) to 20 (for isolated or

[25] Following Refs. [313, 314] we monitor the maximum difference of all energy contributions between steps in units of $\hbar\omega_0 = 2\pi\hbar \times 100\,\mathrm{Hz}$ and stop typically at a tolerance of 10^{-13}.

multiple droplet states). The better performance of the CG algorithm likely has two origins. First, the CG algorithm takes both the first order and second order energy variation into account to compute the next step and second, the step size is automatically adjusted based on the energy landscape (Eq. (2.64) and Eq. (2.65c)). An adaptive time step for imaginary time evolution can be implemented and could partially close this gap in performance [233]. Note that the CG specific formulae (2.65) do not rely on the second order energy variation and only effectively terms in g_j have to be added if H_{GP} is extended for other terms than those we considered here. This property allows for a concise and flexible formulation of the CG algorithm. All steps of the algorithm rely mainly on matrix multiplication (the matrix elements for a discretized wavefunction) and Fourier transforms, suggesting that the algorithm could benefit strongly from graphics processing unit (GPU) acceleration. Thanks to `matlab`'s `gpuarray` function we could straightforwardly port the algorithm to a GPU version and we observed a typical additional speedup of a factor of 20 in convergence[26].

In conclusion the development and implementation of this algorithm allowed to investigate parameter regimes where several low-energy states are near-degenerate at orders of magnitude higher rate and the algorithm together with imaginary time evolution is a tool allowing to check the presence of low-energy states with two independent methods. In the future it could be interesting to leverage developments in machine learning and automating the calculation of the first and second order variations of the energy functional leading to the expression (2.64). Using automatic differentiation [321] where the elementary operations needed to calculate the derivative of a function are learned within the algorithm itself would get rid of the need to be able to calculate the expansion in Eq. 2.63 and only the function $E(\theta_j)$ itself needs to be implemented.

2.6.3. Excitation spectra

The BdG equations in the form (2.41) are implemented in `matlab` by defining the entire operator in Eq. (2.45a) as a function and solving $\hat{A}(f) = \hbar^2\omega^2 f$ using `matlab`'s `eigs` function. This function is a matrix-free iterative implementation of the Arnoldi method [177, 240, 322, 323]. The important property of being matrix-free means that $\hat{A}(f)$ never

[26] Comparing a simulation run on a NVIDIA Tesla K80 GPU with a simulation run using typically ten Intel Xeon E5-2699A v4 CPUs in parallel on our local cluster. With more modern GPUs offering higher CUDA core and tensor core counts we expect the performance gap to increase further [319, 320]. On the present GPU hardware ground state searches for BECs converge for example with grids of size 128^3 points after a few seconds and droplet states or near-degenerate states as we consider in section 4.3 can take from an hour up to a day depending on the energy landscape.

needs to be constructed in a matrix form which would be prohibitively memory intensive, but instead $\hat{A}$ is defined as a function by its action on f.

"I think I can safely say that nobody understands quantum mechanics."

– Richard Feynman

Chapter 3

One-dimensional supersolid arrays of dipolar quantum droplets

Chapter Contents

In this chapter we first briefly discuss our observation of phase coherent dipolar droplet arrays [9] (section 3.1). Together with the results obtained in Pisa and Innsbruck these studies provided first experimental evidence for supersolid properties in dipolar quantum gases [9, 96, 97]. We introduce the superfluid fraction and discuss the supersolid phase diagram obtained both theoretically and experimentally.

While the overall shape of the supersolid droplet arrays is influenced by the trap confinement, the droplets giving rise to the crystal structure are not spatially pinned. In contrast to lattice supersolids where the crystal structure is externally imposed [51, 100,

324–327], the one-dimensional dipolar supersolids self-organize due to interactions between the droplets and allow for the propagation of phonon modes throughout the supersolid. Superfluidity in general is intimately connected to the elementary excitation spectrum, as we have introduced conceptually in section 2.5.1. Supersolids combine superfluidity with a crystal structure and the spectrum reflects this bipartite nature.

We study the spectrum of elementary excitations in section 3.2 and review our studies of Goldstone [8] and Higgs amplitude [7] modes in this system. Parts of these publications have been included in previous theses [129, 153, 205]. These Goldstone and Higgs amplitude modes closel relate to the density fluctuations across the superfluid to supersolid phase transition [5], which will be our focus in section 3.2.

In section 3.3 we consider our most recent theoretical study of toroidally trapped supersolids, allowing us to compare to the harmonically trapped cases and infinitely extended supersolids [1].

3.1. Ground states of dipolar supersolids in tubular traps

In this section we introduce the basic structure of the ground state phase diagram of supersolids in harmonic traps and the superfluid fraction. Parts of this section have been published in further detail in the theoretical and experimental study

- F. Böttcher, J.-N. Schmidt, M. Wenzel, J. Hertkorn, M. Guo, T. Langen, and T. Pfau, "Transient supersolid properties in an array of dipolar quantum droplets", Phys. Rev. X **9**, 011051 (2019).

3.1.1. Superfluid fraction

Here we introduce the concept of the superfluid fraction, its relevance for the characterization of the supersolid state of matter, and an approximate measure for superfluidity. We investigate a system that is infinitely extended in one direction, which permits the calculation of the superfluid fraction. We consider $N = 100 \times 10^3$ ^{162}Dy atoms in a harmonic trap with trapping frequencies $\omega_{x,y,z}/2\pi = (0, 53, 81)\,\mathrm{Hz}$ within a simulation box of length $L_x \simeq 12\,\mu\mathrm{m}$ and apply periodic boundary conditions along the x-direction [153, 205]. We

apply a linear boost to the system

$$i\hbar\partial_t\psi = (H_{\mathrm{GP}} - v_x\hat{p}_x)\,\psi, \tag{3.1}$$

where v_x is a small velocity and $\hat{p}_x = -i\hbar\partial_x$ is the momentum operator and H_{GP} is given by Eq. (2.33). Here and in the following we consider the eGPE theory introduced in section 2.4. Solving for the ground state for a range of scattering lengths we find a phase transition of an unmodulated BEC to a linear array of quantum droplets (Fig. 3.1). In the insets of Fig. 3.1 we show the z-integrated density $\tilde{n}(x,y) = \int \mathrm{d}z\, n(x,y,z)$ in a logarithmic scale ($\log(\tilde{n}(x,y)/n_0)$) normalized to the maximum density n_0 across all scattering lengths. In the limit[1] $v_x \to 0$ the final states approach the ground states of the stationary system and the superfluid fraction

$$f_s = 1 - \lim_{v_x\to 0} \frac{\langle \hat{p}_x \rangle}{NMv_x} \tag{3.2}$$

with the mass M can be evaluated. The superfluid fraction characterizes the fraction of particles displaying superfluidity in the system [328, 329]. Equation (3.2) provides the intuitive interpretation that f_s is given by the fraction of particles that remain at rest in the moving frame [147, 205] and allows for a rigorous identification of a superfluid to supersolid phase transition. The superfluid is characterized by $f_s = 1$ and in the supersolid $f_s < 1$ decays towards smaller scattering lengths. Qualitatively one can identify a third regime of isolated quantum droplets with a vanishing superfluid fraction. The regime cannot be identified rigorously within the eGPE framework as the ground state is described with a single wavefunction leading to a finite overlap between the droplets which leads to a finite superfluid fraction.

A drawback of this definition for f_s is that the experimental realization of an infinite system which can be set into linear motion is a priori not straightforward. In the finite traps we consider in the following sections, a simple measure of the superfluid fraction is needed. We define the overlap as the ratio $\sigma_s = \min_x n(x)/\max_x n(x)$ of a one-dimensional density $n(x)$ over a range x covering the droplet spacing. In the infinite system this covers a unit cell of the droplet array and we show the obtained overlap in Fig. 3.1. The overlap

[1] In practice we vary v_x and identify when f_s becomes independent of v_x. Here we find and use $v_x \simeq 1\,\mu\mathrm{m/s}$.

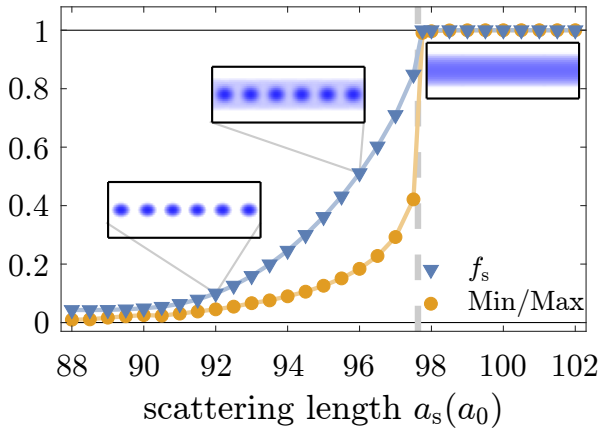

Figure 3.1.: **Characterization of superfluidity in an infinite system.** Superfluid fraction f_s calculated from Eq. (3.2) (blue triangles) and overlap (yellow circles) as a function of scattering length in an infinite tube. The overlap is a simple approximate lower bound of the superfluid fraction that can be applied to finite systems. Insets show the z-integrated density $\tilde{n}(x, y)$ in a logarithmic scale and arbitrary units.

in a finite trap[2] will prove useful as an interpretation of the ability of particles to tunnel from one droplet to another [205, 332–334] but has also been shown to be a lower bound of f_s in two dimensions [335, 336]. The realization of dipolar supersolids in harmonic traps has motivated very recent developments of the characterization of the superfluid fraction of density modulated superfluids in general [259, 330, 331, 336–339]. The rapid progress in this direction underlines that quantifying superfluidity in realistic and experimentally achievable systems is of central interest to the community but also a motivation to consider geometries allowing for accurate estimates of the superfluid fraction.

Originally in the context of superfluid helium, rotating cylindrical trapping geometries were considered that intrinsically realize periodic boundary conditions [328, 329]. In such geometries the superfluid fraction

$$f_s = 1 - \lim_{\Omega \to 0} \frac{\langle \hat{L}_z \rangle}{NM \langle r^2 \rangle \Omega} \tag{3.3}$$

can be evaluated through the resistance of particles to rotational motion in a finite system rather than to linear motion in an infinite system. The angular rotation frequency Ω and

[2] Other simple measures have been defined [330] such as the contrast $\mathcal{C} = (\max_x n(x) - \min_x n(x))/(\max_x n(x) + \min_x n(x)) = (1 - \sigma_s)/(1 + \sigma_s)$ which under specific assumptions of the density profile $n(x)$ can be evaluated further and related to f_s [331]. These measures are alternative and closely related to the overlap $\sigma_s = (1 - \mathcal{C})/(1 + \mathcal{C})$.

the angular momentum operator $\hat{L}_z = x\hat{p}_y - y\hat{p}_x$ define the nonclassical rotational inertia (NCRI) $\mathcal{I} = \langle \hat{L}_z \rangle / \Omega$ [257, 340, 341] and comparison to the classical inertia $\mathcal{I}_0 = M \langle r^2 \rangle$ gives f_s. With this context, Eq. (3.2) can be seen as a relationship between f_s and nonclassical translational inertia [147, 335, 342–344]. The NCRI can be evaluated in the rotating frame

$$i\hbar\partial_t\psi = \left(H_{\mathrm{GP}} - \Omega\hat{L}_z\right)\psi, \tag{3.4}$$

in systems that are rotationally symmetric around the z-axis. One important example, in particular due to its rising experimental relevance [345, 346], is the toroidal trap which we consider in section 3.3.

In cases where the superfluid is uniform and the translational symmetry breaking occurs along one direction, upper and lower bounds on the superfluid fraction have been obtained by Leggett [328, 329]. These bounds have the advantage that they can be directly obtained from the ground state density distribution in the rest frame without having to solve for it in the translating or rotating frame. These bounds were shown to be tight for dipolar supersolids [331], have been used in hydrodynamic models of supersolids [342, 343], cosine-modulated and other trial wavefunctions for supersolids [169, 226, 330], and have been extended to two-dimensional density distributions [238, 337]. For example the upper Leggett bound is given by $f_s \leq \frac{1}{\bar{n}}\left(\frac{1}{L}\int_0^L \mathrm{d}x\, n(x)^{-1}\right)^{-1}$ where x is the coordinate along which the symmetry is broken, $\bar{n} = \frac{1}{L}\int_0^L \mathrm{d}x\, n(x)$ is the average of the density $n(x)$ and the length of the unit cell is L. This upper bound has the additional advantage that only the density distribution along the coordinate x must be known and it becomes an equality if the density is separable and the other two directions can be integrated out [328, 330]. This property allowed direct measurements of the superfluid fraction of BECs in optical lattices recently [259, 339] and studies of dipolar supersolids in toroidal traps showed that the behvaior of f_s is modified as the density modulation is not externally induced [1, 347]. In contrast, the lower Leggett bound on f_s [329, 348] requires knowledge of the three-dimensional density distribution.

3.1.2. Phase diagram

To investigate whether arrays of dipolar quantum droplets constitute a supersolid phase we need to show that density modulation and phase coherence coexist in an extended range of parameters – in a phase diagram (Fig. 3.2). We consider dipolar quantum droplet states as a function of a_s and N in a finite system with trapping applied along the longitudinal

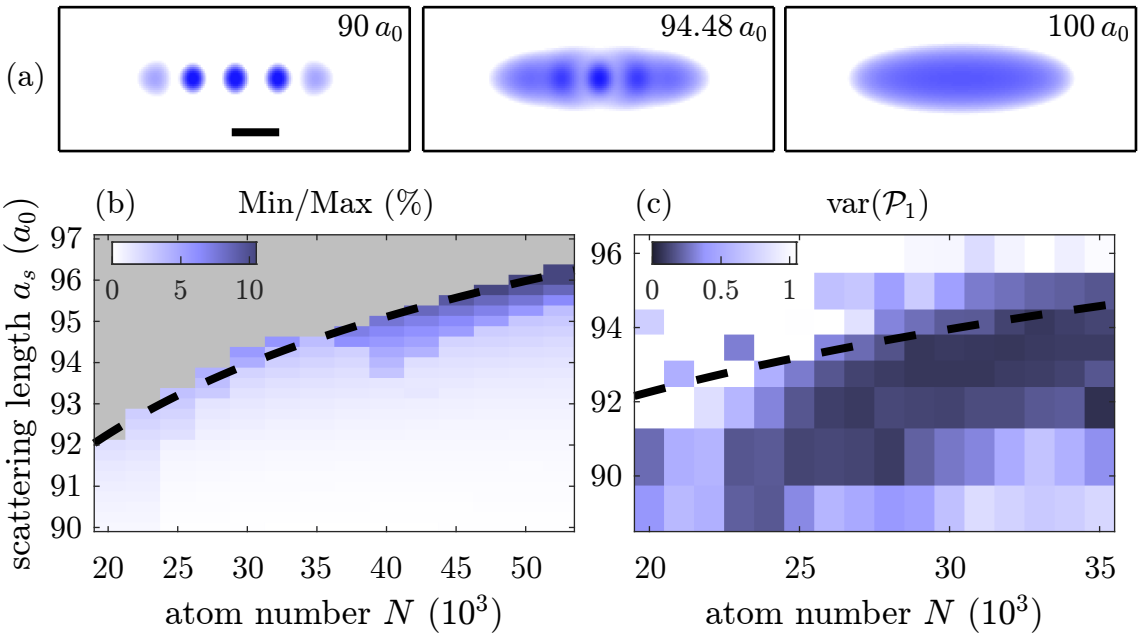

Figure 3.2.: **Phase diagram of dipolar droplet arrays in a finite trap.** (a) Density profiles across the superfluid to supersolids phase transition. The z-integrated density in a logarithmic scale is shown for three scattering lengths at $N = 35 \times 10^3$ of (b). The bar in the first image corresponds to 5 µm. (b) Theoretical phase diagram showing the droplet overlap of the ground states in a harmonic trap with $\omega_{x,y,z}/2\pi = (18.5, 53, 81)$ Hz. The gray area indicates the superfluid regime. (c) Experimental phase diagram showing the normalized variance of the amplitude of the first order interference fringe var($\mathcal{P}_1$) in time of flight experiments in a similar trap with $\tilde{\omega}_{x,y,z}/2\pi = (19(1), 53(1), 87(1))$ Hz. This variance is a robust measure of nearest-neighbor droplet phase coherence [9]. In (b)-(c) the same black dashed line indicates the superfluid to supersolid transition boundary (see main text).

direction x of the droplet array. Theoretically we consider a harmonic trap with trapping frequencies $\omega_{x,y,z}/2\pi = (18.5, 53, 81)$ Hz (ω_x added to the trap of the previous section) which is close to the trap that we experimentally realize [9, 153].

The trap limits the droplet array to a finite longitudinal extent, breaks the translational symmetry of the BEC, and leads to a local density variation in the longitudinal direction (Fig. 3.2(a)). Despite these differences to the infinite system (section 3.1) the same three regimes of superfluid, overlapping droplet arrays, and isolated droplet arrays can be identified. Although the finite trapping breaks the translational symmetry already in the BEC, within a local density approximation it is useful to consider the droplet formation within the BEC as (approximate) translational symmetry breaking of the (approximately) uniform superfluid [9]. The finite trapping in the longitudinal direction has important

implications for the elementary excitations (sections 3.2-3.3). Theoretically we find for a wide range of atom numbers that a narrow range of scattering lengths exists in which overlapping arrays of quantum droplets form (Fig. 3.2(b)). When the droplet number changes towards higher atom numbers for a given scattering length in the phase diagram, discontinuities in the overlap are observed (b).

Experimentally we prepare a quasi-pure BEC at a temperature $T \simeq 20\,\mathrm{nK}$ with $N \simeq 45 \times 10^3$ atoms in a harmonic trap with trapping frequencies $\tilde{\omega}_{x,y,z}/2\pi = (19(1), 53(1), 87(1))\,\mathrm{Hz}$. We ramp the scattering length from the BEC regime to the final scattering lengths shown in Fig. 3.2(c) and obtain various atom numbers by binning the experimental data featuring a distribution of atom numbers due to fluctuations in initial atom number and the dynamics of the droplet formation process [9, 153]. In total we analyze more than 300 experimental realizations for each scattering length. We investigated the dynamics in more detail in [9] and found that the droplet formation process near the transition boundary maintains the phase coherence of the superfluid. Experimentally the density modulation is characterized through the spectral weight [9] which is the Fourier amplitude at the spatial frequency $k/2\pi = 1/d$ corresponding to droplet distance d. This measure is enabled by the in-situ imaging capability [130]. Here we focus on the experimental evidence of phase coherence across the droplet array (Fig. 3.2(c)) measured through time of flight (TOF) experiments by suddenly switching off the trap. The atomic cloud expands during TOF and the droplets interfere. If the droplets are incoherent the interference peaks occur at different positions and with different amplitudes in the interference image in each realization [146, 153]. For increasing droplet coherence the interference peak variance in position and amplitude decreases [9, 153] which can be used to experimentally quantify the phase coherence of the droplet array. As shown in Fig. 3.2 we find that the region of overlapping quantum arrays coincides with the region in which we experimentally find phase coherence of the droplets. While the overlap from the theory monotonically decays towards the isolated droplet regime the experiment reveals that both the nearest-neighbor and next-nearest-neighbor coherence peak near the phase transition boundary [9, 153].

The discontinuity of the overlap at the transition boundary and hysteretic behavior we addionally investigated [9, 205] are consistent with a first order phase transition, as indicated by earlier studies on supersolids [147, 344, 349–351]. In dipolar BECs the magnitude of the discontinuity and hysteretic behavior depend on the density of the system [205] and it was suggested that there is a density range in which the phase transition is second order [238, 331, 338, 352–354]. This qualitative change of the phase diagram occurs at densities

beyond the reach of current experiments and will be discussed further in section 4.3.

An Ansatz based on the Thomas-Fermi profile of the BEC and a rotonic dispersion relation near the transition leads to the prediction that the critical scattering length scales as $a_{s,c}(N) = a_{\mathrm{dd}} - N^{1/\beta}/\alpha$ with two constants α, β [96, 125]. The Ansatz predicts that a phase transition occurs when the roton gap Δ_{rot} vanishes where $\beta \simeq -2.32$ [96]. Fitting $a_{s,c}$ to our theoretical ground state phase diagram (black dashed line in Fig. 3.2(b)-(c)) we obtain $\beta = -8.8(7)$ and $\alpha = 0.0086(2)/a_0$ [153]. The applicability of simple scaling relations and analytic equations is limited since the phase transition in harmonic traps actually occurs at a finite roton gap as we show in the following sections. At the same time this limitation underlines the necessity of numerical calculations and motivates a more detailed knowledge of the excitation spectrum near the superfluid to supersolid phase transition.

3.2. Excitations of finite tubular supersolids

In section 3.2 we discuss the elementary excitation spectrum of supersolids in harmonic traps and we focus on the identification of excitations driving the superfluid to supersolid phase transition. This identification and further details on the structure factor across the transition have been published in:

- J. Hertkorn, J.-N. Schmidt, F. Böttcher, M. Guo, M. Schmidt, K. S. H. Ng, S. D. Graham, H. P. Büchler, T. Langen, M. Zwierlein, and T. Pfau, "Density Fluctuations across the Superfluid-Supersolid Phase Transition in a Dipolar Quantum Gas", Phys. Rev. X **11**, 011037 (2021).

This section also briefly introduces the properties of the low-energy Goldstone mode and amplitude Higgs mode in the spectrum of harmonically trapped supersolids due to their fundamental role for the supersolid behavior but also in order to compare to the spectrum of supersolids in toroidal traps. More experimental and theoretical details of Goldstone and Higgs modes were significant parts in theses [153, 205] and have been published in:

- M. Guo, F. Böttcher, J. Hertkorn, J.-N. Schmidt, M. Wenzel, H. P. Büchler, T. Langen, and T. Pfau, "The low-energy Goldstone mode in a trapped dipolar supersolid", Nature (London) **574**, 386 (2019).
- J. Hertkorn, F. Böttcher, M. Guo, J. N. Schmidt, T. Langen, H. P. Büchler, and T. Pfau, "Fate of the Amplitude Mode in a Trapped Dipolar Supersolid", Phys. Rev. Lett. **123**, 193002 (2019).

3.2.1. Trap and overlap

With the interpretation of an overlap between the droplets supporting phase coherence across the droplet array, a goal for the observation of elementary excitations requiring superfluid flow is to increase this overlap. A higher density is a direct route to achieve this increase. Within experimental limitations of the atom number of typically $N \lesssim 40 \times 10^3$ an increase in density can be independently obtained by confining the available atoms in tighter traps. In this section and the following we consider such tighter traps and focus on the excitations across the superfluid to supersolid phase transition.

We theoretically consider $N = 30 \times 10^3$ atoms confined in a harmonic trap with trapping frequencies $\omega_{x,y,z}/2\pi = (30, 110, 90)\,\mathrm{Hz}$. The geometry is consistent with the trap we experimentally realize with trapping frequencies $\tilde{\omega}_{x,y,z}/2\pi = (30(1), 108(2), 89(2))\,\mathrm{Hz}$

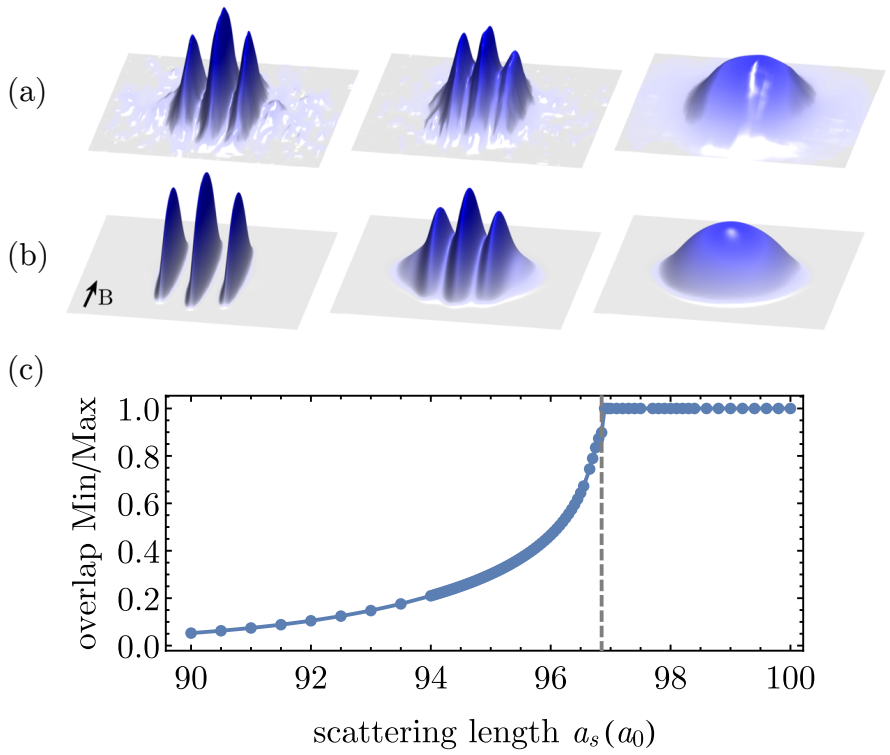

Figure 3.3.: **Comparison between experiment and theory.** (a) Experimental single-shot realizations of the isolated droplet, overlapping droplet, and BEC regime at scattering lengths $a_s \simeq (93.5,\ 96,\ 99)\,a_0$. (b) Theoretical ground states for the same regimes at $a_s \simeq (90,\ 96.5,\ 100)\,a_0$. (c) Droplet overlap across the transition from (b). The tigher trap allows for a very high droplet overlap and leads to a close correspondence of the density profiles observed in theory and experiment up to a systematic shift in scattering length [138].

in which we prepare a quasi-pure BEC ($T \simeq 20\,\mathrm{nK}$) with typically $N \lesssim 40 \times 10^3$ atoms. In the experiments the magnetic field was tilted orthogonal to the imaging direction such that magnetostriction occurs in the plane visible with the imaging system. This setup allows to resolve individual droplets more easily[3] [8, 153]. Using this trap geometry we find a close correspondence between density profiles in single-shot realizations of experiment and theory (Fig. 3.3(a)-(b)). Additionally we find a scattering length range of multiple a_0 with an appreciable overlap (Fig. 3.3(c)). The shift in scattering length between theory and experiment has been observed by multiple groups [97, 128, 138, 142, 355]. Reasons for the shift have been suggested including deviations of quantum fluctuations from the

[3] Experimentally the imaging direction stayed the same and the field was tilted along the y-direction. We keep the notation in the text consistent with the B-field always aligned the z-direction meaning that in this frame of reference it is as if the imaging changed to the y-direction.

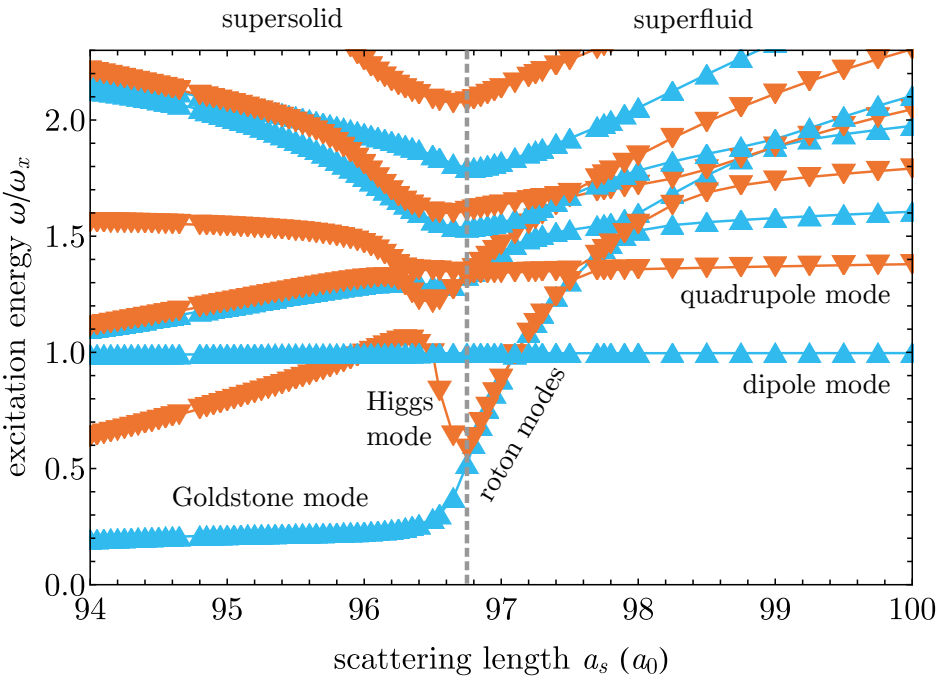

Figure 3.4.: **Excitation energies across the superfluid to supersolid phase transition in a tubular harmonic trap.** Antisymmetric (symmetric) modes are shown as upward blue (downward orange) triangles. Modes are ordered by their parity in the superfluid. Two degenerate roton modes soften towards the critical point and trigger the phase transition to the supersolid state where they split into the low-energy Goldstone mode and the Higgs amplitude mode associated to the translational symmetry breaking. The points indicate the sampling of the ground states.

LHY correction term [138, 227] and finite temperature effects [138, 316] which are not fully resolved and still under investigation [227, 317].

3.2.2. Excitation spectrum

The substantial overlap in an extended scattering length range is a good starting point for considering the direct observation of superfluid flow throughout the droplet array and to prove the supersolid nature of overlapping dipolar quantum droplets. To see how such a flow is realized in dipolar supersolids we first theoretically investigate the spectrum of elementary excitations by solving the BdG equations (section 2.4.4) across the superfluid to supersolid phase transition (Fig. 3.4).

Deep in the superfluid modes are alternating in parity[4] as their kinetic energy increases

[4] We define the symmetry of the modes with respect to the center of the trap as antisymmetric if $\delta n(\boldsymbol{r}) = -\delta n(-\boldsymbol{r})$ and as symmetric if $\delta n(\boldsymbol{r}) = \delta n(-\boldsymbol{r})$ at $y = z = 0$.

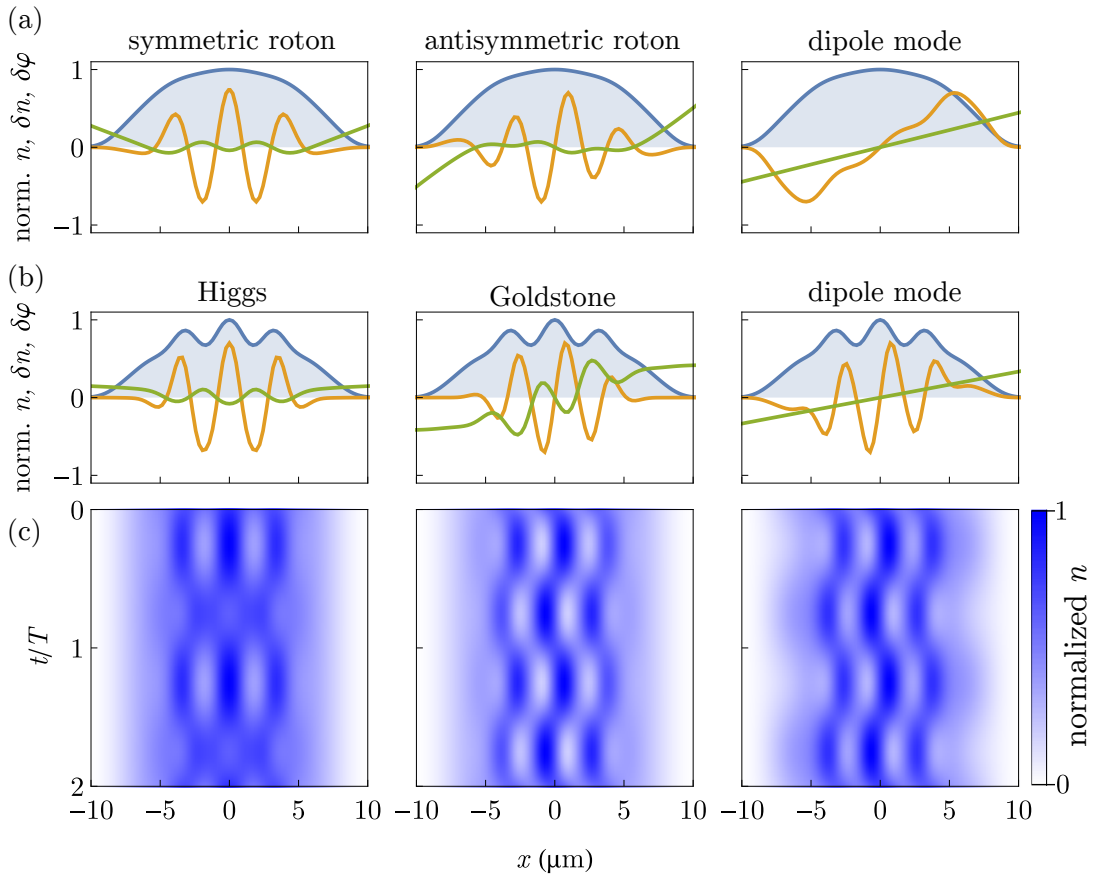

Figure 3.5.: **Spatial and temporal character of elementary excitations.** (a)-(b) Normalized density profile n (blue background), density fluctuation pattern δn (orange), and phase fluctuation pattern $\delta\varphi$ (Eq. (2.46)) as a function of x at $y = z = 0$. Relevant modes near the critical point on the superfluid side (a) and supersolid side (b) are shown for $a_s = 98.0\,a_0$ and $a_s = 96.5\,a_0$, respectively. (c) Linearized time evolution $n(t)$ (Eq. (2.47)) of the excited states in (b) for two periods $T = 2\pi/\omega$.

and are identified as dipole, quadrupole, and higher modes. The dipole mode is a center of mass (COM) oscillation of the atomic cloud as a whole at the longitudinal trap frequency ω_x. Consistent with Kohn's theorem [207, 240, 356, 357] the dipole mode is independent of interaction parameters and remains at the trap frequency. In the superfluid a bundle of higher energy modes decrease in energy (soften) towards the quantum critical point at $a_{s,c} \simeq 96.8\,a_0$ which are nearly degenerate roton modes. The lowest two roton modes lose this degeneracy at $a_{s,c}$ where they give rise to the low-energy Goldstone mode and the Higgs-amplitude mode associated to the broken translational symmetry of the supersolid [7, 8].

The spatial and temporal structure of these relevant modes (Fig. 3.5) explains their

energetic behavior as a function of a_s and provide intuition about their character. The symmetric roton mode (Fig. 3.5(a)) shows three strong modulations in the center of the trap aligned with the emerging three droplets at the critical point and develops into the Higgs amplitude mode in the supersolid (Fig. 3.5(b)). Both roton modes have a finite momentum $k_{\mathrm{rot}} = 2\pi/d$ corresponding to the droplet spacing d at the critical point but the antisymmetric roton mode is spatially shifted by $d/2$ with respect to the symmetric roton mode. In the superfluid where the density is approximately uniform this spatial phase shift does not cost energy and leads to a degeneracy of the roton modes. As the density modulation of the supersolid emerges the degeneracy is lifted and the antisymmetric roton mode develops into the low-energy Goldstone mode in the supersolid (Fig. 3.5(a)-(b)).

Due to the finite trapping frequency in the longitudinal direction the transition occurs at a finite Higgs gap and leads to a small but finite energy for the Goldstone mode. Towards the thermodynamic limit of lower trapping frequencies and more elongated systems at similar densities, this gap is expected to decrease and the Goldstone mode will be gapless with a linear dispersion relation. We studied the Higgs and Goldstone modes in detail in Refs. [7, 8]. Here we shortly review their most important properties and set the stage for a comparison with the toroidal trap (section 3.3).

The Higgs mode [7] is an amplitude modulation of the superfluid fraction facilitated by flow of atoms from the superfluid background into the droplets and vice versa (Fig. 3.5(c)). This behavior leads to an increase of the Higgs energy away from the phase transition point as the modulation becomes more costly towards a lower superfluid fraction (Fig. 3.4). The Higgs amplitude mode in our system is not protected by Lorentz invariance or particle-hole symmetry and therefore expected to be strongly damped [7, 11]. Remarkably the Higgs amplitude mode exists nonetheless in an isolated state in a narrow range of scattering lengths close to the phase transition as the discretization of the modes provided by the trapping frequency separates other modes from the Higgs amplitude mode. Away from the critical point, the Higgs mode couples to all higher-lying modes with the same symmetry and leads to a plenitude of avoided level crossings and hybridization, which are the corresponding phenomena to the strong damping of the Higgs amplitude mode in the thermodynamic limit. The Higgs mode has yet to be observed experimentally and the splitting of the roton modes as well as the strong coupling of higher-lying modes with an energetically rising mode serve as signatures that can be used to probe this mode in future experiments [7].

The low-energy Goldstone mode [8] is an out-of-phase oscillation between the droplet

crystal structure and the superfluid background (Fig. 3.5(c)) which leads to an almost constant COM. This behavior originates from the phase fluctuation pattern $\delta\varphi$ shown in Fig. 3.5(b) where the gradients on the droplet position and on the superfluid background between the droplets have opposite sign. Alternatively the density fluctuation pattern δn can be used to identify this behavior. The resulting dynamics show that as the crystal structure moves to the right (left) the density of the right (left) droplet transfers to the left (right) droplet. This anticorrelation between crystal displacement and droplet imbalance was used to prove the existence of the Goldstone mode in our experiment [8]. The fact that overlapping droplets constitute an extended region in parameter space and that they support elementary excitations requiring superfluid flow and phase rigidity across the droplet array show that they are a realization of a supersolid.

In an infinite system we expect to identify two gapless Goldstone modes with a linear dispersion relation: the superfluid phonon associated to the broken $U(1)$ symmetry and the supersolid phonon associated to the broken translational symmetry. In our finite system the dipole mode and the low-energy Goldstone mode are the corrsponding modes. The trap fixes the energy of the superfluid phonon to the trap frequency and raises the energy of the supersolid phonon to a finite value. The toroidal trap we investigate in section 3.3 is consistent with this picture and shows how these trapping effects can be partially circumvented in an experimentally realizable setup. The harmonic trap furthermore divides all modes into only two symmetries. Since all modes are limited to these two symmetries avoided crossings between multiple modes are an inherent part of harmonically trapped dipolar supersolids (Fig. 3.4). Nonetheless one can broadly recognize in Fig. 3.4 that on the supersolid side certain modes stiffen (rise in energy) and others soften (fall in energy). The coupling obscures the relationship between the different branches but as we show in section 3.3, the rising and falling branches together with the Higgs branch correspond to three distinct elementary excitations that are predicted in infinite supersolids and occur in a decoupled form in toroidal traps.

3.2.3. Density fluctuations

A connection between the elementary excitations and density fluctuations in the system is provided by the dynamic structure factor $S(\boldsymbol{k}, \omega)$ (section 2.4.4). The structure factor reveals the linear density response strength of the system due to a perturbation. Within the BdG formalism this connection is highlighted as the eigenmodes f_j correspond to

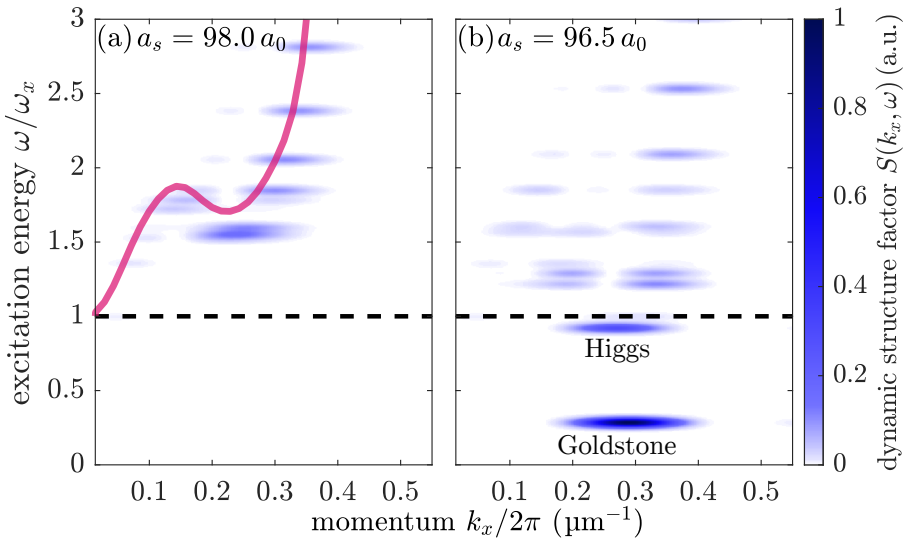

Figure 3.6.: **Dynamic structure factor in the vicinity of the quantum critical point** in the superfluid (a) and supersolid (b). The roton minimum of the superfluid defines the Brillouin zone edge of the supersolid where the low-energy Goldstone and the Higgs amplitude mode lie while higher energy excitations split around the Brilloin zone. The red line in (a) shows the Feynman-Bijl upper bound on the dispersion relation (Eq. (2.55)).

density fluctuations $\delta n_j = f_j \psi_0$ whose Fourier spectra are the components of the dynamic structure factor Eq. (2.48).

The dynamic structure factor obtained at zero temperature from our BdG analysis in the vicinity of the critical point is shown in Fig. 3.6. In this vicinity the superfluid has developed a significant roton minimum at the roton momentum $k_{\mathrm{rot}}/2\pi = 0.3\,\mu\mathrm{m}^{-1}$ associated to the roton modes (Fig. 3.5(a)-(b)). In the supersolid the roton modes have split up into the low-energy Goldstone mode and the Higgs amplitude mode. The first symmetric and antisymmetric phonon modes above the dipole mode in Fig. 3.6(b) show a splitting around the Brillouin zone edge at k_{rot}. The momentum k_{rot} sets the quasimomentum $\tilde{q} = 0$ point of the dispersion relation folded back to the first Brillouin zone which is the quasimomentum of the Goldstone and Higgs modes at the transition point. The phonons directly above the dipole mode are the lowest modes with a finite quasi momentum $|\tilde{q}| > 0$ in the first Brillouin zone. The finite trapping frequency along x leads to coupling of COM and linear motion, hybridization [7] and a dependency of the mode structure on the scattering length. The identification of a Brillouin zone and quasimomenta, despite their complication due to a finite trap, is useful to establish analogies to an infinite system and to contrast with the toroidal trap (section 3.3). The Feynman-Bijl approximation to the dispersion relation

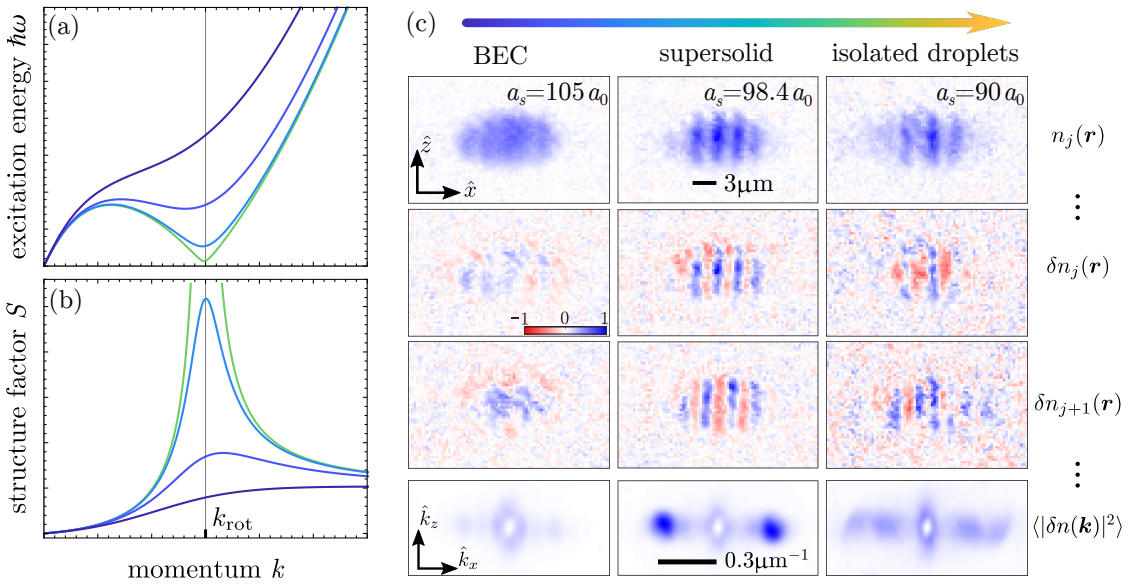

Figure 3.7.: **Density fluctuations across the superfluid to supersolid phase transition in tubular harmonic traps.** Schematic of the dispersion relation $\hbar\omega(k)$ (a) and corresponding static structure factor $S(k)$ (b) of an elongated dipolar superfluid [358]. Towards the supersolid phase transition the softening roton minimum at $k_{\rm rot}$ is associated to enhanced density fluctuations δn leading to a peak in $S(k)$. (c) Experimental observation of density fluctuations across the superfluid to supersolid phase transition. For each a_s a large number of in-situ images $n_j(\boldsymbol{r})$ is collected and density fluctuation images $\delta n_j(\boldsymbol{r}) = n_j(\boldsymbol{r}) - \langle n_j(\boldsymbol{r})\rangle$ are given by the deviation from their mean $\langle n_j(\boldsymbol{r})\rangle$. The mean power spectrum of the fluctuations $\langle|\delta n(\boldsymbol{k})|^2\rangle$ are directly related to the amplitude of $S(\boldsymbol{k})$. The colormap in (c) indicates the amplitude of densities, density fluctuations, and mean power spectra, respectively normalized to each row separately. Figure adapted from [5].

$\epsilon(\boldsymbol{k}) = \hbar^2k^2/2mS(\boldsymbol{k})$ (Eq. (2.55)) is a meaningful continuous estimate and an upper bound of the discrete dispersion relation (Fig. 3.6) for an excitation spectrum that is dominated by a single mode. In the supersolid multiple modes contribute to the excitation spectrum and the splitting into multiple branches around the Brillouin edge leads to a deviation from the single-mode approximation towards smaller scattering lengths.

The Feynman-Bijl equation suggests which density fluctuations are predominantly excited and consequently observable in the experiment as the superfluid to supersolid phase transition is crossed. Lower-energy excitations of the superfluid lead to a larger contribution to $S(\boldsymbol{k})$ and are enhanced near the transition point as compared to higher-energy excitations (Fig. 3.7(a)-(b)). To measure fluctuations and the structure factor experimentally (Fig. 3.7(c)), we begin with a quasi-pure BEC at $a_s \simeq 105\,a_0$, linearly ramp the scattering length to final values between this start value and $a_s = 90\,a_0$ within 30 ms,

and wait for 15 ms for the system to equilibrate. For each scattering length we repeat the experiment about 200 times acquiring statistics of the density fluctuations present in the system due to the droplet formation dynamics and finite temperature. We briefly describe the measurement of the static structure factor and focus on the in-situ observation of specific elementary excitations using principal component analysis (PCA) further below. The structure factor measurement has taken a significant role in the thesis [129] to which we refer for further details.

First we center the in-situ images $n_j(\boldsymbol{r})$ to remove residual COM excitations [8]. Subsequently we obtain the average density $\langle n(\boldsymbol{r})\rangle$ and the density fluctuation images $\delta n_j(\boldsymbol{r}) = n_j(\boldsymbol{r}) - \langle n(\boldsymbol{r})\rangle$. With the Fourier transform of the density fluctuations $\delta n_j(\boldsymbol{k}) = \int \mathrm{d}^3 r \delta n_j(\boldsymbol{r}) e^{i\boldsymbol{k}\cdot\boldsymbol{r}}$ we obtain the mean power spectrum of the fluctuations $\langle|\delta n(\boldsymbol{k})|^2\rangle$. The static structure factor in homogeneous systems is related to the density fluctuation power spectrum by $S(\boldsymbol{k}) = \langle|\delta n(\boldsymbol{k})|^2\rangle / N$, where N is the atom number [27, 260, 262]. In a trapped system the second-order pair-correlation function that the structure factor derives from in general depends on two coordinates rather than only the relative coordinate in uniform systems [129, 255, 263, 359, 360]. Provided the local-density approximation is valid the quantity $S(\boldsymbol{k}) = \langle|\delta n(\boldsymbol{k})|^2\rangle / N$ corresponds to a volume-integrated version of this pair correlation function [263] and still relates to the strength of the local density fluctuations [360–364]. Our evaluation gains access to this density fluctuation strength simultaneously at all momenta between $k_{\mathrm{min}}/2\pi \simeq 0.08\,\mu\mathrm{m}^{-1}$ and $k_{\mathrm{max}}/2\pi \simeq 1\,\mu\mathrm{m}^{-1}$ due to the finite system size and the finite resolution of our imaging system, respectively [260, 360]. The imaged atomic densities are integrated along the line-of sight y which translates to a cut through the static structure factor $S(k_x, k_y = 0, k_z)$ according to the Fourier-slice theorem[5] [129, 365]. The dominant structure occurs along $k_z = 0$ in the structure factor (Fig. 3.7(c)) consistent with mostly longitudinal excitations along x and suppressed transverse excitations in the z-direction.

The line profiles of the structure factor $S(k_x, k_z = 0)$ are shown across the transition in Fig. 3.8. Already far in the superfluid regime a small peak at $k/2\pi \simeq 0.25\,\mu\mathrm{m}^{-1}$ can be seen indicating a finite roton population in the BEC [8] which underlines a deviation from the dispersion relation of purely contact-interacting gases. The peak rises towards smaller a_s in accordance to the Feynman-Bijl equation and the expectation that density fluctuations rise approaching the transition. The peak position moves towards larger momenta for

[5] For an arbitrary function $f(x, y, z)$ and its projection $p(x, y) = \int \mathrm{d}z\, f(x, y, z)$ the Fourier-slice theorem reads $\mathcal{F}[f](k_x, k_y, 0) = \mathcal{F}[p](k_x, k_y)$ where $\mathcal{F}$ is the Fourier transform.

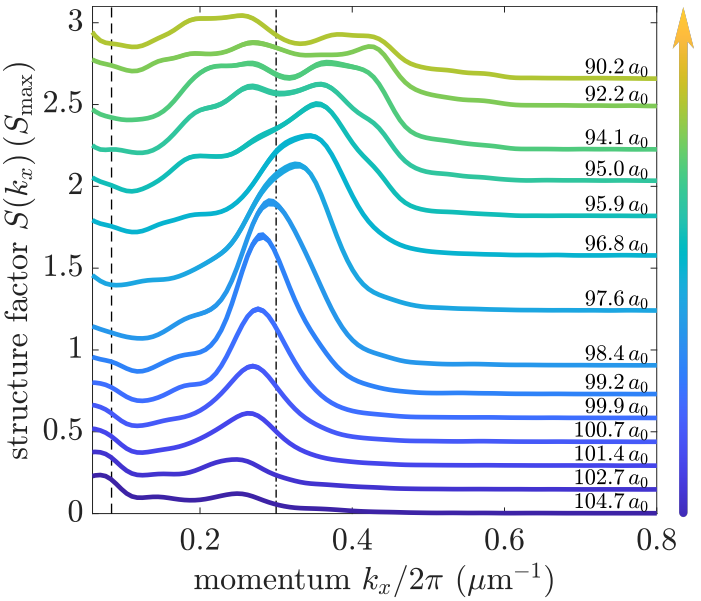

Figure 3.8.: **Measured static structure factor across the transition.** The dashed line at $k_{\min} \simeq 0.08\,\mu\mathrm{m}^{-1}$ indicates the smallest physical momentum due to the finite size of the system along the x-direction. The dash-dotted line at $k_x/2\pi \simeq 0.3\,\mu\mathrm{m}^{-1}$ roughly indicates the inverse droplet spacing at the transition point. For better visibility, the lines shifted up for smaller a_s. The structure factor is shown in units of $S_{\max} = 260$ and the line thickness indicates the error bars obtained by bootstrapping [366–369]. Figure adapted from [5].

smaller a_s consistent with predictions based on a variational theory of elongated dipolar BECs [358, 370].

The structure factor peak amplitude attains its maximum $S_{\max} = 260$ at $a_s \simeq 98.4\,a_0$. This scattering length is near the center of the supersolid region $a_s \simeq 96 - 100\,a_0$ we previously determined [8, 129] through interference analysis similar to the one described in section 3.1 and measurements of the Goldstone mode correlation [8]. The magnitude of $S_{\max}$ can be mainly explained by thermal enhancement of the populated low-energy modes [5]. As the roton gap Δ_{rot} decreases towards the transition point, the peak of the static structure factor scales as $S_{\max} \propto T/\Delta_{\mathrm{rot}}^2$ given that the roton gap is small compared to the temperature ($\hbar\Delta_{\mathrm{rot}}/k_{\mathrm{B}}T \lesssim 1$) and that the spectrum is dominated by a single mode. At $T = 0$ the Feynman-Bijl equation predicts an amplitude $S_{\max} \simeq 6$ for a roton gap $\Delta_{\mathrm{rot}} \simeq 0.6\omega_x$ at k_{rot} (Fig. 3.4). We obtain a corresponding amplitude by numerically evaluating the static structure factor within the BdG theory [129]. The corresponding thermal enhancement factor $2k_{\mathrm{B}}T/\Delta_{\mathrm{rot}}$ assuming temperatures between 15 nK and 20 nK is between 30 and 50 and explains the value $S_{\max}$ that we experimentally observe. This

large factor underlines the importance of finite temperature for the superfluid to supersolid phase transition. For a more detailed analysis including an estimation of the excitation spectrum based on this structure factor and its temperature dependence we refer to [5, 129]. Recent theoretical studies considering finite-temperature extensions of the GPE framework [315–317] have shown that small finite temperatures lead to a roton softening similar to a decrease in scattering length. The systematic shift between the critical scattering length in experiments and the the eGPE framework that has been reported by multiple groups [125, 128, 138, 148, 371] can be partially[6] explained by such finite temperature effects [316, 317].

Towards smaller scattering lengths in the supersolid and towards the isolated droplet regime the structure factor amplitude decreases and eventually splits around the Brillouin zone edge (Fig. 3.8). The splitting is reminiscent of the contributions of higher-lying phonon modes from our theoretical analysis (Fig. 3.6).

To investigate which density fluctuation pattern are the most dominant in our experiments, we use PCA on a dataset combining all scattering lengths. PCA is a model-free statistical analysis method used to extract the main variance from datasets and the principal components correspond to BdG eigenmodes for small cross-pixel correlations in the images [372]. We provide additional details in appendix B. The first principal component (PC) has no structure and represents atom number fluctuations [372]. The subsequent PCs (Fig. 3.9(a)-(b)) have a periodic structure and show either a clear reflection symmetry or antisymmetry with respect to the center of the trap. The projection of the PCs onto the x-axis (Fig. 3.9(c)-(d)) shows excellent agreement with the line profiles of the density fluctuation patterns of the two degenerate roton modes obtained from the BdG analysis. The weight of these PCs (Fig. 3.9(e)) increases sharply towards the supersolid region and attains its peak within this region. In the vicinity of this peak often even single-shot in-situ images show the characteristic spatial variance of the symmetric and antisymmetric roton modes (Fig. 3.7(c), middle column). The weight of both PCs is similar for the considered scattering length range which is consistent with the degeneracy of the two roton modes from BdG theory up to the critical point. The change of the density flucutation patterns in the supersolid due to hybridization shown in BdG theory is indirectly captured by the decay of the weight of these PCs towards smaller scattering lengths: overall more PCs are needed to describe the spatial variance.

[6] We independently implemented this finite-temperature extension of the eGPE and find that the shift in a_s is not fully explained by finite temperature. Further discussion is found in Refs. [153, 197] using a simpler model proposed in Ref. [315].

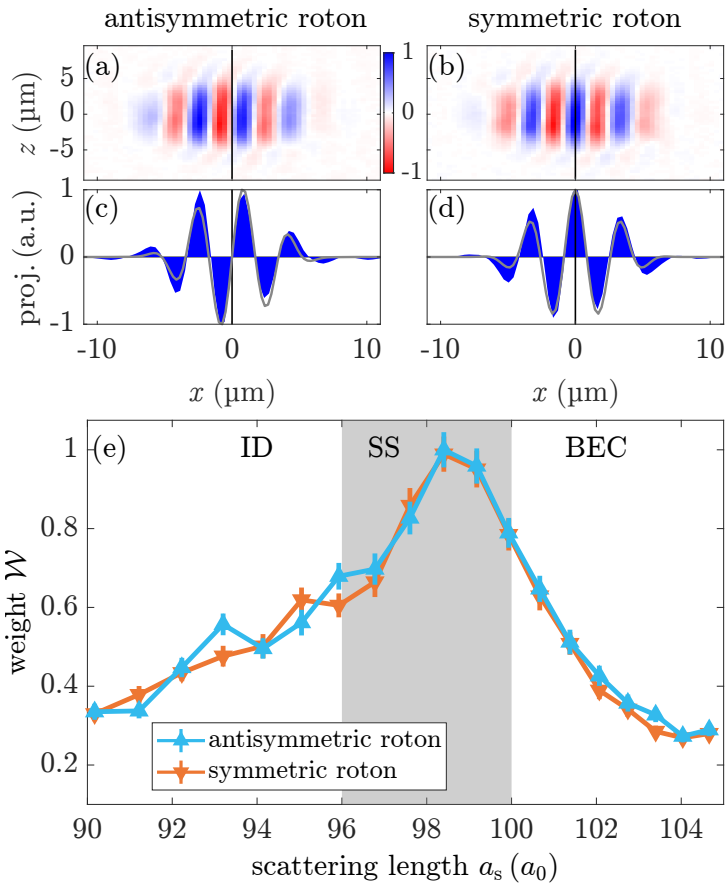

Figure 3.9.: **In-situ observation of roton modes across the transition.** (a)-(b) Spatial structure of the two most dominant PCs in the experimental dataset. (c)-(d) Projections of (a)-(b) onto the x-axis (blue) and the density fluctuation patterns from the BdG calculation (gray). (e) Mean of the absolute value of the weights $\mathcal{W}$ of the PCs (a)-(b) normalized to the weight of (a) at the transition point, which is the maximum weight of all PCs for all a_s. The gray area in(e) indicates the supersolid region previously determined [8] and error bars are the standard error of the mean.

The next three important PCs (Fig. 3.10(a)-(c)) can be identified as phonon modes. The superfluid or BEC phonon PC (a) correponds to the quadrupole mode density fluctuation pattern we find with the BdG analysis. The antisymmetric (b) and symmetric (c) crystal phonon modes are consistent with the two modes above the Higgs branch near the phase transition ($a_s \simeq 95.5\,a_0$ in Fig. 3.4). These modes are also visible in the dynamic structure factor as the two branches splitting around the Brillouin zone (Fig. 3.6). The power spectrum of the experimentally found crystal phonon PCs (e)-(f) additionally confirms this assignment and reveals that the emergence of these crystal phonons is the reason for the splitting in the structure factor towards small a_s (Fig. 3.8). In contrast the power spectrum

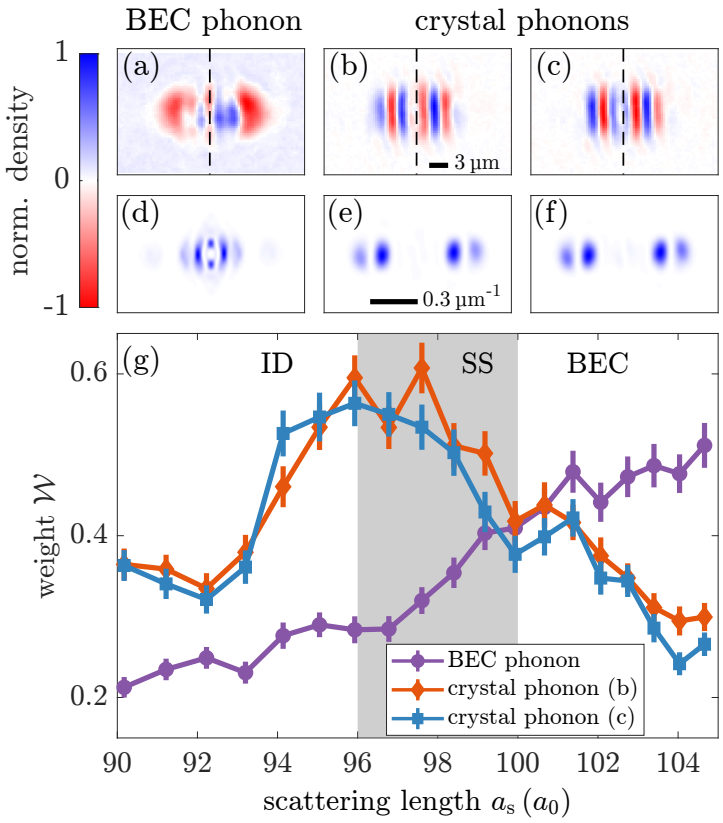

Figure 3.10.: **In-situ observation of phonon modes across the transition.** (a)-(c) Spatial structure of the third to fifth most dominant PCs in the experimental dataset and (d)-(f) corresponding spatial power spectra. With our BdG analysis (a) can be identified as the quadrupole excitation of the superfluid and (b)-(c) as antisymmetric and symmetric phonon modes in the supersolid near criticality. (g) Mean of the absolute value of the weights $\mathcal{W}$ of the PCs (a)-(c). The normalization and gray region are the same as in Fig. 3.9 and error bars indicate the standard error of the mean.

of the BEC phonon (d) shows that this is a low-momentum excitation. The weights of the phonon PCs (g) show that in the supersolid phase, both superfluid and crystal phonons coexist with appreciable weight. The superfluid phonon weight continuously decreases from BEC to islated droplets while the crystal phonons weights rise far into the supersolid regime. Towards the isolated droplet regime the weights decrease which can be attributed to the hybridization of these phonons with other phonon modes and a change in the spatial structure of the density fluctuation patterns (Fig. 3.4). Yet more PCs are required to describe all spatial variance in the isolated droplet regime where we find that the assignment of individual PCs to BdG modes becomes increasingly difficult and PCs can become superpositions of BdG modes.

3.3. Supersolids in toroidal traps

In previous sections we have explored the making, probing, and various properties of dipolar supersolids in tubular harmonic traps. The finite trapping potential in the direction of the density modulation has a strong influence on the behavior of such supersolids. We have shown that the trap leads to formation of a few crystal sites at a finite roton gap, that the corresponding Goldstone and Higgs modes have a finite energy, and that the spectrum is characterized by multiple avoided crossings and coupling between the Higgs mode and phonon modes of the same symmetry. These properties not only have to be taken into account for an accurate description of trapped dipolar supersolids, but they also obscure the correspondence to macroscopic supersolids arising through spontaneous breaking of a continuous symmetry.

The experimental evidence for such supersolidity as first proposed to be found in helium remains elusive [83, 91, 373] but helium has played a central role in our understanding of superfluidity. In superfluids at zero temperature, the Goldstone mode emerges as superfluid sound from breaking the $U(1)$ symmetry [27, 374]. The presence of a non-superfluid component can lead to a second sound mode through coupling to the superfluid component. Historically this concept of second sound originates from a hydrodynamic two-fluid model describing the out-of-phase oscillation between thermal and superfluid components of helium [375, 376]. In a supersolid [69, 71, 78], the translational symmetry breaking of the superfluid introduces a Goldstone mode in the supersolid which is closely connected to the superfluid flow throughout the crystal structure (section 3.2). For the supersolid, the crystal structure can be considered a non-superfluid component at zero temperature. This point of view allows to draw analogies between the supersolid Goldstone mode and second sound in finite temperature helium.

The finite trapping potential of dipolar supersolids has complicated the identification of this Goldstone mode [8, 377] as a second sound of supersolids at zero temperature and developing a consistent picture to describe the different sound modes has proven challenging, both experimentally and theoretically [2, 5, 7, 8, 96, 148, 378–380]. The identification is complicated by harmonic trap confinement, where elementary excitations couple to center of mass (COM) modes. In addition, hydrodynamic theories which can identify the two sound modes are unable to capture gapped modes such as the Higgs mode [347, 381–383], which is yet to be observed experimentally in a supersolid. Even box potentials [384] that have been recently applied to study second sound in short-range interacting ultracold

gases [385, 386] are no straightforward option for ultracold dipolar gases: Due to dipolar repulsion, dipolar superfluids accumulate a significant density at the edge of the box and rotonic density oscillations form towards the center of the box [237, 387]. Fine-tuning of the box edge steepness is required to obtain a homogeneous dipolar superfluid [388] and depends on the interaction strength. Here, toroidal potentials [341, 389–392] are a better choice: The continuous rotational symmetry and periodic boundary conditions along the azimuthal direction link experimentally achievable finite-size supersolids with those in the bulk addressed by mean-field [338, 383] and quantum Monte Carlo methods [350, 351].

In this section we theoretically investigate the superfluid to supersolid phase transition in a toroidal trap. Parts of this section have been published in:

- J. Hertkorn, P. Stürmer, K. Mukherjee, K. Ng, P. Uerlings, F. Hellstern, L. Lavoine, S. Reimann, T. Pfau, and R. Klemt, "Decoupled sound and amplitude modes in trapped dipolar supersolids", arXiv:2404.12384 (submitted for peer review) (2024).

In section 3.3.1 we show how first sound, second sound, and the Higgs amplitude modes emerge by following their origin from superfluid modes across the transition. The spatial symmetries of the eigenmodes are classified using group theory and we show how a quasimomentum $\tilde{q}$ is assigned to the eigenmodes. The assignment establishes a direct correspondence between the excitations of finite-sized systems and infinite systems in which the description using band structures becomes meaningful. The spectrum and the following assignments can be directly compared to the trapped case (section 3.2). In section 3.3.2 we show that the second (first) sound is an out-of-phase (in-phase) oscillation between superfluid and crystal components and that both sound modes emerge from the superfluid sound branch near the roton momentum q_{rot}, which defines the crystal periodicity. At the critical point, q_{rot} becomes the $\tilde{q} = 0$ point of the emergent Brillouin zone, at which the superfluid sound mode splits into the $\tilde{q} = 0$ instance of the second sound branch – the zero-energy Goldstone mode – and a separate isolated Higgs amplitude mode. As we show in section 3.3.3, the analysis of these modes allows us to design experimental protocols for the spectroscopy of toroidal supersolids, probing single elementary excitations of the supersolid.

3.3.1. Ground states and excitation spectrum

We introduce a toroidal trap geometry by setting the external trapping potential to $V_{\mathrm{ext}} = M\omega_r^2 \left[(\rho - \rho_0)^2 + \lambda^2 z^2\right]/2$. Such spatially dependent trapping potentials can be

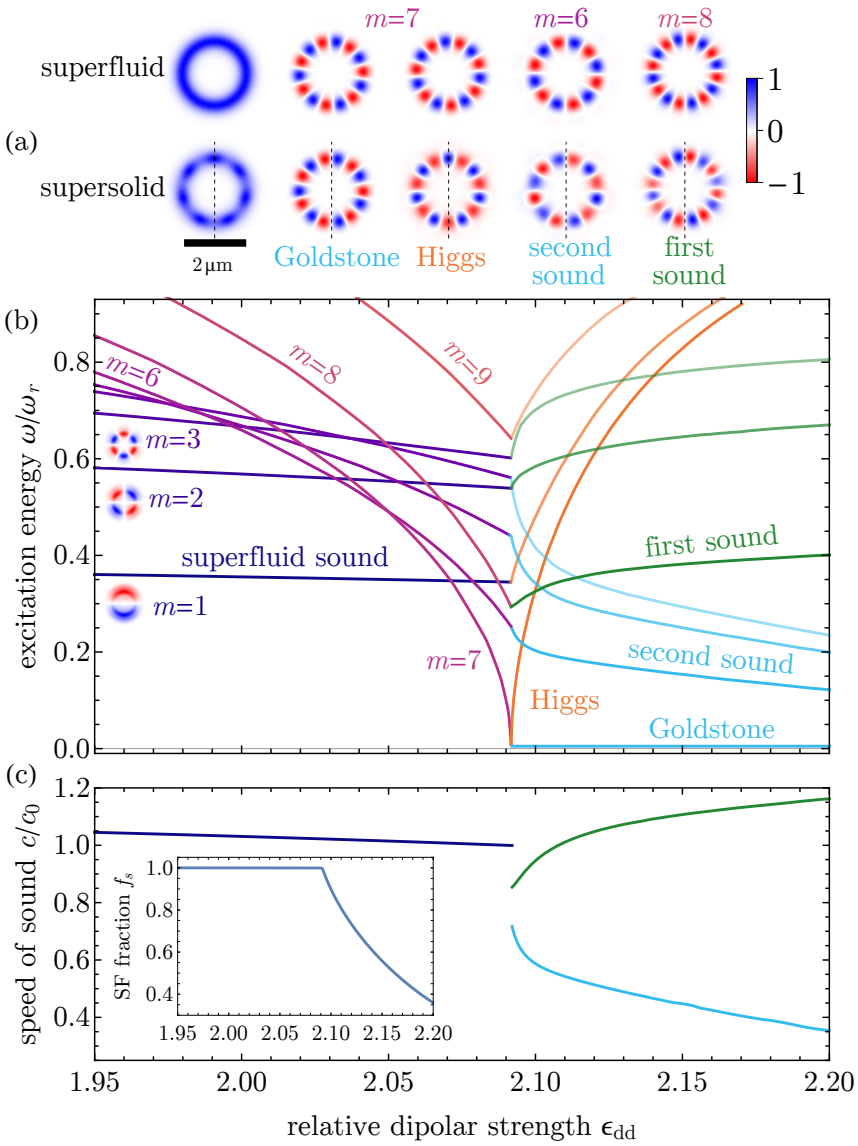

Figure 3.11.: **Elementary excitations across the superfluid-to-supersolid phase transition.** (a) Ground state density $n(x, y, z = 0)$ and Bogoliubov mode patterns $f_i(x, y, z = 0)$ in arbitrary units for a selection of modes in the superfluid (top row) and supersolid (bottom row) regime in the vicinity of the transition point ($\epsilon_{\mathrm{dd}} \in \{2.090, 2.093\}$). Atoms flow in the direction of the gradient of f_i, where red indicates a depletion and blue an increase of atomic density. (b) Bogoliubov excitation energies ω_i as a function of ϵ_{dd}. Superfluid excitations are labelled by their circulation quantum number m. The superfluid sound branch (dark blue) features higher m states (purple) that soften towards the transition point, which are angular roton modes. The supersolid has three excitation branches: two Goldstone phonon branches (first [green] and second [blue] sound) and the Higgs amplitude branch. A lighter color corresponds to a higher quasimomentum $\tilde{q}$. The $\tilde{q} = 0$ instance of the second sound branch is labeled 'Goldstone' analogous to the low-energy Goldstone mode in harmonic traps (section 3.2). (c) Speed of sound of the phonons in units of the superfluid sound velocity at the phase transition $c_0 \simeq 2.2\,\mathrm{mm/s}$ (colors as in (b)). The inset shows the superfluid fraction based on the non-classical rotational inertia (Eq. (3.3)). Figure adapted from [1].

achieved using digital micromirror devices (DMDs) or spatial light modulators (SLMs) [384]. We focus on parameters yielding $n_d = 7$ droplets along the torus which we find assuming a torus radius $\rho_0 = 1\,\mu\text{m}$, radial trap frequency $\omega_r/2\pi = 1\,\text{kHz}$, aspect ratio $\lambda = 1.7$, and particle number $N = 5\times10^3$. We calculate the ground state between $a_s = 59a_0$ and $a_s = 67a_0$, corresponding to relative dipolar strengths $\epsilon_{\text{dd}} = a_{\text{dd}}/a_s \in [1.95, 2.20]$[7].

As a function of ϵ_{dd} we find the ground state to be either superfluid ($\epsilon_{\text{dd}} \lesssim 2.09$) or supersolid[8] (Fig. 3.11). Upon further increasing ϵ_{dd} the supersolid eventually develops into a state of n_d isolated droplets. The rotational symmetry of the trap allows us to classify the ground states based on the superfluid fraction calculated from the nonclassical rotational inertia (Eq. (3.3))[9]. The superfluid fraction is unity in the superfluid and continuously drops in the supersolid towards higher ϵ_{dd}.

The spectrum of the low energy modes across the superfluid to supersolid phase transition is shown in Fig. 3.11(b). We focus on the low-energy behavior ($\omega < \omega_r$) of longitudinal excitations along the torus. Modes in the superfluid are labeled by the integer circulation number $m > 0$ and are twofold degenerate due to the combination of the rotational symmetry around the $\hat{\boldsymbol{z}}$-axis and the mirror symmetry with respect to vertical planes through the origin [124, 240, 283, 393, 394]. Deep in the superfluid the energy of the modes increases monotonically with the circulation number m due to an increase in kinetic energy analogous to the situation in harmonic traps (section 3.2). For a sufficiently large torus radius, where the curvature of the torus is smaller than the typical length scales of the mode patterns, we can interpret m as a quantization of the linear momentum scale $q_m = 2\pi m/\Theta$, where Θ is the circumference of toroidal density distribution[10]. Deep in the superfluid regime and the long-wavelength limit we expect a phononic dispersion relation $\omega_m = c_s q_m$ with the superfluid speed of sound c_s. Due to the influence of the dipolar interactions (for the given system size) only the lowest mode ($q = q_1$) falls into this linear regime for the lowest ϵ_{dd} considered here. Towards higher ϵ_{dd} a number of states with higher m decrease in energy. These modes correspond to angular roton modes [4, 5, 124, 240, 241, 283, 393–395] that have so far been mostly studied in harmonic trapping geometries.

[7] In this regime, the quantum fluctuation term in the eGPE has an imaginary part that is still $< 3\%$ of the real part. The approximation $Q_5(\epsilon_{\text{dd}}) \simeq 1 + 3\epsilon_{\text{dd}}^2/2$ is still justified. One can also scale atom number and torus radius to achieve a lower value of ϵ_{dd} at which the supersolid forms [347].

[8] In this section we present results as a function of $\epsilon_{\text{dd}} = a_{\text{dd}}/a_s$ as opposed to a_s in order to be easily transferable to systems with other a_{dd} as well.

[9] Herein $\Omega = 10^{-7}\omega_r$.

[10] Note that $\Theta \approx 2\pi(1.1\rho_0)$ as the dipolar interaction effectively increases the radius around which the density distribution is centered compared to the actual trap radius [347].

The superfluid to supersolid phase transition is triggered when the two degenerate $m = 7$ modes reach zero excitation energy, defining the quantum critical point $\epsilon_{\mathrm{dd}}^{\mathrm{crit}} \simeq 2.09$. Corresponding to the density fluctuation periodicity of the $m = 7$ modes (Fig. 3.11 (a)), $n_d = 7$ droplets form with a high overlap and spontaneously break the rotational symmetry of the ground state. At the critical point towards the supersolid the two degenerate $m = 7$ roton modes split into a zero-energy Goldstone mode[11] and Higgs amplitude mode. In contrast to tubular harmonic traps where the translational symmetry is strictly speaking already broken by the trap (section 3.2) the splitting in toroidal traps occurs at zero energy due to the continuous rotational symmetry. The zero-energy Goldstone mode pattern is spatially phase-shifted by half a period with respect to the density, while the Higgs pattern is in phase (Fig. 3.11(a)). For the zero-energy Goldstone mode (Higgs amplitude mode) the gradients (peaks) of the density fluctuation patterns are aligned with the droplet centers corresponding to a rotation of the droplets along the torus (an amplitude modulation between superfluid background and droplets). The two modes correspond to a pure phase and amplitude mode, with striking clarity compared to supersolids in tubular harmonic traps where the amplitude mode couples to other modes which consist of mixed phase and amplitude character. While the finite lowest momentum available to the toroidal superfluid $q_1 > 0$ is given by the torus size, the vanishing roton modes define a precise momentum q_7 that becomes the quasimomentum $\tilde{q}_0 = 0$ point of the emerging Brillouin zone as the supersolid forms. Accordingly the so-far discussed Higgs and Goldstone modes have a quasimomentum $\tilde{q}_0 = 0$.

More generally, all excitations of the supersolid belong to three distinct excitation branches (Fig. 3.11): two Goldstone phonon branches and a Higgs amplitude branch. The periodic boundary conditions allow us to clearly identify these three branches predicted for infinitely extended supersolids [169, 338] in finite and experimentally feasible systems. Higher-lying $\tilde{q} > 0$ instances of each branch can be seen and are indicated with a lighter color in Fig. 3.11. We label the lower (upper) Goldstone branch in this zero-temperature supersolid as second (first) sound in analogy to the sounds of helium at finite temperature. The two sound modes show a weaker dependence on ϵ_{dd}, with the first sound branch rising in energy while the second sound branch is decreasing, consistent with a smaller superfluid fraction [347, 382]. The analogy will be detailed further below and in section 3.3.2. The

[11] The zero-energy Goldstone mode numerically shows a finite energy $\omega/\omega_r < 0.01$ for the spatial grid size employed here. We have confirmed that this energy decreases for finer spatial grids and tighter convergence criteria, consistent with a gapless Goldstone mode and with our following considerations of the continuous rotational symmetry of the trap [1].

zero-energy Goldstone mode corresponds to the $q = 0$ limit of the second sound branch. An alternative point of view is that as the zero-energy Goldstone mode is not a physical degree of freedom because it lies at $\omega = q_0 = 0$ and represents the degeneracy of the ground state with respect to droplet crystal orientation. We find that the identification of the zero-energy Goldstone mode as the first instance on the second sound branch is nonetheless useful, in particular since this interpretation is consistent with the lowest energy Goldstone mode as a second sound in harmonic traps, lifted to a finite energy due to the already broken translational symmetry. Analogously a breaking of the rotational symmetry of the torus elevates the zero-energy Goldstone mode to a finite energy and allows exciting this mode (section 3.3.3).

Based on the structure factor (section 3.3.2) and the circulation number of modes in the superfluid m, we can attribute the quasimomentum $\tilde{q}_m = 2\pi m/\Theta$, with $m = 0, 1, 2, 3$, to the modes in the supersolid. The former assignment is directly related to the experimentally measurable density response of the system. The latter method is supported by employing group theory allowing an a priori assignment of correspondences between all modes of the superfluid to all modes of the supersolid. The superfluid ground state has the symmetry of the point group $C_{\infty,v}$, describing its invariance under rotation and reflection. At the superfluid-supersolid transition this symmetry is broken, $C_{\infty,v} \to C_{7,v}$, where $C_{7,v}$ contains the irreducible representations $A_1,\ A_2,\ E_1,\ E_2,\ E_3$, with symmetries of $A_{1,2}$ corresponding to an $m = 7$ angular roton mode, and of E_j to one with $m = j$ compatible with quasimomentum $\tilde{q}_j$. The allowed quasimomenta, purely based on symmetry arguments, are thus $\tilde{q}_m$ for $m = 0, 1, 2, 3$. This analysis directly generalizes to an arbitrary droplet number n_d through subduction of $C_{\infty,v}$ to $C_{n_d,v}$. We provide more details on this correspondence in appendix C. In short the number of two-dimensional irreducible representations E_i in $C_{n_d,v}$ grows up to $(n_d - 1)/2$ (n_d odd) or $n_d/2$ (n_d even) defining the center of the first Brilloin zone at $\tilde{q}_{n_d/2}$ up to which m increases and above which m decreases in the assignment $m \to \tilde{q}_m$. An example of this compatibility between modes of the superfluid and modes of the supersolid can be seen for the $m = 6$ and $m = 8$ modes before and after the transition (Fig. 3.11 (a)). In the supersolid these modes give rise to the second and first sound at quasimomentum $\tilde{q}_1$ and show a reflection antisymmetry described by E_1.

The dispersion relation of the two supersolid phonons is expected to flatten off close to the edge of the Brillouin zone after the initial linear rise. The flattening is reflected in Fig. 3.11(b) as a decrease in energy spacing towards higher $\tilde{q}$. In contrast the Higgs mode

energy is a convex function of the quasimomentum with an increasing energy spacing towards higher $\tilde{q}$.

Using the energies of the superfluid phonon at q_1 and the supersolid phonons at $\tilde{q}_1 = q_1$ we calculate the speed of sound $c_i = \omega_i/\tilde{q}_1$ across the transition, where $i = s, 1, 2$ corresponds to superfluid sound, first sound, and second sound. The results are shown in Fig. 3.11(c) and agree with recent descriptions using hydrodynamic models of supersolids [338, 347, 382, 383].

In a hydrodynamic description of superfluids [27] the speed of sound can be defined based on ground state properties of the system. The sound speed $c_\kappa = 1/\sqrt{M\bar{n}\kappa}$ is defined based on the compressibility $\kappa = (1/\bar{n}^2)\partial\bar{n}/\partial\mu$ where μ is the chemical potential and $\bar{n}$ is the average density. In the superfluid, c_κ coincides with the superfluid speed of sound c_s [27, 347] providing a definition of this speed of sound independent of the BdG analysis. For comparison we calculate c_κ in the superfluid. To do so we note that $\bar{n}\kappa$ is independent of the unit of $\bar{n}$, and so is c_κ. Therefore we can write $\bar{n}\kappa = \mathrm{d}\ln\bar{n}/\mathrm{d}\mu$[12]. The average azimuthal density $\bar{n} = N/\Theta$ is independent of the detailed spatial dependence of the density $n(x, y, z)$. To estimate $\bar{n}\kappa$ we vary N by a few percent, calculate the ground state, and obtain $\mu(\bar{n})$. We obtain reasonable agreement with the BdG description, with c_κ typically $\simeq 20\%$ larger compared to the BdG speed of sound. Similar deviations have been reported [347] and are likely due to the finite torus size. Very recent hydrodynamic descriptions of supersolids also provide expressions of the speeds of sound of supersolid phonons in terms of c_κ, the superfluid fraction f_s, and the layer compressibility modulus B [347, 382, 383]. These expressions show that $\partial c_1/\partial f_s < 0$ and $\partial c_2/\partial f_s > 0$ and serve as a classification of the individual phonon modes of supersolids into first and second sound. Modes of second sound soften and modes of first sound stiffen as the superfluid fraction decreases (Fig. 3.11(b)).

The discontinuity between the speed of superfluid sound and first sound at the phase transition point is consistent with a second-order phase transition at intermediate densities in the corresponding bulk system [338][13]. The discontinuity can be identified by perturbing the system and studying the available phonon modes just based on the eGPE dynamics [347, 396]. Our BdG analysis reveals the underlying elementary excitations of the superfluid giving rise to first and second sound (Fig. 3.11(b)). For our parameters the $m = 6$ and

[12] We find that $\Theta/2\pi$ varies by less than 0.01 µm in the SF for our parameters, allowing alternatively and to a good approximation to calculate c_κ using $\bar{n}\kappa \approx \mathrm{d}\ln N/\mathrm{d}\mu$.

[13] The speed of sound is related to a first order derivative of the chemical potential which in turn is a first order derivative of the total energy. A discontinuity in a second order derivative of the thermodynamic potential (the total energy at zero temperature) points to a second order phase transition [338, 383]

$m = 8$ modes give rise to the lowest quasimomentum first and second sound modes. Notably the $m = 8$ mode drops below the $m = 1$ mode of the superfluid before the transition point and the $m = 1$ mode becomes the $\tilde{q}_1$ Higgs mode of the supersolid. This reordering is consistent with an avoided crossing of Higgs and first sound branches described in an infinite system [338]. As modes with the same $\tilde{q}$ correspond to the same symmetry these modes can couple to each other and lead to level repulsion between second sound and first sound at $\tilde{q}_1$ and first sound and Higgs mode at $\tilde{q}_1$, respectively. The apparent splitting between first sound and second sound as a result of these symmetry properties have also been described as bifurcation [96, 304, 397] and was suggested as a signature for the supersolid transition.

The interpretation of excitation spectra of previously reported for finite harmonically trapped systems [7, 8, 96, 97, 148] in terms of the three characteristic supersolid excitation branches and the origin of the bifurcation was complicated by the absence of well-defined quasimomenta and Brillouin zones due to the coupling of linear and COM motion. The elongated trapping geometry permits only two distinct symmetries of the low-energy excitations even for larger droplet numbers: either even or odd with respect to the center of the trap. In contrast as we have shown here, toroidal supersolids increase the number of available symmetries of the low-energy excitations with every additional droplet. As a result less avoided crossings appear in the spectra of toroidal supersolids and allow modes to maintain their character further away from the transition point.

Most strikingly the Higgs branch keeps its character even relatively far away from the transition point. This isolation allows us to evaluate the dispersion relation of this new and stable Higgs quasipartle within the self-generated periodic structure of the supersolid. We find that the Higgs quasiparticle has a linear dispersion relation close to the phase transition that changes to a quadratic behavior further away. An effective band mass $M^* = \hbar^2(\partial^2 E/\partial\tilde{q}^2)^{-1}$ can be assigned to this quasiparticle (Appendix D).

3.3.2. Spatial and temporal character of elementary excitations

Beyond the characterization of the sound and amplitude modes in terms of their energetic behavior as a function of interaction strengths, the BdG approach allows us to characterize them in terms of their spatial and temporal character (Fig. 3.12).

We define the angular spectrum of the structure factor $\tilde{S}(k_\phi, \omega) = \int \mathrm{d}\phi\, e^{ik_\phi\phi}\tilde{S}(\phi, \omega)$, shown in Fig. 3.12(a)-(c). The structure factor and its angular spectrum is directly

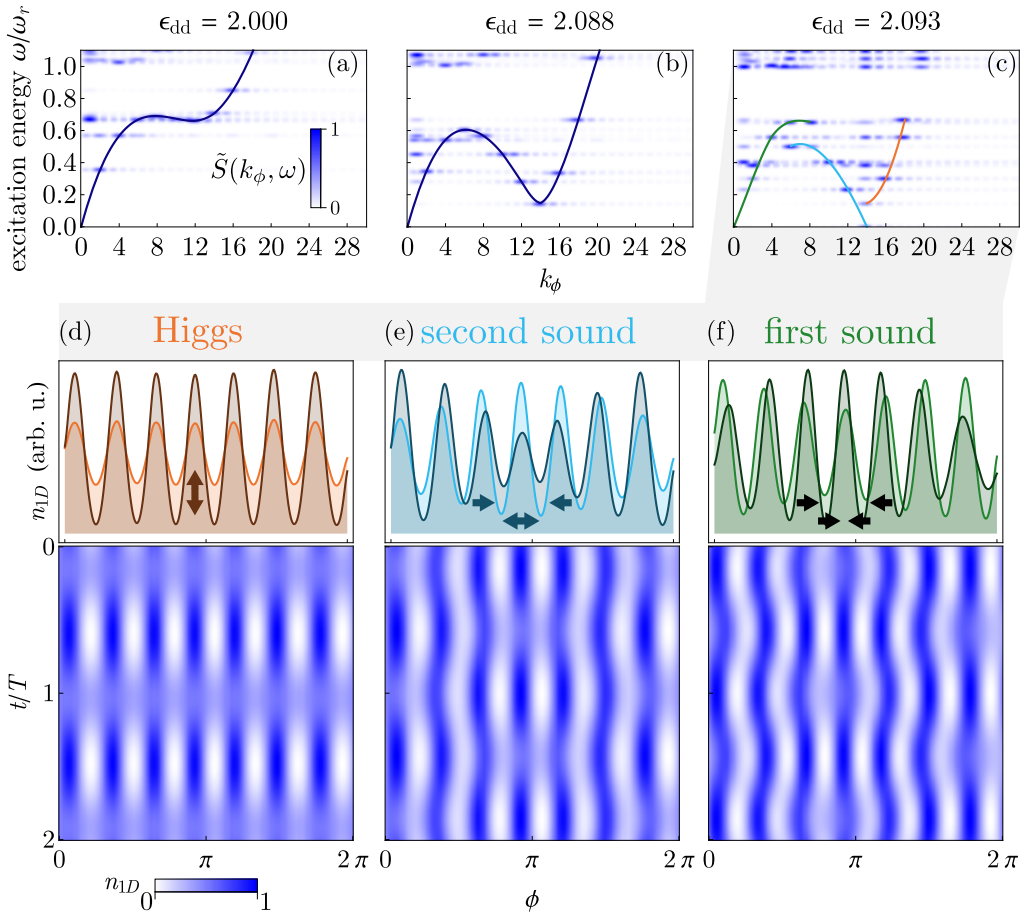

Figure 3.12.: **Spatial and temporal character of sound and amplitude modes.** (a-c) Angular spectrum of the dynamic structure factor $\tilde{S}(k_\phi, \omega)$ across the phase transition. We normalize $\tilde{S}$ at each ω_i for visual clarity. Lines through the most prominent peaks of $\tilde{S}$ are guides to the eye. (d-f) The upper panel shows cuts of the density along the torus $n_{1D}(\phi, t)$ at $t/T = 0,\ 1/2$ during the time evolution, where $T = 2\pi/\omega$. The lower panels show the full density evolution $n_{1D}(\phi, t)$ for two periods T of the Higgs mode, second sound, and first sound at $\tilde{q}_1$ from (c). The Higgs mode is an amplitude oscillation of the superfluid fraction. The second (first) sound is an out-of-phase (in-phase) oscillation between crystal structure and superfluid background. Figure adapted from [1].

accessible in experiments (section 3.2, 4.1). To obtain $\tilde{S}$ we transform the structure factor at $z = 0$ to polar coordinates $S(x, y, \omega) \to S(k, \phi, \omega)$, fix k to the radial momentum at which S displays a maximum, and are left with the angular distribution of the structure factor $\tilde{S}(\phi, \omega) = S(\phi, \omega) - \overline{S}$ where $\overline{S}$ indicates the average of $S(\phi, \omega)$ along ϕ. A mode with an m-fold angular symmetry, corresponding to an excitation at momentum q_m, shows up as a peak in $\tilde{S}(k_\phi, \omega)$ at $k_\phi = 2q_m/q_1 = 2m$. In the superfluid regime (Fig. 3.12(a)-(b)),

$\tilde{S}$ reproduces a discretized version of the known Bogoliubov dispersion relation, which is linear at small k_ϕ and quadratic towards larger k_ϕ. Near the phase transition, a roton minimum develops. On the supersolid side (Fig. 3.12(c)), the superfluid branch splits up into the first sound, second sound, and Higgs branches.

In an infinite system these three characteristic excitation branches are intuitively obtained by splitting up the dispersion relation of the superfluid at the transition point: the section from $q = 0$ to $q = q_{\mathrm{rot}}/2$ becomes first sound, from $q = q_{\mathrm{rot}}/2$ to $q = q_{\mathrm{rot}}$ becomes second sound, and $q > q_{\mathrm{rot}}$ becomes the Higgs branch after folding the sections back into the first Brillouin zone [169, 338]. In a torus of finite size, the momenta are discretized and the branches are identified by analyzing the peaks of $\tilde{S}$ as a function of k_ϕ.

For the first sound branch, the first mode shows peaks at $k_\phi = 2,\ 14,\ 16$, the second mode at $k_\phi = 4,\ 14,\ 18$, and the third mode at $k_\phi = 6,\ 8,\ 14$. The peak at $k_\phi = 14$ corresponds to a modulation at the spatial frequency of the crystal structure and the other peaks can be mapped to a quasimomentum of $|\tilde{q}_m|$ with $m = 1, 2, 3$. The excitation patterns correspondingly displays a $m-$fold rotational symmetry. The second sound branch has no peak $k_\phi = 14$ for all modes. Instead the main peaks are at 12 ($m = 1$), 10 ($m = 2$), and $(6, 8)$ for $m = 3$. The structure of the Higgs modes similarly maps to a quasimomentum of $|\tilde{q}_m| = 0, 1, 2$ [14].

While modes of different branches can be assigned the same symmetry and quasimomentum their temporal character is strikingly different between each branch (Fig. 3.12(d)-(f)). The Higgs mode Fig. 3.12(d) has a clear amplitude character with atoms flowing from the superfluid brackground into the droplets and vice versa. The second (first) sound modes are an out-of-phase (in-phase) oscillation between crystal compression and superfluid flow (Fig. 3.12(e)-(f)). As the crystal compresses towards one node on the torus, the superfluid density flows towards the opposite (same) direction, reducing (increasing) the density where the droplet spacing is smaller. The crystal compression is associated with an energy cost due to the dipolar repulsion of the droplets. The out-of-phase (in-phase) superfluid flow of second (first) sound reduces (increases) this cost and leads to an intuitive understanding of second sound being slower than first sound. The interplay between the superfluid flow and the crystal structure in this zero-temperature supersolid is reminiscent of the in- and out-of-phase oscillations between superfluid and normal fluid flow in a (non-dipolar)

[14] Apart from the contributions discussed so far, there is a low-frequency contribution at $k_\phi = 1$ which does not correspond to a specific quasimomentum but rather a slow modulation of the envelope of the excitation pattern most likely caused by residual coupling between the two degenerate modes within our numerical framework.

superfluid within the two-fluid model [376, 386, 398]. This similarity motivates our labeling of the corresponding modes as first and second sound. Another analogy is the behavior of the first and second sound speed as a function of the superfluid fraction. Both in finite temperature superfluid helium and unitary Fermi gases the second sound speed decreases towards zero as the temperature approaches the critical temperature, the superfluid fraction decreases, and the normal component approaches unity. It is by itself remarkable that strongly interacting superfluid helium and the unitary Fermi gas show a similar behavior of their first and second sound velocities [386, 398, 399]. Analogously the zero-temperature supersolids we consider here have a vanishing second sound velocity towards higher relative dipolar strengths, the superfluid fraction decreases, and the crystal component approaches unity. The second sound velocity can be used as a direct measure of the superfluid fraction [347, 386, 396, 399, 400]. For dipolar supersolids f_s can be directly calculated if c_κ, c_1, and c_2 are known [347, 396].

3.3.3. Spectroscopy of supersolids

Given that two sound modes exist, answering how these sound modes can be excited and measured has played a central role in understanding first and second sound in both superfluid helium and unitary Fermi gases [376, 386, 399].

The understanding of elementary excitations developed in this section helps devise simple and experimentally feasible schemes to excite them selectively (Fig. 3.13). The absence of strong coupling of the Higgs mode in toroidal supersolids in contrast to the harmonically trapped counterparts suggests that the toroidal trap is a suitable platform for pursuing a first measurement of this characteristic supersolid excitation. For selectively exciting one of either sound mode our symmetry considerations and the energetic behavior of the respective modes come into play.

To assess the our excitation schemes we use PCA on the time evolution after an initial excitation procedure on the ground state ψ_0 at $\epsilon_{\mathrm{dd}} \simeq 2.1$. The state is time evolved for typically 100 ms (or longer for the low-energy Goldstone mode). We obtain the spatial principal components $\mathrm{PC}(x, y)$ and their weights $w(t)$ quantifying their contribution to the spatial variance of the time evolution. The selectivity s is defined as the amount of variance described by the time evolution for a given PC. The overlap integral between the strongest PC and the corresponding BdG density fluctuation pattern $\delta n_j = f_j \psi_0$ is above

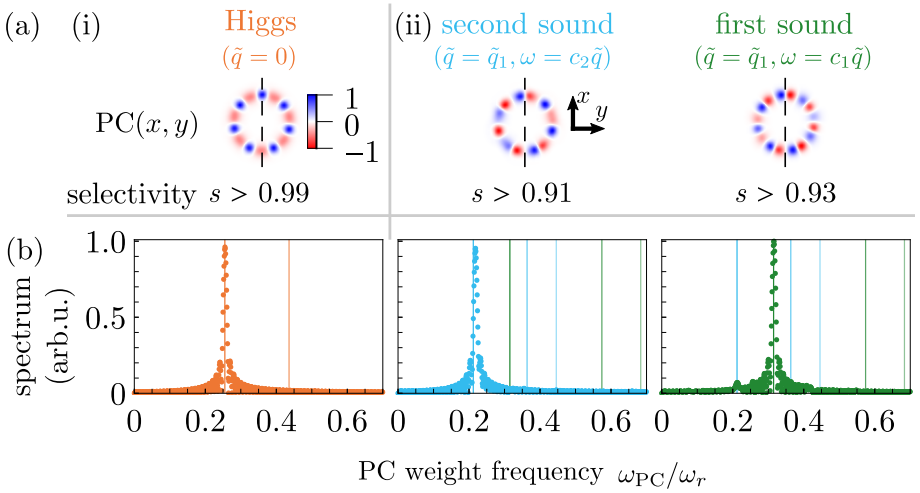

Figure 3.13.: **Spectroscopy of supersolids.** (a) Dominant PCs after applying an excitation scheme (i)-(ii) (see main text) to the ground state at $\epsilon_{\mathrm{dd}} \simeq 2.1$. (b) Fourier spectra $|\mathcal{F}_w(\omega_{\mathrm{PC}})|^2$ of the dominant PC weights $w(t)$. Vertical lines in the spectra indicate BdG energies (Fig. 3.11(b)). All modes are individually excited with $> 90\%$ selectivity and the PCs show above 99% overlap with the density fluctuation pattern obtained from the BdG analysis (Fig. 3.11(a)) and oscillate at frequencies corresponding to the BdG energies. Figure adapted from [1].

99% in all cases of Fig. 3.13[15].

The Higgs mode (Fig. 3.13(i)) can be selectively excited by modulating the scattering length, which can be implemented as a modulation of the magnetic offset field in the vicinity of a Feshbach resonance. This scheme directly modulates the superfluid fraction, couples to the (symmetric) A_1 symmetry, and allows us to excite the $\tilde{q}=0$ Higgs mode with a selectivity of $> 99\%$. We modulate the scattering length $a_s(t) = a_s(0) + a_{s,\mathrm{mod}} \sin(\omega_{\mathrm{mod}} t)$ with an amplitude of $a_{s,\mathrm{mod}} = 0.05\, a_0$ for a duration $t_{\mathrm{mod}} = 4T_{\mathrm{mod}}$ with $T_{\mathrm{mod}} = 2\pi/\omega_{\mathrm{mod}}$ and the driving frequency $\omega_{\mathrm{mod}}/2\pi = 50\,\mathrm{Hz}$. We deliberately choose a drive that does not match the Higgs frequency, highlighting that the excitation of the $\tilde{q}_0$ mode does not require resonant driving. Further simulations using this modulation scheme with different parameters confirmed that similar selectivity and spectral purity of the Higgs mode is reached with frequencies below $\omega_{\mathrm{mod}}/2\pi = 100\,\mathrm{Hz}$. At sufficiently high modulation frequencies ($\gtrsim 200\,\mathrm{Hz}$) multiple modes are excited. In these cases, the PCs become superpositions of BdG modes and the corresponding (multiple) BdG frequencies show up in the spectra of the PC weights. A similar effect is observed towards higher amplitudes $a_{s,\mathrm{mod}} \gg 0.1\, a_0$.

[15] The overlap with the BdG mode functions f_i alone is above 95% in all cases of Fig. 3.13

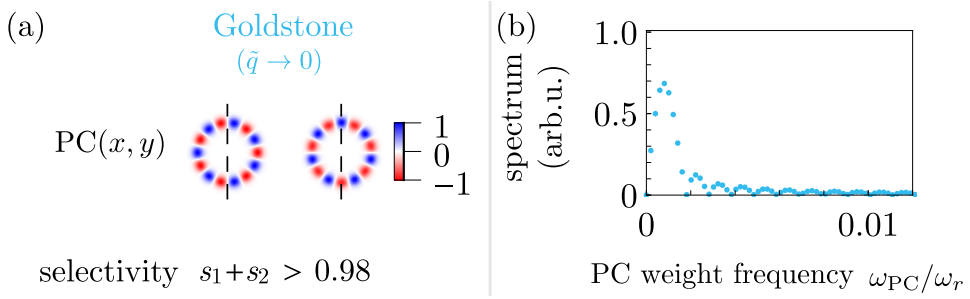

Figure 3.14.: **Exciting the low-energy Goldstone mode**. (a) Dominant PCs after magnetostirring the ground state at $\epsilon_{\mathrm{dd}} \simeq 2.1$. (b) Fourier spectrum $|\mathcal{F}_w(\omega_{\mathrm{PC}})|^2$ of the dominant PC weights $w(t)$. Figure adapted from [1].

The two sound modes at $\tilde{q}_1$ (Fig. 3.13(ii)) share the symmetry E_1. Expecting these modes to couple to a dipole excitation pattern we modulate a linear gradient $\Delta V = px\sin(\omega t)$ on top of the toroidal trap where x corresponds to the direction of a symmetry axis of the supersolid[16]. The individual sound mode selectivity is accomplished by modulating[17] at the respective resonance frequency $\omega_i = c_i\tilde{q}_1$ with only a few percent weight in the other sound mode. This selectivity can be further increased by optimizing duration, amplitude, and other details of the modulation scheme. We choose an amplitude of $p \simeq 6.3 \times 10^{-3}\hbar\omega_r/\rho_0$ ($p/2\pi\hbar = 6.3\,\mathrm{Hz}/\mu\mathrm{m}$). We find that the scheme is robust with respect to the specific values chosen for modulation time t_{mod}, ω, and p. We find that this scheme does not couple to the modes at $\tilde{q}_2$. Their symmetry E_2 has no overlap with the symmetry E_1. Coupling to E_3 modes is possible in principle but here suppressed due to the frequency detuning. Similarly a quadrupole (hexapole) excitation scheme can be used to selectively excite the $\tilde{q}_2$ ($\tilde{q}_3$) sound modes with no coupling to modes at $\tilde{q}_{1,3}$ (small coupling to modes at $\tilde{q}_1$) [1]. These observations can be generalized to a set of selection rules based on the symmetries of the individual modes. The absence of linear and COM motion coupling ensures that a mode retains its character over time and a range of interaction strengths providing the basis of a such spectroscopic selection rules. Deviations of ω from ω_i, of x from the symmetry axis, and towards large p result increasingly in the excitation of superpositions of first and second sound [347, 396]. With a misalignment of x from the symmetry axis it is also possible to set the supersolid into rotation (excitation of the Goldstone mode).

The zero-energy Goldstone mode corresponds to a ground state degeneracy due to

[16] Note that a magnetic field gradient would create a spatially varying scattering length and superfluid fraction leading to a combination of dipole excitation pattern and supersolid amplitude mode

[17] We modulate for a time $t_{\mathrm{mod}} = 4T_{\mathrm{mod}}$ and the frequencies are ($i = 1,\ \omega_1/2\pi \simeq 212\,\mathrm{Hz}$) for first sound and ($i = 2,\ \omega_2/2\pi \simeq 315\,\mathrm{Hz}$) for second sound.

the rotational symmetry of the torus or a pure rotation in the limit $q \to 0$. Breaking the cylindrical symmetry elevates this mode to a finite frequency and enables imparting angular momentum into the system. Options to directly couple to this mode are deforming and rotating the trapping potential or using magnetostirring [401] where the magnetic offset field is tilted from the $\hat{\boldsymbol{z}}$-axis and rotated. We employ the latter technique by tilting the field in 0.2 s to 10°, rotate for 1 s with a rotation frequency of 2 Hz, tilt back to 0° in 0.2 s and time-evolve for 1 s. PCA captures the resulting slow rotation by two PCs, identical up to rotation of $2\pi/14$, oscillating in time $\pi/2$ out of phase (Fig. 3.14(a)). The PCs have a mode pattern overlap with the zero-energy Goldstone mode of $> 92\%$ and the symmetry A_2. A very low frequency of the rotational mode is obtained (Fig. 3.14(b)) that can be controlled by the amount of imparted angular momentum. To further validate this approach we have explicitly calculated the excitation spectrum for 10° tilt angle. For these small tilt angles the low-energy Goldstone mode is still well isolated for all values of ϵ_{dd} and the overall structure of the spectrum remains intact. The main qualitative difference is that twofold degenerate modes split up as the rotational symmetry is broken with a tilted magnetic field. The main challenge in exciting this mode through a tilted magnetic field and time-resolving it is the requirement of a long time evolution which is in competition with the droplet lifetime [8]. Implementing a non-destructive imaging technique and measuring correlations between two rapid single shots of the atomic cloud could give access to the angular velocity of the droplets.

3.3.4. Conclusion and outlook

Toroidal traps are an exceptionally clean and experimentally upcoming [345, 346] platform suitable for the study of amplitude and sound modes of dipolar supersolids. The rotational symmetry avoids edge effects of box traps [387, 388] and provides periodic boundary conditions useful to establish correspondeces between finitely trapped and bulk supersolids [338, 347, 383]. We discussed the origin of zero-temperature supersolid second sound and Higgs amplitude modes and put the excitation spectra reported for harmonic traps [7, 8, 96, 97, 148] in a general context. Interesting extensions both theoretically and experimentally are the study of scattering of the Higgs excitation at an obstacle, such as a weak link on the torus and its dispersion in larger tori. Considering the dispersion relation of the Higgs quasiparticle is the starting point for studies of massive quasiparticles in supersolids. The analogy between second sound in supersolids at zero temperature and second sound in

superfluids at finite temperature is that both are realized through out-of-phase oscillations between superfluid and non-superfluid components and in both systems the speed of second sound is a direct measure of the superfluid fraction. Future studies considering finite temperature supersolids [315–317] in toroidal traps could provide insight into the origin of further sound modes arising through the presence of two non-superfluid (crystal and thermal) components.

"The first principle is that you must not fool yourself and you are the easiest person to fool."

*– **Richard Feynman***

Chapter 4

Two-dimensional structures of dipolar quantum fluids

Chapter Contents

Chapter 3 presents investigations of supersolid structures where the crystal structure self-organizes along one coordinate or one direction. The cigar-shaped trap geometries have been the primary focus for studies of one-dimensional dipolar supersolids [9, 97, 147, 378] but also experiments investigating the roton spectrum in trapped dipolar superfluids have focussed on this geometry [125, 128].

In chapter 4 we consider oblate-shaped trapping geometries. Mainly theoretical studies informed in these geometries about the presence of the roton spectrum in the quasi 2D regime (section 2.5.1) and of new types of angular roton modes in a variety of traps within the mean-field framework of the GPE [124, 126, 240, 393, 394]. In section 4.1 we

review these excitation spectra including the beyond mean-field quantum fluctuations and study experimentally the density fluctuations across the superfluid to droplet crystal phase transition. Drawing from the methodology developed in the cigar-shaped trap case (section 3.2.3) to connect the density fluctuations with the elementary excitations, we present experimental evidence for angular roton excitations in trapped dipolar quantum fluids.

We explain theoretically how the transition occurs for parameters allowing for two-dimensional droplet crystals with high overlap, forming two-dimensional supersolids, in section 4.2. Experimental evidence for phase coherence in two-dimensional droplet crystals has since been suggested by the group in Innsbruck [402, 403].

In general the supersolids as initially proposed in the context of liquid helium [68, 69, 74, 78, 328, 373] would form in a more macroscopic and higher density system compared to the few crystal site supersolids in dipolar quantum fluids we discussed so far. We investigate oblate dipolar quantum fluids towards higher densities in section 4.3 and find beyond the droplet regime that the superfluid self-organizes in honeycomb, stripe, and labyrinthine shapes.

4.1. Roton excitations in oblate dipolar quantum fluids

In this section we investigate the crystallization mechanism of two-dimensional droplet crystal structures in oblate harmonic traps. First we theoretically calculate the excitation spectrum in the superfluid regime and identify radial and angular roton excitations that soften towards smaller scattering lengths. Experimentally in situ measurements are used to characterize the density fluctuations in a similar trapping geometry. The static structure factor is evaluated and used to identify radial and angular roton excitations by their characteristic symmetries. The observed emergence of angular structure is directly linked to softening angular roton modes presenting the first experimental evidence for angular roton modes in trapped dipolar quantum fluids.

Parts of this section have been published in:

- J.-N. Schmidt, J. Hertkorn, M. Guo, F. Böttcher, M. Schmidt, K. S. H. Ng, S. D. Graham, T. Langen, M. Zwierlein, and T. Pfau, "Roton Excitations in an Oblate Dipolar Quantum Gas", Phys. Rev. Lett. **126**, 193002 (2021).

Here we focus on angular roton modes. For a more detailed analysis of radial excitations and further experimental details we refer to Refs. [4, 129].

4.1.1. Structure of low-energy excitations

Our goal in this section is to review the structure of low-energy excitations of oblate dipolar superfluids for a specific trap which we experimentally realize. In such geometries two types of roton excitations have been predicted to play a crucial role in the crystal structure formation towards smaller scattering lengths [124, 126, 240, 393]. These two types are known as radial and angular roton modes. Despite the early predictions of these modes their connection to the crystallization has remained elusive and they have not been observed experimentally prior to Ref. [4].

We calculate the excitation spectrum of the low-lying modes for $N = 15 \times 10^3$ ^{162}Dy atoms in a harmonic trap with trapping frequencies $\omega_{x,y,z}/2\pi = (35,\, 35.1,\, 110)\,\mathrm{Hz}$ as a function of the scattering length a_s. We focus on the superfluid regime $a_s \in [77,\, 82]\,a_0$. The asymmetry of 0.3 % leads to an alignment of the symmetry axes of the excitation patterns with the principal axes x,y of the trap and has a negligible effect on their energies and spatial structure[1].

The excitation patterns corresponding to density fluctuations $\delta n(\boldsymbol{r})$ are shown in the upper row of Fig. 4.1(a). In addition to the angular roton modes we discussed in the context of toroidal superfluids (section 3.3), cylindrically symmetric harmonically trapped superfluids allow for low-lying radial roton modes. Radial roton modes are cylindrically symmetric and represent ring-like density modulations at non-zero radial wave vector. These rotons in toroidal traps correspond to radial excitations gapped to energies at or higher than the radial trapping frequency and therefore transverse to the low-lying modes driving the structure formation. In contrast, oblate harmonic traps allow for both radial and angular excitations at a comparable energy. Angular rotons have an angular oscillatory structure in addition to a ring-like radial density modulation. The angular structure is described by $\cos(m\phi)$ where ϕ is the azimuthal angle and the integer $m > 0$ corresponds to an m-fold rotational symmetry of the mode pattern. Angular roton modes are twofold degenerate due to the rotational symmetry of the trap (see section 3.3) and radial rotons have no degeneracy.

[1] This alignment is mainly convenient to more easily distinguish and numerically analyze the excitation patterns [340].

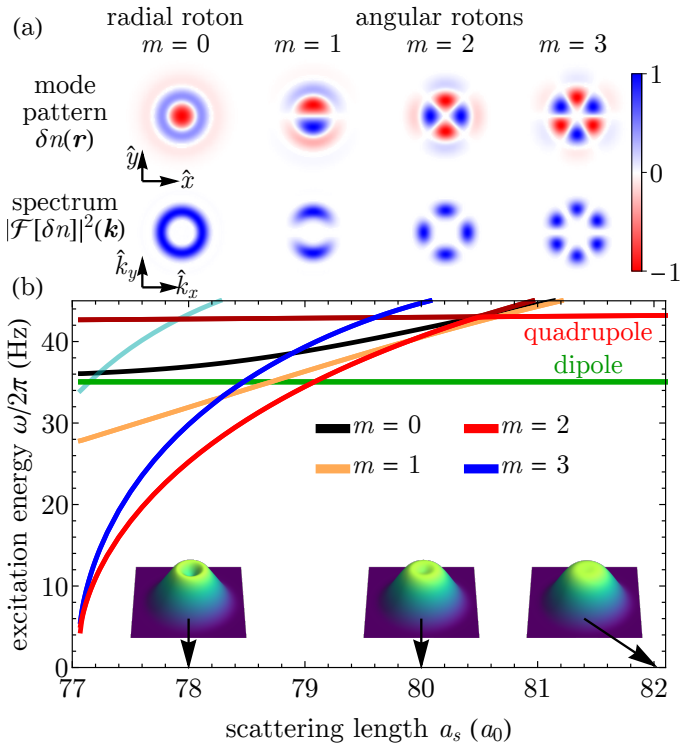

Figure 4.1.: **Low-lying excitations of oblate dipolar superfluids.** (a) Normalized density fluctuation patterns corresponding to elementary excitations of oblate dipolar superfluids and their spatial power spectra in the x-y-plane at $a_s = 77.5\,a_0$. The lowest radial ($m = 0$) and angular rotons ($m = 1$, 2, 3) are shown. The power spectra indicate individual contributions to the static structure factor. (b) Excitation energies as a function of scattering length a_s with the insets indicating the emergence of a blood cell shape in the ground-state density close to the instability at $a_s \simeq 77.1\,a_0$. The cyan line is for an $m = 4$ angular roton mode and the dark red line corresponds to an angular roton mode with $m = 2$, displaying an avoided crossing with the quadrupole mode. Figure adapted from [4].

The rotational symmetry allows every density fluctuation to occur with any orientation. To distinguishing their individual contributions to the crystallization with an experimentally accessible quantity we calculate their individual contributions to the static structure factor (Fig. 4.1(a), lower row). These are the spatial power spectra given by the squared modulus of the Fourier transform of the density fluctuation patterns $|\mathcal{F}[\delta n]|^2(\boldsymbol{k})$ [5, 27, 241, 404–406]. Similar to our discussion in section 3.3 the spatial power spectrum with a $2m$-fold rotational symmetry corresponds to an angular roton mode with an m-fold rotational symmetry. The power spectra of low-lying radial and angular roton modes have a radial peak corresponding to the roton momentum k_{rot}. The quadrupole mode and higher-lying

phonon modes can share the same azimuthal symmetries with low-lying roton modes but have a smaller radial wave vector.

The low-lying excitation energies and ground state shapes are shown in Fig. 4.1(b) as a function of a_s. The excitation spectrum deep in the superfluid regime ($a_s \gtrsim 81\,a_0$) has similarities with the one of toroidal superfluids. The excitation energy increases with m due to the corresponding increase in kinetic energy. The lowest superfluid mode is the dipole mode at the trap frequency [356] and next higher is the quadrople mode[2]. Angular and radial roton modes soften towards lower a_s. The $m = 2$ and $m = 3$ angular roton modes exhibit a steeper decrease towards the transition point than the $m = 1$ mode. The roton mode ordering near the crystallization transition point $a_{s,c} \simeq 77\,a_0$ in general depends on a nontrivial interplay between the trap aspect ratio and the interaction strength [283]. Around $a_{s,c}$ the $m = 2$ mode separated only by a few Hz from the $m = 3$ mode and these two modes have the lowest excitation energy. The degeneracy of multiple roton modes near $a_{s,c}$ translates into a complex situation on the crystal side. We find a number of competing ground states reflecting the different symmetries of the roton precluding a further meaningful BdG-analysis for the given parameters.

The ground states change from parabola shaped deep in the superfluid to a biconcave blood cell-like shape near $a_s \simeq 80.5\,a_0$. Blood cells form as it is energetically favorable to push part of the density to the outer rim due to dipolar repulsion of the higher density in the center of cylindrical trap [240, 295]. Given the biconcave shape angular rotons present modulations of the ring-shaped region of maximal density [126]. Blood cell shaped ground states have been reported previously [124, 126, 237, 240, 241, 283, 322, 393, 394, 407] without beyond mean-field (LHY) corrections in the GPE formalism [133]. We confirm that the blood cell shapes are still present if we set the beyond mean-field correction to zero in our numerical framework[3].

[2] The quadrupole mode exhibits an avoided crossing with the $m = 2$ angular roton mode [4].

[3] The range of a_s in which blood-cell shaped ground states form with the LHY correction included is approximately $1\,a_0$ larger than without the LHY correction for our present parameters.

4.1.2. Experimental structure factor

Experimentally we prepare a BEC with typically 15×10^3 ^{162}Dy atoms at a temperature $T \simeq 20\,\mathrm{nK}$. After evaporation at a magnetic field[4] of $B_z \simeq 30\,\mathrm{G}$ the crossed optical dipole trap is adjusted to an almost cylindrical trap with trapping frequencies $\omega_{x,y,z}/2\pi = [35(1), 37(1), 110(1)]\,\mathrm{Hz}$ and the magnetic field along $\hat{\boldsymbol{z}}$. The scattering length is ramped within 50 ms to its final value and after a wait time of 80 ms the atomic cloud is imaged in situ with a resolution of 1 µm. All scattering lengths in this section are quoted relative to a reference scattering length $a_{\mathrm{ref}} = 91(10)\,a_0$ corresponding to the experimentally observed crystallization point (see below) due to a large uncertainty in the width of the used Feshbach resonance [129]. The uncertainty leads to a large shift of the absolute value of a_s but does not influence the accuracy of relative changes in a_s. The experiment is repeated in total around 200 times for a statistical analysis of the atomic densities and for evaluating the static structure factor. We post-select in an interval of $\pm 15\,\%$ with respect to the mean atom number at each scattering length [129].

The static structure factor connects the spectrum of elementary excitations to the major contributing modes in the density fluctuations [5, 27, 241, 404–406]. We show the intermediate steps of evaluating the structure factor in oblate geometries in Fig. 4.2 for four distinct scattering lengths: in the BEC regime, closer to the transition, in the transition region and for a droplet crystal. The methodology is analogous to the one employed in section 3.2.3.

The in situ densities $n_j(\boldsymbol{r})$ (Fig. 4.2(a)) are shifted to their center of mass to remove residual excitations of the dipole mode from our analysis. The crystal structure is randomly oriented in individual images highlighting the continuous rotational symmetry of the trap and the spontaneous rotational symmetry breaking in the crystal phase. Consequently azimuthal structure in the average image washes out (Fig. 4.2(b)) leading to a ring-shaped average density distribution. To determine which angular contributions are present in the angular structure formation we develop a rotation algorithm that lets us investigate the angular fluctuations relative to a reference angle for every image. The individual rotation angles θ_j are determined by calculating the power spectrum of the in situ density, transforming to polar coordinates, integrating out the radial direction, and finding the angle

[4] The magnetic field used here is different from the field of about $\simeq 5\,\mathrm{G}$ used in previous chapters. At $B_z \simeq 30\,\mathrm{G}$ lower three-body losses lead to droplet crystal lifetimes on the order of 200 ms after crossing the phase transition [129]. This lifetime is roughly a factor ten higher compared to previous experiments at similar densities [9]

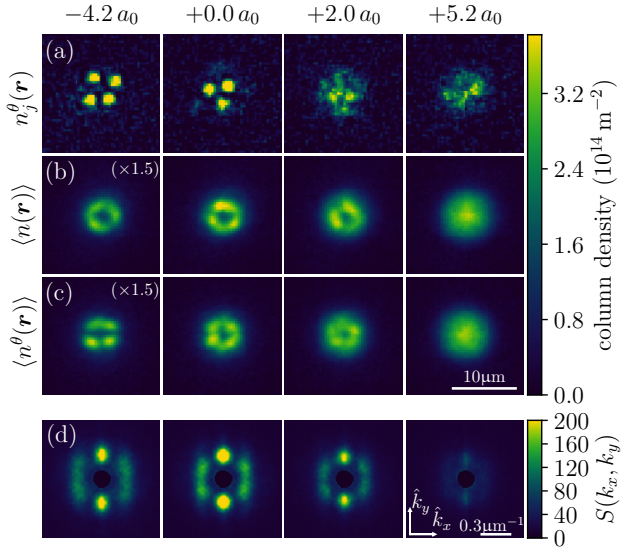

Figure 4.2.: **In situ observation of droplet crystal structure formation.** (a) Single-shot images in the BEC regime (+5.2 a_0), near the transition point (+2.0 a_0), in the transition region (+0.0 a_0), and for a droplet crystal (−4.2 a_0). (b) Mean images of the unrotated images showing the rotational symmetry of the trap. (c) Rotated images (see text) indicate the presence of droplets in the mean image. (d) Static structure factor showing an increasing height of the peaks at finite momentum $|\boldsymbol{k}|$ indicating the approaching transition point. The central area below $k_{\mathrm{min}}/2\pi \simeq 0.11\,\mu\mathrm{m}^{-1}$ (see text) was masked out. Figure adapted from [4].

θ_j at which the power spectrum attains its maximum[5]. Rotated images $n_j^\theta(\boldsymbol{r})$ are created by rotating each image individually by $-\theta_j$. If a crystal structure is present the rotation aligns one of the droplets to the same axis $\hat{\boldsymbol{y}}$ across images. New mean images $\langle n^\theta(\boldsymbol{r})\rangle$ are created revealing the emergence of angular structure in the crystal phase while the rotation does not affect the mean image in the BEC regime Fig. 4.2(c)). From here we follow the same methodology as in section 3.2.3 in obtaining the structure factor and connecting it to elementary excitations [27, 260, 262, 360–364]. We calculate fluctuation patterns about the mean image $\delta n_j^\theta(\boldsymbol{r}) = n_j^\theta(\boldsymbol{r}) - \langle n^\theta(\boldsymbol{r})\rangle$. The mean power spectrum $\langle|\delta n^\theta(\boldsymbol{k})|^2\rangle$ from a Fourier transform $\delta n_j^\theta(\boldsymbol{k}) = \int \mathrm{d}^2 r\, \delta n_j^\theta(\boldsymbol{r}) e^{i\boldsymbol{k}\cdot\boldsymbol{r}}$ of these fluctuation patterns and the static structure factor $S(\boldsymbol{k}) = \langle|\delta n^\theta(\boldsymbol{k})|^2\rangle/N$ (Fig. 4.2(d)) are obtained.

We transform $S(\boldsymbol{k})$ to polar coordinates $S(k_x, k_y) \to S(k, \phi)$ allowing to analyze its radial and angular behavior separately. The structure factor $S(\boldsymbol{k})$ has several peaks that lie approximately on a ring with radius $k/2\pi = d^{-1}$ informing about the spacing d of the

[5] In practice the radial direction is integrated out starting from $k = k_{\mathrm{min}}$ where the smallest momentum $k_{\mathrm{min}} \simeq 0.11\,\mu\mathrm{m}^{-1}$ is given by the finite cloud size.

emerging structures. Following our discussion in section 4.1.1 this momentum scale is the roton momentum $k = k_{\mathrm{rot}}$ acting as a precursor to the emergence of a crystal structure in the superfluid and determining a droplet spacing d in the crystal regime. Analogous to the structure factor in tubular traps (section 3.2.3) k_{rot} has a weak dependence on a_s and the amplitude of $S(k) = \int \mathrm{d}\phi S(k, \phi)$ is related to the density fluctuation strength [129]. We refer to Ref. [129] for details on this radial distribution. In short, the amplitude peaks at a_{ref} and defines together with the behavior of the spectral weight and the mean peak density a transition region $a_{\mathrm{ref}} \pm 1.5\, a_0$ [129]. The peak of $S(k)$ broadens and decreases for $a_s < a_{\mathrm{ref}} - 1.5 a_0$ indicating a competition between different droplet numbers and spacings [129]. In the following we focus on the angular distribution of $S(\boldsymbol{k})$ related to the presence of angular roton modes.

4.1.3. Experimental evidence of angular roton modes

We obtain the angular distribution $S(\phi)$ by integrating $S(k, \phi)$ over the interval $k/2\pi \in [0.2, 0.45]\,\mu\mathrm{m}^{-1}$ encapsulating the weak change of k_{rot} for all a_s. This angular distribution allows us to attribute the enhancement of the fluctuations to individual modes (Fig. 4.3).

In the BEC regime only two peaks at $\phi = 0$ and $\phi = \pi$ are visible which increase for lower a_s. These angles can be mainly attributed to the rotation algorithm while the increase in their amplitude is connected to enhanced fluctuations similar to the behavior of $S(k)$. This behavior is reproduced by applying the same rotation algorithm to low-lying Bogoliubov modes in cylindrically symmetric dipolar superfluids [300] such as the ones presented in Fig. 4.1.

Four additional peaks at $\phi = \pm\pi/3$ and $\phi = \pm 2\pi/3$ emerge closer to the transition region corresponding to a discrete sixfold rotational symmetry indicative of an $m = 3$ angular roton mode. In the crystal regime these intermediate peaks start to wash out presumably due to the competition of the three- and four-droplet configurations [129].

To analyze the contributions of angular roton modes to the distribution $S(\phi)$ quantitatively we use the Fourier series expansion $S(\phi) = \sum_n \alpha_n \cos(2\pi n\phi/p + \varphi_n)$ within $\phi \in [0, p)$ where $p = \pi$ is the period. The Fourier weights $\alpha_n = \sqrt{a_n^2 + b_n^2}$ and phase $\varphi = \arctan(b_n/a_n)$ are given by $a_n = (2/p) \int_0^p \mathrm{d}\phi S(\phi) \cos(2\pi n\phi/p)$ and $b_n = (2/p) \int_0^p \mathrm{d}\phi S(\phi) \sin(2\pi n\phi/p)$.

On the BEC side, the Fourier coefficients α_n give an indication of the underlying symmetries of the fluctuations driving the crystallization transition and are connected to the low-lying modes described with the simulation of Fig. 4.1. Corresponding to the

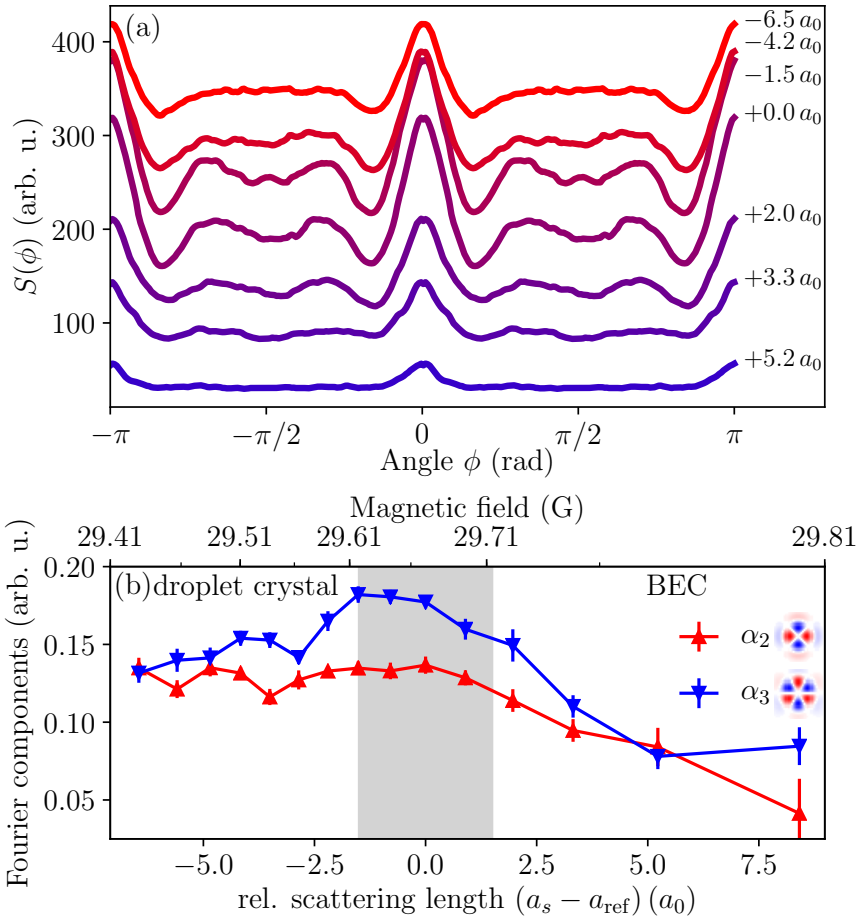

Figure 4.3.: **Angular structure of density fluctuations.** (a) Angular distribution of the static structure factor $S(\phi)$ for different relative scattering lengths. (b) Weights of a Fourier series of $S(\phi)$ matching the symmetry of the lowest two angular roton modes $m = 2$ and $m = 3$ in the superfluid. For clarity, the lines in (a) were shifted vertically for smaller scattering lengths. The gray area in (b) indicates the transition region (see text). Error bars are obtained by bootstrapping [366]. Figure adapted from [4].

lowest-lying angular roton modes we focus on the contributions of α_2 and α_3 (Fig. 4.3(b)) describing a fourfold and sixfold discrete rotational symmetry, respectively. Both α_2 and α_3 increase towards the transition region in agreement with the simulation.

While α_2 saturates towards the crystal regime α_3 weight peaks in the transition region and decreases towards in the crystal regime. As the $m = 2$ mode has a slightly lower energy than the $m = 3$ mode in the simulation towards the transition point a higher α_3 weight than α_2 cannot be explained only based on the simulation. The experimental data are influenced by the dynamical formation process of the droplets and the theoretical

description assumes a beyond mean-field correction based on a homogeneous gas [134–136] that could explain larger deviations between experiment and theory towards more isolated crystal structures [128].

In the crystal domain the two weights approach each other again indicating that neither of the two angular roton modes are dominant. In this domain $S(\boldsymbol{k})$ does not measure excitations on top of the crystalline ground state but increasingly the crystalline structure itself because of competing crystal structures with a varying droplet number. We find that the number of droplets increases towards smaller a_s starting with 3 droplets being the most likely occurence in the transition region and most likely 4 droplets for $a_s \lesssim a_{\mathrm{ref}} - 2$ [129]. Deep in the crystal regime the similarity of the α_2 and α_3 weight indicates similar probabilities to find a droplet crystal with fourfold or sixfold symmetry.

In conclusion our measurement of the static structure factor of oblate dipolar BECs provides first evidence of angular roton modes as precursors to the droplet crystal formation. Additionally we see that for the given trap geometry and atom number multiple nearly degenerate angular roton modes lead to a competition between different crystal symmetries and droplet numbers with a small droplet overlap. Such competition together with the rotational degree of freedom, that both the BEC and droplet states possess, makes the analysis of potential phase coherence between droplets pointing towards two-dimensional supersolidity more challenging [129]. On the other hand these insights provide us with an intuition of what could be optimized to produce two-dimensional supersolid structures: choosing a trap geometry with a smoother transition from superfluid to droplet states and studying the influence of different atom numbers on the transition in oblate dipolar superfluids. We approach these topics in the following sections.

4.2. Two-dimensional arrays of supersolid quantum droplets

Having observed the crystallization mechanism for oblate dipolar superfluids we show in this section theoretically how the excitation spectrum continues across the transition to two-dimensional droplet crystals with a high overlap. We identify collective excitations such as Goldstone and Higgs modes characteristic of the supersolid phase and show how parameter regimes favorable for two-dimensional supersolid droplet arrays can be systematically identified. We study the droplet formation dynamics across the transition and show that these supersolids can be realized with standard protocols in state-of-the-art experiments.

Parts of this section have been published in:

- J. Hertkorn, J.-N. Schmidt, M. Guo, F. Böttcher, K. S. H. Ng, S. D. Graham, P. Uerlings, H. P. Büchler, T. Langen, M. Zwierlein, and T. Pfau, "Supersolidity in Two-Dimensional Trapped Dipolar Droplet Arrays", Phys. Rev. Lett. **127**, 155301 (2021).

4.2.1. Excitation spectrum of two-dimensional supersolid droplets

It is a priori unclear which parameters are generally favorable for the formation of two-dimensional arrays of supersolid quantum droplets[6]. In this section we first present an example of a two-dimensional supersolid featuring key collective modes in its excitation spectrum underlining that two-dimensional supersolid ground states exist in dipolar quantum fluids.

We consider $N = 20 \times 10^3$ ^{162}Dy atoms confined in an oblate harmonic trap with trapping frequencies $\omega_{x,y,z}/2\pi = (125,\, 125.5,\, 250)\,\mathrm{Hz}$[7], and aspect ratio $\lambda \simeq 2$. We map out the ground states and the spectrum of elementary excitations across the superfluid to two-dimensional supersolid phase transition as a function of a_s (Fig. 4.4).

The chosen trap geometry and atom number lead to: (1) the most elementary supersolid with a two-dimensional crystal structure, namely $n_d = 3$ droplets that self-organize in a

[6] For the sake of brevity we refer to these arrays forming in a three-dimensional oblate harmonic trap within this section as two-dimensional supersolids noting that we do not refer to strictly reduced dimensions.

[7] As in the previous section a small trap asymmetry is included to provide a slight preference in orientation for the collective modes.

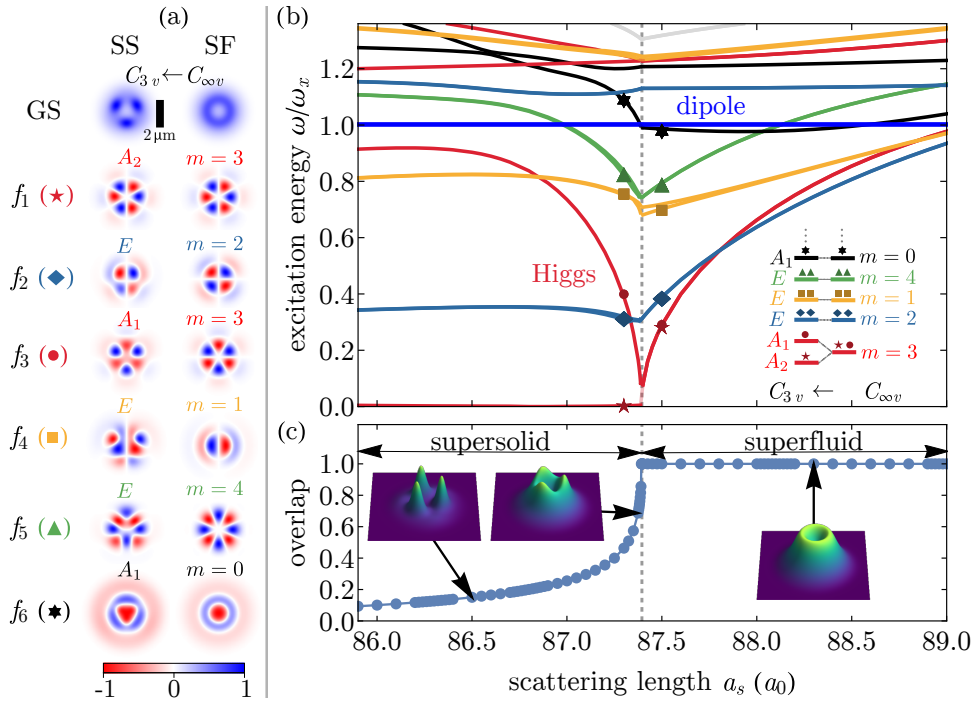

Figure 4.4.: **Elementary excitations across the oblate superfluid to supersolid phase transition.** (a) Ground state (GS) density and mode patterns f_i in the superfluid (SF) and supersolid (SS) near the transition point. In the supersolid, modes are labelled according to the irreducible representation of the remaining symmetry group (here for $C_{3,v}$: A_1, A_2, E) after the spontaneous rotational symmetry breaking $C_{\infty,v} \to C_{3,v}$. Modes f_1-f_6 are numbered according to their energies on the droplet side (see (b)) and normalized to 1 for visual clarity (colorbar in arbitrary units). (b) Excitation energies of the low-lying modes across the transition. The $m = 3$ angular roton modes trigger the transition at $a_{s,c} \simeq 87.35\, a_0$ (dashed vertical line) giving rise to $n_d = 3$ droplets. (c) Ground states and droplet density overlap as a function of a_s. The points show the sampling of the ground states.

triangular array (Fig. 4.4(a)), (2) isolation of a single low-lying angular roton mode near the transition point $a_{s,c} \simeq 87.35\, a_0$ (Fig. 4.4(b)), and (3) a high density overlap[8] between the droplets near $a_{s,c}$ (Fig. 4.4(c)).

The considered trap geometry shares the presence of linear and COM motion coupling of tubular harmonic traps (section 3.2) and the rotational symmetry of the toroidal trap (section 3.3) as well as the harmonic trap of the previous section (section 4.1.1). These shared properties allow us transfer much of the understanding gained in the previous sections and contrast with the behavior of collective modes in this section.

The rotational symmetry allows for the characterization of superfluid modes in terms

[8] The overlap is determined in polar coordinates at the radius on which the droplets form.

of radial ($m = 0$) and angular ($m > 0$) roton modes with the circulation number m. Our group theoretical attribution of the compatibility between superfluid roton modes and elementary excitations of the supersolid directly transfers from and is consistent with our investigation of toroidal supersolids. At $a_{s,c}$ the continuous rotational symmetry is broken $C_{\infty,v} \rightarrow C_{3,v}$ to a discrete threefold symmetry. The point group $C_{3,v}$ has two one-dimensional irreducible representations (A_1, A_2) and one two-dimensional irreducible representation E (Fig. 4.4(a)). The modes split at the superfluid to supersolid transition according to the compatible irreducible representations of $C_{3,v}$ as $m = 3 + 3k \rightarrow (A_1, A_2)$ for any integer $k \geq 0$, $m = 0 \rightarrow A_1$ and $m = 1, 2, 4, 5, ... \rightarrow E$ (Fig. 4.4(b)). The critical angular roton modes with $m = 3$ drive the transition to $n_d = 3$ droplets and are compatible with A_1 and A_2 in complete analogy to section 3.3. A relatively small jump of the droplet overlap at the transition (Fig. 4.4(c)) is consistent with a first-order quantum phase transition [238, 257, 350, 408, 409]. The mode compatible with A_2 fixes its nodes at the droplet positions (Fig. 4.4(a), f_1), exhibits a very low energy determined by the trap asymmetry and corresponds to a rotation of the droplet array. In a perfectly symmetric trap this mode accounts for the rotational ground state degeneracy and represents the long-wavelength limit $q \rightarrow 0$ of a Goldstone mode associated to the spontaneous rotational symmetry breaking (section 3.3). The mode compatible with A_1 matches its spatial maxima to the droplet positions (Fig. 4.4(a), f_3) and rises quickly with energy. This is the corresponding Higgs amplitude mode presenting an amplitude modulation between the droplet density and the superfluid background [7, 170, 173].

In contrast to tubular systems this two-dimensional supersolid arises from the breaking of a continuous (rotational) symmetry despite the presence of a trap, leading to the phase transition when the critical roton modes reach zero energy[9]. This property is shared with the exctations of toroidal systems. Contrary to toroidal systems the coupling of linear and COM motion in the present harmonic trap leads to a strong avoided crossing and hybridization of the Higgs mode with higher modes sharing the symmetry A_1 (Fig. 4.4(b)). Contrary to the harmonically trapped supersolid in the toroidal system the number of available symmetries increases with increasing droplet number. Here the three droplet supersolid limits the available symmetries to three and each two-dimensional excitation

[9] The small asymmetry used in the simulation yields a small finite gap of the Higgs mode at the transition point (Fig. 4.4(b)). The lowest mode with symmetry A_2 has an energy $\omega/\omega_x \lesssim 4 \times 10^{-4}$ reflecting the trap asymmetry. Another indication of the presence of the asymmetry is the lifting of the degeneracy of the $m = 1$ angular roton mode which is particularly sensitive to the asymmetry. We confirmed that these effects decrease towards perfectly symmetric traps.

features the same symmetry E. Towards systems with more droplets in harmonic traps it is expected that the droplet crystal assumes a hexagonal crystal structure [311] which shares the symmetry with the three droplet crystal here and will similarly show hybridization between two-dimensional excitations.

Similar to the tubular harmonic systems the Higgs amplitude mode exists here in a narrow range of a_s in a decoupled form due to the discretization of the excitation spectrum provided by the trap (section 3.2, [7]). The strong increase in energy and the hybridization of the Higgs amplitude mode serve as signatures that could be probed in experiments with the goal of observing the Higgs mode in two-dimensional supersolids for the first time. Techniques such as Bragg spectroscopy [125, 128, 371] and direct in-situ measurements of density fluctuations [4, 5] or dynamics [378, 410] could be used to probe these features and would provide an indication of supersolidity in oblate traps.

The lowest-lying modes compatible with E (Fig. 4.4(a), f_2 and its degenerate partner) feature translations along x- and y-directions, with a density adjustment that keeps the COM close to the trap center. This behavior allows these modes to have a low energy in the droplet regime similar to the low-energy Goldstone mode in tubular traps [8].

While the above discussion about the elementary excitation spectrum is based on a specific trap geometry our observations directly generalize to other trap geometries and atom numbers. We consider that the transition is driven by two degenerate roton modes, splitting at the transition point into a low-energy mode and a Higgs mode that strongly hybridizes with higher-lying modes as general properties of two-dimensional harmonically trapped supersolids. For instance we have computed the spectrum for $N = 50 \times 10^3$ in the same trap geometry and find a transition from superfluid to four droplets facilitated by the softening of two degenerate $m = 4$ angular roton modes. After the spontaneous rotational symmetry breaking, the remaining symmetry group is $C_{4,v}$ [411] and the mode compatibility[10] is consistent with the general analysis provided in section 3.3.

The two limiting cases (cylindrically symmetric harmonic trap in Fig. 4.4 and tubular harmonic traps in section 3.2) of the BdG spectrum allow us to anticipate the behavior throughout the intermediate regime. In this regime droplets are expected to arrange in a zigzag geometry similar to the structures known in ion crystals [412, 413]. We consider the behavior of a pair of degenerate angular roton modes in cylindrically symmetric trap geometries (Fig. 4.4), when the trap is slowly deformed to a more elongated geometry.

[10] $m = 4 + 4k \to (A_1, A_2)$, $m = 2 + 4k \to (B_1, B_2)$ for any integer $k \geq 0$ and $m = 0 \to A_1$, $m = 1, 3, 5, ... \to E$.

As the asymmetry is increased one mode rises and the other decreases in energy – their density fluctuation pattern changes shape and the corresponding momentum distribution becomes an increasingly elongated ellipsoid. One of the modes will eventually be associated to density fluctuations along the tight direction (the rising mode) and the other along the loose direction (the softening mode). If the density is sufficiently elongated the softening occurs on top of a quasi-homogeneous density in the center of the trap allowing for a degeneracy of the lowest-lying symmetric and antisymmetric roton modes defined by the mirror symmetry about the center of the trap. In an intermediate ellipsoidal trap there are low-lying modes with structure both along the long and the short direction and the mode predominantly associated to density fluctuations along the long direction will eventually soften close to zero, triggering the phase transition to a zigzag pattern. This transition has been observed experimentally [293, 402].

Near the transition point the usual parabola-shaped superfluid ground state develops into a biconcave blood cell-like shape (Fig. 4.4(c), section 4.1.1). The biconcave shape of the ground state is dynamically mean-field unstable when one of the angular roton modes reaches zero energy or becomes imaginary [124, 126, 237, 240, 241, 283, 322, 393, 394, 407]. With the beyond mean-field stabilizing quantum fluctuations included, we investigate in the following whether a phase coherent ground state of these supersolids can be dynamically approached.

4.2.2. Dynamical supersolid formation

To investigate whether the dynamical formation two-dimensional supersolids is experimentally feasible we consider $N = 20 \times 10^3$ atoms (cf. Fig. 4.4) and perform real-time simulations of the eGPE following a standard experimental procedure, as shown in Fig. 4.5.

Starting from the ground state in the superfluid regime at $a_{s,1} = 99.0\,a_0$, we ramp a_s linearly in 30 ms to final scattering lengths $a_{s,2} = \{87.2,\ 86.0,\ 83.0\}\,a_0$ in the droplet regime. The initial dynamics are seeded with thermal noise corresponding to a temperature of 20 nK according to the truncated Wigner description [96, 97, 143, 145, 148, 348, 414] in order to include possible experimental imperfections[11]. The simulation is repeated 20 to acquire dynamics representative of multiple experimental realizations. The droplets have

[11] In this description the single-particle harmonic oscillator eigenstates are computed up to the energy $k_{\mathrm{B}}T$ and added to the initial state.

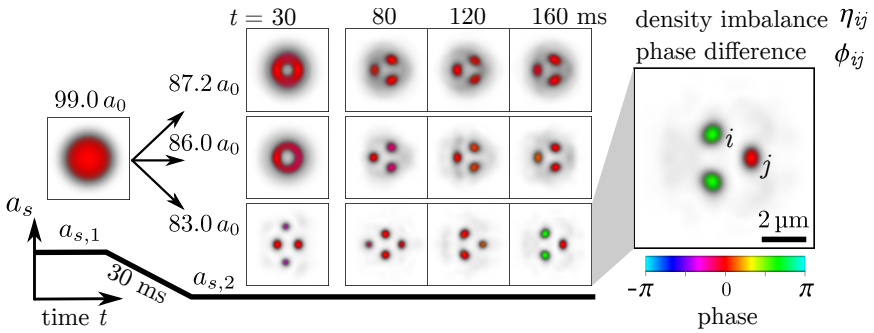

Figure 4.5.: **Dynamical scheme and droplet formation dynamics.** (a) Real-time evolution of the eGPE with a linear scattering length ramp, starting from a the superfluid ground state at $a_{s,1} = 99.0\,a_0$ and ending at $a_{s,2} = \{87.2, 86.0, 83.0\}\,a_0$ after 30 ms. Dynamics are run 20 times with different initial noise, seeded at $t = 0$ ms (not shown). The images show density cuts $n(x, y, 0)$ color coded with the phase of the wavefunction for one realization of the time evolution.

formed in all realizations after $t = 40$ ms.

The phase[12] difference $\phi_{ij} = \phi_i - \phi_j$ and the density imbalance[13] $\eta_{ij} = |n_i - n_j| / \max(|n_i - n_j|)$ are computed for $t \geq 50$ ms between all pairs of droplets $\{i, j\}$ (Fig. 4.6). These quantities allows us to monitor how much the dynamic density deviates from the ground state density after the droplet formation and whether droplets maintain or establish phase coherence. Strongly imbalanced or incoherent droplets are far away from the ground state [9].

Ramping the scattering length close to the transition ($a_{s,2} = 87.2\,a_0$) where the droplets have a high overlap results in a smooth droplet formation process with all droplets forming at the same time (Fig. 4.4), with a minimal imbalance, and the formation process does not lead to a loss of phase coherence (Fig. 4.6(a)). Further away from the transition point ($a_{s,2} = 86.0\,a_0$) the droplet formation process leads to stronger excitations of the droplet crystal and consequently a larger imbalance (Fig. 4.6(b)). The phase difference between droplets for all realizations is generally small and roughly bounded by $|\phi_{ij}| \lesssim \pi/8$. Coherent dynamics between the droplets after their formation can be observed, indicating that the global phase coherence is not lost in the formation process and that a slightly excited two-dimensional supersolid state has been obtained. The phase rigidity of the supersolid is

[12] In practice we use the density weighted average of the phases $\phi_i \simeq \bar{\phi}_i = \int_{\mathcal{A}_i} n(x, y, 0)\phi(x, y, 0)\mathrm{d}^2 r / \int_{\mathcal{A}_i} n(x, y, 0)\mathrm{d}^2 r$ in areas $\mathcal{A}_i$ around the density peak positions to avoid contributions of arbitrary phases where the density is close to zero, for example for isolated droplets.

[13] Metrics such as the euclidean distance between ground state $n_0(x, y, z)$ and dynamic densities $n(x, y, z, t)$ indicate similarly to the imbalance used here how the ground state is approached [2].

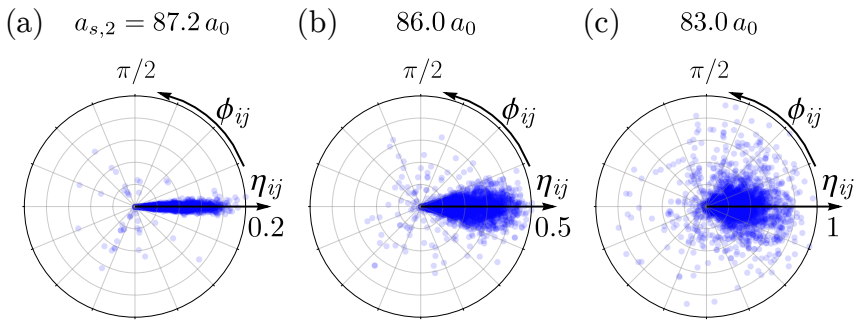

Figure 4.6.: **Density imbalance and phase difference.** The droplet density imbalance η_{ij} and phase difference ϕ_{ij} evaluated for $t \geq 50\,\mathrm{ms}$ between all pairs $\{i, j\}$ of droplets for the dynamics (Fig. 4.4) after ramping to $a_{s,2}\{87.2,\, 86.0\}\,a_0$ (a-c). The radii of the polar plots indicating the imbalance are scaled to maintain visibility of ϕ_{ij} even for the smaller imbalances

facilitated by the high droplet overlap maintaining a coherent exchange of atoms between the droplets. The droplet formation becomes more violent as a_s is ramped further into the droplet regime, which is reflected in a larger density imbalance (Fig. 4.6(c)). In contrast to the simulations for $a_{s,2} \gtrsim 86.0\,a_0$, the droplets dephase during the dynamics and do not reestablish a global phase coherence[14]. The droplets form an isolated and incoherent crystal. In several dynamical realizations at this final scattering length the blood-cell shaped density initially splits up into four droplets (Fig. 4.5) indicating a competition of threefold and fourfold symmetric droplet crystals. Such dynamical effects show similarities to the competing crystal structures found in our investigation of angular roton modes (section 4.1, [129]) suggesting the that several low-lying roton modes are excited [300].

Longer or optimized scattering length ramp schemes could be used to counteract the more violent droplet formation process [320, 417–419]. Another route mitigating the excitations involved in a scattering length ramp has been suggested by evaporating directly in to the droplet state while holding a_s constant [402, 403].

In this section, we have shown that two-dimensional supersolids can be dynamically reached in a narrow region of scattering lengths. The presence of several low-lying modes which become coupled towards smaller scattering lengths (Fig. 4.4) together with the rotational degree of freedom suggests that the system is more susceptible to enter an excited state due to an imperfection in the preparation process, thermal fluctuation or asymmetries in the trap [402, 403, 410].

[14] The randomness of the dynamical phases can be further quantified [2] using the circular variance $V = 1 - R$ [415, 416], where $R = \left|\sum_{k=1}^{M} z_k\right| / M$ with $z_k = e^{i\phi_k}$ (ϕ_k is ϕ_{ij} indexed linearly by $k = 1, 2, \ldots, M$). One obtains $V \simeq \{1.2,\, 3.1,\, 12\}\,\%$ for $a_{s,2} = \{87.2,\, 86.0,\, 83.0\}\,a_0$.

4.2.3. Scaling droplet supersolids to other parameters

So far we have presented an example of a two-dimensional supersolid ground state, that it can be dynamically reached and we emphasized the generality of characteristic features of its excitation spectrum. Given a two-dimensional supersolid the question arises how parameters favorable for similar supersolids can be systematically identified. While exploring a large parameter space theoretically is feasible at the cost of some extra computational time, an uninformed search for favorable parameters in the experiment can be time- and labor-intensive. Furthermore the search could lead to parameter regions that are experimentally inaccessible or enforce unfavorable trade-offs between parameters of the experiment.

The scaling relations introduced in section 2.4.3 help in understanding similarities between different regions in parameter space. In particular in cylindrically symmetric traps $V_{\text{ext}}(\boldsymbol{r}) \simeq M\omega_0^2(x^2+y^2+\lambda^2 z^2)/2$ dimensionless units based on the length scale $x_s = \sqrt{\hbar/M\omega_0}$ with a wavefunction normalized to unity [236] reveal that the mean-field interactions are controlled by the dimensionless contact and dipolar interaction strengths $C \propto a_s N/x_s$ and $D \propto a_{\text{dd}} N/x_s$ [240, 241]. The dimensionless quantum fluctuation strength scales as $Q \propto C^{5/2}/N$. While holding N/x_s constant, higher trapping frequencies and notably lower atom numbers enhance the stabilizing quantum fluctuations. This enhanced stabilization is expected to provide a higher droplet overlap.

We illustrate the utility of these scaling arguments in Fig. 4.7. We take a three droplet ground state and vary Q explicitly by a few percent (Fig. 4.7(a)) which can be utilized in experiments using the scaling $N\sqrt{\omega_0} = \text{const.}$ for different atom numbers sN and trap geometries ω_0/s^2. At small Q more atoms accumulate in the attractive head-to-tail configuation in the droplets. For larger Q the droplet overlap grows by an expulsion of atoms out of the droplets, facilitated by a stronger repulsive quantum fluctuation contribution until the blood cell states are recovered. Varying confinement provides experimentally a trade-off between optical resolution for the observation of well-separated droplets and realizing supersolids at smaller atom numbers with enhanced quantum fluctuations.

An explicit example of this scaling is shown in Fig. 4.7(b) by reducing the trapping frequencies by a factor of two while keeping the aspect ratio $\lambda = 2$ constant. We consider a ground state at $a_s = 87\,a_0$ on the left and expect to find a similar ground state for a factor of $\sqrt{2}$ higher atom number if there were no quantum fluctuations. Due to the effective reduction of Q, a higher scattering length and atom number[15] are required to obtain a

[15] We need additional 11 % of $\sqrt{2}N$ to reach a three-droplet ground state in the new trap geometry, whereas two droplets are the ground state at $a_s = 93\,a_0$ and $\sqrt{2}N$ atoms.

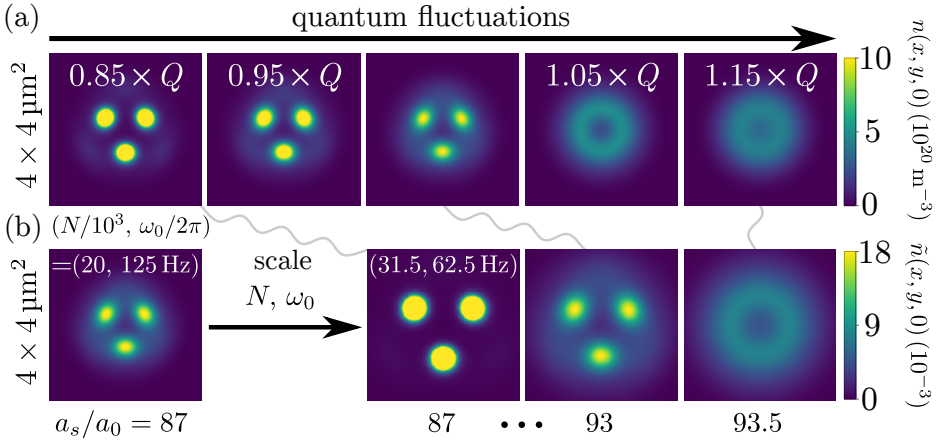

Figure 4.7.: **Scaling properties applied to two-dimensional droplet supersolids.** (a) Behavior of the ground state by explicitly varying the quantum fluctuations $Q \to sQ$ by an arbitrary scale factor s, while leaving mean-field interactions constant. The ground state for $1.00 \times Q$ was chosen with $(N,\, \omega_0/2\pi,\, a_s) = (20 \times 10^3,\, 125\,\mathrm{Hz},\, 87\,a_0)$ and was recomputed for every modified Q. (b) Ground state at $a_s = 87\,a_0$ (same as with $1.00 \times Q$ in (a)) and ground states across the superfluid to supersolid phase transition for scaled atom number and trap geometry. The density $n = |\psi|^2$ and the dimensionless density $\tilde{n} = nx_s^3/N$ at $z = 0$ are shown shown in (a) and (b), respectively, to compare the ground states in both trapping geometries. The light gray lines indicate similarity between states where quantum fluctuations are varied artificially (a) and implemented through confinement and atom number (b).

similar ground state. Despite the additionally provided atoms, the system in the lower confinement at the same scattering length $a_s = 87\,a_0$ has a lower droplet overlap due to reduced quantum fluctuations. The dimensionless peak densities of the states close to the transition (near $\{87,\, 93\}\,a_0$) for both trap geometries are $\tilde{n}_0 \simeq 0.0183(2)$ and the states have a similar droplet overlap. We have demonstrated the scaling relations here for the case of supersolid droplets but as described in section 2.4.3, the scaling relations apply in general to the eGPE.

Compared to the parameters in section 4.1 we have chosen a smaller aspect ratio and higher overall trapping frequencies while keeping a comparable atom number. Smaller aspect ratios lead to smoother transitions from superfluid to droplet states. This is a general phenomenon not limited to supersolid droplet arrays and already observed with variational models describing isolated single droplets [144]. Intuitively less confinement in the magnetic field direction inhibits magnetostriction less and leads to a smaller frustration of the system. Aspect ratios $\lambda \lesssim 1$ prevent bistability in the ground state phase diagram and lead to an elongation of the superfluid without splitting into multiple crystal sites,

preventing studies of supersolids.

In summary this section provides a description of characteristic excitation spectra of two-dimensional dipolar supersolids, their dynamical formation process, and scaling relations useful to find two-dimensional supersolids for a wide range of parameters. Extending on the two-dimensional crystal structure formation mechanism [4, 129] studies have found indications of phase coherence [402, 403] and very recently possible presence of vortices, indicating superfluidity in rotating dipolar supersolids [420].

Having investigated the self-organization of supersolids droplet arrays in one and two dimensions a next step towards fully characterizing the macroscopic pattern formation of dipolar quantum fluids is to explicitly increase the atom number yielding both enhanced mean-field interactions and quantum fluctuations.

4.3. Self-organized patterns of oblate quantum ferrofluids

The first study describing the observation of quantum droplet arrays forming from a strongly dipolar superfluid [130] pointed out an analogy to classical ferrofluids which form droplet structures due to the Rosensweig instability [106]. As quantum droplets emerge from a superfluid [137, 138, 142], much attention has been given to the potential of these droplets to form supersolids [9, 96, 97].

Classical ferrofluids can develop a variety of macroscopic patterns in equilibrium beyond the droplet structures [106, 109–111]. These patterns – also commonly referred to as morphologies – emerge in a large variety of physical systems irrespective of their microscopic structure and interactions [109, 110]. The morphologies notably include honeycomb ("foam") and labyrinthine ("stripe") phases in addition to the droplet ("bubble") phase [106, 109–111, 421–426]. The ubiquity of these patterns in nature has established classical ferrofluids as a model system for self-organization. The patterns can be found in equilibrium in systems as diverse as superfluid helium [427–429], the intermediate phase of type-I superconductors [430–433], optically nonlinear media and optically coupled cold atoms [353, 434–447], colloidal systems [109, 110, 448–450], biological matter [276, 451–453], nuclear pasta in ultra-dense neutron stars [454–456] as well as in out-of-equilibrium systems [14] in convection patterns arising from the Rayleigh-Bénard instability [457–459], and in a plenitude of chemical mixtures displaying reaction-diffusion ("Turing") patterns [13, 15].

The competition between repulsive and attractive interactions at different length and density scales are key components leading to self-organization [109–111, 284]. In dipolar superfluids the competition between attractive dipolar and repulsive contact interaction leads to mean-field instabilities that are stabilized by the stronger density scaling of the quantum fluctuations [6, 133, 296, 409] and gives rise to the quantum droplets of quantum ferrofluids. In this section we show that trapped quantum ferrofluids self-organize in honeycomb, labyrinth, and futher morphologies towards high densities.

Part of the results presented in this section have been published in:

- J. Hertkorn, J.-N. Schmidt, M. Guo, F. Böttcher, K. S. H. Ng, S. D. Graham, P. Uerlings, T. Langen, M. Zwierlein, and T. Pfau, "Pattern formation in quantum ferrofluids: From supersolids to superglasses", Phys. Rev. Res. **3**, 033125 (2021).

Prior to this publication the ground-state phase diagram of infinitely extended two-

dimensional arrangements of dipolar supersolids showed honeycomb supersolid structures [238]. Earlier studies investigating the potential 2D honeycomb and labyrinthine phases in BECs considered more complex multi-component systems [395, 460–462] and their dynamical (Rayleigh-Taylor) instabilities [463–465] or infinite quasi-2D geometries with three-body interactions instead of quantum fluctuations [409].

We theoretically predicted honeycomb and labyrinth phases in trapped quantum ferrofluids [3], and in exchange with Y. Zhang, T. Pohl, and F. Maucher [302] we clarified the presence of metastable states in the phase diagram.

Since then multiple theoretical studies have been motivated by the description of these phases. Several further studies are linked to the phases. We highlight studies of the superfluid properties of honeycombs [466], crystal field models extended to honeycomb and labyrinth patterns [467], frustration induced by an underlying optical lattice [468], the appearance of labyrinth structures when quantum ferrofluids are merged from multi-well potentials [400], the potential for molecular dipolar BECs [247] to realize regimes currently challenging for atomic gases [246], metastability of quantum ferrofluids [469], extensions of variational theories for flattened dipolar BECs to include quantum fluctuations and capturing honeycomb and stripe phases [336, 470, 471], the characterization of the superfluid fraction of two-dimensional patterns [337], stripe phases in mixtures or in systems with multiple spin components [472, 473], parallels to patterns in the grasshopper model [474, 475], and links to neutron stars [476].

We present the phase diagram and the morphologies of quantum ferrofluids in an oblate trap geometry in section. 4.3.1. In section 4.3.2 we discuss the origin of the pattern formation (morphogenesis). The influence of the trapping geometry on the morphologies is discussed in section 4.3.3. Near-degeneracy and metastability between patterns is the focus of section 4.3.4 and we conclude in section 4.3.5.

4.3.1. Morphologies

We consider the same oblate harmonic trapping geometry as in the previous section with frequencies $\omega_{x,y,z}/2\pi = (125, 125, 250)\,\mathrm{Hz}$ and note that the shape of the phase diagram will be similar at other parameters due to scaling relations (sections 2.4.3, 4.2.3).

We focus on scattering length regimes where structured states of matter emerge from

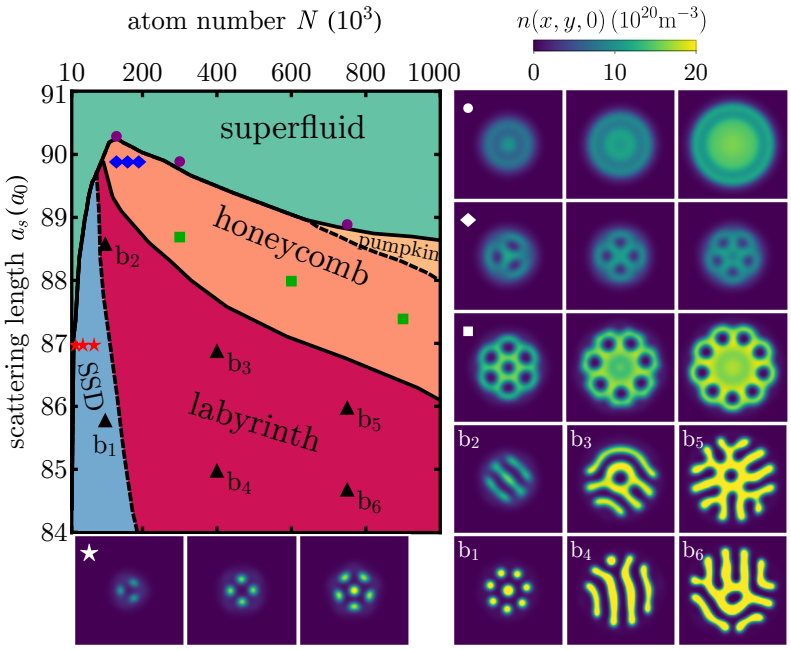

Figure 4.8.: **Phase diagram of oblate quantum ferrofluids.** Top-left panel shows the N-a_s phase diagram for trap frequencies $\omega_{x,y,z}/2\pi = (125, 125, 250)$ Hz. Density cuts $n(x, y, 0)$ are shown at relevant points in the phase diagram with the corresponding markers. The density distributions for a specific marker are ordered by N from left to right. An example of the pumpkin state can be seen in Fig. 4.10. Dashed lines indicate crossovers between different regions. The transition between droplets and honeycombs occurs via stripes (b_2) that break up into droplets at small a_s (b_1) or curve and connect towards higher N and small a_s, forming labyrinths (b_3-b_6). The field of view for the density cuts is $14 \times 14\,\mu m^2$.

superfluid states below a critical scattering length $a_{s,c}$. We set a random initial state[16] for every ground state search allowing us to avoid hysteresis effects when crossing phase boundaries in parameter space [9]. We return to the relevance of this numerical detail in section 4.3.4. The boundaries are determined by individually searching through the final states. If near-degenerate states occur near the boundary of two phases, such as in a crossover from droplets to labyrinths, the drawn boundary line indicates the middle between the regions in which only one of the phases is present.

The superfluid BEC states for $a_s \geq a_{s,c}$ are characterized by their continuous rotational symmetry. Spontaneous rotational symmetry breaking occurs for $a_s < a_{s,c}$ leading to a variety of structured states of matter (Fig. 4.8).

Two-dimensional arrays of supersolid quantum droplets form at low atom numbers

[16] In practice we choose either pixelwise uniformly distributed noise or perlin noise [477]. Here we use perlin noise [3].

$N \lesssim 100 \times 10^3$ (Fig. 4.8, ★). As we studied in depth in previous sections these structures form from a biconcave blood-cell shaped BEC states. The phase diagram reveals that the biconcave superfluid states are a special case of the superfluid states near $a_{s,c}$ with a radial substructure in the range $N \simeq 60\text{-}200 \times 10^3$ (Fig. 4.8, ●). These superfluid states have a ring of depleted density near their boundary in addition to the maximum density in the center of the trap. Depending on the atom number and size of the condensate multiple such radial density modulations can occur ($N \simeq 200\text{-}400 \times 10^3$) until the the trap center is filled with atoms ($N \gtrsim 400 \times 10^3$) and a single depleted density ring near the boundary remains (Fig. 4.8, ●, right column).

The honeycomb phase (Fig. 4.8, ◆-■) appears for $a_s < a_{s,c}$ from these superfluids with a radial substructure. High density bridges across the radial density minima form at discrete angles leading to multiple density minima in a honeycomb pattern. The honeycomb states are characterized by an emerging discrete rotational symmetry. A fully developed honeycomb pattern gives rise to a discrete translational symmetry and a crystal structure. Together with the strong density bridges facilitating superfluid flow along the honeycomb pattern these states form a supersolid phase [409, 442, 478]. The density bridges can have an almost uniform density along the honeycomb pattern (Fig. 4.8, ◆) poviding a very high superfluid fraction [336, 466] even when the modulation contrast with the density minima becomes large. A comparison between the three-, four-, six-droplet states (★) with the three-, four-, six-minima honeycomb states (◆) suggests that there is a symmetry between positive droplets and negative droplets on top of a background density distribution. In the infinite quasi-2D system [238], it was shown that this is indeed a symmetry where the honeycomb structure becomes energetically favorable over the hexagonal droplet crystal beyond a critical density.

In a window of atom numbers where the superflid-supersolid droplet boundary changes to the superfluid-honeycomb boundary the transition below $a_{s,c}$ occurs via stripes (Fig. 4.8, b_2) or honeycomb patterns deforming into stripes toward smaller a_s. The emergence of the stripe phase between supersolid droplets and honeycomb phases has been observed with Quantum Monte Carlo simulations [478] and in a mean-field theory in a scenario where three-body interactions $\propto n^3$ [409] take the stabilizing role instead of quantum fluctuations $\propto n^{5/2}$ [131, 133, 296]. Since our description of this phase diagram in quantum ferrofluids [3] multiple studies have shown the existence of an extended stripe phase in infinitely extended systems [302, 336, 466, 471]. When a_s is further reduced, these stripes break up their connections and reenter the supersolid droplet phase (b_1). However, toward

higher N and smaller a_s, these stripes can curve and form overlap with neighboring stripes, representing a small region in the larger labyrinthine phase.

The labyrinthine phase (Fig. 4.8, b_3-b_6) consists of elongated and curved density stripes. With the curvature of the density stripes their discrete translational symmetry is lost and an amorphous spatial structure remains. The presence of an amorphous spatial structure is characteristic of glasses [479]. A high and nearly uniform density can be maintained along the stripes, supporting superfluid flow through a labyrinth structure. Due to the simultaneous presence of superfluid flow and an amorphous or glassy spatial structure the labyrinth phase can be classified as a superglass [78, 480]. Associated to the amorphous nature of the labyrinths, we find for fixed N and a_s many morphologically distinct labyrinthine patterns that are almost degenerate [409, 421, 422, 424, 460–462], with total energy differences of a few single Hz per atom. In this regime the true ground state by cannot be unequivocally determined by setting a random initial wavefunction or by choosing a previously found low-energy state. We find the labyrinth states to be robust against small perturbations [422, 424, 460, 462], be it in changes of scattering length or trap deformations. Corresponding to the near-degeneracy of multiple morphologically distinct states is the presence of metastability of those states as studied recently [469].

4.3.2. Morphogenesis

The emergence of honeycomb and labyrinth phases coincides with an important change in the phase diagram of Fig. 4.8, namely that the critical scattering length $a_{s,c}$ begins to decrease as a function of N for $N > N_c$ with the critical atom number N_c (here $N_c \simeq 100 \times 10^3$). Similarly other phase boundaries have a decreasing a_s towards higher N. In the infinite system [238, 336, 471] the decrease happens roughly above a critical density at which the three phases of superfluid, droplet and honeycomb are connected by a second-order phase transition[17].

The shape of the phase boundaries can be understood by noting that the energy functional contains the three distinct scalings $\propto n$ (single-particle), $\propto n^2$ (mean-field), and $\propto n^{5/2}$ (quantum fluctuations) [6, 131, 133]. At low atom numbers quantum pressure (kinetic energy) dominates the phase diagram [27, 141] and the interplay between mean-

[17] The authors considered either an expansion of the eGPE energy functional up to fourth order in a density wave amplitude or a variational ansatz to describe the density in the magnetic field direction. Generally, it cannot a priori be ruled out that the transition could still be of first order if higher orders of the amplitude were considered.

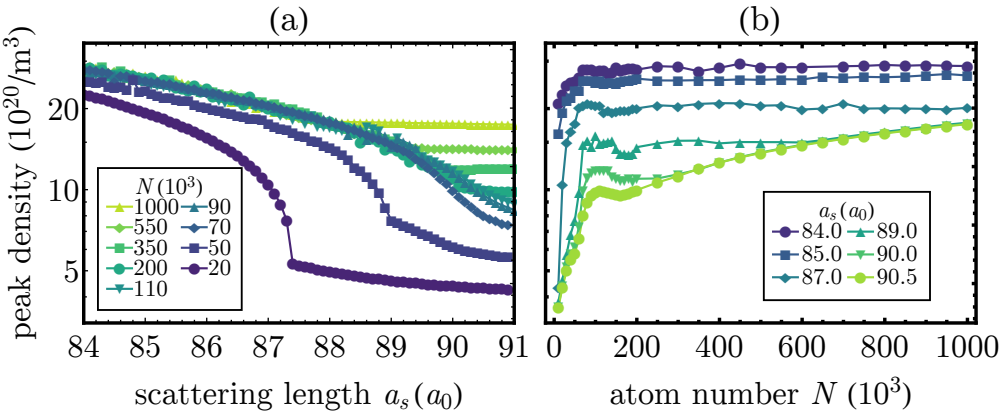

Figure 4.9.: **Density saturation of quantum ferrofluids.** Peak density in the phase diagram shown in as a function of a_s at fixed N (a) and as a function of N for fixed a_s (b). Discontinuities in (a) across $a_{s,c}$ become particularly small in the vicinity of N_c, the curves converge towards small a_s for $N > N_c$ describing a density saturation function $n_{\mathrm{sat}}(a_s)$ [246]. The curves in (b) highlight that only deep in the superfluid regime the ground states grow in density as well as size while for a_s near or below $a_{s,c}$ density saturation occurs starting from $N \simeq 100 \times 10^3$, defining N_c. Fluctuations of the points in (a)-(b) are due convergence to one of multiple near-degenerate ground state morphologies.

field interactions and quantum fluctuations determines where $a_{s,c}$ rises quickly with atom number. At N_c the stabilizing effect of quantum fluctuations is strong enough to allow for a smaller contact repulsion with the same effective stabilization, hence the phase boundaries (including $a_{s,c}$) decrease with atom number [238, 302, 336]. For $N \gtrsim N_c$ the peak density in the ground states begins to saturate (Fig. 4.9).

Density saturation of the patterns for $a_s < a_{s,c}$ signals increasingly quantum liquid-like behavior and reduced compressibility compared to the superfluid state, like for a liquid as compared to a gas. As has been observed in the case of single and isolated quantum droplets [6, 131, 133, 137–139, 142, 223, 233, 481, 482] the saturation leads to a flat-top (spatially saturated) density distribution for sufficiently high N where increasing N leads to an increase in size while the density is maintained at its saturation value. In the case of the honeycomb and labyrinthine phases this effect can be seen in the low density variation along the high-density regions of the patterns (Fig. 4.8). The saturation in density leads to an intuitive understanding of the pattern formation.

The presence of a saturation density in the vicinity of $a_{s,c}$ leads to the single depleted density ring near the boundary of superfluid states separating them into a core and a crust region (Fig. 4.10(a)). The core density is close to saturation and dipolar repulsion ensures

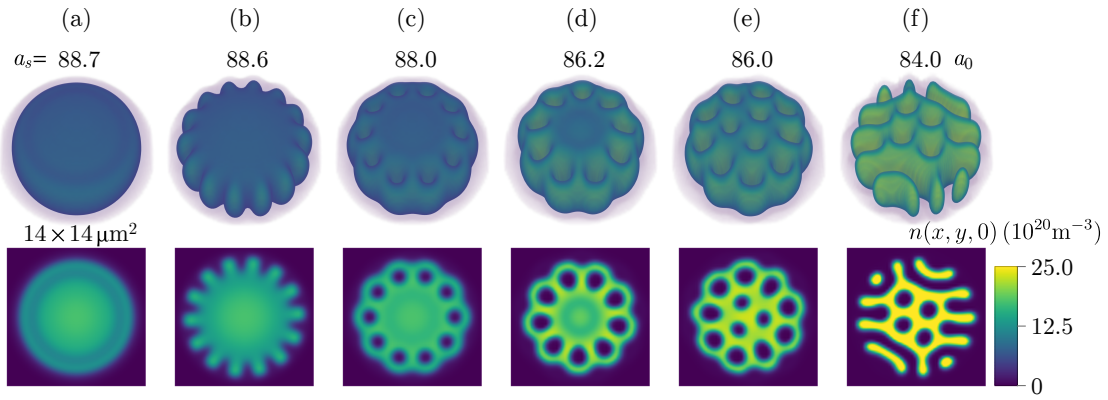

Figure 4.10.: **Superfluid shell structure and core destabilization.** Density distributions at $N = 1000 \times 10^3$ atoms as a function of a_s are shown (Fig. 4.8). Competition between quantum fluctuations and mean-field interactions lead to a shell structure of the superfluid near $a_{s,c}$ (a). The outer high-density ring becomes unstable and breaks in for smaller a_s yielding the pumpkin-like state (b). As a_s is reduced further the core is increasingly destabilized with density minima wandering closer into the core region giving rise to the honeycomb phase (c-e). Eventually the stabilization is insufficient to uphold the honeycomb density bridges – the connections break up and yield a labyrinthine pattern (f). Top and bottom rows show 3D density distributions and 2D density cuts $n(x, y, 0)$, respectively.

that it is energetically favorable to expel some density from the core. This radial structure is reminiscent of the shell structure of ultra-dense neutron stars [182, 454–456].

The core of neutron stars is believed to be a uniform superfluid at the nuclear saturation density stabilized by degeneracy pressure from inward gravitational forces [455, 456]. The outer crust hosts a crystal phase at densities several orders of magnitude below saturation. In the inner crust at intermediate densities it is predicted that competition between nuclear attraction between neutrons and protons and coulomb repulsion between protons favors the formation of nonuniform states of matter known as nuclear pasta [454, 456].

The core of the dipolar superfluid (Fig. 4.10(a)) is stabilized by quantum fluctuations and is density saturated, preventing (droplet) crystallization. Instead the system minimizes its energy by depleting density toward smaller a_s. Towards higher N, the core region grows and the depleted density ring shifts outwards. The superfluid to honeycomb transition is crossed toward smaller a_s up to about $N \simeq 700 \times 10^3$ with density minima forming in the depleted region.

For $N \gtrsim 700 \times 10^3$ the depleted ring is located so close to the boundary that an instability occurs at $a_{s,c}$ similar to the fingering instability known from classical ferrofluids [106, 110, 421–423, 425, 426]. At these high atom numbers, the superfluid passes through an

intermediate state when a_s is reduced (Fig. 4.10(b)) where density minima form sufficiently outwards in the crust so that high density "fingers" are left. We call this the pumpkin phase (Fig. 4.8) occurring in equilibrium in contrast to the dynamical fingering instability of classical ferrofluids [106, 110, 421–423, 425, 426]. Toward smaller a_s the repulsive contact interaction and quantum fluctuations become weaker, destabilizing the core. As the density minima wander further into the core, transitions through honeycomb states occur until some of its density connections break up, giving rise to the labyrinthine phase (Fig. 4.10(c)-(f)).

At lower atom numbers, special cases of the transitions from superfluid to stripe and superfluid to droplet supersolid occur. Consistent with investigations [336, 471] subsequent to our initial report of the phase diagram [3, 302] we find that the transition from superfluid to stripe states around the turning point of $a_{s,c}$ occurs more smoothly with no clear discontinuity in peak density between $N \simeq 60 \times 10^3$ and $N \simeq 110 \times 10^3$ compared to the superfluid to supersolid droplet or honeycomb phase at lower or higher atom numbers, respectively. Stripes curve and transition smoothly to labyrinth structures towards higher N and lower a_s. This observation is explained by considering that the characteristic length scale (here the stripe spacing) rises towards higher density and lower a_s [302, 336] and the harmonic trap imposes an increasing energy penalty for linear stripes as their spacing grows. We note that this scaling of the characteristic length scale is the same as for the roton momentum in quasi-2D trapped dipolar superfluids [104]. The morphogenesis of supersolid droplets is explained in depth in previous sections.

4.3.3. Influence of trap shape

An overall scaling of trapping frequencies can be absorbed into the dimensionless interaction strengths thanks to scaling relations (section 4.2.3). In contrast the aspect ratio $\lambda = \omega_z/\omega_r$ is an independent parameter. The anisotropy of the dipolar interaction causes the stability of a phase in quantum ferrofluids to depend on λ [118, 119, 144, 282, 394]. There is a difference between changing λ by modifying ω_z with constant ω_r and vice versa since the magnetic field along $\hat{\boldsymbol{z}}$ breaks the symmetry between radial and axial directions. We investigate the two arising cases, namely changes in vertical confinement or radial confinement, in the following two sections.

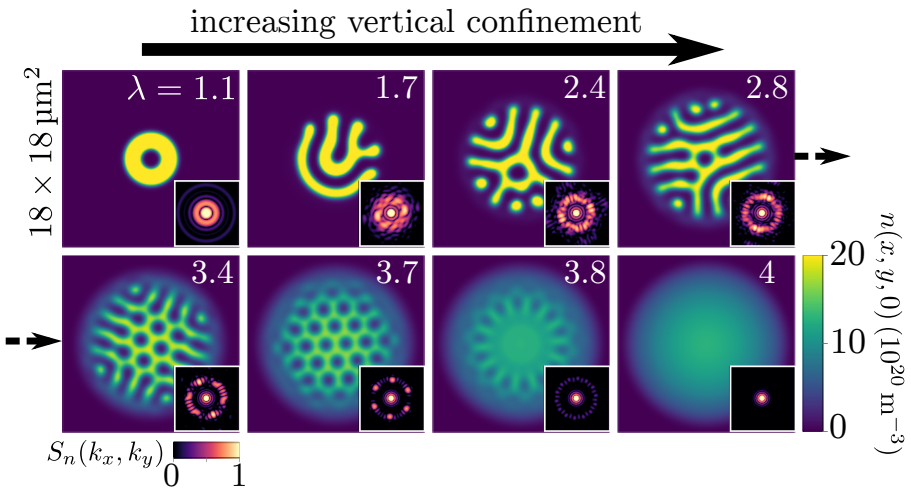

Figure 4.11.: **Vertical confinement influence on morphologies.** (a) Increasing ω_z with constant $\omega_r/2\pi = 125\,\mathrm{Hz}$ yields trap geometry change induced transitions through the labyrinth, honeycomb, pumpkin, and superfluid phase. Atom number and scattering length are fixed to $(N,\, a_s) = (500 \times 10^3,\, 85\,a_0)$. Insets in the lower right corners show the spatial power spectrum $S_n(k_x, k_y)$ in arbitrary units.

Vertical confinement

Figure 4.11 shows that a change in vertical confinement leads to phase transitions from the labyrinthine phase to increasingly macroscopically developed honeycomb phase to the pumpkin phase and finally to the superfluid. The patterns become finer as the vertical confinement increases, analogous to the situation in classical ferrofluids confined between two plates [109, 422–424]. Higher vertical confinement counteracts magnetostriction and leads to a stronger frustration of the morphologies.

The spatial power spectrum $S_n(k_x, k_y) = |\mathcal{F}[n(x, y, 0)](k_x, k_y)|^2$, shown in the insets of Fig. 4.11, reveals information about how many length scales are involved in the morphologies, the crystallinity, and the spacing (fineness) of the structures. The states have no modulation along z so that the power spectrum of the cut suffices to analyze the structures. The crystallinity can be seen from the diffuseness of the power spectrum along the ring with radius $|\boldsymbol{k}| = k^*$. Labyrinthine states have a powdered (diffuse) power spectrum at k^*, reflecting the amorphous or glassy density distribution [483–485]. Toward honeycomb states, the power spectrum concentrates in a triangular pattern indicating a cleaner crystal structure. Compared to the sixfold angular symmetry of the honeycomb pattern the pumpkin state power spectrum ($\lambda = 3.8$) shows more angular peaks at k^* corresponding to its higher discrete rotational symmetry.

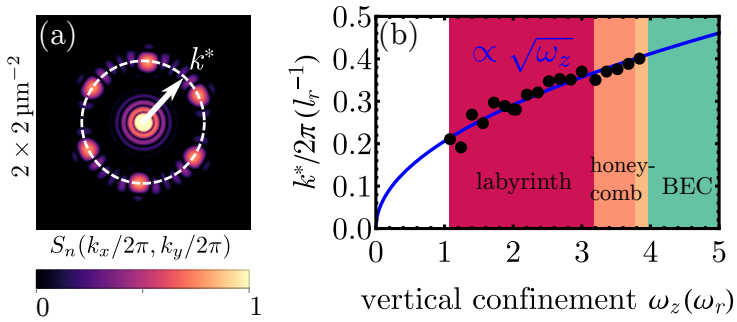

Figure 4.12.: **Characteristic momentum throughout geometry induced phase transitions.** (a) Example power spectrum at $\lambda = 3.7$ of Fig. 4.11. The main radial peak $|\boldsymbol{k}| = k^*$ of $S_n(k_x, k_y)$ is found in polar coordinates. (b) The characteristic momentum scales as $k^* \propto 1/l_z \propto \sqrt{\omega_z}$ where $l_z = \sqrt{\hbar/M\omega_z}$ is the harmonic oscillator length along the magnetic field direction (vertical direction). N and a_s are the same as in Fig. 4.11 and $l_r = \sqrt{\hbar/M\omega_r} \simeq 0.71\,\mu\mathrm{m}$.

The concentration of the power spectrum at a single characteristic momentum k^* throughout the phases shows that there is only a single characteristic length scale in the morphologies, corresponding to $2\pi/k^*$. Figure 4.12 reveals that the spacing scales as $2\pi/k^* \propto l_z$, where $l_z = \sqrt{\hbar/M\omega_z}$ is the harmonic oscillator length along the magnetic field direction. This scaling behavior is known from the roton momentum k_{rot} of infinitely extended flattened dipolar superfluids [104, 470, 486]. A least-squares fit to $k^*/2\pi = c/l_z$ as a function of vertical confinement yields $c = 0.206(2)$.

Relating the domain spacing to the roton momentum suggests that the coefficient c mostly depends on chemical potential and maximum density in the system [104, 125, 470, 486]. As the density is saturated for the labyrinthine and honeycomb phases, the chemical potential varies weakly with atom number in these regimes. Therefore c is expected to vary weakly with atom number and to yield a robust characterization of the fineness of the structures for a given interaction strength and trap geometry. We repeat the analysis shown in Fig. 4.12 with a different scattering length $a_s = 84\,a_0$ and atom numbers $N = \{700,\ 1000\} \times 10^3$ and find that c varies by less than than 2%. Toward lower N the peak density and chemical potential become more sensitive to interaction parameters and trapping frequencies and c is generally a function of these parameters. However, the scaling $k^* \propto 1/l_z$ remains.

The fact that the characteristic length scale across a structural phase transition can be interpreted to originate from softening or energetically low-lying excitations on the higher-symmetry-side of the transition is a generic result of linear stability analysis in nonlinearly interacting systems, such as classical ferrofluids [421, 422] or nonlinear optics

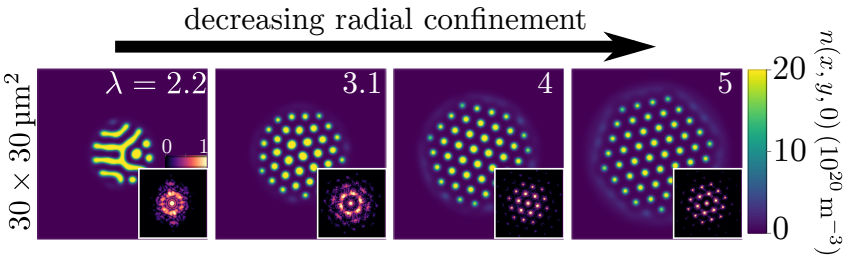

Figure 4.13.: **Radial confinement influence on morphologies.** Reducing the radial confinement ω_r with fixed vertical confinement $\omega_z/2\pi = 250\,\text{Hz}$ causes the labyrinth to transition to the crystal phase. Atom number and scattering length $(N,\, a_s) = (500 \times 10^3,\, 85\,a_0)$ are fixed as in Fig. 4.11. Across the transition the characteristic momentum $k^*/2\pi \simeq 0.43\,\mu\text{m}^{-1}$ stays roughly constant up to $\lambda = 5$. Toward higher λ, k^* weakly increases. The power spectrum (insets) concentrates into a triangular pattern, presenting the emergence of multiple Brillouin zones of of the macroscopic crystalline pattern with a lattice constant $2\pi/k^*$. As labyrinthine patterns lose some density connections they transition through a mixture of stripes and elliptical droplets for which the power spectrum is still is diffuse on the ring with $|\boldsymbol{k}| = k^*$ toward the pristine crystal at larger aspect ratios ($\lambda \simeq 5$). Figure adapted from [3].

[353, 439, 440, 442, 443] and general beyond the situation in quantum ferrofluids [284, 450]. We have highlighted this point of view for the the supersolid droplet regime in previous sections and Fig. 4.12(b) shows that the roton momentum scaling behavior persists from the superfluid state to the honeycomb phase and throughout the multistable labyrinthine phase.

Radial confinement

Reducing the radial confinement or increasing the vertical confinement both increase the aspect ratio, but the effective change in the morphologies is drastically different between the two cases. In contrast to the the previous section when radial confinement is decreased with a fixed vertical confinement $\omega_z/2\pi = 250\,\text{Hz}$ a state initially in the labyrinth phase transitions to a droplet crystal (Fig. 4.13). The characteristic momentum k^* does not change during the transition. These observations are understood as follows.

By considering the dimensionless interaction strengths $C \propto Na_s/x_s$, $D \propto Na_{\text{dd}}/x_s$, and $Q \propto C^{5/2}/N$ with $x_s = \sqrt{\hbar/M\omega_r}$ one finds that lower ω_r lead to the reduction of (C, D, Q) similar to lower N. In the phase diagram (Fig. 4.8) this decrease corresponds to a crossing of the labyrinthine-droplet boundary at constant a_s, explaining the transition seen in Fig. 4.13. The behavior is not exactly equivalent to a change in N because lower ω_r increase both $x_s \propto 1/\sqrt{\omega_r}$ and $\lambda \propto x_s^2$ describing a trajectory through four-dimensional

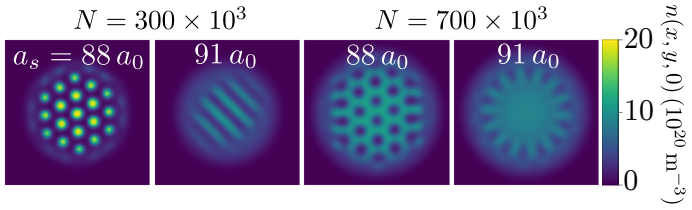

Figure 4.14.: **Similar patterns between traps without parameter fine-tuning.** Morphologies in a trap with trapping frequencies $\omega_{x,y,z}/2\pi = (83.3,\, 83.3,\, 250)\,\mathrm{Hz}$ ($\lambda = 3$). Shown are 2D density cuts $n(x, y, 0)$ in a field of view of $30 \times 30\,\mu\mathrm{m}^2$. Within the larger bulk density available in lower aspect ratios, the same patterns as in traps with higher aspect ratio emerge (cf. Fig. 4.8). Figure adapted from [3].

parameter space (C, D, Q, λ).

The spacing of the structures at constant (C, D, Q) decreases as $2\pi/k^* \propto 1/\sqrt{\lambda}$ (Fig. 4.12), but for the case of decreasing ω_r the natural length scale $x_s \propto \sqrt{\lambda}$ expands at the same rate so that these two effects roughly balance and lead to a constant k^*.

We note that combined changes of aspect ratio and atom number according to $\lambda \to \infty$, $N \to \infty$ at a constant average density correspond to systems approaching the thermodynamic limit [104, 336, 350, 351, 408, 470, 471, 486, 487]. Accordingly one expects quantum ferrofluids to form more macroscopic structures toward larger aspect ratios. We recalculate the phase diagram for an aspect ratio of $\lambda = 3$ by keeping $\omega_z/2\pi = 250\,\mathrm{Hz}$ constant and reduce the radial trapping frequencies to $\omega_r/2\pi = 83.3\,\mathrm{Hz}$. The droplet, labyrinth, honeycomb and pumpkin phases can be found in the new phase diagram as well (Fig. 4.14) and the relative location of the phase boundaries are qualitatively similar to Fig. 4.8. The shift of the boundaries in lower radial confinements can be intuitively understood by considering that quantum fluctuations are reduced and therefore higher a_s and N are required to reach similar patterns [3, 246, 302]. The fact that in different trap geometries the overall structure of the phase diagram is similar and that all patterns prevail underlines that no fine-tuning of the trap geometry or the atom number is necessary for the self-organization of these structures.

4.3.4. Nearly degenerate patterns

This section serves to underline that the near-degeneracy of morphologically distinct amorphous patterns is an inherent property of the labyrinth phase and we compare them with other metastable symmetric states found in the labyrinth phase.

With a large number of nearly degenerate low-energy states the final state obtained

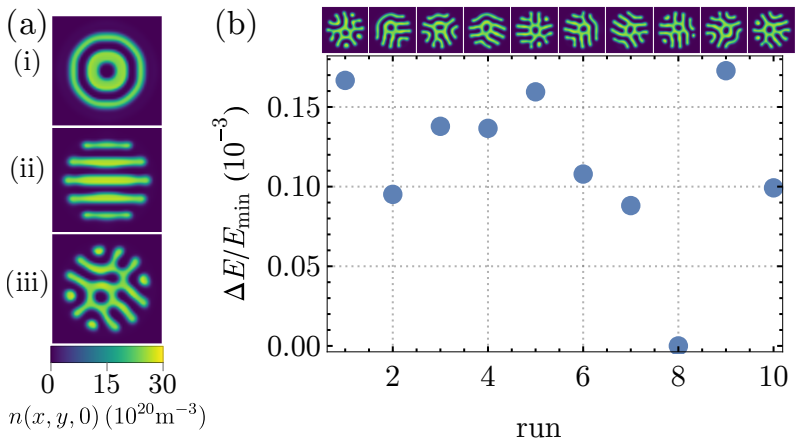

Figure 4.15.: **Near-degeneracy of symmetric and amorphous patterns.** (a) Lowest energy states found using an initial state of a (i) Gaussian, (ii) Gaussian modulated with a plane wave, and (iii) pixelwise uniform random distribution. The total energy per particle of (iii) is lowest with $E/N \approx 2\pi\hbar \times 6.3949\,\mathrm{kHz}$ and the energies in (ii) and (i) are just $0.35 \times 10^{-2}\,\%$ and $6.16 \times 10^{-2}\,\%$ larger, respectively. (b) Relative energy deviation $\Delta E/E_{\mathrm{min}}$ of the lowest energy states (small top insets) found by repeating the ground state search 10 times using each time a different random initial state created by Perlin noise. Here $\Delta E = E_j - E_{\mathrm{min}}$ with the energy E_j for run j and the minimum energy of all runs is denoted $E_{\mathrm{min}} = \mathrm{min}_j\, E_j$. In (a)-(b) density cuts $n(x, y, 0)$ are shown in in a field of view of $14 \times 14\,\mu\mathrm{m}^2$ and other parameters are the same as in Fig. 4.8 with $(N,\, a_s) = (750 \times 10^3,\, 84.7\,a_0)$ fixed.

with either imaginary time evolution or conjugate gradient minimization of the energy functional depends on the initial state (Fig. 4.15(a)). Setting initially a radially symmetric Gaussian state converges to a ring pattern (i), a Gaussian modulated with a plane wave converges to the stripe pattern (ii) and a completely random initial state converges to a labyrinth (iii). Symmetric ring states compared to labyrinths have typically an order of magnitude larger relative energy than the labyrinth states compared among each other or to the stripe phase [3, 302, 488]. The absolute scale is extremely small with the ring state lying energetically just $\lesssim 4\,\mathrm{Hz}$ per particle above the labyrinth state. Striped states are particularly close in energy to labyrinth states and lie energetically within the variation seen from labyrinth to labyrinth[18]. Similarly when setting a previously found low-energy state as the initial state for the ground state search at a lower scattering length, the higher symmetry state is maintained towards lower a_s than predicted by setting a random initial

[18] For example at the chosen parameters the stripe in Fig. 4.15(a)(ii) is energetically above the labyrinth (iii) and run eight of (b) but below all other runs in (b).

wavefunction. We find these observations independent of the detailed numerical setup[19].

The higher-energy symmetric states represent metastable states [469]. The metastability is an inherent property associated to the labyrinth regime and relevant for future experiments. When performing real-time simulations ramping the scattering length across the superfluid to honeycomb or stripe transition, ring states can form that are long-lived[20] on experimental timescales. Associated to the near-degeneracy of multiple states are slow timescales for the transitions between them [469].

The degeneracy of multiple competing morphologies could already be seen in the supersolid droplet phase at parameters at which the droplet number changes (previous sections, [147, 300]). These parameters correspond to fine transition regions in the phase diagram that are surrounded by larger regions in which the droplet number is constant and ground states of different droplet numbers have an appreciable energy gap [205, 293, 300, 311]. Contrarily a generic point in the labyrinth phase is characterized by a range of different labyrinths that are very similar in energy (Fig. 4.15(b)). In the labyrinth regime it is neither obvious which Ansatz or initial wavefunction to choose in order to find the true ground state, nor is it clear whether one can determine what the true ground state is. Describing the labyrinth regime within a variational Ansatz is complicated by its amorphous structure. Typical variational Ansätze used to describe honeycomb, droplet or stripe phases assume the symmetry of these states by a superposition of a discrete set of plane waves [238, 302, 336, 471]. In Fourier space this corresponds to a set of points on a hexagon for honeycomb and droplet states and on a line for the stripe phase. The labyrinth has a diffuse spatial power spectrum (Fig. 4.11) corresponding to a continuous distribution of plane waves that could only partially be approximated with a superposition of a high number of plane waves.

It is not determined yet whether labyrinth patterns in an infinite system can have a lower energy than stripe patterns [197, 336]. The long-range nature of the dipolar interaction

[19] We have varied the number of points (states in Fig. 4.15 were calculated on a grid with 128^3 points and grids with 256^3 points gave similar results) and varied the numerical box size to reduce dipolar cutoff effects and spurious periodic image interaction. We employed two separate algorithms with tight convergence criteria and obtain the same results. For instance the state in Fig. 4.15(a)(ii) was found in imaginary time while the other states were found using conjugate gradient minimization. For the conjugate gradient algorithm a state is considered converged when all relative energy contributions between steps and their second order differences change by less than 10^{-13} and for imaginary time the same tolerance was employed for all relative energy contributions, the peak density, and the spatial variances. The noise type by which the initial state is seeded also does not change these observations (value noise was used in Fig. 4.15(a)(iii) and Perlin noise in Fig. 4.15(b)).

[20] We evolved the states up to 120 ms after the ramp is complete and found them to be stable.

makes bulk systems sensitive to boundary effects provided by confinement [387, 388]. It would be interesting to perform a sensitivity analysis of stripe states to boundary imperfections and whether a defect at the boundary could disrupt the long-range order of the stripe phase.

The exploration of phases beyond the supersolid droplet phase, especially of the labyrinth regime, presents a challenge to all aspects of the study of quantum ferrofluids.

- Numerically ground states cannot be unequivocally determined as the energy landscape is flat enough to allow for multiple stripe and amorphous labyrinth states with energy separations smaller than the variation seen by choosing different random initial states [3, 302, 336, 469].

- Theoretically the shape of the phase diagram and where the honeycomb and labyrinth phases emerge depends on the quantum fluctuation term, which has shown reasonable agreement with past experiments but is based on assumptions that could lead to a larger deviation between theory and experiments in the high density regimes [134–136, 138, 227].

- Experimentally reaching the required density regime is challenging [489, 490]. Yet experiments set to explore the phase diagram will be important in deciding whether the quantum fluctuation term is accurate enough and whether honeycomb and labyrinth phases are observable.

4.3.5. Conclusion and outlook

We identify new phases in quantum ferrofluids beyond the supersolid droplet regime. The general phase diagram of quantum ferrofluids in an oblate trap reveals supersolid droplets at low densities and labyrinthine, honeycomb, and pumpkin states towards higher densities. Quantum fluctuations play an increasingly dominant role towards higher densities providing the underlying stabilization mechanism of these morphologies. The strength of the stabilization can be tuned and different morphologies can be accessed by changing the trapping geometry. Squeezing the quantum ferrofluid morphologies along the magnetic field direction reveals that their characteristic length scale follows the same scaling behavior as the roton wavelength known from flattened superfluid states.

The labyrinth states point towards a large degeneracy of the ground state within the framework of an effective mean-field description. An interesting possibility is that the

various labyrinthine morphologies we find to be degenerate in our effective description might actually be selected upon by quantum fluctuations [491].

A linear stability analysis similar to the one employed for the superfluid to supersolid droplet transition (sections 3.2, 4.2.1) may allow identification of modes characteristic of the supersolid or superglass nature of these patterns [492].

Dipolar molecules [246, 493, 494] allow for dipolar interaction strengths orders of magnitude greater than in atomic gases. Once cooled to quantum degeneracy [247] these dipolar condensates will have a less stringent requirement on densities for the same effective interaction strengths and allow exploration of honeycomb and labyrinth phases [246]. Further interesting phases are expected in regimes where strong correlations and the granular nature of matter play an important role [449, 450].

"Machines take me by surprise with great frequency."

– Alan Turing

Chapter 5

A next-generation quantum gas experiment setup

Chapter Contents

In this chapter we describe the design and construction of a new quantum gas experiment setup and present first measurements achieving strongly dipolar BECs with the setup. Our previous experimental setup required optical transport by shifting a laser focus with a stage from a metal chamber over 375 mm to a glass cell to perform evaporative cooling for Bose-Einstein condensation. The optical access in the magneto-optical trap (MOT) chamber was limited and transport towards the glass cell lead to atom loss and heating

[152, 495].

The new setup produces MOTs and BECs without transport in one main chamber, overcoming atom number and optical access limitations of the previous experiment. Experiments with bulk dipolar quantum fluids in optical dipole traps (ODTs) [6] as presented in the previous chapters are enabled by this stage of the setup. The setup also lays the foundation for a second type of experiment, namely quantum gas microscopy of dipolar atoms in optical lattices [51, 129]. The second part of the experiment is still being designed and constructed and will be enabled by attaching a microscope chamber to our present setup and optical transport of cold atoms from the main chamber to the microscope chamber underneath an in-vacuum objective.

We begin with a brief summary of useful information about dysprosium related to its cooling and trapping and compare with other dipolar species.

5.1. Dysprosium

Our choice of atomic species for the realization of strongly dipolar quantum fluids is dysprosium. Dysprosium is an element in the group of the lanthanides with atomic number 66. Its ground state electronic configuration is $[\mathrm{Xe}]4f^{10}6s^2$ with orbital angular momentum $L = 6$, total spin $S = 2$, total angular momentum $J = L + S = 8$, and the term symbol $^5\mathrm{I}_8$. Among seven stable isotopes [496] most of the natural abundance is accounted for by two fermionic isotopes ^{161}Dy (abundance 18.9 %), ^{163}Dy(24.9 %) and two bosonic isotopes ^{162}Dy(25.5 %), ^{164}Dy(28.2 %). In this thesis we focus on the bosonic isotope ^{162}Dy which has nuclear spin $I = 0$. The melting (boiling) temperature is $T_{\mathrm{m,Dy}} = 1412\,^\circ\mathrm{C}$ ($T_{\mathrm{b,Dy}} = 2567\,^\circ\mathrm{C}$). Typical operating temperatures for effusion ovens as a source for atoms in dysprosium quantum gas experiments are 1000–1300 °C for vapor pressures on the order of 10^{-3} mbar [152, 497].

In its stretched state $|m_J| = 8$, dysprosium attains a magnetic moment of $\mu_m/\mu_B = g_J m_J \approx 10$ which is the highest in the periodic table, matched only by terbium [152, 497]. Here g_J is the Landé factor for the ground state $g_J \simeq 1.24$ [500, 502]. Due to the open $4f$-shell, multiple other lanthanide atoms such as europium and erbium have high magnetic moments (Fig. 5.1) in comparison to alkali atoms such as rubidium. Experiments with chromium have pioneered the field of strongly dipolar quantum gases [112]. Dysprosium and erbium BECs [113, 116] were achieved later and very recently a BEC of europium has been created [117]. The combination of a high mass and magnetic moment amplify the

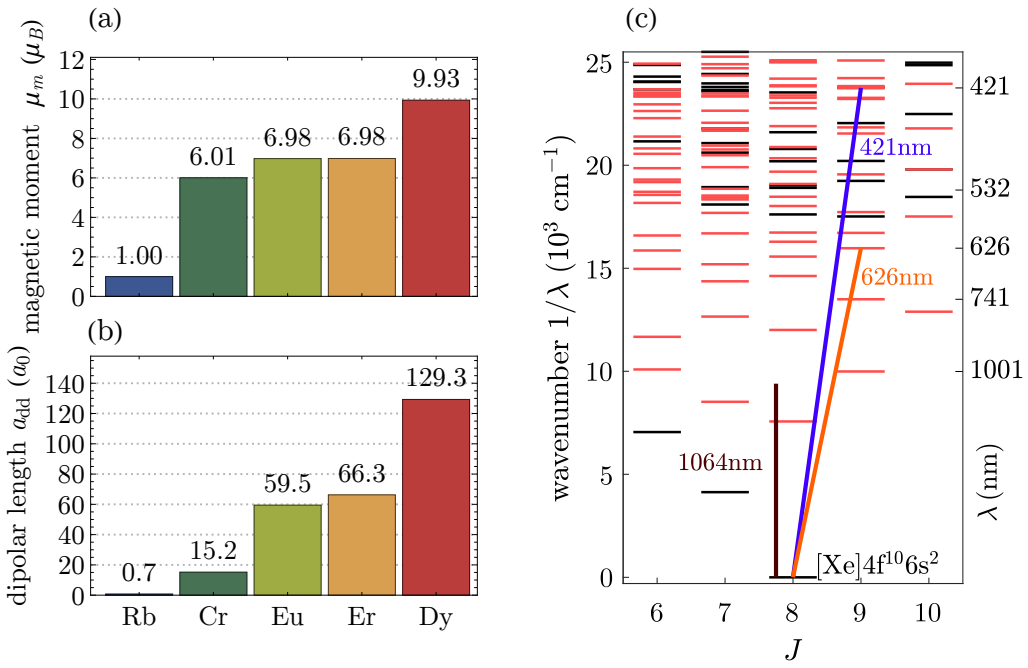

Figure 5.1.: **Magnetic moment and optical transitions of dysprosium.** (a) Comparison of the magnetic moment of the alkali atom rubidium [498], of the transition metal chromium [499], and of the lanthanides europium, erbium, and dysprosium [117, 500]. (b) Corresponding dipolar lengths $a_{dd} \propto M\mu_m^2$ rise at a high rate with mass and magnetic moment. (c) Excerpt of the optical spectrum of dysprosium [500, 501] with black (red) lines indicting even (odd) parity. The broad 421 nm transition is used for slowing, transversal cooling, and imaging, the 626 nm transition for magneto-optical trapping, and 1064 nm lasers are far detuned from resonances providing optical dipole trap potentials [181].

differences between the elements and leads to a dipolar length of $a_{dd} \approx 130\,a_0$ (Fig. 5.1(b)) for dysprosium. Potential candidates to increase the dipolar interaction of quantum gases even further are polar molecules. While they are more technically challenging to cool to quantum degeneracy [494], they offer dipolar lengths $a_{dd} > 10^3$ [266, 312] which translates, using the scaling relations in section 2.4.3, into a relaxation of the stringent atom number requirements in atomic dipolar quantum gases [246] for reaching the regimes discussed in section 4.3. The first BEC of polar molecules has very recently been reported [247].

The submerged $4f$ shell of dysprosium also leads to a complex optical excitation spectrum (Fig. 5.1(c)). The main transitions relevant for the cooling and trapping of dysprosum are the 421 nm and 626 nm transition [152, 497]. The 421 nm transtion has a natural linewidth of $\Gamma_{421} = 2\pi \times 32.2\,\mathrm{MHz}$, saturation intensity $I_{\mathrm{sat},421} = 56.4\,\mathrm{mW/cm^2}$ and the excited

state has a Landé factor $g_e = 1.22$. For the 626 nm transition, $\Gamma_{626} = 2\pi \times 136.6\,\mathrm{kHz}$, $I_{\mathrm{sat},626} = 72\,\mu\mathrm{W/cm^2}$, and $g_e = 1.29$ [152, 497]. The broad linewidth of the 421 nm transition and the low wavelength are favorable for a high scattering rate and a high resolution for optical imaging, respectively. In contrast the comparably narrow 626 nm transition is beneficial for cooling the atoms corresponding to a low Doppler temperature of below 10 µK. Lasers with wavelengths of 1064 nm are far red detuned from the dominant 421 nm transition and are used to trap atoms in optical dipole traps [181]. At this wavelength, Nd:YAG lasers are available with high powers up to hundreds of watts.

In dysprosium, there are other narrow transitions including 741 nm [503] and 1001 nm [504, 505] that are useful for further cooling and specialized imaging applications [129]. Due to the similarity of the electronic structure, other lanthanides have similar broad and narrow transitions at comparable wavelengths [497, 506, 507].

Feshbach resonances occur in dysprosium at low fields starting from about 1 G and are plentiful [508]. Towards higher fields many overlapping resonances lead to a chaotic Feshbach spectrum [152, 509]. The main employed transitions for the observation of dipolar quantum droplets and other structured states of matter were two resonances near 5 G [8] and a resonance near 22.5 G [4]. The background scattering length far from resonances for ^{162}Dy is $a_{\mathrm{bg}} \simeq 140(20)\,a_0$ [510–512].

Overall the high magnetic moment, high mass, low-field Feshbach resonances, and optical transitions available for the efficient cooling, trapping, and imaging of atoms make dysprosium a good choice in studying self-organization of quantum fluids.

5.2. Experimental setup

The initial design of the experimental setup has been partially described in previous theses [129, 513, 514]. In particular the design and characterization measurements of oven and magnetic field systems have been detailed in Refs. [513, 514]. We describe here comprehensively the construction and state of the setup required for the production and measurement of BECs.

5.2.1. Construction

The construction of the setup is shown in Fig. 5.2. We begin with an empty optical table (a) and assemble an ultra-high vacuum system in which MOTs and BECs are created and

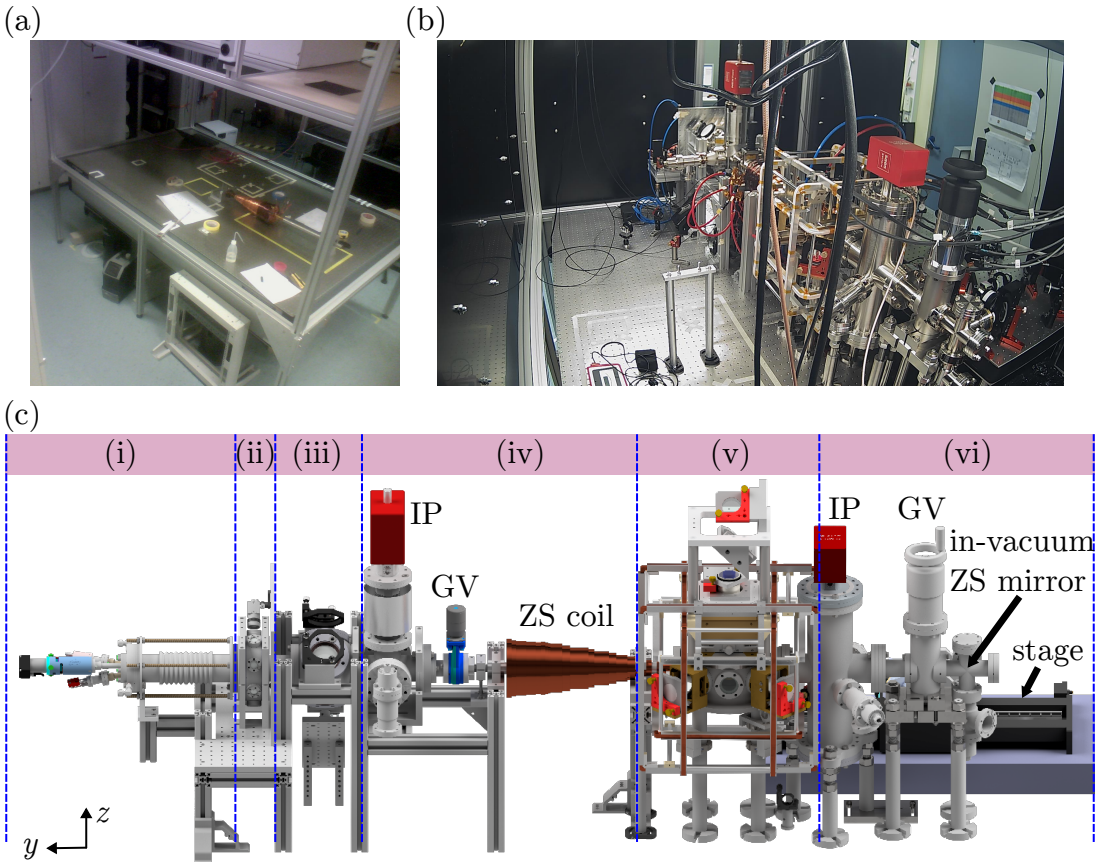

Figure 5.2.: **Experimental setup.** (a) Image at the start of the build 07/2020. (b) Image of the state of the setup 11/2021, producing magneto-optically trapped ^{162}Dy clouds with the main components built. (c) Computer assisted drawing of the setup. (i) Oven section with a dual filament effusion cell, (ii) spectroscopy section, (iii) transverse cooling section, (iv) ion pump (IP), gate valve (GV), and Zeeman slower (ZS) coil, (v) main chamber and compensation coils, and (vi) in-vacuum ZS-mirror accessible through a viewport behind the GV and air-bearing translation stage.

manipulated (b). The different sections used for the cooling and trapping of atoms are shown in detail in (c). The oven section (i) consists of a dual filament effusion cell[1] oven attached with a bellow to the spectroscopy chamber (ii). The bellow allows alignment of the atomic beam to the rest of the setup. The oven has a motor driven electrically controlled mechanical shutter. The spectroscopy chamber (ii) allows to perform spectroscopy on the oven atomic beam mainly for characterization and diagnostic purposes [514]. The transversal cooling section (iii) uses the 421 nm transition to reduce the transversal velocity distribution width, effectively collimating the atomic beam and leading to higher atom flux

[1] DFC-40-25-285-SHE-Col by Createc Fischer [153, 513, 514]

in the main chamber. Wide elliptical 421 nm laser beams are retroreflected and aligned to the atomic beam [497, 514]. Section (iv) includes an ion pump, a gate valve, and the Zeeman slower (ZS) coil. The gate valve separates the high vacuum region (i)-(iii) (typical pressures 10^{-8}–10^{-9} mbar) from the ultra-high vacuum region (v) (typical pressures 10^{-10}–10^{-11} mbar). With a closed gate valve the vacuum system (i)-(iii) can be opened for refilling the oven without influencing the vacuum condition in sections (v)-(vi). The ZS coil is wound around a nonmagnetic 316Ti stainless steel tube with a small inner clear aperture of 26 mm [513], acting as a differential pumping stage. The main chamber section (v) includes MOT retroreflectors, three pairs of magnetic field compensation coils, and a stage construction for the mounting of an objective[2] on top of the main chamber [514]. The main chamber is a spherical octagon[3] made from nonmagnetic 316L steel with an enlarged pumping port attached to a nearby ion pump in section (vi). Section (vi) also contains an in-vacuum mirror for the ZS beam [515] separated by a gate valve from the rest of the setup. The gate valve can be closed to exchange the ZS mirror in case dysprosium atoms coat the mirror over time and reduce its reflectivity [129]. The stage[4] carries a cat-eye retroreflector prepared to move the focus of a transport laser for future quantum gas microscope chamber experiments [516].

5.2.2. Main chamber and laser light

The main chamber is shown in Fig. 5.3. MOT1-2 and ODT1-2 beams are overlapped using dichroic mirrors before the main chamber and intersect at 90° in the horizontal x-y plane (Fig. 5.3(a)). The ODT1-2 beams come from two independent 1064 nm fiber lasers[5]. ODT3 is a fiber laser[6] that will eventually be used for the transport. We have also employed ODT3 in assisting BEC production. Both the MOT3 beam and the vertical imaging beam propagate along the vertical z-axis. The ZS beam propagates along y. The horizonal MOT beams are retroreflected using a custom brass construction (Fig. 5.3(b)) holding a retroreflector with an integrated $\lambda/4$ waveplate and a dichroic. The dichroic is reflective for 1064 nm and 421 nm but transmissive for 626 nm, allowing to separate ODT

[2] Custom infinity-corrected objective by Special Optics with a numerical aperture of NA = 0.5 and expected resolution of 520 nm at 421 nm imaging [129, 514].
[3] MCF600-SphOct-F2E1C7 by Kimball physics.
[4] ABL 1500-400 by Aerotech.
[5] ALS-IR-1064-50-I-SF by Azurlight systems [246].
[6] Initially YLR-LP 1030–1070 nm by IPG Photonics and later replaced with YLR-LP-SF 1064 nm by IPG Photonics.

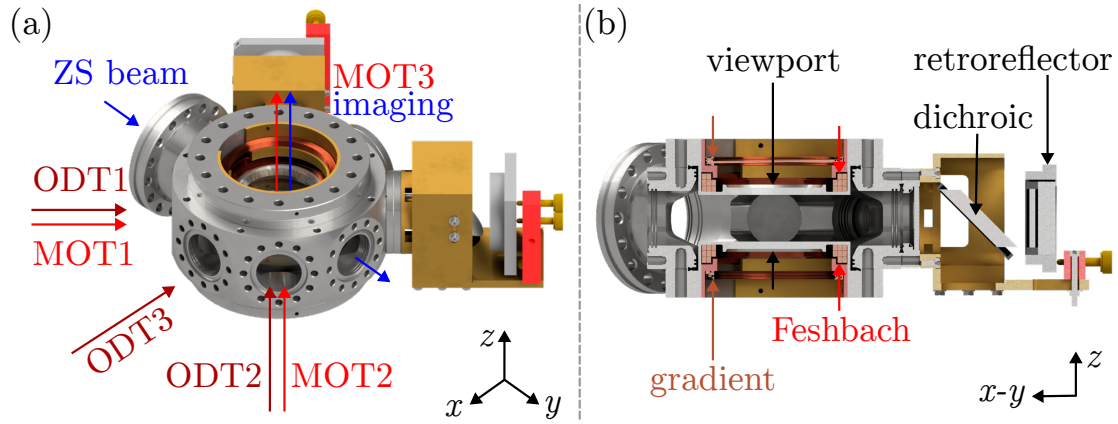

Figure 5.3.: **Main chamber.** (a) Top-side view of the main chamber. The chamber design allows imaging access from side and top and optical access for three ODTs and MOT beams in addition to the ZS beam (see main text). (b) Side view cross section of the main chamber. Viewports are recessed and MOT gradient and Feshbach coils are mounted in a custom brass structure. The horizontal MOT beam retroreflector is held by a brass structure containing a dichroic separating infrared from orange MOT light and reflecting blue light (see main text).

light from MOT light and directing the high power ODT light into beam dumps behind the chamber. The reflectivity at 421 nm allows to send imaging light through the side viewports, counterpropagating to the ODT light, and enables side imaging [517]. ODTs operate far-detuned from optical transitions [181], MOT beams red-detuned from the 626 nm transition, ZS and TC beams red-detuned from the 421 nm transition, and the imaging beam on resonance at 421 nm for absorption imaging [517] or red detuned for phase contrast imaging [495]. The vertical MOT3 beam is not retroreflected, which is used to realize a five-beam MOT [518] (section 5.4), allowing the top viewport to be used for imaging. We use absorption imaging from the top in section 5.4, and both absorption and phase contrast imaging in section 5.5, set up as described in Ref. [495] using a temporary camera[7]. The viewports are recessed allowing objectives to be placed in closer proximity to the atoms for high numerical aperture imaging. Feshbach coils and MOT gradient coils are integrated into a custom brass mounting structure attached to the main chamber (Fig. 5.3(b)) [514].

The 626 nm and 421 nm laser systems are described in detail in theses of the previous experiment setup [107, 152, 197]. The light is delivered to the optical table of the new experiment via optical fibers. Minor modifications on these laser systems have been made related to the fiber delivery of the light. Mainly we optimized the beam shape and the

[7] Machine vision camera BFS-U3-70S7M-C by FLIR

fiber coupling of the 421 nm light to have as much power available on the experiment table as possible. For each of the two transversal cooling beams up to 200 mW and for the ZS beam up to 300 mW are available. While for the ZS the power is not a limiting factor, the atom number in the MOT chamber would benefit from more power available in the TC beams (section 5.4). We also observe that the transmission efficiency of the 421 nm silica-based fibers degrades over time. A long term solution could be to exchange these fibers with larger mode field diameter photonic crystal fibers or adding a 421 nm laser system directly on the new optical table for free space 421 nm light delivery. The 626 nm laser system remained mostly the same since Ref. [153] except for additional waveplates installed before the incouplers to stabilize the polarization and the coupling efficiency over time.

The ODT1-2 setups were moved to the new optical table, rebuilt and realigned [152, 497]. Acousto-optical modulators (AOMs) are used to stabilize and regulate the power of ODT1-2 and the light is delivered onto an optical breadboard in front of the main chamber with high-power photonic crystal fibers[8]. On this breadboard the beams are shaped for a given desired waist (see section 5.5). Additionally we set up an acousto-optical deflector (AOD) system for creating time-averaged potentials with ODT1-2 in the horizontal plane as described in detail in Refs. [519, 520]. This system allows to increase the trapping volume of the crossed ODT (cODT) formed by ODT1-2 provided that sufficient ODT power is available, allowing for a better mode matching between compressed MOT (cMOT) (section 5.4.3) and cODT. The ODT3 system is aligned to the chamber after retroreflection off of the cat-eye on the stage without using a fiber.

We avoided magnetic materials near the main chamber as best as we could[9]. Our Feshbach field has a better stability as compared to the previous experiment using highly stable power supplies[10] with a smaller amperage range. We stabilize[11] the field with a digital proportional-integral-derivative controller in our new experimental control software (section 5.3) and obtain < 1 mG rms noise integrated up to 2.5 kHz and a relative stability of $\Delta B/B \simeq 1 \times 10^{-5}$

The chamber for quantum gas microscopy in the future will be attached to the remaining

[8] LMA-PM-15 by NKT Photonics

[9] In particular most types of steel and stainless steel are avoided. Non-magnetic materials are characterized by a low magnetic permeability $\mu_r - 1 \ll 1$. If possible we used aluminum, brass, nonmagnetic stainless steel (316L, 316LN, 316Ti), titanium, ceramics, or plastics [129].

[10] BCS line by HighFinesse

[11] The numbers we state are measured based on the current in the coils.

free viewport on the main chamber (on the $-x$ side in Fig. 5.3). Flooding the vaccum system with high-grade nitrogen and using a glove bag to cover this part of the vacuum system during the attachment should avoid contaminants to enter, circumventing re-baking the system [129].

5.3. Experimental control and data processing network

Our new experimental control is based on a real-time (RT) controller[12] that allows for tens of digital and analog in- and outputs which are individually programmable via interfaces to multiple programming languages. The RT controller has a processor with a 1 GHz clock rate and controls most other devices in our lab.

Since the beginning of the experiment build, the experimental control software was changed twice. Initially the `LabVIEW`-based control software of the previous experimental setup [521, 522] was replaced by a `C#`-based software [523] with some `python` interfacing capability. After working with this software for approximately 1.5 years we realized the necessity to implement a new control software[13].

For the base code of the experimental control software we choose `labscript` [524–527]. `labscript` is open-source, `python`-based, and is widely adapted by multiple groups working in atomic physics[14] due to its flexibility and extensibility. The wide usage of an open-source experimental control software whose base code is shared by many groups [524, 528–534] has the advantage of collaborative efforts in understanding, adapting, and improving the

[12] ADwin-Pro II by Jäger Computergesteuerte Messtechnick GmbH

[13] Multiple motivations for the switch existed. Major motivating examples follow. (1) For every experimental cycle the entire state of the RT controller was precomputed for every timestep at a predefined sampling rate and sent to the RT controller in this form. This table of instructions is mostly redundant for vast time intervals in which the state of few or no output channels change. Long experimental cycles (such as with slow evaporative cooling steps) implied instruction tables that could exceed the memory of the control computer. (2) Live control of the RT controller was absent. (3) Direct software-controlled feedback during experimental cycling operation was absent (indirect control was temporarily implemented through a `python` interface between the `C#` code and a database keeping track of variables external to the `C#` code). (4) Programmatic modification of experimental sequences is absent. The usage of a graphical user interface (GUI) to arrange experimental sequences is required where the number of GUI actions rises steeply with the number of output channels required in the modification.

[14] Monash [524], MIT/Harvard [528], Maryland/NIST [529, 530] Heidelberg [531], Vienna [532], Darmstadt [533, 534] and others [535].

software in short times and for experiments with specific requirements[15]. In addition to considering these advantages, our choice was made by the possibility to address all motivators for the switch from the previous software by combining `labscript` with an open-source interface to the RT controller initially developed by J. Schabbauer [532] in J. Léonard's group in Vienna [537].

5.3.1. `labscript` components

For an in-depth discussion of the infrastructure and the principles of `labscript` we refer to the PhD theses and publications of the developers [524–527]. Here we briefly cover the main aspects needed to understand our experimental control scheme based on `labscript` (Fig. 5.4). `labscript` consists of four main packages, namely `runmanager`, `blacs`, `lyse`, and `runviewer` (a). Experimental sequences are programmed directly in `python` and have access to global variables defined in `runmanager`. A variable manager in `runmanager` allows for convenient definition and manipulation of groups of variables. Variables can also be defined through any valid `python` expression depending on other global variables. We find that text-based creation of experimental sequences has several advantages over graphical user interface (GUI)-based creation [527, 538]. The readability of complex experimental sequences is enhanced, the ability to abstract subsequences in functions, programmatically modify the code that generates sequences, and to version control a growing number of experimental sequences is enabled by text-based sequence generation. `runmanager` reads the `python` code of a sequence and generates hardware instructions that are saved to a `.h5` file [539]. This file is an efficient storage format allowing to save and append multiple data structures including metadata, which is used to save everything related to a single experimental run in a single file. That includes the code used to generate the experimental sequence, the hardware instructions, and results generated at a later stage in the data processing. The experimental sequence uses definitions from another file, called the connection table, which defines the available hardware channels that physically exist in the lab. `blacs` uses the connection table to generate a GUI that can be used to control all devices in the lab live[16] without cycling a specific experimental sequence. To run an experimental sequence `runmanager` sends the path of the `.h5` file to `blacs` which reads the contained hardware instructions and executes them. Prior to the execution `blacs`

[15] An active `labscript` forum exchange is a demonstration of these advantages [536].
[16] Within `labscript` this is called the static mode.

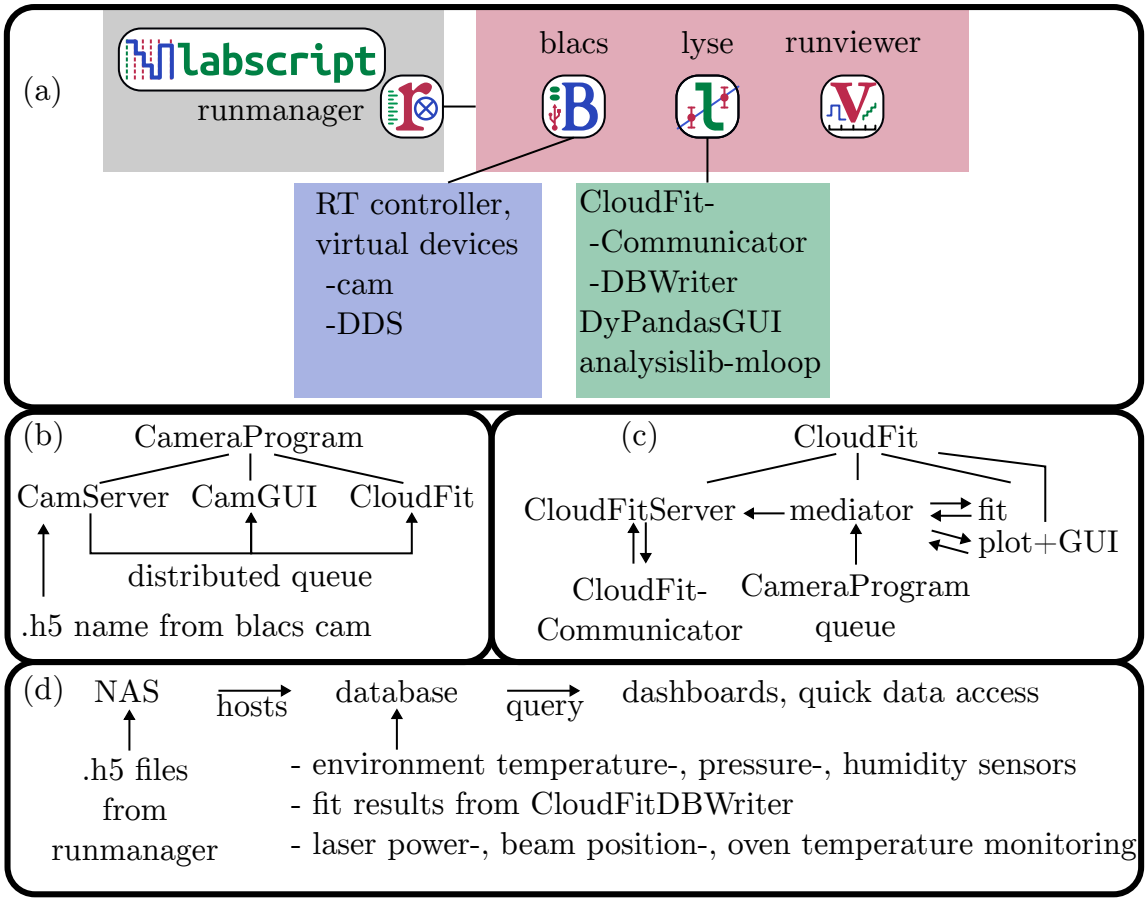

Figure 5.4.: **Experimental control and data processing network.** (a) `labscript` serves as the base of our experimental control software. `labscript` consists of `runmanager`, `blacs`, `lyse`, and `runviewer`, responsible for experiment preparation, execution, analysis, and visualization, respectively. `blacs` is interfaced with the RT controller and hosts virtual camera and DDS devices. The virtual camera device is a client for the camera program (b). `lyse` is connected to routines `CloudFitCommunicator` and `CloudFitDBWriter` for communicating with fitting routines (c) and the database (d), respectively, a graphical user interface `DyPandasGUI` for visualizing results, and a machine-learning package `analysislib-mloop` implementing feedback to the experimental control. The camera and fitting routines (b)-(c) consist each of a server and several other processes enabling communication between them and `lyse`. (d) A network attached storage (NAS) server provides a shared storage medium and hosts a database, written to by several environmental sensors and accessed for manual data analysis or dashboards for graphical overview. The main text provides a more detailed description.

checks that the connection table used to generate the experimental sequence is consistent with the connection table used to generate the `blacs` interface, restricting the chances

for human error[17]. `lyse` is responsible for post-processing and analyzing measurements taken right after `blacs` reports that one experiment cycle has completed. `lyse` is a GUI that collects a table (a dataframe within the `pandas` `python` library) of so-far completed experimental shots reported by `blacs` and a list of user-defined python-based evaluation routines. The routines can be chosen to be applied on manually selected sets of shots in the `lyse` table, on newly completed single experimental runs (single-shot evaluation), or on multiple experimental runs (multi-shot evaluation) for evaluation routines involving data of past or future experimental runs. Hardware instructions from the `.h5` files can be visualized and compared using `runviewer`.

The communication between the different `labscript` components is achieved with an open-source low-latency asynchronous networking library[18]. In `blacs` we implement an interface to the RT controller and two virtual devices.

5.3.2. User devices

Starting from the Vienna code interface between `blacs` and the RT controller [532], we extend the interface to be compatible with digital ouput cards without a separate processor[19]. The table of hardware instructions for the RT controller for an experimental sequence is efficient as it contains only the changes and corresponding times [532] required for the experimental sequence in contrast to a fixed sampling rate table of all channel states. The code for the RT controller (ADbasic) has been extended to allow for a digital proportional-integral-derivative (PID) controlled analog output given any of the analog input channels. In this way, the combination of `labscript` and the RT controller allows for as many digital PIDs as there are analog-in and analog-out channels with a PID bandwidth of up to $1/2\tau_0 = 250\,\mathrm{kHz}$. This value is the theoretical maximum based on the processing time (process delay) τ_0 of the RT controller code [532]. The achievable PID bandwidth using digital feedback controllers is often limited by the total system delay time τ including circuitry after the digital output value generation for sufficiently low processing time of the controller [541–543]. PID controllers become unstable and increase noise at a phase lag $\varphi = \pi$ corresponding to a frequency $f_\varphi = \varphi/2\pi\tau$ [541, 542]. The frequency f_π is

[17] If hardware connections in the lab change or new ones are created `blacs` and its connection table have to be kept up to date. `blacs` will not execute hardware instructions for experimental sequences generated with connection tables prior to the hardware changes, preventing unintentional signals or voltage levels sent to a given device.

[18] ZMQ [540].

[19] We have no TiCo processor in the AdWin-II Pro digital output cards.

known as "servo-bump" [543, 544] due the appearance of a maximum at f_π in the noise spectrum of a PID-controlled system with delay τ. In practice PID controllers often fail to suppress noise below the unstabilizied signal starting from phase lags of $\pi/2$ corresponding to a noise-suppression bandwidth $f_{\pi/2} = 1/4\tau$ [543]. For example in our case the delay caused by analog buffer cards, high-gain photodiodes, and other analog devices could limit stabilization schemes depending on these components to $1/4\tau \simeq 40\,\mathrm{kHz}$. Depending on the application such delays or bandwidths can be acceptable [532]. In these cases digital PIDs offer a more flexible and programmable alternative with no additional device or space required in the lab in comparison to analog PIDs.

Virtual devices are implemented in software, with no hardware components in the lab. The `cam` device is a network client that connects to the camera server in our camera program (Fig. 5.4(b)) and forwards the `.h5` filepath every time `blacs` reports that an experimental cycle has completed. The `DDS` device sets up direct digital synthesis (DDS) devices via serial communication prior to the start of an experimental cycle. The DDS devices control acousto-optical modulators (AOMs).

5.3.3. Data post-processing

In `lyse` the `CloudFitCommunicator` and `CloudFitDBWriter` programs are responsible for obtaining fit results from the fitting program `Cloudfit` (c) for further use in `lyse` and writing the results to the database (d). We develop `DyPandasGUI`, a GUI that accesses the `lyse pandas` dataframe and allows to plot any field in the dataframe against any other field in the dataframe via drag-and-drop[20]. A typical usage example is scanning an experimental parameter and looking for a quick and live assessment of the atom number as a function of this parameter. We also integrated `analysislib-mloop` [546] into our `lyse` configuration which implements machine-learning (ML) online optimization of our experiment. By accessing results contained in the `lyse` dataframe and feeding them to a (software) controller, the controller determines the next set of parameters, and updates the global variables defined in `runmanager` via the network connection to the new values for the next cycle. Currently in our implementation `analysislib-mloop` realizes the ML capabilities through `M-LOOP` [547], providing several controllers including neural networks and Gaussian processes among others [548]. Despite its name, `analysislib-mloop` is not

[20] The source code of `pandas_GUI` version 0.2.14 [545] was modified to implement this program. The main changes include automatic accessing of the `lyse pandas` dataframe and selection of fit results from `CloudFit`.

limited to `M-LOOP` and allows implementation of other controllers [546]. Following a long history [549] ML has emerged as a powerful tool in complex atomic, molecular and optical experiments [547, 550, 551]. Among others, a strong motivation for us having ML methods ready for the optimization of experiments is the recent demonstration of ML-assisted productions of quantum gases in shorter times or with higher atom numbers compared with time- and labor-intensive human optimization of experimental parameters [528, 547, 552, 553].

`CameraProgram` and `CloudFit` (Fig. 5.4(b)-(c)) are programs that receive images from a camera[21] and post-process them, respectively. Both programs are made up of several processes that run simultaneously to provide as much independence of the data processing steps as possible. The processes and communication between them rely on `python`'s `multiprocessing` package. GUIs are created in `pyqt` and `qt-designer` and both programs host a server built with the same structure as realized for the communication between the `labscript` components, allowing to seamlessly transmit data between each other and `labscript`. The functions along the data processing chain are best understood by following the procedure for a given experimental cycle.

During an experimental cycle the RT controller triggers the camera to take images which are held in memory. The virtual `cam` device in `blacs` sends the `.h5` file path to the camera server, signaling that one cycle is complete. `CameraProgram` saves the images locally and sends the path and the images into a `queue` which is distributed to the GUI for displaying the images and the `CloudFit` program. The images are then saved to the `.h5` file while the remaining post-processing is ongoing. The `mediator` process within the `CloudFit` program receives the images and the `.h5` path and sends the data to the `fit` process. This process fits Gaussian functions to the atomic cloud in the images and reports the results back to the `mediator`[22]. The `mediator` reports to the server that results are available and sends them to the plot and GUI process for display. A `queue` between the `CloudFitServer` and the `mediator` acts as a local memory for `CloudFit` which is accessed from the `lyse` `CloudFitCommunicator` routine. Once `CloudFitCommunicator` receives the results from `CloudFit`, they are saved to the dataframe and read from `CloudFitDBWriter` which writes to a database (Fig. 5.4(d)).

Multiple servers throughout the data processing chain allow to distribute the programs

[21] FLIR machine vision cameras BFS-U3-63S4M-C (side imaging) or BFS-U3-70S7M-C (top imaging).
[22] The `fit` and GUI programs are independent and communicate only indirectly via `pipes` through the `mediator`.

over several computers. Typically `runmanager` and `blacs` (and `runviewer` if temporarily desired) run on a computer, `CameraProgram` and `CloudFit` on a second computer, and `lyse` on a third computer. The separation into control, imaging, and analysis distributes computational power and provides independence along the post-processing chain, ensuring that earlier steps in the chain succeed even if later steps are interrupted or fail.

5.3.4. Data storage and database

The database (Fig. 5.4(d)) is hosted by a network-attached storage (NAS) server. The NAS has six slots for hard disk drives, is in a RAID 6-configuration for data redundancy, and provides a shared storage medium accessible from all lab and office computers. The database is implemented in `MySQL`, providing fast data access using a simple query language. We install multiple sensors around the lab which report to the database in addition to `lyse`. A notable example is a WIFI-enabled microcontroller[23] connected to an environmental sensor[24] reporting temperature, pressure, and humidity. The combination is space and cost-efficient and we deployed several sensors throughout the lab. Data pertaining to the lab environment is monitored through an open-source dashboard service[25] which accesses the database and allows fast graphical overview of the lab state and correlating changes in experimental results with environmental factors that would otherwise be difficult to discover.

5.4. Five-beam magneto-optical trap

This section outlines our typical mode of operation to cool and trap atoms from the oven to a compressed magneto-optical trap (MOT) ready for loading atoms into optical dipole traps (ODTs).

5.4.1. Oven and Zeeman slower

We filled the oven with 50 g [513] 99.9 % purity dysprosium granulate and operate the effusion cell (EC) and hot lip (HL) at temperatures $T_{\mathrm{EC}} = 1100\,^{\circ}\mathrm{C}$ and $T_{\mathrm{HL}} = T_{\mathrm{EC}} + 50\,^{\circ}\mathrm{C}$, respectively. The HL is kept at a higher temperature compared with the EC to avoid

[23] NodeMCU
[24] Bosch BME280
[25] Grafana

accumulation of dysprosium atoms on the HL and potential clogging [514]. Atoms are slowed with a spin-flip Zeeman slower (ZS) [193, 554]. The ZS design has been described in detail in Ref. [513]. After operating the ZS at the therein described design parameters we found that we could not achieve competitive MOT atom numbers, even with substantial MOT optimization efforts. We decided to experimentally optimize the ZS magnetic fields and the ZS beam detuning using Doppler spectroscopy with the narrow 626 nm transition [555]. With this approach we were able to achieve satisfactory MOT atom numbers. The final values for the ZS currents correspond to the optimal field assuming a safety factor[26] $s = 0.3$ given the ZS coil winding plan and the fixed ZS length of $l = 405\,\mathrm{mm}$ [513]. The optimal ZS captures atoms with a start velocity of $\simeq 379\,\mathrm{m\,s^{-1}}$, has a peak-to-peak magnetic field of $\simeq 520\,\mathrm{G}$, the ZS beam detuning is $\Delta_{\mathrm{ZS}} = -7.5\,\Gamma_{421}$, and the final velocity in the main chamber is approximately $v_f = 6\,\mathrm{m/s}$. The ZS beam is focused at the oven aperture and operates with a power of 100–150 mW. Up to $\simeq 110\,\mathrm{mW}$ we observe a rapid increase in MOT atom number and for powers $\gg 150\,\mathrm{mW}$ we find a decreasing atom number at a small rate. The decline is explained by sufficiently slow atoms being pushed back for sufficiently high powers. The safety factor, start velocity, and detuning are consistent with other efficient setups with ZSs of comparable length [497, 555]. The improved operation at parameters optimal for the safety factor $s = 0.3$ is related to two differences compared with our previous experimental setup [152]. The smaller of the two is a 12 % lower oven temperature leading to a most probable velocity of $\simeq 460\,\mathrm{m/s}$ [497], about 5 % lower than for the previous experimental setup. We expect that the dominant effect is the 38 % shorter ZS while assuming a safety factor of 0.85 that is even 9 % larger in the initial design [513] as compared to the previous setup [152]. In short, we find experimentally that the previously assumed safety factor and the associated starting velocity of $\simeq 600\,\mathrm{m/s}$ for a ZS of length l [513] overestimates the possible ZS performance and a more conservative choice of s is appropriate [497, 555].

5.4.2. Magneto-optical trap

After the ZS we capture atoms in the MOT. A MOT is characterized by the dimensionless parameter $R = \hbar k\Gamma/2Mg$ [556, 557] describing the maximum scattering force relative to gravity with the gravitational acceleration g. R describes the narrowness of a MOT.

[26] The security factor is the ratio between actual and maximal acceleration produced by the scattering force of the ZS light [497, 513]. It is used to secure a sufficiently low final velocity assuming less than idealized deceleration of the atomic beam and takes design imperfections in the ZS build into account.

Typical broad alkali MOTs have $R > 10^4$ and very narrow MOTs are characterized by R of order unity such as in ^{88}Sr [556]. The important role of gravity is characteristic for narrow MOTs. We use the 626 nm transition with a linewidth of $\Gamma_{626} \simeq 2\pi \times 136.6\,\mathrm{kHz}$ to implement a five-beam MOT for ^{162}Dy [497] which is relatively narrow ($R \simeq 170$). This unusual MOT type takes advantage of the high mass of ^{162}Dy, allowing to use only one circularly polarized vertical beam against the direction of gravity with no backreflection. In the horizontal plane the five-beam MOT uses two retroreflected circularly polarized beams and a MOT gradient field as for a six-beam MOT [193]. The gained optical access from the top allows to implement imaging along this direction in addition to imaging through side viewports.

It is instructive to discuss the working principle of this MOT [556, 557] to gain an intuition on trade-offs of its operation. The radiative force on an atom for a single beam of the MOT is

$$\boldsymbol{F}(\boldsymbol{v}, \boldsymbol{r}) = \frac{\hbar \boldsymbol{k} \Gamma}{2} \frac{s}{1 + s + 4\left(\Delta + \boldsymbol{k} \cdot \boldsymbol{v} + \boldsymbol{\beta} \cdot \boldsymbol{r}\right)^2 / \Gamma^2}, \tag{5.1}$$

where $\Delta = \Delta_{626}$ is the detuning, $\boldsymbol{k} = \boldsymbol{k}_{626}$ is the wave vector, $\Gamma = \Gamma_{626}$ is the linewidth, $s = I/I_{\mathrm{sat},626}$ the saturation parameter, $\boldsymbol{v}$ the velocity, $\boldsymbol{r}$ the position, and $\boldsymbol{\beta} = \mu_Z \nabla B(\boldsymbol{r})$ is the Zeeman shift with the differential magnetic moment $\mu_Z/\mu_B = g_e m_e - g_g m_g$ between ground state and excited state with magnetic quantum numbers m_g, m_e and Landé factors g_g, g_e, respectively [556, 557]. To discuss the working principle of the five-beam MOT we focus on the z direction along gravity $F_z(v_z, z)$ at $x = y = 0$ (Fig. 5.5). A relatively narrow six-beam magneto-optical trap (a) has steep forces $F_z(v_z, z; -k, -\beta) - F_z(v_z, z; k, \beta)$ relatively far apart that lead to a box potential, tilted by gravity $-Mg$ (b). The width (depth) of the box is determined by the combination of detuning and gradient (saturation parameter) and the tilt is fixed by the mass of the atomic species. The depth of the six-beam box can be large as atoms at $z > 0$ are pushed back to $z = 0$ due to the combination of the gradient field and the sixth beam. If the sixth beam is removed (c) the upper wall of the box disappears and atoms can still be trapped thanks to the competition of gravity and upward radiation force. In equilibrium, atoms rest several millimeters up to centimeters below the magnetic field zero leading automatically to a spin polarized MOT [506, 558]. The effective maximum trap depth is reduced to the potential difference between trap minimum and the value at the magnetic field gradient zero crossing. Atoms that reach the zero field lose their quantization axis and can be excited to higher-lying Zeeman states, leading to spin polarization loss and expulsion of these atoms from the trap [558].

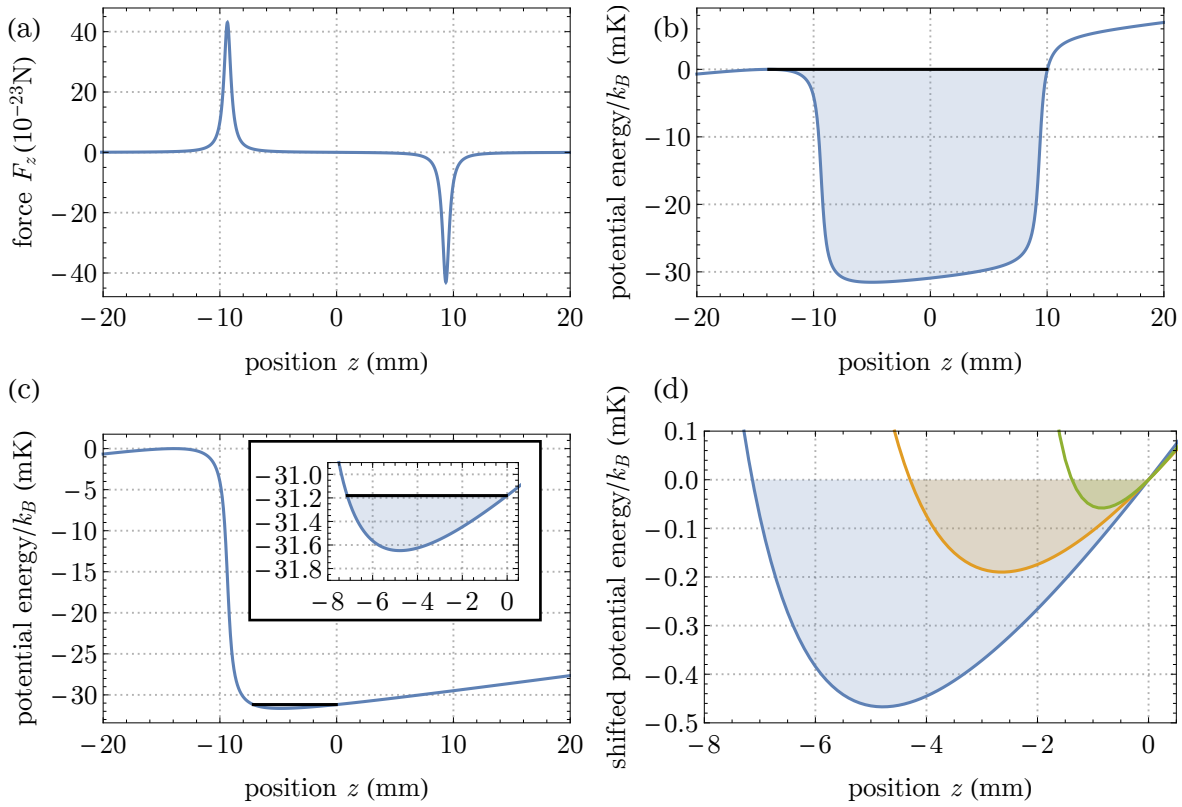

Figure 5.5.: **Theory of operation for a five-beam magneto-optical trap.** (a) Radiative force $F_z(z)$ at $v_z \approx 0$ for a six-beam MOT without gravity. (b) The corresponding six-beam MOT potential including gravity acquires a tilted box shape with relatively hard walls. The depth is controlled by the laser intensity, the width by the detuning and magnetic field gradient, and the tilt by the atomic mass. Atoms in the box undergo mostly free flight, becoming damped only in the limit of low intensity, detuning, or gradient where the two force peaks approach each other. (c) Five-beam MOT potential by removing the beam along gravity from (b) yields atoms trapped by a competition of radiative force and gravity. The absence of the upper beam results in a damping coefficient that is only intensity dependent. The inset magnifies the potential minimum region. (d) Five-beam MOT potential towards a cMOT, from MOT (blue) to intermediate (orange) and cMOT (green). The potentials are shifted each to the reference at $z = 0$ representing the magnetic zero field. The MOT parameters $(\partial_z B, \Delta, s) \simeq (2.7\,\mathrm{G\,cm^{-1}}, -65\,\Gamma_{626}, 24)$ (see main text) have been used for (a)-(c) and the blue curve in (d). The green curve in (d) is for the cMOT parameters $(\partial_z B, \Delta, s) \simeq (1.35\,\mathrm{G\,cm^{-1}}, -8\,\Gamma_{626}, 0.6)$ and the orange curve for the average of MOT and cMOT parameters.

To reduce (increase) the temperature (density) of the MOT, a sequence of steps can be taken (Fig. 5.5(d)), producing a compressed MOT (cMOT). Typically this is done by reducing $|\partial_z B|$, $|\Delta|$, and s [503, 518, 555, 558, 559]. The equilibrium position z_0 at which

$F(0, z_0) = 0$ is given by the local dimensionless detuning

$$\frac{\Delta + \beta z_0}{\Gamma} = \frac{1}{2}\sqrt{s(R-1)-1}. \tag{5.2}$$

If Δ or β change, the position z_0 adjusts automatically such that $\Delta + \beta z_0$ remains constant [556, 558]. This relation shows that the vertical position of a five-beam MOT is tightly coupled to the detuning, the gradient field, and the laser power. The damping coefficient

$$\alpha = -\frac{2\hbar k^2 \sqrt{s(R-1)-1}}{R^2 s} \tag{5.3}$$

in the vicinity of the potential minimum is determined from $F_z(v_z, z_0) \approx \alpha v_z$ by expanding F_z at $z = z_0$ to first order in v_z [556, 557]. The diffusion coefficient $D_z = \hbar^2 k^2 \Gamma \langle \rho_{22} \rangle \simeq \hbar^2 k^2 \Gamma / 2R$ with the excited state population $\langle \rho_{22} \rangle$ [556–558] is used to estimate the equilibrium temperature

$$T = \frac{D_z}{k_\mathrm{B}|\alpha|} = \frac{\hbar\Gamma\sqrt{s}}{2k_\mathrm{B}} \frac{R}{2\sqrt{R-1-1/s}}. \tag{5.4}$$

As the MOT is compressed, the motion of the atoms becomes increasingly damped and the temperature decreases. Notably the damping coefficient and temperature are independent of Δ and β which only leads to an automatic adjustment of z_0. Whist this description captures the essential working principle of the five-beam MOT, the full three-dimensional dynamics of MOTs can be modeled using Monte Carlo simulations [489, 560, 561].

Our MOT beams have Gaussian beam diameters of $d \simeq 27\,\mathrm{mm}$ leading to a capture velocity of $v_c \simeq 16\,\mathrm{m/s}$ [497], suitable to capture the atoms escaping the ZS at final velocities $v_f < 10\,\mathrm{m/s}$. We load the MOT at a gradient of $\partial_z B \simeq 2.7\,\mathrm{G\,cm^{-1}}$, detuning $\Delta \simeq -65\,\Gamma_{626}$, and intensity $I \simeq 24\,I_{\mathrm{sat},626}$ (Fig. 5.6(a)). The MOT is shifted further below the ZS beam with a magnetic offset field which we found to be beneficial for the loading rate in agreement with Ref. [518]. The atoms in Fig. 5.6(a) acquire an ellipsoidal shape at the bottom characteristic of the steep wall potential (Fig. 5.5(c)) of a far detuned narrow line MOT [556, 562]. We found steady improvement in the atom number for lower vertical positions. A lower MOT position avoids radiation from the ZS beam and moves the MOT out of the way of insufficiently cooled atoms from the ZS coil side.

To load the MOT we use the transverse cooling (TC) unit with typically 100–180 mW of power per beam at a detuning of $\simeq -0.5\,\Gamma_{421}$ [152, 497]. We could achieve a factor two to four increase in MOT atom number depending on the alignment and the power available

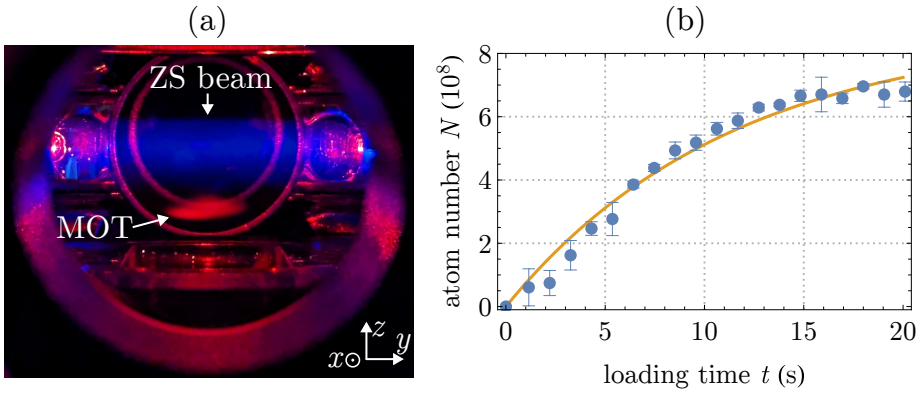

Figure 5.6.: **Magneto-otical trap.** (a) Picture of magneto-optically trapped (MOT) atoms along the $-x$-direction in steady state below the Zeeman slower (ZS) beam. The orange MOT fluorescence and blue ZS fluorescence is captured with a cell phone camera. (b) Loading curve of the MOT. Points show measured atom numbers from absorption images along the z-axis and error bars are the standard deviation over three averages. The orange line is a least-squares fit to the data (see main text).

in the TC. The MOT atom number continually increases with the available power here, which is limited by the overall available laser power and the coupling efficiency of the fibers delivering the light from the laser table. We also apply a spectral broadening to the 626 nm light [497, 555, 556, 559] of about $\pm 5\,\Gamma_{626}$ that effectively increases the capture volume of the MOT and yields approximately a factor two increase in loading rate.

The loading data (Fig. 5.6(b)) is fit with the loading curve function $N(t) = N_{\mathrm{ss}}(1 - \exp(\gamma t))$ where N_{ss} is the steady state atom number, γ is the one-body loss rate, and $R = N_{\mathrm{ss}}\gamma$ is the loading rate [518, 563]. We obtain $N_{\mathrm{ss}} = 8.7(6) \times 10^8$, $\gamma = 0.088(11)\,\mathrm{s}^{-1}$, and $R = 0.77(11) \times 10^8\,\mathrm{s}^{-1}$. In the low-density regime of an uncompressed MOT, the two-body collisional rate can be neglected as compared to γ [563]. The values we obtain are comparable to the optimized first reported five-beam magneto-optical trap of dysprosium [518]. We also saw that we can increase the loading rate roughly by a factor of two with every 100 °C increase in oven temperature [518].

We noticed that intensities above $\simeq 25\,I_{\mathrm{sat},626}$ are detrimental for the loading rate of the five-beam MOT for the best MOT parameters we found. This occurs because of the trap depth limitation of the five-beam MOT (Fig. 5.5(c)) and the increase in temperature (Eq. (5.4)) for higher powers. A larger detuning would allow for higher powers, compensating vertical position shift and attaining higher atom numbers at higher temperatures, but there is a trade-off between a very low vertical position being beneficial for the loading of the MOT and a longer compression distance and time to reach a cMOT closer to the

magnetic zero point.

5.4.3. Magneto-optical trap compression

The compression of the MOT serves several purposes that are ideally simultaneously fulfilled. The cMOT should have a high atom number, low temperature, form at a vertical position that is accessible with optical dipole trap (ODT) lasers for later evaporative cooling, and mode match to those ODTs. Since several MOT parameters for the five-beam MOT are strongly coupled, fulfilling all requirements optimally is challenging. At the same time this coupling provides an opportunity to explore using optimal control with the new experimental control in the future [564]. In this section we present a compression sequence that was satisfactory to move on with ODT loading but we believe that there is further potential in cMOT optimization.

Our optimal compression sequence turns out to be similar to previous experiments [518, 555, 559]. For the compression we close shutters for the ZS and TC light and close the oven shutter so that the oven atomic beam does not heat the cMOT as it shifted up during the compression. We turn off the frequency broadening of the 626 nm light and ramp the ZS coils off in 20 ms. Simultaneously the compensation and gradient fields are adjusted to minimize the positional displacement of the MOT due the ZS magnetic field change, which was experimentally optimized. Overall the gradient field is reduced to $\partial_z B \simeq 1.35\,\mathrm{G\,cm^{-1}}$, the detuning to $\Delta \simeq -8\,\Gamma_{626}$, and the intensity to $I \simeq 0.6\,I_{\mathrm{sat},626}$ in a total compression time of $\simeq 200\,\mathrm{ms}$. These values have been used in Fig. 5.5(d). With typically 4 s MOT loading time we reach in the end $N \simeq 100\text{–}150 \times 10^6$ atoms at temperatures 10–20 µK in the cMOT. The corresponding estimated cMOT volume [558] is $V/(2\pi)^{3/2} \simeq (0.5\,\mathrm{mm})^3\text{–}(1\,\mathrm{mm})^3$, peak densities $n_0 = N/V$ on the order of $10^{10}\,\mathrm{cm^{-3}}$, and classical phase space densities $\mathrm{PSD_c} = n_0\lambda_{\mathrm{dB}}^3$ in the range $10^{-6}\text{–}10^{-5}$, which are typical starting conditions for evaporation in ODTs [555, 558, 565]. We observed cMOT lifetimes of several hundreds of milliseconds which is sufficient for ODT loading [518].

A better trade-off between atom number and temperature of the cMOT for ODT loading could be to compress further than we presented in this section. After working with the ODTs (see following sections) our experience suggests that sacrificing atom number for a lower temperature and reduced size with a better mode matching to the ODTs is favorable [490].

5.5. Dysprosium Bose-Einstein condensate

In this section we describe the first ^{162}Dy BEC production with the new experimental setup. The results in this section are preliminary in the sense that the imaging system is rudimentary and was not explicitly characterized. In sections 5.5.1-5.5.2 we use a simple machine vision camera[27] and the atomic cloud is imaged using a $4f$-configuration with two singlet 100 mm lenses. The lenses are mounted in a lens tube to form a telescope and the magnification $M_g = 1$ is measured in a test setup with an error of $< 1\,\%$. By manually adjusting the telescope position as opposed to with a micrometer stage, the focus position is determined by minimizing the apparent widths of a thermal cloud in absorption images. The adjustment would be improved by using a micrometer stage and repeating the adjustment at colder temperatures. Due to the imaging setup we assume that defocus aberration is the largest source of systematic error in sections 5.5.1-5.5.2, leading to lower optical densities and larger widths than expected. These effects quantitatively influence the absolute values of densities, widths, and temperatures but not qualitative observations.

After we observed the first BEC with the new setup using absorption imaging (ABI) (sections 5.5.1-5.5.2) we implemented phase-contrast imaging (PCI) allowing us to see then density in-situ [495, 566] using an objective with a magnification of $M_g \simeq 76.6$. PCI with a detuning $\Delta_{421} \simeq -30\,\Gamma_{421}$ was used for our BEC production using machine learning (section 5.5.3). The change from ABI to PCI is not necessary for the observations presented in section 5.5.3 but occurred during our continuing efforts to upgrade the new experiment. At this stage we did not yet characterize the imaging system in-depth and the objective was slightly defocussed, allowing us to obtain Gaussian fits to the data from the thermal cloud to the BEC regime and qualitatively assess atom numbers and widths. Thermal clouds and BECs are clearly distinguishable even with this temporary imaging setup[28].

5.5.1. Loading optical dipole traps

We start from a compressed MOT (cMOT) with 100–150 $\times\, 10^6$ atoms at temperatures 10–20 µK. Our goal is to load atoms into a crossed ODT (cODT) formed by ODT1-2 (section 5.2.2) that each approximately have waists of $w_{x,y} \simeq 62(5)$ µm. By directly loading

[27] FLIR BFS-U3-70S7M-C

[28] BECs appear as an Airy disc point-spread function since they are presumably smaller than the resolution attained with the defocussed objective. The BEC density was too high for the chosen polarizer angle in PCI when the atomic cloud was perfectly in focus, leading to saturated images.

from the cMOT into the cODT at a power of $P_0 = 7.5\,\mathrm{W}$ each, we only retain typically $\simeq 0.1 \times 10^6$ atoms in the relatively shallow dimple. By changing the holding time after the cODT loading we see that many atoms get lost in the wings of the ODTs and only atoms in the vicinity of the dimple remain trapped. The low loading efficiency results from a combination of the cMOT to cODT mode matching and the cODT trap depth. The cMOT has a volume of approximately $1 \times 1 \times 1\,\mathrm{mm}^3$ while the capture volume of the cODT is on the order of the waist cubed. The trap depth of the cODT with P_0 each is approximately $\Delta V_{x,y}/k_\mathrm{B} \simeq -30\,\mu\mathrm{K}$ and $\Delta V_z = 2\Delta V_{x,y}$. These limitations could be addressed by more laser power. Increasing the overall laser power would allow to create spatially larger time-averaged potentials with greater trapping depths by activating the scanning AODs and beam shaping the ODTs to smaller waists. In our setup here the power was limited to P_0 due to losses at AOMs and fibers in the beam preparation for the experiment. Due to these limitations we decided to temporarily use the high-power multifrequency[29] 100 W, 1070 nm fiber laser as ODT3 [495] with a waist of $w \simeq 30\,\mu\mathrm{m}$ to initially capture atoms in a trap with better mode matching to the cODT and to increase the density of the atoms from the cMOT. We capture 10–20 $\times 10^6$ atoms in this laser at a power of $P_{0,I} \simeq 72\,\mathrm{W}$ and reduce the power for simplicity with a single exponential ramp $P_I(t) = P_{0,I}\exp(-\Gamma_I t)$ to pre-evaporate the atomic cloud into the cODT. Other ramp shapes could lead to higher evaporation efficiencies [568, 569]. We optimize the rate Γ_I and the final power by monitoring atom number and temperature in the cODT. We find $\Gamma_I \simeq 2\,\mathrm{s}^{-1}$ for a final power $P_I/P_{0,I} = 0.03$ which amounts to an evaporation time of $\simeq 1.8\,\mathrm{s}$. At this stage 1–2 $\times 10^6$ atoms remain in the vicinity of the ODT3 focus, which are transferred without significant losses to the cODT. The linear polarization of the ODTs is adjusted to maximize the atom number in the cODTs and we find that this polarization minimizes the temperature. The dependence originates from the fact that the Rayleigh scattering rate in the ODTs is angle-dependent due to the tensor polarizability. As a result the heating rate due to the gained recoil energy is angle dependent and expected to be minimal when the the ODT polarization is orthogonal to the magnetic field [567]. We confirm that the cODT atom number and temperature are sinusoidal and π out of phase

[29] IPG Photonics YLR-LP 1030–1070 nm. The temporary laser is a suboptimal choice as we likely reproduce previously reported heating effects due to the multiple frequency components [152, 197, 567]. The heating effect imposes an upper limit on the initial power used to temporarily capture atoms and a lower limit on the rate with which the laser power is ramped down in order to trade off temperature and atom number. Towards the end of this thesis we replaced the laser with the single frequency YLR-LP-SF 1064 nm model. The single frequency laser was not available to us at the time we first needed it.

as a function of the polarization angle θ [567].

The Feshbach magnetic field is calibrated using radio frequency spectroscopy [152, 197] in the cODT. Using this standard method for the calibration, we accurately reproduced previously reported Feshbach spectra by scanning the magnetic field and observing atom number and temperature starting from atoms at $\simeq 5\,\mu\mathrm{K}$ after partial evaporation in the cODT [6, 138, 508]. Our measurement also produced the current to field conversion expected from the coil design [514] with deviations of less than 5 mG/A. We set the field to 1.8 G which is far from Feshbach resonances [508].

We measure the cODT trap frequencies by displacing the ODTs horizontally by 0.5–1 waist using the AODs during the transfer from ODT3 to cODT and observe the COM oscillations. The frequencies in the two directions transverse to the top imaging are $\omega_{x,y} = [237(5), 266(4)]\,\mathrm{Hz}$. Assuming that the ODTs are intersecting at approximately 90° we infer $\omega_z = \sqrt{2}\bar{\omega}_{x,y} \simeq 355(5)\,\mathrm{Hz}$. The geometric mean trapping frequency $\bar{\omega}_{x,y} \simeq 251(3)\,\mathrm{Hz}$ is consistent with beam waists of $\simeq 64\,\mu\mathrm{m}$ at a power of $P_0 = 7.5\,\mathrm{W}$. In this cODT we find a $1/e$ lifetime of a few seconds. The overall geometric mean trapping frequency $\bar{\omega} = (\omega_x\omega_y\omega_z)^{1/3} \simeq 2\pi \times 282(3)\,\mathrm{Hz}$ is useful to define the classical phase space density (PSD) [528, 568]

$$\mathrm{PSD_c} = N\frac{(\hbar\bar{\omega})^3}{(k_\mathrm{B}T)^3}. \tag{5.5}$$

This PSD is connected to the peak density $n_0 \simeq \mathrm{PSD_c}/\lambda_T^3$ and the simple measure $N/x_\mathrm{th}^6 \propto \mathrm{PSD_c}$ for estimating the in-situ PSD from time of flight images containing atomic clouds with thermal spatial widths x_th[30].

5.5.2. Evaporative cooling and Bose-Einstein condensation

To achieve a BEC with the new experimental setup we first choose a single exponential ramp $P(t) = P_0\exp(-\Gamma t)$ of both ODT powers simultaneously starting from $P_0 = 7.5\,\mathrm{W}$. We first fix the final power to be $P/P_0 = 0.3$ and optimize the evaporation duration, finding an optimum of $t_\mathrm{evap} = 8\,\mathrm{s}$ ($\Gamma \simeq 0.15\,\mathrm{s}^{-1}$). Next we vary the final power P/P_0 while keeping this evaporation time t_evap fixed (Fig. 5.7). Overall this optimization could be improved by varying both the rate and the final power. As P/P_0 approaches 0.1 we observe a drastic decrease in atomic cloud width while the atom number decreases at a slower rate (Fig. 5.7(a)-(b)). The temperature $T = (M/2)\bar{\omega}_{x,y}^2 x_\mathrm{th}^2/(1+\bar{\omega}_{x,y}^2 t^2)$ (Fig. 5.7(c)) is calculated

[30] The width $x_\mathrm{th} = \sqrt{2}\sigma$ is related to the variance σ of a normalized Gaussian distribution $\exp(-x^2/2\sigma^2)/\sqrt{2\pi\sigma^2}$.

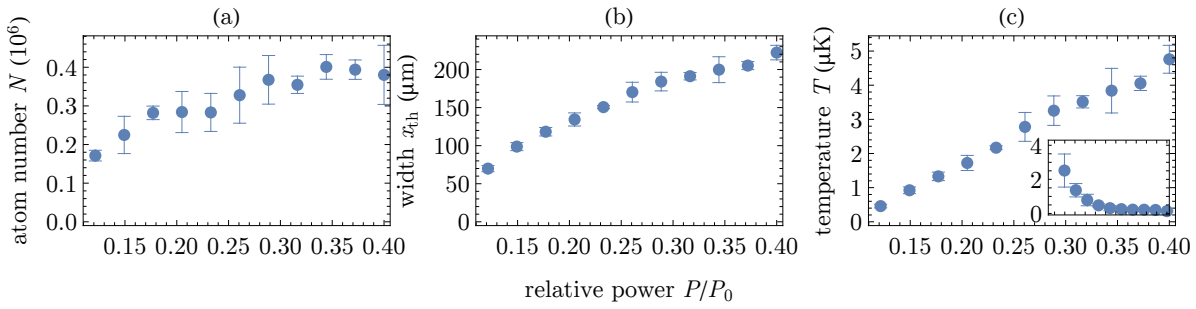

Figure 5.7.: **Evaporative cooling.** (a) Atom number, (b) Gaussian width, and (c) temperature along the evaporation to different ODT powers P relative to $P_0 = 7.5\,\mathrm{W}$ after 10 ms time of flight. The inset in (c) shows $100 \times \mathrm{PSD_c}$ as a function of P/P_0 (see main text). Error bars indicate the standard deviation of four experiment repetitions.

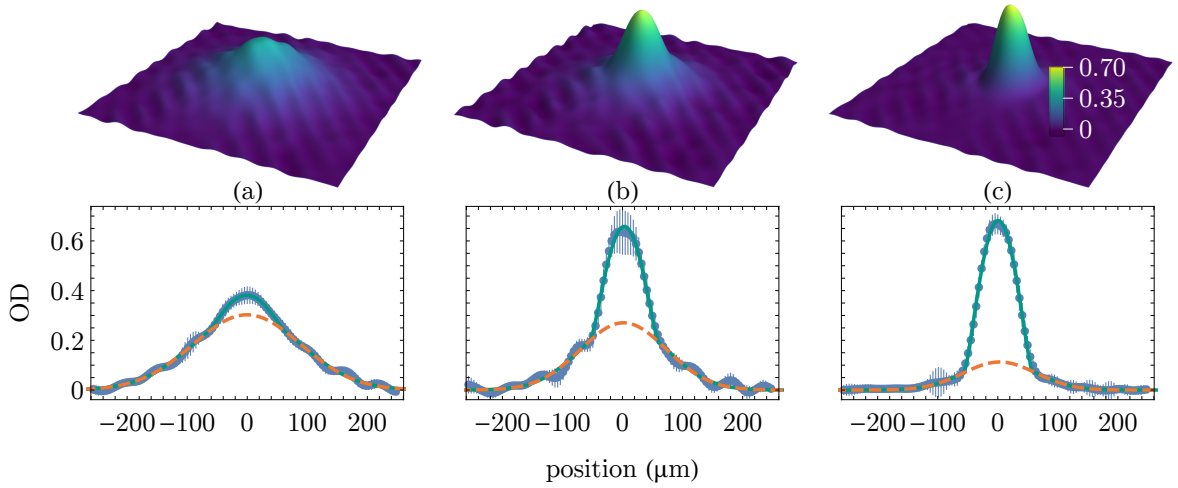

Figure 5.8.: **Bose-Einstein condensation.** Optical density (OD) distributions after 20 ms time of flight in a field of view of $250 \times 250\,\mu\mathrm{m}^2$ (top row) and one-dimensional cuts through the center (bottom row) for final relative powers $P/P_0 = (0.115, 0.105, 0.095)$ in (a), (b), (c), respectively. The OD is averaged over four single shots and error bars in the bottom row show the standard deviation. The bottom row shows the emergence of a bimodal density distribution where the orange dashed line is the thermal component and the green line is the sum of thermal and condensate components. The estimated condensate fractions are $\simeq (8, 35, 69)\,\%$ from left to right. Systematic errors are discussed in the main text.

from (b) assuming ballistic expansion during $t = 10\,\mathrm{ms}$ time of flight [155, 570, 571]. The associated $\mathrm{PSD_c} \propto N/x_{\mathrm{th}}^6$ increases by a factor of 20, reaching values $\simeq 2.5 \times 10^{-2}$, and the temperature drops below 500 nK. The temperature (PSD) is likely overestimated (significantly underestimated) systematically due to the temporary imaging setup.

To investigate the regime near $P/P_0 \simeq 0.1$ more closely we increase the time of flight to 20 ms such that the atomic clouds expand longer and their thermal wings are larger in the images. At relative powers $P/P_0 \simeq 0.115$ and below we observe the emergence of a bimodal density distribution (Fig. 5.8), characteristic of Bose-Einstein condensation [112, 113, 116, 117]. A sum of a Gaussian and a column-integrated inverted parabolic function is fit to the data. The functions account for the thermal component and the BEC component in the Thomas-Fermi limit, respectively [112, 113, 116, 117]. The range for the thermal component fit is limited to the outer wings and bosonic enhancement is neglected [155, 572]. Total atom numbers $N \simeq [186(6), 128(21), 58(1)] \times 10^3$ and temperatures $T \simeq [388(17), 245(17), 177(10)]$ nK are obtained in Fig. 5.8(a)-(c). Theoretically the standard BEC transition temperature with $N \simeq 130 \times 10^3$ atoms and trapping frequencies $\omega_{x,y,z}/2\pi \simeq 80 \times (1, 1, \sqrt{2})$ Hz at a power of $P/P_0 \simeq 0.1$ is expected to be $T_c \simeq 209$ nK[31] [183, 185]. Assuming either a thermal fit range that differs by ± 5 µm or a broadening effect of 10 % of the density distribution due to the imaging setup is sufficient for a good agreement between the theoretical expectation $N_0/N = 1 - (T/T_c)^3$ and the temperatures and condensate fractions N_0/N determined experimentally in (b)-(c). The PSDs in (b)-(c) are consistent with $\simeq 0.9$ corresponding to peak densities on the order of $n_0 \simeq 1/\lambda_T^3 \simeq 0.5 \times 10^{20}\,\mathrm{m}^{-3}$ which is typical for dipolar BECs [113].

5.5.3. Machine learning Bose-Einstein condensation

In the last section we obtained a BEC using a single exponential ramp from $P_0 = 7.5$ W to $0.1P_0$ in 8 s, optimized by ourselves. This section serves as a proof of principle that machine learning techniques as set up with the new experimental control software allow to improve experimental parameters live in our lab without human intervention.

To test the efficiency of the machine learning capabilities of the new control we choose here three consecutive exponential ramps for evaporative cooling. The evaporation rates Γ_j ($j = 1, 2, 3$) are optimization parameters while we constrain the powers to begin at $0.8P_0$ and to be $P_j/P_0 = (0.5, 0.2, 0.1)$ after step j. The rates Γ_j are each constrained between 0.12–0.73 s^{-1} which constrains the total evaporation time between 2.8–17.0 s. The time τ_j for power P_j to be ramped exponentially down to power P_k is related to the rate Γ_j via $\tau_j = \ln(P_j/P_k)/\Gamma_j$. By ending evaporation at a power of $P_3/P_0 = 0.1$ we know that the

[31] Finite size and interaction corrections to T_c [185] amount in total to $\simeq -13\%$ at $a_s = a_{\mathrm{bg}} \simeq 140(20)\,a_0$ [138] for our present parameters.

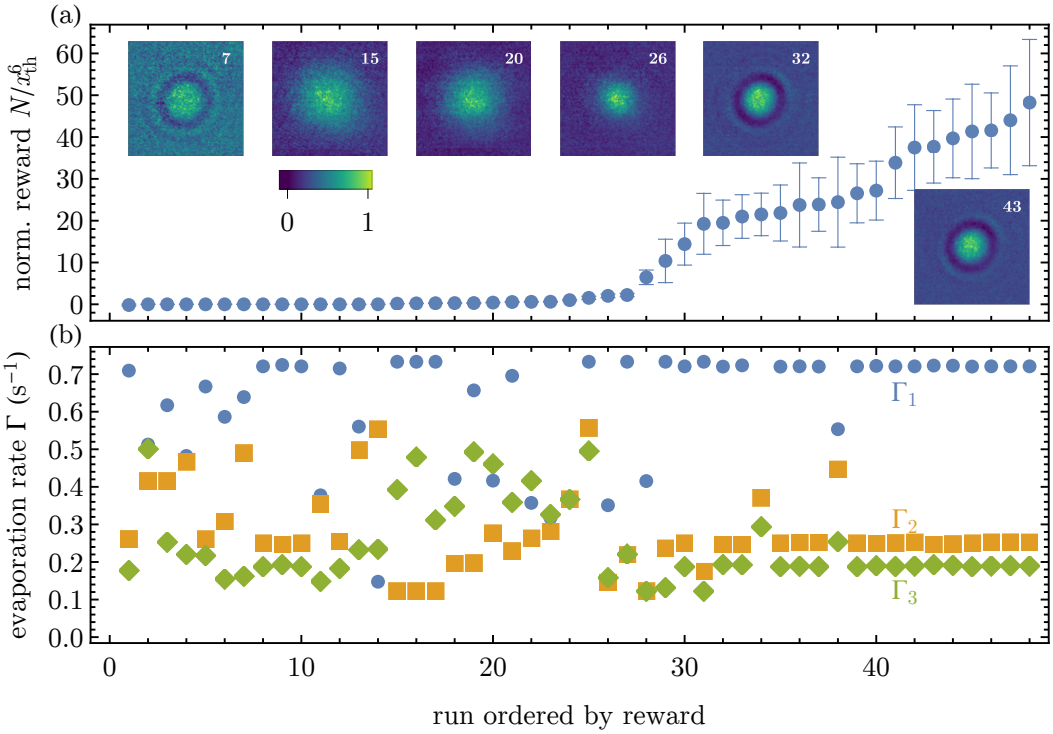

Figure 5.9.: **Machine learning of evaporative cooling.** (a) Reward $N/x_{\mathrm{th}}^6 \propto \mathrm{PSD_c}$ as a function of the reward-ordered run index. Insets show the single-shot normalized in-situ optical density in a field of view of $50 \times 50\,\mu\mathrm{m}^2$ for the run indices denoted in the top right. Rewards are normalized to the reward of the starting parameters (ordered run index 24) corresponding to a thermal gas and error bars show the propagated error from the standard error of the Gaussian fit parameters used to determine N and x_{th}. The machine finds sequences suitable for the generation of BECs (run $\gtrsim 30$) despite failed fits at similar parameters (e.g. run seven, see inset) and the optimal parameters correspond to a fast initial ramp followed by two slow and smooth ramps (see main text). (b) Optimization parameters (Γ_1, Γ_2, Γ_3) (blue circles, orange squares, green diamonds) as a function of the reward-ordered run index.

final trapping potential is roughly the same as in our manually optimized experiment and that finding suitable combinations of rates should be sufficient for the machine to obtain BECs.

To set up the optimization we use a Gaussian process alternating with a single differential evolution step if no better parameters are found for four consecutive Gaussian process runs[32]. For our purpose a Gaussian process [573] is an optimization method trading off convergence time with noise resilience [547, 574]. The single differential evolution step serves to interrupt the stagnation of the Gaussian process with a random selection of

[32] In the `analysislib_mloop` setup file the parameter `max_num_runs_without_better_params` = 4.

optimization parameters. We define the reward as N/x_{th}^6, which is proportional to $\mathrm{PSD_c}$ and can be evaluated for every single shot. The optimization goal is to maximize the reward[33]. We run 50 single experimental shots with this machine learning setup starting with $\Gamma_j = 0.3\,\mathrm{s}^{-1}$ for all j, corresponding to a thermal gas. Figure 5.9 shows the rewards and the optimization parameters for the entire run in the order of increasing reward.

During the optimization the machine discovers evaporation sequences reaching BECs (run $\gtrsim 30$). At about run 30 there is a characteristic increase in PSD by an order of magnitude and the density profile changes qualitatively to that observed with our manual BEC evaporation sequence. The optimal parameters Γ_j^{opt} found by the machine for the highest PSDs have interesting properties. $\Gamma_1^{\mathrm{opt}} \simeq 0.73\,\mathrm{s}^{-1} \gg \Gamma_{2,3}^{\mathrm{opt}}$ corresponds to a fast evaporation near the upper constraint for Γ_j followed by two slow evaporation steps $\left(\Gamma_2^{\mathrm{opt}}, \Gamma_3^{\mathrm{opt}}\right) = (0.25,\, 0.19)\,\mathrm{s}^{-1}$. Not only do the precise value of all evaporation rates lead to a total evaporation time of 7.95 s similar to our manually optimized evaporation time but the values for $\left(\Gamma_2^{\mathrm{opt}}, \Gamma_3^{\mathrm{opt}}\right)$ lead to a minimal discontinuity of $\partial_t P(t)$ at the interface between ramps two and three. Discontinuities in $\partial_t P(t)$ far into the evaporation sequence can heat the atomic sample and lead to a reduction in PSD. The rates give two ramps of nearly equal duration 3.65(1) s that combine smoothly to a single ramp matching at their interface both P as constrained by us and $\partial_t P$ as found by the machine to be beneficial for the PSD.

Failed fits (run seven and several others up to run 13 in Fig. 5.9) due to image noise at parameters near an efficient evaporation sequence could have prevented the machine from exploring efficient parameters further. A high number of failed fits during a run are detrimental for the convergence over time since they force the machine to explore other parameters although the best ones might have been found already. The combination of the Gaussian process and differential evolution prevented the machine to learn (conclude) that shots like seven correspond to an inefficient evaporation and allowed the machine to explore an efficient regime for a substantial amount of the total runs (runs $\gtrsim 26$). Due to the change in imaging setups that occurred during our characterization of the BEC production (section 5.5.2) and the machine learning characterization we cannot quantitatively compare the BECs reached between the two approaches.

Our proof of principle demonstration in this section can be extended and improved in several ways. By improving the laser stability and the lab environmental conditions,

[33] In optimization the objective function is known as reward (cost) if the goal is to maximize (minimize) the function.

especially the lab temperature, the number of single shot noisy images can be reduced. Typical reasons for noisy images are slight laser power fluctuations near the moment the image is taken and laser lock stability limitations. The `analysislib-mloop` script defining the machine learning setup was used as a single-shot routine in `lyse`, accessing only one shot for the objective function evaluation. By setting it as a multi-shot routine, averages of the objective function over several shots can be used. Both these improvements benefit the convergence of the optimization over time. To optimize BECs for atom number and temperature, a separate objective function definition can be helpful [528]. For the evaporation, more steps and parameters can be included and other controllers, including the neural net, could yield improved evaporation sequences [528]. More generally the machine learning capabilities could be applied to other stages of the experiment. For example optimizing the MOT or cMOT sequences before the ODT loading could yield higher atom numbers in the cMOT or better mode matching to the ODTs and therefore better starting conditions for high atom number BECs.

5.5.4. Conclusion and outlook

In this section we demonstrated the first production of a ^{162}Dy BEC using our new machine. Despite the very simple single evaporation ramp for the production of this BEC we could achieve atom numbers that are already competitive with good conditions of the previous experimental setup [152, 246]. At multiple stages of the way towards this first BEC we pointed out possible improvements of the experimental conditions that will clearly benefit the achievable atom numbers of this experiment going forward. Our new experimental control software offers several improvements over previous controls including a live control of the experiment, monitoring of environmental conditions, the ability to abstract and programmatically change experiment sequence-generating code, and we have implemented a closed-loop interface for the experiment enabling automatic optimization of experimental parameters through several feedback controllers from classical optimization to machine learning based algorithms. The machine learning capabilities of the new control were demonstrated by letting the experiment optimize a more complex evaporation sequence which, given loose constraints, yielded BECs in the absence of human intervention. In the future it will be interesting to probe the highest density regimes achievable with this experiment setup and compare with the theoretically predicted phase diagram of oblate quantum ferrofluids [3, 302]. With additional control over the optical trapping potential

as provided by a digital micromirror device whose implementation is currently underway, investigations of the so-far experimentally unexplored Higgs amplitude mode of trapped dipolar supersolid droplets [7] and the behavior of supersolids in toroidal traps will be possible [1, 345]. Cold atomic clouds from compressed magneto-optical traps or BECs in optical dipole traps are also the basis for the transport to the microscope chamber in the future.

"Life is like riding a bicycle. To keep your balance, you must keep moving."

– Albert Einstein

Chapter 6

Conclusion and Outlook

This thesis investigates self-organized structures and excitations of dipolar quantum fluids and presents the implementation of a new dysprosium quantum gas experimental setup, paving the way for future studies of new quantum phases in dipolar quantum fluids. The results of this thesis are presented in three parts spanning chapters 3-5. We briefly summarize the results, draw conclusive insights, and outline future prospects following a similar structure.

One-dimensional structures

The starting point of this thesis is the first dipolar supersolid of dipolar quantum droplets in a tubular trap [9, 96, 97]. We realize this state with dysprosium Bose-Einstein condensates in a narrow interaction range, where the interplay of interactions combined with quantum fluctuations lead to a stable droplet crystal structure immersed in a superfluid background [6].

We observe experimentally that the structure formation is driven by low-energy roton excitations [5]. Comparison with our numerical simulations shows that these are two degenerate roton modes which split up into the low-energy Goldstone mode and Higgs amplitude mode, associated to the translational symmetry breaking of the supersolid [7, 8]. Through in situ observation of the density fluctuations, we demonstrate that the overall density fluctuation strength is thermally enhanced. Moreover we identify that the supersolid is characterized by the simultaneous presence of crystal and superfluid phonon modes. Our analysis indicates that these phonon modes mix with other modes in tubular harmonic traps due to coupling between collective excitations and center of mass motion. Additionally the phonons couple to the Higgs amplitude mode due to a symmetry

limitation of low-energy elementary excitations in tubular traps.

In collaboration with S. Reimann's group [1] we investigate a toroidal trap, where the superfluid is initially uniform along the azimuthal direction and a center of mass is absent. With varying interactions the toroidal superfluid undergoes a quantum phase transition to a droplet supersolid, where Goldstone phonons and Higgs amplitude modes appear in a decoupled form. The decoupling allows a clearer observation of the connections to elementary excitations that are predicted for infinitely extended supersolids. We identify that the supersolid excitation spectrum is characterized by three distinct branches, including two Goldstone phonons and a Higgs amplitude mode. The amplitude mode exists in a decoupled form since the toroidal trap provides with every droplet a new symmetry to which the low-energy excitations belong, while the lowest energy Higgs amplitude mode belongs to and remains in a distinct symmetry. One Goldstone phonon originates from the superfluid phonon prior to the phase transition. In the supersolid phase, it manifests as an in-phase oscillation between the superfluid background and the crystal structure. The second Goldstone phonon originates from one of two low-energy roton excitations (the other becoming the Higgs amplitude mode) and presents in the supersolid an out-of-phase oscillation between the superfluid background and the crystal structure, allowing this phonon to remain at lower energy than the first Goldstone mode. Together these two phonons are shown to have remote analogies to the first and second sound in superfluid helium at finite temperature. Our characterization of Goldstone phonons and Higgs amplitude modes based on their symmetry allows us to devise experimental protocols for selectively exciting individual collective modes, setting the stage for observations of Goldstone and Higgs amplitude modes in experimentally feasible systems.

Two-dimensional structures

Our experimental investigations of density fluctuations in oblate trapped dipolar quantum fluids reveals that the crystallization mechanism is driven by angular roton modes [4]. The structure formation mechanism is analogous to the one in tubular traps with the lowest-lying roton modes contributing most of the density fluctuations at the transition point. The competition between several angular roton modes of different symmetry and a limited atom number in our experiments leads to a competition of crystal structures with different droplet numbers.

Theoretically we show that tighter traps and higher atom numbers are favorable for

obtaining a droplet crystal immersed in a superfluid background with a substantial density overlap between the droplets [2]. The density overlap was shown to stabilize the phase of the droplet array when tuning the interactions dynamically from the superfluid into the supersolid regime. Analogous to the rotationally symmetric toroidal trap the lowest angular roton modes split up into a low-energy Goldstone phonon and a Higgs amplitude mode. In the oblate harmonic trap, these modes couple to other modes due to the presence of center of mass motion, similar to the tubular trap system. The parameters favorable for supersolidity were further discussed based on the scaling properties of the extended Gross-Pitaevskii theory. Evidence for supersolids with two-dimensional crystal structures has since been reported by the Innsbruck team [403, 410].

Our investigation of the phase diagram in these oblate traps towards higher atom numbers demonstrates that supersolid honeycomb and amorphous labyrinth phases form beyond the supersolid droplet phase [3]. The change is in the phase diagram is characterized by a density saturation in the ground states or low-energy metastable states. An increasingly dominant role of the quantum fluctuations allows for a decreasing repulsive interaction strength with the same effective stabilization in the density saturated regime. The honeycomb phase represents a novel type of supersolid and the labyrinth phase is characterized by multiple near-degenerate metastable amorphous patterns, reminiscent of characteristics found in glasses [78, 480, 492]. Superfluid flow is possible through a honeycomb density pattern, which was shown to have a very high superfluid fraction in an extended study of this new phase by A. Gallemí and L. Santos [466]. The self-organization of a superfluid in an amorphous density pattern suggests that the labyrinth is a candidate for a superglass [78, 480, 492, 575]. We show that the stability of the patterns depends on the trap aspect ratio and that the characteristic length scale of the patterns scales like the roton momentum in the quasi 2D regime. The ability of the dipolar BEC to form various patterns in equilibrium and the controllability of the pattern formation with interaction strength, density, and trapping geometry suggests this system as a model for self-organized equilibrium in weakly interacting quantum many-body systems.

New experimental setup

Simultaneous to the investigations of self-organized one-dimensional and two-dimensional structures and excitations of dipolar quantum fluids, we design and construct a new experimental setup for dysprosium. The design of the new setup allows to form both

magneto-optical traps and Bose-Einstein condensates in the same experimental chamber. An unconventional five-beam magneto-optical trap [518] exploiting the high mass of dysprosium atoms and narrow linewidth of the trapping light allows to implement a high-resolution objective from the missing sixth beam direction along gravity. We devise a new experimental control software based on the open-source software `labscript` [524]. Extending an interface between this software and a real-time controller initially developed by J. Schabbauer in J. Léonard's group [532] and integrating it into a network of processes that automatically analyzes images of magneto-optical traps and Bose-Einstein condensates, we establish a flexible and modern approach for experimental control of dipolar quantum fluids. The control software allows to use live and automatic feedback to the experiment from measured quantities. We realize this functionality by implementing a machine learning package for optimizing experimental parameters [546–548]. Using this experimental control we achieve the first ^{162}Dy Bose-Einstein condensate with the new setup. We also show that the machine learning capabilities are ready for further optimization of the experiment by letting the machine optimize a cooling sequence under loose constraints, realizing a Bose-Einstein condensate in the absence of human intervention.

Outlook

The Higgs amplitude mode of dipolar supersolids [1, 2, 7] has not been experimentally observed to this day. This Higgs amplitude mode is stabilized by the absence of modes with the same symmetry which allows for the stability within a narrow range of interaction strengths in harmonic traps and within a wider range in toroidal traps. Finding experimental evidence for the Higgs mode would allow to complete the picture of the excitation spectrum of trapped dipolar supersolids together with the so-far observed Goldstone [8], higher compressional [148, 371, 576], and roton [4, 5, 125] excitations. Work towards the experimental realization of toroidal traps for dipolar supersolids is already underway [345, 346]. In the future, it would be interesting to study whether the stabilization of the Higgs amplitude mode can be achieved with a fundamentally different mechanism. The Higgs mode in the superfluid to Mott insulator transition [167, 168, 173, 577] and in supersolids in crossed optical cavities [170, 578] is stable due to the effective particle-hole symmetry in these systems. The tricritical point, where the droplet supersolid and honeycomb supersolid become degenerate in infinite oblate dipolar quantum fluids [3, 238, 302] could potentially have a significant role for the stabilization of the Higgs amplitude mode. Given that the

energy functional becomes symmetric with respect to the density wave amplitude which gives rise to the droplet or honeycomb (”particle“ or ”hole“) solutions one can speculate that the Higgs quasiparticle is particularly stable in the vicinity of this region in the phase diagram.

Finite temperature investigations as a whole are interesting extensions of the work presented in this thesis. We saw that the density fluctuation strength at the superfluid to supersolid phase transition is thermally enhanced [5] and the Innsbruck team showed that finite temperature results in a shift of the critical scattering length, allowing to drive the crystallization counter-intuitively by heating the superfluid [316]. Furthermore cooling into the supersolid regime was used to retain phase coherence for two-dimensional supersolids [402, 403] and the decoupled Goldstone phonons in the toroidal trap showed behavior remotely analogous to first and second sound in helium at finite temperature [1]. These are several indications of the importance of finite temperature effects in dipolar supersolids. The thermodynamics of these supersolids has so far not been studied in depth. With concrete proposals suggesting a finite temperature extension of the extended Gross-Pitaevskii theory [315–317], investigating the supersolid thermodynamics is a major topic for a deeper understanding of the supersolid phase.

As we have outlined at the end of section 2.5, the self-organized honeycomb and labyrinth structures are interesting for future studies of dipolar quantum fluids since they challenge fundamentally the state-of-the-art of the numerical and theoretical framework, and necessitate experiments capable of reaching the high-density regimes. We believe realizing these regimes will be crucial for a further development in the description of dipolar quantum fluids. Mapping out the phase diagram experimentally would allow to probe the validity of the quantum fluctuation correction as included in the extended Gross-Pitaevskii theory in new regimes [138, 227]. It is theoretically interesting to investigate what the minimal conditions for the structure formation are [276, 284]. The honeycomb and labyrinth patterns can also be seen in classical reaction-diffusion systems [274] and similar models that do not feature an anisotropic interaction. Exploring these minimal conditions could help classifying the complexity of dipolar Bose-Einstein condensates in terms of their suitability as model systems. It could also help determine whether realistic, potentially simpler, and more controllable quantum systems possess similar self-organization capabilities. A milestone achievement in S. Will’s group with the observation of Bose-Einstein condensation of dipolar molecules [247] was reported right at the end of this thesis. These dipolar molecules allow for tunable dipolar lengths [246] and for absolute values of the dipolar interaction

strength several orders of magnitude higher than in atomic Bose-Einstein condensates. As outlined in section 2.4.3, this enhancement in the dipolar lengths can be rescaled into effective parameters, enabling the realization of the effective high-density regimes at much lower atom numbers, densities, and in looser traps compared to atomic Bose-Einstein condensates [3, 246].

Lastly our new experimental setup holds the potential to address the above-mentioned avenues for physics with dipolar quantum fluids. The experimental control is equipped with a flexible programmable interface for the generation of experimental sequences and allows for direct feedback from measurements. The machine learning package, alongside other optimization algorithms that can be easily integrated into the new experimental control, allows for the optimization of experimental parameters. Using computer assistance in this way, quantum fluids with higher atom numbers or shorter production times will allow for a more efficient exploration of the self-organized phases presented in this thesis. Furthermore the experimental setup in its current state is the foundation for incorporating an additional vacuum chamber and deploy a quantum gas microscope for studying extended Hubbard physics [51, 326].

Appendix

A. A new numerical toolbox

The starting point for the numerical toolbox developed during the course of this thesis is a code initially provided by M. Wenzel [197] which was used, modified, and described more in depth in our previous work [205]. This code solves the eGPE dynamics using the finite difference Cranck-Nicolson method [579] in real and imaginary time. The code is based on `C/C++`. An initial version to solve the BdG equations was also developed by M. Wenzel, which was `matlab`-based and separate from the `C/C++` code. The matlab code uses a split-step Fourier method with Lie splitting to solve for the ground state in imaginary time and did not have the capability to simulate specific real-time dynamic simulations of the eGPE.

From this starting point we experimented with different programming languages and algorithms with the goal of achieving better computational performance, a unified code base, and to be able to share it more easily and teach how to use the code for other members in our team. First we implemented a BdG solver in `C/C++` based on `spectra` [580], which is a linear algebra library implementing among others matrix-free eigenvalue solvers similar to the `arpack` library that `matlab` relies on. The solution of the BdG equations in `C/C++` and `matlab` were comparable in speed and give identical results for simulations of BECs. For quantum droplets we found the convergence using the `spectra` package slower as compared to the `matlab` implementation. We implemented a split step method for imaginary time evolution additionally in `mathematica` and `julia`. The best performance among all codes including the `C/C++` version was achieved in the `matlab` implementation. The increased speed could be traced to the lowest time of the discrete Fourier transforms in the `matlab` implementation. The split step method relies heavily on discrete Fourier transforms and takes advantage of the `fft` implementation in `matlab` which by default uses multithreading. Matrix operations in the `C/C++` code were based on a custom class which was not highly optimized and performance could likely be gained by using a specialized matrix operation library like `eigen` [581]. We expect that the `C/C++` code with a more efficient implementation could provide similar or improved performance compared to the `matlab` implementation. `julia` is a relatively new programming language that ought to combine speed comparable to `C/C++` code and convenience comparable to `matlab` or `python` code due to its design based on multiple dispatch [582]. Due to the

convenience of having other numerical functions in the `matlab` suite directly connected to the numerical simulations and the advantageous performance outright we decided to develop the code in `matlab` further.

B. Principal component analysis

This appendix introduces the basic idea of principal component analyis (PCA). Our discussion closely follows the thesis [153] having introduced the most important concepts related to the BdG solutions and our previous work [7, 205]. For detailed information about PCA we refer to the book [583].

PCA is a model-free statistical analysis method to extract information of large or noisy datasets by representing the main variance in these datasets with a few uncorrelated variables, known as principal components (PCs). The technique was developed originally by Pearson [584] and Hotelling [585]. In ultracold atom experiments PCA has been used to filter noise [586], to identify the largest noise sources [587], to map out the critical trap aspect ratio in the formation of dipolar quantum droplets [282], and to measure collective excitations [5, 148, 372]. To probe angular oscillations of dipolar supersolids a PCA-related method was proposed [410]. In the following our main goal is to establish a connection between PCA and BdG theory.

We consider a set of $\tilde{N}$ images where each image contains p pixels. We write the individual images as a vector $\boldsymbol{X}_i$, with the pixel values of each image i as components and obtain the mean image

$$\boldsymbol{M} = \frac{1}{\tilde{N}} \sum_j \boldsymbol{X}_j. \tag{B1}$$

We subtract the mean from the images and define a new $p \times \tilde{N}$ matrix

$$\boldsymbol{B} = [\boldsymbol{X}_1 - \boldsymbol{M}, \ldots, \boldsymbol{X}_{\tilde{N}} - \boldsymbol{M}] \tag{B2}$$

and the covariance matrix

$$\boldsymbol{C}_{\boldsymbol{B},\boldsymbol{B}} = \mathrm{cov}\,(\boldsymbol{B}, \boldsymbol{B}) = \frac{1}{\tilde{N}-1} \boldsymbol{B}\boldsymbol{B}^{\mathrm{T}}. \tag{B3}$$

This $p \times p$ matrix is in general quite large and it is costly to diagonalize directly [372]. The ability to use PCA for reducing dimensionality in the data lies in the observation that the

rank of $\boldsymbol{C}_{\boldsymbol{B},\boldsymbol{B}}$ is at most $\tilde{N}$ and it has the same spectrum as a $\tilde{N} \times \tilde{N}$ matrix [372, 586]. PCA diagonalizes the covariance matrix $\boldsymbol{C}_{\boldsymbol{B},\boldsymbol{B}}$ yielding a set of eigenvectors $\hat{\boldsymbol{X}}_j$, the PCs, and eigenvalues λ_j. This is in general computationally expensive but in PCA, a subset of the eigenvectors of the full spectrum sorted by largest variance is obtained using iterative methods [372]. Then the initial images can be represented as a linear combination of the new ortho-normal eigenvectors $\boldsymbol{X}_i = \boldsymbol{M} + \sum_j \alpha_j \hat{\boldsymbol{X}}_j$, with the respective weights α_j of each PC. The weights are obtained by projecting the centered image onto the corresponding PC [372] and are related to the $\tilde{N} \times \tilde{N}$ matrix with a linear transformation [586]. Since the PCs are sorted by variance in practice a small set of PCs is sufficient to represent most of the variance in the dataset and higher PCs play a negligible role [153, 205, 372, 586]. This way PCA is used for dimensionality reduction in datasets.

We show in the following that PCA is directly related to the density fluctuations obtained by the BdG equations [372]. Using a hydrodynamic model [232] or the linearized time evolution with the BdG density fluctuation (2.47) with multiple modes excited one can write

$$n(\boldsymbol{r}, t) = n_0(\boldsymbol{r}) + \sum_j c_j \delta n_j(\boldsymbol{r}) \cos(\omega_j t + \phi_j) \tag{B4}$$

for the density time evolution where δn_j is the j-th normal mode or BdG density fluctuation pattern [372] with frequency ω_j and phase ϕ_j. Analyzing time series or discrete shots in either experiment or numerical simulations of the time evolution, one observes discrete positions $\boldsymbol{r}_{i,j}$ and times $t_{i,j}$. Further including a contribution $\Delta(\boldsymbol{r}_i, \boldsymbol{r}_j)$ due to technical noise in the preparation and the imaging of the atomic cloud for experimental data, we can write the entries of the covariance matrix as [372]

$$C_{i,j} = \frac{N}{2(N-1)} \sum_k c_k^2 \delta n_k(\boldsymbol{r}_i) \delta n_k(\boldsymbol{r}_j) + \Delta(\boldsymbol{r}_i, \boldsymbol{r}_j). \tag{B5}$$

Provided the noise covariance $\Delta(\boldsymbol{r}_i, \boldsymbol{r}_j)$ between pixels i and j is small, it can be shown that the functions $\delta n_k(\boldsymbol{r})$ are the eigenvectors or PCs with eigenvalue $\sim c_k^2/2$ [372]. These relations establish a direct connection between the PCs of a dataset in which the fluctuations either over time or over multiple averages correspond to BdG excitations.

Standard implementations of PCA are available in data analysis packages of nearly all programming languages, with which the PCs and their weights are readily obtained. In this thesis we have used the `pca` function of `matlab` for the results presented in section 3.2

and we implemented in our previous work [205] a `mathematica` [588] program, that uses the `KarhunenLoeveDecomposition` [589] as a generalization of the `PrincipalComponents` [590] function, which we used in section 3.3.

C. Group theory

This appendix provides additional details on the group $C_{n_d,v}$, describing the modes of a supersolid with n_d droplets in a cylindrically symmetric trap. Our discussion concerning groups closely follows standard group theory texts [411], to which the interested reader is referred for further information and the discussions in the following sections follow Ref. [1].

Symmetries of seven droplets in a toroidal trap and comparison to harmonically trapped droplets

Before we state the general compatibility assignment between superfluid and supersolid modes starting from cylindrically symmetric superfluids, we focus in this section on the specific case of seven droplets in a toroidal trap. Starting with this example, we can introduce the notions of the symmetries, irreducible representations and character tables involved in the following section.

Consider a $n_d = 7$ droplet supersolid ground state in a toroidal trap. The ground state symmetries are described by the point group $C_{7,v}$. The character table of the group $C_{7,v}$ is reproduced in Tab. Eq. (C.1), where classes are arranged along the columns, irreducible representations along the rows and the body of the table shows their character.

The ground state is symmetric with respect to the identity (E), rotation (C_7) around $\pm 2\pi/7$, rotation (C_7^2) around $\pm 4\pi/7$, rotation (C_7^3) around $\pm 6\pi/7$ around the z-axis, and reflection (σ_v) through the seven vertical planes intersecting the z-axis and the droplets. These five types of symmetries divide the group $C_{7,v}$ into the five classes E, $2C_7$, $2C_7^2$, $2C_7^3$, $7\sigma_v$ yielding five irreducible representations A_1, A_2, E_1, E_2, and E_3 [411]. A_i and E_i are one-dimensional and two-dimensional irreducible representations, respectively. The notations used for the symmetries and irreducible representations are known as Schoenflies and Mulliken symbols, respectively.

To get an intuition on the symmetries compatible with each of the irreducible representations, we consider the example basis functions given in Tab. C.1. Modes compatible with A_1 transform as z – symmetric with respect to all rotations and reflections in the group.

Table C.1: Character table for the group $C_{7,v}$. The irrotational character values are $\chi_n = 2\cos(2\pi n/7)$.

$C_{7,v}$	E	$2C_7$	$2C_7^2$	$2C_7^3$	$7\sigma_v$	example basis
A_1	1	1	1	1	1	z
A_2	1	1	1	1	-1	R_z
E_1	2	χ_1	χ_2	χ_3	0	$\{x, y\}$
E_2	2	χ_2	χ_3	χ_1	0	$\{x^2 - y^2, xy\}$
E_3	2	χ_3	χ_1	χ_2	0	$\{x(x^2 - 3y^2), y(3x^2 - y^2)\}$

Modes compatible with A_2 transform as R_z (rotation around the z-axis) – antisymmetric with respect to $7\sigma_v$ and symmetric otherwise. The $m = 7$ angular roton modes therefore split into a zero energy Goldstone mode compatible with A_2 and a Higgs amplitude mode compatible with A_1. The two-dimensional representations E_i share the same symmetry with the $m = i$ angular roton modes. For example, modes compatible with E_1 are either antisymmetric with respect to x or y, exactly like the two degenerate $m = 1$ angular roton modes. This identification allows generally, to think of the $m = i$ angular roton modes as basis functions, representing the symmetry of modes compatible with E_i. E in $C_{3,v}$ and $C_{4,v}$ transforms just as E_1 in the point groups of higher symmetry.

A different special case for three droplets is discussed in our publication [2] considering the cylindrically symmetric case of a two-dimensional supersolid in a harmonic trap (section 4.2).

The large number of symmetries in a toroidal trap, growing with the droplet number, can be contrasted with the situation in tubular traps [7, 8, 148]. In these traps, the low-energy supersolid excitations are found to be either symmetric or antisymmetric with respect to the center of the trap. This symmetry corresponds to the group $C_{1,v}$ (which is identical to C_s and isomorphic to C_2 and the symmetric group S_2). Modes for a ground state with $C_{1,v}$ symmetry are either symmetric and compatible to A_1 or antisymmetric and compatible to A_2.

Cylindrically symmetric superfluid to supersolid mode compatibility

When a cylindrically symmetric superfluid transitions to a supersolid phase with n_d droplets, driven by angular roton modes with circulation number $m = n_d$, the continuous rotational symmetry $C_{\infty,v} \to C_{n_d,v}$ is spontaneously broken.

Table. C.2 shows the compatibility between $m-$angular roton modes and irreducible representation across every point group (up to $m = n_d = 13$). The table is obtained by considering that modes compatible with E_i transform as $m = i$ angular roton modes. The periodicity in the pattern in Tab. C.2 has a physical interpretation. When the symmetry is broken $C_{\infty,v} \to C_{n_d,v}$ momenta that were continuously increasing corresponding to the angular roton modes with m up to ∞ can be folded back to the first Brillouin zone in which only momenta up to $m = n_d/2$ for even n_d and $m = (n_d - 1)/2$ for odd n_d are available. Therefore angular roton modes are assigned to E_i with increasing i for $i < m/2$, to $B_1 + B_2$ right at the edge of the Brillouin zone $i = m/2$, and to E_i with decreasing i for $i > m/2$. For example in $C_{4,v}$ modes compatible with E transform as $m = 1$ angular roton modes and modes compatible with B_1, B_2 transform as $m = 2$ angular roton modes. Angular roton modes with $m = 1, 3, 5, ...$ remain degenerate (E) and those with $m = 2, 6, 10, ...$ split up into two levels (B_1, B_2).

Table C.2: Compatible irreducible representations between the angular roton modes of the superfluid to elementary excitations of the supersolid with n_d droplets when the rotational symmetry is spontaneously broken $C_{\infty,v} \to C_{n_d,v}$. A section of the full table which continues indefinitely to the right and bottom is shown. The row for the symmetry $C_{7,v}$ of the ground state in the main text is highlighted. The pattern emerging in the body of the table towards higher n_d along the rows continues predictably and has a physical interpretation, see main text.

m ($C_{\infty,v}$)	0	1	2	3	4	5	6
$C_{1,v}$	A_1	$A_1 + A_2$	$A_1 + A_2$	$A_1 + A_2$	$A_1 + A_2$	$A_1 + A_2$	$A_1 + A_2$
$C_{2,v}$	A_1	$B_1 + B_2$	$A_1 + A_2$	$B_1 + B_2$	$A_1 + A_2$	$B_1 + B_2$	$A_1 + A_2$
$C_{3,v}$	A_1	E	E	$A_1 + A_2$	E	E	$A_1 + A_2$
$C_{4,v}$	A_1	E	$B_1 + B_2$	E	$A_1 + A_2$	E	$B_1 + B_2$
$C_{5,v}$	A_1	E_1	E_2	E_2	E_1	$A_1 + A_2$	E_1
$C_{6,v}$	A_1	E_1	E_2	$B_1 + B_2$	E_2	E_1	$A_1 + A_2$
$C_{7,v}$	A_1	E_1	E_2	E_3	E_3	E_2	E_1
$C_{8,v}$	A_1	E_1	E_2	E_3	$B_1 + B_2$	E_3	E_2
$C_{9,v}$	A_1	E_1	E_2	E_3	E_4	E_4	E_3
$C_{10,v}$	A_1	E_1	E_2	E_3	E_4	$B_1 + B_2$	E_4
$C_{11,v}$	A_1	E_1	E_2	E_3	E_4	E_5	E_5
$C_{12,v}$	A_1	E_1	E_2	E_3	E_4	E_5	$B_1 + B_2$
$C_{13,v}$	A_1	E_1	E_2	E_3	E_4	E_5	E_6

Table C.2: (Continuation)

m ($C_{\infty,v}$)	7	8	9	10	11	12	13
$C_{1,v}$	$A_1 + A_2$	$A_1 + A_2$	$A_1 + A_2$	$A_1 + A_2$	$A_1 + A_2$	$A_1 + A_2$	$A_1 + A_2$
$C_{2,v}$	$B_1 + B_2$	$A_1 + A_2$	$B_1 + B_2$	$A_1 + A_2$	$B_1 + B_2$	$A_1 + A_2$	$B_1 + B_2$
$C_{3,v}$	E	E	$A_1 + A_2$	E	E	$A_1 + A_2$	E
$C_{4,v}$	E	$A_1 + A_2$	E	$B_1 + B_2$	E	$A_1 + A_2$	E
$C_{5,v}$	E_2	E_2	E_1	$A_1 + A_2$	E_1	E_2	E_2
$C_{6,v}$	E_1	E_2	$B_1 + B_2$	E_2	E_1	$A_1 + A_2$	E_1
$C_{7,v}$	$A_1 + A_2$	E_1	E_2	E_3	E_3	E_2	E_1
$C_{8,v}$	E_1	$A_1 + A_2$	E_1	E_2	E_3	$B_1 + B_2$	E_3
$C_{9,v}$	E_2	E_1	$A_1 + A_2$	E_1	E_2	E_3	E_4
$C_{10,v}$	E_3	E_2	E_1	$A_1 + A_2$	E_1	E_2	E_3
$C_{11,v}$	E_4	E_3	E_2	E_1	$A_1 + A_2$	E_1	E_2
$C_{12,v}$	E_5	E_4	E_3	E_2	E_1	$A_1 + A_2$	E_1
$C_{13,v}$	E_6	E_5	E_4	E_3	E_2	E_1	$A_1 + A_2$

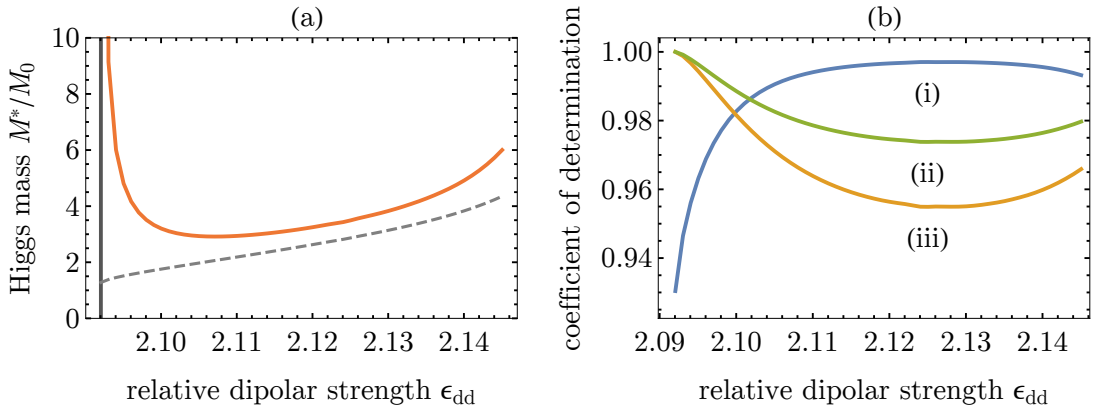

Figure D.1: **Effecitive mass of the Higgs amplitude mode.** (a) Effective mass of the Higgs amplitude mode $M^* = \hbar^2(\partial_{\tilde{q}}^2 E(\tilde{q}))^{-1}$ (full orange line). For comparison we show the mass obtained if one assumes a quadratic behavior for the dispersion relation and obtains the mass with a least squares fit (gray dashed line). The vertical line indicates the transition point. The Higgs mass diverges near the transition point, suggesting a linear dispersion relation in the vicinity of the transition. (b) Coefficient of determination in form of the adjusted R^2 coefficient for a quadratic fit (i), R^2 coefficient for a linear fit (ii), and adjusted R^2 coefficient for a linear fit (iii). Case (iii) is equivalent to the Pearson correlation coefficient, a measure for linear correlation in the dataset [591]. The Higgs dispersion is a near-perfect linear function of $\tilde{q}$ in the vicinity of the transition point. It becomes more quadratic around $\epsilon_{dd} \simeq 2.1$ and towards $\epsilon_{dd} \gtrsim 2.13$ the linear fits rise in quality, suggesting that both linear and quadratic contributions to the dispersion relation are present.

D. Higgs effective mass in a toroidal trap

In previous studies of dipolar supersolids in harmonic traps the linear quasimomentum couples to the COM momentum. As a result the Higgs character of the amplitude mode was only maintained in a narrow range of interaction strengths before coupling to other modes occurs [2, 7]. Due to the absence of the COM in the toroidal traps we are able to distinguish Higgs amplitude modes at several quasimomenta $\tilde{q}_m = 2\pi m/\Theta$ with $m = 0, 1, 2$. The isolation of the Higgs mode over the range we have studied in Fig. 3.11 allows us to define an effective mass $M^* = \hbar^2(\partial_{\tilde{q}}^2 E(\tilde{q}))^{-1}$ of the excitation. The effective mass describes the dispersion of a localized Higgs quasi-particle wavepacket excited at some position on the torus. Three $\tilde{q}$-points are just enough to calculate the derivative with the centered second order finite difference formula $E''(\tilde{q}_1) = (E(\tilde{q}_2) - 2E(\tilde{q}_1) + E(0))/\tilde{q}_1^2$. The unit $M_0 = \hbar\tilde{q}_1/c_0 \simeq 29\,\mathrm{u}$ is defined with the superfluid speed of sound at the critical point c_0

and relates the mass M^* directly to the momentum scale $\tilde{q}_1$. Moreover $M^*/M_0 = \hbar\omega_0/E''$ where $\omega_0 = c_0\tilde{q}_1$.

Figure D.1(a) shows the effective mass of the Higgs mode. The mass diverges near the transition point[1]. Assuming a series expansion for the Higgs dispersion relation, the divergence would be consistent if terms of second and higher order vanish and a linear Higgs dispersion relation is obtained. To investigate this possibility we separately fit a linear and a quadratic function to the data $E(\tilde{q})$ and observe the coefficient of determination for these fits as a function of ϵ_{dd} (Fig. D.1(b)). The coefficient of determination, or (adjusted) R^2 coefficient, is a measure for the amount of variance explained in the fit, with values close to unity indicating a good fit [591]. The Higgs dispersion relation is near-perfect linear in the vicinity of the phase transition and approximately quadratic at intermediate values $\epsilon_{\mathrm{dd}} \simeq 2.1$–$2.13$. Towards larger values the importance of the linear contribution in the dispersion fit rises again (b). The results for the change in Higgs dispersion relation could be compared to models of infinite supersolids [169, 338] and the general dispersion relation form giving rise to a change from linear to quadratic behavior [11, 153, 159].

[1] The nearest point in the supersolid is approximately at $\epsilon_{\mathrm{dd}} - \epsilon_{\mathrm{dd}}^{\mathrm{crit}} \simeq 3.0 \times 10^{-3}$ where the mass is $M^*/M_0 \simeq 150$ whereas at the next point $\epsilon_{\mathrm{dd}} - \epsilon_{\mathrm{dd}}^{\mathrm{crit}} \simeq 3.3 \times 10^{-3}$ the mass has dropped to $M^*/M_0 \simeq 9.1$. The divergence is also suggested by the near-perfect fit with linear functions.

List of Figures

Bibliography

[1] J. Hertkorn, P. Stürmer, K. Mukherjee, K. Ng, P. Uerlings, F. Hellstern, L. Lavoine, S. Reimann, T. Pfau, and R. Klemt, "Decoupled sound and amplitude modes in trapped dipolar supersolids", arXiv:2404.12384 (submitted for peer review) (2024). pp. 39, 48, 51, 70, 72, 76, 79, 80, 148, 150, 152, 153, 158

[2] J. Hertkorn, J.-N. Schmidt, M. Guo, F. Böttcher, K. S. H. Ng, S. D. Graham, P. Uerlings, H. P. Büchler, T. Langen, M. Zwierlein, and T. Pfau, "Supersolidity in Two-Dimensional Trapped Dipolar Droplet Arrays", Phys. Rev. Lett. **127**, 155301 (2021). pp. 26, 39, 68, 98, 99, 151, 152, 159, 162

[3] J. Hertkorn, J.-N. Schmidt, M. Guo, F. Böttcher, K. S. H. Ng, S. D. Graham, P. Uerlings, T. Langen, M. Zwierlein, and T. Pfau, "Pattern formation in quantum ferrofluids: From supersolids to superglasses", Phys. Rev. Res. **3**, 033125 (2021). pp. 26, 38, 39, 104–106, 110, 113–115, 117, 147, 151, 152, 154

[4] J.-N. Schmidt, J. Hertkorn, M. Guo, F. Böttcher, M. Schmidt, K. S. H. Ng, S. D. Graham, T. Langen, M. Zwierlein, and T. Pfau, "Roton Excitations in an Oblate Dipolar Quantum Gas", Phys. Rev. Lett. **126**, 193002 (2021). pp. xvii, 4, 30, 39, 71, 85–87, 89, 91, 96, 102, 122, 150, 152

[5] J. Hertkorn, J.-N. Schmidt, F. Böttcher, M. Guo, M. Schmidt, K. S. H. Ng, S. D. Graham, H. P. Büchler, T. Langen, M. Zwierlein, and T. Pfau, "Density Fluctuations across the Superfluid-Supersolid Phase Transition in a Dipolar Quantum Gas", Phys. Rev. X **11**, 011037 (2021). pp. xvii, 4, 30, 38, 39, 48, 62, 64, 65, 68, 71, 86, 88, 96, 149, 152, 153, 156

[6] F. Böttcher, J.-N. Schmidt, J. Hertkorn, K. S. H. Ng, S. D. Graham, M. Guo, T. Langen, and T. Pfau, "New states of matter with fine-tuned interactions: quantum droplets and dipolar supersolids", Rep. Prog. Phys. **84**, 012403 (2021). pp. 39, 103, 107, 108, 120, 142, 149

[7] J. Hertkorn, F. Böttcher, M. Guo, J. N. Schmidt, T. Langen, H. P. Büchler, and T. Pfau, "Fate of the Amplitude Mode in a Trapped Dipolar Supersolid", Phys. Rev. Lett. **123**, 193002 (2019). pp. 12, 27, 30, 39, 48, 58, 59, 61, 68, 75, 81, 95, 96, 148, 149, 152, 156, 159, 162

[8] M. Guo, F. Böttcher, J. Hertkorn, J.-N. Schmidt, M. Wenzel, H. P. Büchler, T. Langen, and T. Pfau, "The low-energy Goldstone mode in a trapped dipolar supersolid", Nature (London) **574**, 386 (2019). pp. xvii, 5, 30, 39, 48, 56, 58–60, 63, 64, 66, 68, 75, 81, 96, 122, 149, 152, 159

[9] F. Böttcher, J.-N. Schmidt, M. Wenzel, J. Hertkorn, M. Guo, T. Langen, and T. Pfau, "Transient supersolid properties in an array of dipolar quantum droplets", Phys. Rev. X **9**, 011051 (2019). pp. xvi, xvii, 4, 5, 39, 47, 52, 53, 83, 88, 98, 103, 105, 149

[10] P. W. Anderson, "More Is Different", Science **177**, 393 (1972). pp. xiii, xiv, 1, 2, 10

[11] D. Pekker and C. M. Varma, "Amplitude / Higgs Modes in Condensed Matter Physics", Annu. Rev. Condens. Matter Phys. **6**, 269 (2015). pp. xiii, 1, 11, 12, 59, 163

[12] L. D. Landau, "On the theory of phase transitions", Zh. Eksp. Teor. Fiz. **7**, [Ukr. J. Phys.53,25(2008)], 19 (1937). pp. xiii, 1, 10

[13] A. M. Turing, "The chemical basis of morphogenesis", Phil. Trans. Roy. Soc. London Series B, Bio. Sci. **237**, 37 (1952). pp. xiii, 1, 32, 35, 103

[14] M. C. Cross and P. C. Hohenberg, "Pattern formation outside of equilibrium", Rev. Mod. Phys. **65**, 851 (1993). pp. xiii, 1, 32, 35, 103

[15] Q. Ouyang and H. L. Swinney, "Transition from a uniform state to hexagonal and striped turing patterns", Nature (London) **352**, 610 (1991). pp. xiii, 1, 103

[16] V. Castets, E. Dulos, J. Boissonade, and P. De Kepper, "Experimental evidence of a sustained standing turing-type nonequilibrium chemical pattern", Phys. Rev. Lett. **64**, 2953 (1990). pp. xiii, 1

[17] A. J. Koch and H. Meinhardt, "Biological pattern formation: from basic mechanisms to complex structures", Rev. Mod. Phys. **66**, 1481 (1994). pp. xiii, 1

[18] E. Meron, "From patterns to function in living systems: dryland ecosystems as a case study", Annu. Rev. Condens. Mat. Phys. **9**, 79 (2018). pp. xiii, 1

[19] E. Meron, "Vegetation pattern formation: The mechanisms behind the forms", Phys. Today **72**, 30 (2019). pp. xiii, 1

[20] M. Rietkerk and J. van de Koppel, "Regular pattern formation in real ecosystems", Trends in Ecology & Evolution **23**, 169 (2008). pp. xiii, 1

[21] S. Wolfram, *A new kind of science* (Wolfram Media, 2002). pp. xiii, 1, 32

[22] M. Gardner, "Mathematical games", Sci. Am. **223**, 120 (1970). pp. xiii, 2, 32

[23] H. K. Onnes, "Investigations into the properties of substances at low temperatures, which have led, amongst other things, to the preparation of liquid helium", Nobel Lectures Physics 1901-1921, 306 (1913). pp. xiv, 2

[24] P. Kapitza, "Viscosity of Liquid Helium below the λ-Point", Nature (London) **141**, 74 (1938). pp. xiv, 2, 33

[25] J. F. Allen and A. D. Misener, "Flow of Liquid Helium II", Nature (London) **141**, 75 (1938). pp. xiv, 2

[26] S. Balibar, "The Discovery of Superfluidity", J. Low Temp. Phys. **146**, 441 (2007). pp. xiv, 2

[27] L. Pitaevskii and S. Stringari, *Bose-Einstein Condensation and Superfluidity*, International series of monographs on physics (Oxford University Press, 2016). pp. xiv, xv, 2, 3, 13–15, 18, 21–23, 29–31, 35, 38, 63, 68, 74, 86, 88, 89, 107

[28] M. W. Zwierlein, "High-Temperature Superfluidity in an Ultracold Gas", PhD Thesis (Masssachusetts Institute of Technology, 2006). pp. xiv, xv, 2, 3

[29] S. Bose, "Plancks Gesetz und Lichtquantenhypothese", Z. Phys. **26**, 178 (1924). pp. xiv, 2, 13

[30] A. Einstein, "Quantentheorie des einatomigen idealen Gases", in *Albert einstein: akademie-vorträge* (Sitzungsberichte der Preussischen Akademie der Wissenschaften, 2006), pp. 237–244. pp. xiv, 2, 13

[31] A. Einstein, "Quantentheorie des einatomigen idealen Gases. Zweite Abhandlung", in *Albert einstein: akademie-vorträge* (Sitzungsberichte der Preussischen Akademie der Wissenschaften, 2006), pp. 245–257. pp. xiv, 2, 13

[32] J. Bardeen, L. N. Cooper, and J. R. Schrieffer, "Theory of superconductivity", Phys. Rev. **108**, 1175 (1957). pp. xiv, 2, 11

[33] W. D. Phillips, "Nobel Lecture: Laser cooling and trapping of neutral atoms", Rev. Mod. Phys. **70**, 721 (1998). pp. xiv, 2

[34] H. Feshbach, "Unified theory of nuclear reactions", Ann. Phys. **5**, 357 (1958). pp. xiv, 2, 18

[35] C. Chin, R. Grimm, P. Julienne, and E. Tiesinga, "Feshbach resonances in ultracold gases", Rev. Mod. Phys. **82**, 1225 (2010). pp. xiv, 2, 18

[36] M. H. Anderson, J. R. Ensher, M. R. Matthews, C. E. Wieman, and E. A. Cornell, "Observation of Bose-Einstein Condensation in a Dilute Atomic Vapor", Science **269**, 198 (1995). pp. xiv, 2

[37] K. B. Davis, M. .-. Mewes, M. R. Andrews, N. J. van Druten, D. S. Durfee, D. M. Kurn, and W. Ketterle, "Bose-Einstein Condensation in a Gas of Sodium Atoms", Phys. Rev. Lett. **75**, 3969 (1995). pp. xiv, 2

[38] M. R. Matthews, B. P. Anderson, P. C. Haljan, D. S. Hall, C. E. Wieman, and E. A. Cornell, "Vortices in a Bose-Einstein Condensate", Phys. Rev. Lett. **83**, 2498 (1999). pp. xv, 3

[39] K. W. Madison, F. Chevy, W. Wohlleben, and J. Dalibard, "Vortex Formation in a Stirred Bose-Einstein Condensate", Phys. Rev. Lett. **84**, 806 (2000). pp. xv, 3

[40] J. R. Abo-Shaeer, C. Raman, J. M. Vogels, and W. Ketterle, "Observation of Vortex Lattices in Bose-Einstein Condensates", Science **292**, 476 (2001). pp. xv, 3

[41] R. P. Feynman, "Simulating physics with computers", Int. J. Theor. Phys. **21**, 467 (1982). pp. xv, 3

[42] C. A. Regal, M. Greiner, and D. S. Jin, "Observation of Resonance Condensation of Fermionic Atom Pairs", Phys. Rev. Lett. **92**, 040403 (2004). pp. xv, 3

[43] M. Greiner, O. Mandel, T. Esslinger, T. W. Haensch, and I. Bloch, "Quantum Phase Transition from a Superfluid to a Mott Insulator in a Gas of Ultracold Atoms." Nature (London) **415**, 39 (2002). pp. xv, xvi, 3, 4

[44] I. Bloch and M. Greiner, "The superfluid-to-Mott insulator transition and the birth of experimental quantum simulation", Nat. Rev. Phys. **4**, 739 (2022). pp. xv, 3

[45] T. D. Stanescu, V. Galitski, and S. Das Sarma, "Topological states in two-dimensional optical lattices", Phys. Rev. A **82**, 013608 (2010). pp. xv, 3

[46] M. Aidelsburger, M. Atala, M. Lohse, J. T. Barreiro, B. Paredes, and I. Bloch, "Realization of the Hofstadter Hamiltonian with Ultracold Atoms in Optical Lattices", Phys. Rev. Lett. **111**, 185301 (2013). pp. xv, 3

[47] M. Lohse, C. Schweizer, O. Zilberberg, M. Aidelsburger, and I. Bloch, "A thouless quantum pump with ultracold bosonic atoms in an optical superlattice", Nat. Phys. **12**, 350 (2016). pp. xv, 3

[48] M. Saffman, T. G. Walker, and K. Mølmer, "Quantum information with Rydberg atoms", Rev. Mod. Phys. **82**, 2313 (2010). pp. xv, 3

[49] S. Ebadi, T. T. Wang, H. Levine, A. Keesling, G. Semeghini, A. Omran, D. Bluvstein, R. Samajdar, H. Pichler, W. W. Ho, S. Choi, S. Sachdev, M. Greiner, V. Vuletić, and M. D. Lukin, "Quantum phases of matter on a 256-atom programmable quantum simulator", Nature (London) **595**, 227 (2021). pp. xv, 3

[50] D. Bluvstein et al., "Logical quantum processor based on reconfigurable atom arrays", Nature (London) **626**, 58 (2024). pp. xv, 3

[51] L. Su, A. Douglas, M. Szurek, R. Groth, S. F. Ozturk, A. Krahn, A. H. Hébert, G. A. Phelps, S. Ebadi, S. Dickerson, F. Ferlaino, O. Marković, and M. Greiner, "Dipolar quantum solids emerging in a hubbard quantum simulator", Nature (London) **622**, 724 (2023). pp. xv, xvi, 3, 4, 47, 120, 154

[52] T. Hartke, B. Oreg, C. Turnbaugh, N. Jia, and M. Zwierlein, "Direct observation of nonlocal fermion pairing in an attractive Fermi-Hubbard gas", Science **381**, 82 (2023). pp. xv, 3

[53] C. Gross and W. S. Bakr, "Quantum gas microscopy for single atom and spin detection", Nat. Phys. **17**, 1316 (2021). pp. xv, 3

[54] S. Huth, P. T. H. Pang, I. Tews, T. Dietrich, A. Le Fèvre, A. Schwenk, W. Trautmann, K. Agarwal, M. Bulla, M. W. Coughlin, and C. Van Den Broeck, "Constraining neutron-star matter with microscopic and macroscopic collisions", Nature (London) **606**, 276 (2022). pp. xv, 3

[55] M. J. H. Ku, A. T. Sommer, L. W. Cheuk, and M. W. Zwierlein, "Revealing the Superfluid Lambda Transition in the Universal Thermodynamics of a Unitary Fermi Gas", Science **335**, 563 (2012). pp. xv, 3

[56] W. Hofstetter, J. I. Cirac, P. Zoller, E. Demler, and M. D. Lukin, "High-Temperature Superfluidity of Fermionic Atoms in Optical Lattices", Phys. Rev. Lett. **89**, 220407 (2002). pp. xv, 3

[57] P. A. Lee, N. Nagaosa, and X.-G. Wen, "Doping a Mott insulator: Physics of high-temperature superconductivity", Rev. Mod. Phys. **78**, 17 (2006). pp. xv, 3

[58] A. Mazurenko, C. S. Chiu, G. Ji, M. F. Parsons, M. Kanász-Nagy, R. Schmidt, F. Grusdt, E. Demler, D. Greif, and M. Greiner, "A cold-atom Fermi-Hubbard antiferromagnet", Nature (London) **545**, 462 (2017). pp. xv, 3

[59] C. Gross and I. Bloch, "Quantum simulations with ultracold atoms in optical lattices", Science **357**, 995 (2017). pp. xv, 3

[60] J. G. Bednorz and K. A. Müller, "Possible high T_c superconductivity in the Ba-La-Cu-O system", Z. Phys. B Condens. Matter **64**, 189 (1986). pp. xv, 3

[61] R. Bistritzer and M. A. H., "Moiré bands in twisted double-layer graphene", Proc. Natl. Acad. Sci. **108**, 12233 (2011). pp. xv, 3

[62] Y. Cao, V. Fatemi, S. Fang, K. Watanabe, T. Taniguchi, E. Kaxiras, and P. Jarillo-Herrero, "Unconventional superconductivity in magic-angle graphene superlattices", Nature (London) **556**, 43 (2018). pp. xv, 3

[63] Y. Cao, V. Fatemi, A. Demir, S. Fang, S. L. Tomarken, J. Y. Luo, J. D. Sanchez-Yamagishi, K. Watanabe, T. Taniguchi, E. Kaxiras, R. C. Ashoori, and P. Jarillo-Herrero, "Correlated insulator behaviour at half-filling in magic-angle graphene superlattices", Nature (London) **556**, 80 (2018). pp. xv, 3

[64] F. Wu, T. Lovorn, E. Tutuc, I. Martin, and A. H. MacDonald, "Topological Insulators in Twisted Transition Metal Dichalcogenide Homobilayers", Phys. Rev. Lett. **122**, 086402 (2019). pp. xv, 3

[65] M. Yankowitz, S. Chen, H. Polshyn, Y. Zhang, K. Watanabe, T. Taniguchi, D. Graf, A. F. Young, and C. R. Dean, "Tuning superconductivity in twisted bilayer graphene", Science **363**, 1059 (2019). pp. xv, 3

[66] Z. Lu, T. Han, Y. Yao, A. P. Reddy, J. Yang, J. Seo, K. Watanabe, T. Taniguchi, L. Fu, and L. Ju, "Fractional quantum anomalous Hall effect in multilayer graphene", Nature (London) **626**, 759 (2024). pp. xv, 3

[67] T. Han, Z. Lu, Y. Yao, J. Yang, J. Seo, C. Yoon, K. Watanabe, T. Taniguchi, L. Fu, F. Zhang, and L. Ju, "Large quantum anomalous Hall effect in spin-orbit proximitized rhombohedral graphene", Science **384**, 647 (2024). pp. xv, 3

[68] O. Penrose and L. Onsager, "Bose-Einstein Condensation and Liquid Helium", Phys. Rev. **104**, 576 (1956). pp. xv, 3, 84

[69] E. P. Gross, "Unified Theory of Interacting Bosons", Phys. Rev. **106**, 161 (1957). pp. xv, 3, 68, 84

[70] E. Gross, "Classical theory of boson wave fields", Ann. of Phys. **4**, 57 (1958). pp. xv, 3

[71] C. N. Yang, "Concept of Off-Diagonal Long-Range Order and the Quantum Phases of Liquid He and of Superconductors", Rev. Mod. Phys. **34**, 694 (1962). pp. xv, 3, 68

[72] Y. Imry and M. Schwartz, "On the possibility of Bose-Einstein condensation in a solid", J. Low Temp. Phys. **21**, 543 (1975). pp. xv, 3

[73] A. F. Andreev and I. M. Lifshitz, "Quatum theory of defects in crystals", Sov. Phys. JETP **29**, 1107 (1969). pp. xv, 3

[74] G. V. Chester, "Speculations on Bose-Einstein Condensation and Quantum Crystals", Phys. Rev. A **2**, 256 (1970). pp. xv, 3, 84

[75] N. V. Prokof'ev, "What makes a crystal supersolid?", Adv. Phys. **56**, 381 (2007). pp. xv, xvi, 3

[76] L. Reatto, "Bose-Einstein Condensation for a Class of Wave Functions", Phys. Rev. **183**, 334 (1969). pp. xv, 3

[77] A. Andreev, K. Keshishev, L. Mezhov-Deglin, and A. Shal'Nikov, "Attempts at Observing Vacancions in ^{4}He Crystals ", JETP Lett. **9**, 306 (1969). pp. xv, 3

[78] M. Boninsegni and N. V. Prokof'ev, "Colloquium: Supersolids: What and where are they?", Rev. Mod. Phys. **84**, 759 (2012). pp. xvi, 3, 13, 68, 84, 107, 151

[79] D. J. Thouless, "The flow of a dense superfluid", Ann. Phys. **52**, 403 (1969). pp. xvi, 3

[80] H. Matsuda and T. Tsuneto, "Off-Diagonal Long-Range Order in Solids*)", Prog. Theor. Phys. Supplement **46**, 411 (1970). pp. xvi, 3

[81] W. J. Mullin, "Cell Model of a Bose-Condensed Solid", Phys. Rev. Lett. **26**, 611 (1971). pp. xvi, 3

[82] K. Liu and M. Fisher, "Quantum lattice gas and the existence of a supersolid", J. Low Temp. Phys. **10**, 655 (1973). pp. xvi, 3

[83] M. H. W. Chan, R. B. Hallock, and L. Reatto, "Overview on Solid ^4He and the Issue of Supersolidity", J. Low Temp. Phys. **172**, 317 (2013). pp. xvi, 3, 4, 68

[84] M. W. Meisel, "Supersolid ^{4}He: an overview of past searches and future possibilities", Phys. B Phys. Condens. Matter **178**, 121 (1992). pp. xvi, 3

[85] S. Balibar and F. Caupin, "Supersolidity and disorder", J. Phys. Condens. Matter **20**, 173201 (2008). pp. xvi, 3

[86] D. E. Galli and L. Reatto, "Solid ^{4}He and the supersolid phase: From theoretical speculation to the discovery of a new state of matter? A review of the past and present status of research", J. Phys. Soc. Jpn. **77**, 111010 (2008). pp. xvi, 3

[87] A. B. Kuklov, N. V. Prokof'ev, and B. V. Svistunov, "Trend: How Solid is Supersolid?", Physics **4**, 109 (2011). pp. xvi, 3

[88] C. Josserand, Y. Pomeau, and S. Rica, "Patterns and supersolids", Eur. Phys. J. Spec. Top. **146**, 47 (2007). pp. xvi, 3

[89] D. Gustavo, J. Christophe, P. Yves, and R. Sergio, "Theory of real supersolids", arXiv:1110.1323 (2011). pp. xvi, 3

[90] E. Kim and M. H. W. Chan, "Observation of Superflow in Solid Helium", Science **305**, 1941 (2004). pp. xvi, 4

[91] E. Kim and M. H. W. Chan, "Probable observation of a supersolid helium phase", Nature (London) **427**, 225 (2004). pp. xvi, 4, 68

[92] D. Y. Kim and M. H. W. Chan, "Absence of Supersolidity in Solid Helium in Porous Vycor Glass", Phys. Rev. Lett. **109**, 155301 (2012). pp. xvi, 4

[93] J. R. Li, J. Lee, W. Huang, S. Burchesky, B. Shteynas, F. Ç. Topi, A. O. Jamison, and W. Ketterle, "A stripe phase with supersolid properties in spin-orbit-coupled Bose-Einstein condensates", Nature (London) **543**, 91 (2017). pp. xvi, 4

[94] K. T. Geier, G. I. Martone, P. Hauke, W. Ketterle, and S. Stringari, "Dynamics of Stripe Patterns in Supersolid Spin-Orbit-Coupled Bose Gases", Phys. Rev. Lett. **130**, 156001 (2023). pp. xvi, 4

[95] J. Leonard, A. Morales, P. Zupancic, T. Esslinger, and T. Donner, "A stripe phase with supersolid properties in spin-orbit-coupled Bose-Einstein condensates", Nature (London) **543**, 87 (2017). pp. xvi, 4

[96] L. Tanzi, E. Lucioni, F. Famà, J. Catani, A. Fioretti, C. Gabbanini, R. N. Bisset, L. Santos, and G. Modugno, "Observation of a Dipolar Quantum Gas with Metastable Supersolid Properties", Phys. Rev. Lett. **122**, 130405 (2019). pp. xvi, xvii, 4, 5, 47, 54, 68, 75, 81, 97, 103, 149

[97] L. Chomaz, D. Petter, P. Ilzhöfer, G. Natale, A. Trautmann, C. Politi, G. Durastante, R. M. W. van Bijnen, A. Patscheider, M. Sohmen, M. J. Mark, and F. Ferlaino, "Long-Lived and Transient Supersolid Behaviors in Dipolar Quantum Gases", Phys. Rev. X **9**, 021012 (2019). pp. xvi, xvii, 4, 5, 47, 56, 75, 81, 83, 97, 103, 149

[98] I. Bloch, J. Dalibard, and W. Zwerger, "Many-body physics with ultracold gases", Rev. Mod. Phys. **80**, 885 (2008). pp. xvi, 4

[99] I. Bloch, J. Dalibard, and S. Nascimbène, "Quantum simulations with ultracold quantum gases", Nat. Phys. **8**, 267 (2012). pp. xvi, 4

[100] S. Baier, M. J. Mark, D. Petter, K. Aikawa, L. Chomaz, Z. Cai, M. Baranov, P. Zoller, and F. Ferlaino, "Extended Bose-Hubbard models with ultracold magnetic atoms", Science **352**, 201 (2016). pp. xvi, 4, 47

[101] L. Landau, "Theory of the Superfluidity of Helium II", Phys. Rev. **60**, 356 (1941). pp. xvi, 4, 33, 34

[102] L. Landau, "The theory of superfluidity of helium II", J. Phys. U.S.S.R. **60**, 71 (1941). pp. xvi, 4, 33, 34

[103] R. P. Feynman, "Atomic Theory of the Two-Fluid Model of Liquid Helium", Phys. Rev. **94**, 262 (1954). pp. xvi, 4, 31, 34

[104] L. Santos, G. V. Shlyapnikov, and M. Lewenstein, "Roton-Maxon Spectrum and Stability of Trapped Dipolar Bose-Einstein Condensates", Phys. Rev. Lett. **90**, 250403 (2003). pp. xvi, xvii, 4, 33, 34, 110, 112, 114

[105] D. G. Henshaw and A. D. B. Woods, "Modes of Atomic Motions in Liquid Helium by Inelastic Scattering of Neutrons", Phys. Rev. **121**, 1266 (1961). pp. xvi, 4, 34

[106] R. Rosensweig, *Ferrohydrodynamics*, Dover Books on Physics (Dover Publications, 1997). pp. xvi, 4, 35, 103, 109, 110

[107] H. Kadau, "Rosensweig Instability and Droplets in a Quantum Ferrofluid of Dysprosium Atoms", PhD thesis (University of Stuttgart, 2016). pp. xvi, 4, 17, 35, 38, 125

[108] T. Langen, "Dipolar supersolids: Solid and superfluid at the same time", Phys. Today **75**, 36 (2022). pp. xvi, 4

[109] M. Seul and D. Andelman, "Domain Shapes and Patterns: The Phenomenology of Modulated Phases", Science **267**, 476 (1995). pp. xvi, 4, 103, 111

[110] D. Andelman and R. E. Rosensweig, "Modulated Phases: Review and Recent Results", J. Phys. Chem. B **113**, 3785 (2009). pp. xvi, 4, 103, 109, 110

[111] P. Bourgine and A. Lesne, *Morphogenesis, Origins of Patterns and Shapes*, Springer Complexity (Springer, Berlin, Heidelberg, 2011). pp. xvi, 4, 32, 103

[112] A. Griesmaier, J. Werner, S. Hensler, J. Stuhler, and T. Pfau, "Bose-Einstein Condensation of Chromium", Phys. Rev. Lett. **94**, 160401 (2005). pp. xvi, 4, 120, 144

[113] M. Lu, N. Q. Burdick, S. H. Youn, and B. L. Lev, "Strongly Dipolar Bose-Einstein Condensate of Dysprosium", Phys. Rev. Lett. **107**, 190401 (2011). pp. xvi, 4, 120, 144

[114] M. Lu, N. Q. Burdick, and B. L. Lev, "Quantum Degenerate Dipolar Fermi Gas", Phys. Rev. Lett. **108**, 215301 (2012). pp. xvi, 4

[115] K. Aikawa, A. Frisch, M. Mark, S. Baier, R. Grimm, and F. Ferlaino, "Reaching Fermi Degeneracy via Universal Dipolar Scattering", Phys. Rev. Lett. **112**, 010404 (2014). pp. xvi, 4

[116] K. Aikawa, A. Frisch, M. Mark, S. Baier, A. Rietzler, R. Grimm, and F. Ferlaino, "Bose-Einstein Condensation of Erbium", Phys. Rev. Lett. **108**, 210401 (2012). pp. xvi, 4, 120, 144

[117] Y. Miyazawa, R. Inoue, H. Matsui, G. Nomura, and M. Kozuma, "Bose-Einstein Condensation of Europium", Phys. Rev. Lett. **129**, 223401 (2022). pp. xvi, 4, 39, 120, 121, 144

[118] T. Lahaye, J. Metz, B. Fröhlich, T. Koch, M. Meister, A. Griesmaier, T. Pfau, H. Saito, Y. Kawaguchi, and M. Ueda, "*d*-Wave Collapse and Explosion of a Dipolar Bose-Einstein Condensate", Phys. Rev. Lett. **101**, 080401 (2008). pp. xvi, xvii, 4, 37, 110

[119] T. Koch, T. Lahaye, J. Metz, B. Fröhlich, A. Griesmaier, and T. Pfau, "Stabilization of a purely dipolar quantum gas against collapse", Nat. Phys. **4**, 218 (2008). pp. xvi, xvii, 4, 22, 37, 110

[120] B. Pasquiou, E. Maréchal, G. Bismut, P. Pedri, L. Vernac, O. Gorceix, and B. Laburthe-Tolra, "Spontaneous Demagnetization of a Dipolar Spinor Bose Gas in an Ultralow Magnetic Field", Phys. Rev. Lett. **106**, 255303 (2011). pp. xvi, 4

[121] B. Pasquiou, E. Maréchal, L. Vernac, O. Gorceix, and B. Laburthe-Tolra, "Thermodynamics of a Bose-Einstein Condensate with Free Magnetization", Phys. Rev. Lett. **108**, 045307 (2012). pp. xvi, 4

[122] T. Chalopin, T. Satoor, A. Evrard, V. Makhalov, J. Dalibard, R. Lopes, and S. Nascimbene, "Probing chiral edge dynamics and bulk topology of a synthetic Hall system", Nat. Phys. **16**, 1017 (2020). pp. xvii, 4

[123] A. Fabre, J.-B. Bouhiron, T. Satoor, R. Lopes, and S. Nascimbene, "Laughlin's Topological Charge Pump in an Atomic Hall Cylinder", Phys. Rev. Lett. **128**, 173202 (2022). pp. xvii, 4

[124] R. N. Bisset, D. Baillie, and P. B. Blakie, "Roton excitations in a trapped dipolar Bose-Einstein condensate", Phys. Rev. A **88**, 043606 (2013). pp. xvii, 4, 35, 71, 83, 85, 87, 97

[125] L. Chomaz, R. M. Van Bijnen, D. Petter, G. Faraoni, S. Baier, J. H. Becher, M. J. Mark, F. Wächtler, L. Santos, and F. Ferlaino, "Observation of roton mode population in a dipolar quantum gas", Nat. Phys. **14**, 442 (2018). pp. xvii, 4, 27, 30, 34, 35, 54, 65, 83, 96, 112, 152

[126] S. Ronen, D. C. E. Bortolotti, and J. L. Bohn, "Radial and angular rotons in trapped dipolar gases", Phys. Rev. Lett. **98**, 030406 (2007). pp. xvii, 4, 35, 83, 85, 87, 97

[127] S. Giovanazzi and D. H. J. O'Dell, "Instabilities and the roton spectrum of a quasi-1D Bose-Einstein condensed gas with dipole-dipole interactions", Eur. Phys. J. D **31**, 439 (2004). pp. xvii, 4

[128] D. Petter, G. Natale, R. M. W. van Bijnen, A. Patscheider, M. J. Mark, L. Chomaz, and F. Ferlaino, "Probing the Roton Excitation Spectrum of a Stable Dipolar Bose Gas", Phys. Rev. Lett. **122**, 183401 (2019). pp. xvii, 4, 30, 35, 56, 65, 83, 92, 96

[129] J.-N. Schmidt, "Density Fluctuations in a Dipolar Quantum Gas – from Superfluids to Supersolids", PhD thesis (University of Stuttgart, 2022). pp. xvii, 4, 6, 17, 30, 34, 36, 39, 48, 63–65, 85, 88, 90, 92, 99, 102, 120, 122, 124, 126, 127

[130] H. Kadau, M. Schmitt, M. Wenzel, C. Wink, T. Maier, I. Ferrier-Barbut, and T. Pfau, "Observing the Rosensweig instability of a quantum ferrofluid", Nature (London) **530**, 194 (2015). pp. xvii, 4, 22, 24, 35, 36, 38, 39, 53, 103

[131] I. Ferrier-Barbut, H. Kadau, M. Schmitt, M. Wenzel, and T. Pfau, "Observation of Quantum Droplets in a Strongly Dipolar Bose Gas", Phys. Rev. Lett. **116**, 215301 (2016). pp. xvii, 4, 22, 24, 106–108

[132] I. Ferrier-Barbut, M. Schmitt, M. Wenzel, H. Kadau, and T. Pfau, "Liquid quantum droplets of ultracold magnetic atoms", J. Phys. B. **49**, 214004 (2016). pp. xvii, 4

[133] D. S. Petrov, "Quantum Mechanical Stabilization of a Collapsing Bose-Bose Mixture", Phys. Rev. Lett. **115**, 155302 (2015). pp. xvii, 4, 5, 22, 24, 38, 87, 103, 106–108

[134] R. Schützhold, M. Uhlmann, Y. Xu, and U. R. Fischer, "Mean-Field Expansion in Bose–Einstein Condensates with Finite-Range Interactions", Int. J. Mod. Phys. B **20**, 3555 (2006). pp. xvii, 4, 24, 92, 117

[135] A. R. P. Lima and A. Pelster, "Quantum fluctuations in dipolar Bose gases", Phys. Rev. A **84**, 041604(R) (2011). pp. xvii, 4, 24, 92, 117

[136] A. R. P. Lima and A. Pelster, "Beyond mean-field low-lying excitations of dipolar Bose gases", Phys. Rev. A **86**, 063609 (2012). pp. xvii, 4, 24, 92, 117

[137] M. Schmitt, M. Wenzel, F. Böttcher, I. Ferrier-Barbut, and T. Pfau, "Self-bound droplets of a dilute magnetic quantum liquid", Nature (London) **539**, 259 (2016). pp. xvii, 5, 38, 103, 108

[138] F. Böttcher, M. Wenzel, J.-N. Schmidt, M. Guo, T. Langen, I. Ferrier-Barbut, T. Pfau, R. Bombín, J. Sánchez-Baena, J. Boronat, and F. Mazzanti, "Dilute dipolar quantum droplets beyond the extended Gross-Pitaevskii equation", Phys. Rev. Res. **1**, 033088 (2019). pp. xvii, 5, 18, 56, 57, 65, 103, 108, 117, 142, 144, 153

[139] D. Baillie, R. M. Wilson, R. N. Bisset, and P. B. Blakie, "Self-bound dipolar droplet: A localized matter wave in free space", Phys. Rev. A **94**, 021602 (2016). pp. xvii, 5, 36, 108

[140] K.-T. Xi and H. Saito, "Droplet formation in a Bose-Einstein condensate with strong dipole-dipole interaction", Phys. Rev. A **93**, 011604 (2016). pp. xvii, 5

[141] F. Wächtler and L. Santos, "Ground-state properties and elementary excitations of quantum droplets in dipolar Bose-Einstein condensates", Phys. Rev. A **94**, 043618 (2016). pp. xvii, 5, 36, 107

[142] L. Chomaz, S. Baier, D. Petter, M. J. Mark, F. Wächtler, L. Santos, and F. Ferlaino, "Quantum-Fluctuation-Driven Crossover from a Dilute Bose-Einstein Condensate to a Macrodroplet in a Dipolar Quantum Fluid", Phys. Rev. X **6**, 041039 (2016). pp. xvii, 5, 56, 103, 108

[143] R. N. Bisset and P. B. Blakie, "Crystallization of a dilute atomic dipolar condensate", Phys. Rev. A **92**, 061603 (2015). pp. xvii, 5, 37, 97

[144] R. N. Bisset, R. M. Wilson, D. Baillie, and P. B. Blakie, "Ground-state phase diagram of a dipolar condensate with quantum fluctuations", Phys. Rev. A **94**, 033619 (2016). pp. xvii, 5, 24, 101, 110

[145] P. B. Blakie, "Properties of a dipolar condensate with three-body interactions", Phys. Rev. A **93**, 033644 (2016). pp. xvii, 5, 97

[146] M. Wenzel, F. Böttcher, T. Langen, I. Ferrier-Barbut, and T. Pfau, "Striped states in a many-body system of tilted dipoles", Phys. Rev. A **96**, 053630 (2017). pp. xvii, 5, 17, 33, 36, 37, 53

[147] S. M. Roccuzzo and F. Ancilotto, "Supersolid behavior of a dipolar Bose-Einstein condensate confined in a tube", Phys. Rev. A **99**, 041601(R) (2019). pp. xvii, 5, 25, 27, 49, 51, 53, 83, 116

[148] G. Natale, R. M. W. van Bijnen, A. Patscheider, D. Petter, M. J. Mark, L. Chomaz, and F. Ferlaino, "Excitation Spectrum of a Trapped Dipolar Supersolid and Its Experimental Evidence", Phys. Rev. Lett. **123**, 050402 (2019). pp. xvii, 5, 30, 65, 68, 75, 81, 97, 152, 156, 159

[149] L. Chomaz, I. Ferrier-Barbut, F. Ferlaino, B. Laburthe-Tolra, B. L. Lev, and T. Pfau, "Dipolar physics: a review of experiments with magnetic quantum gases", Rep. Prog. Phys. **86**, 026401 (2022). p. 4

[150] T. Maier, H. Kadau, M. Schmitt, M. Wenzel, I. Ferrier-Barbut, T. Pfau, A. Frisch, S. Baier, K. Aikawa, L. Chomaz, M. J. Mark, F. Ferlaino, C. Makrides, E. Tiesinga, A. Petrov, and S. Kotochigova, "Emergence of Chaotic Scattering in Ultracold Er and Dy", Phys. Rev. X **5**, 041029 (2015). p. 4

[151] A. Frisch, M. Mark, K. Aikawa, F. Ferlaino, J. L. Bohn, C. Makrides, A. Petrov, and S. Kotochigova, "Quantum chaos in ultracold collisions of gas-phase erbium atoms", Nature (London) **507**, 475 (2014). p. 4

[152] T. Maier, "Interactions in a Quantum Gas of Dysprosium Atoms", PhD thesis (University of Stuttgart, 2015). pp. 6, 17, 18, 36, 120–122, 125, 126, 134, 137, 141, 142, 147

[153] F. Böttcher, "Supersolid Arrays of Dipolar Quantum Droplets", PhD thesis (University of Stuttgart, 2020). pp. 6, 11, 12, 37, 39, 48, 52–56, 65, 123, 126, 156, 157, 163

[154] N. Lang, "One-Dimensional Topological States of Synthetic Quantum Matter", PhD Thesis (University of Stuttgart, 2019). p. 10

[155] S. Stringari, M. Inguscio, and C. E. Wieman (eds), "Making, probing and understanding Bose-Einstein condensates", Proceedings of the International School of Physics "Enrico Fermi" **140**, 67 (1999). pp. 10, 143, 144

[156] A. J. Beekman, L. Rademaker, and J. van Wezel, "An introduction to spontaneous symmetry breaking", SciPost Phys. Lect. Notes, 11 (2019). p. 10

[157] A. Schmitt, *Introduction to Superfluidity: Field-theoretical Approach and Applications*, Lecture Notes in Physics (Springer International Publishing, 2014). pp. 10, 16, 29

[158] V. L. Ginzburg, "On the theory of superconductivity", Il Nuovo Cimento (1955-1965) **2**, 1234 (1955). p. 11

[159] J. Léonard, "A Supersolid of Matter and Light", PhD thesis (ETH Zurich, Zurich, 2017). pp. 11, 12, 163

[160] V. Ginzburg, *On superconductivity and superfluidity: a scientific autobiography* (Springer Berlin Heidelberg, 2008). p. 11

[161] Y. Nambu, "Quasi-particles and gauge invariance in the theory of superconductivity", Phys. Rev. **117**, 648 (1960). p. 11

[162] J. Goldstone, "Field theories with Superconductor solutions", Il Nuovo Cimento (1955-1965) **19**, 154 (1961). p. 11

[163] J. Goldstone, A. Salam, and S. Weinberg, "Broken Symmetries", Phys. Rev. **127**, 965 (1962). p. 11

[164] C. M. Varma, "Higgs Boson in Superconductors", J. Low Temp. Phys. **126**, 901 (2002). pp. 11, 12

[165] P. W. Higgs, "Broken symmetries and the masses of gauge bosons", Phys. Rev. Lett. **13**, 508 (1964). p. 12

[166] H. Nielsen and S. Chadha, "On how to count Goldstone bosons", Nucl. Phys. B **105**, 445 (1976). p. 12

[167] S. D. Huber, E. Altman, H. P. Büchler, and G. Blatter, "Dynamical properties of ultracold bosons in an optical lattice", Phys. Rev. B **75**, 085106 (2007). pp. 12, 152

[168] S. D. Huber, B. Theiler, E. Altman, and G. Blatter, "Amplitude mode in the quantum phase model", Phys. Rev. Lett. **100**, 050404 (2008). pp. 12, 152

[169] T. Ilg and H. P. Büchler, "Ground-state stability and excitation spectrum of a one-dimensional dipolar supersolid", Phys. Rev. A **107**, 013314 (2023). pp. 12, 24, 33, 51, 72, 77, 163

[170] J. Léonard, A. Morales, P. Zupancic, T. Donner, and T. Esslinger, "Monitoring and manipulating Higgs and Goldstone modes in a supersolid quantum gas", Science **358**, 1415 (2017). pp. 12, 95, 152

[171] R. Matsunaga, Y. I. Hamada, K. Makise, Y. Uzawa, H. Terai, Z. Wang, and R. Shimano, "Higgs Amplitude Mode in the BCS Superconductors $Nb_{1-x}Ti_xN$ Induced by Terahertz Pulse Excitation", Phys. Rev. Lett. **111**, 057002 (2013). p. 12

[172] M.-A. Méasson, Y. Gallais, M. Cazayous, B. Clair, P. Rodière, L. Cario, and A. Sacuto, "Amplitude Higgs mode in the $2H - NbSe_2$ superconductor", Phys. Rev. B **89**, 060503 (2014). p. 12

[173] M. Endres, T. Fukuhara, D. Pekker, M. Cheneau, P. Schauß, C. Gross, E. Demler, S. Kuhr, and I. Bloch, "The 'Higgs' amplitude mode at the two-dimensional superfluid/Mott insulator transition", Nature (London) **487**, 454 (2012). pp. 12, 95, 152

[174] U. Bissbort, S. Götze, Y. Li, J. Heinze, J. S. Krauser, M. Weinberg, C. Becker, K. Sengstock, and W. Hofstetter, "Detecting the amplitude mode of strongly interacting lattice bosons by Bragg scattering", Phys. Rev. Lett. **106**, 205303 (2011). p. 12

[175] A. Behrle, T. Harrison, J. Kombe, K. Gao, M. Link, J.-S. Bernier, C. Kollath, and M. Köhl, "Higgs mode in a strongly interacting fermionic superfluid", Nat. Phys. **14**, 781 (2018). p. 12

[176] G. M. Bruun, "Long-lived Higgs mode in a two-dimensional confined Fermi system", Phys. Rev. A **90**, 023621 (2014). p. 12

[177] C. Huepe, L. S. Tuckerman, S. Métens, and M. E. Brachet, "Stability and decay rates of nonisotropic attractive Bose-Einstein condensates", Phys. Rev. A **68**, 023609 (2003). pp. 13, 27–29, 44

[178] J. Rogel-Salazar, "The Gross–Pitaevskii equation and Bose–Einstein condensates", Eur. J. Phys. **34**, 247 (2013). pp. 13, 25

[179] L. P. Pitaevskii, "Properties of the spectrum of elementary excitations near the disintegration threshold of the excitations", JETP **36**, 830 (1959). p. 14

[180] C. Pethick and H. Smith, *Bose-Einstein Condensation in Dilute Gases* (Cambridge University Press, 2002). pp. 14, 15, 17, 18, 25

[181] R. Grimm, M. Weidemüller, and Y. B. Ovchinnikov, "Optical Dipole Traps for Neutral Atoms", Adv. At. Mol. Opt. Phys. **42**, edited by B. Bederson and H. Walther, 95 (2000). pp. 14, 121, 122, 125

[182] C. J. Pethick and D. G. Ravenhall, "Matter at Large Neutron Excess and the Physics of Neutron-Star Crusts", Annu. Rev. Nuc. Part. Sci. **45**, 429 (1995). pp. 14, 109

[183] S. Giorgini, L. P. Pitaevskii, and S. Stringari, "Condensate fraction and critical temperature of a trapped interacting Bose gas", Phys. Rev. A **54**, R4633 (1996). pp. 15, 144

[184] K. Glaum and A. Pelster, "Bose-Einstein condensation temperature of dipolar gas in anisotropic harmonic trap", Phys. Rev. A **76**, 023604 (2007). p. 15

[185] K. Glaum, A. Pelster, H. Kleinert, and T. Pfau, "Critical temperature of weakly interacting dipolar condensates", Phys. Rev. Lett. **98**, 080407 (2007). pp. 15, 144

[186] M. R. Andrews, C. G. Townsend, H.-J. Miesner, D. S. Durfee, D. M. Kurn, and W. Ketterle, "Observation of Interference Between Two Bose Condensates", Science **275**, 637 (1997). p. 15

[187] Z. Hadzibabic, S. Stock, B. Battelier, V. Bretin, and J. Dalibard, "Interference of an Array of Independent Bose-Einstein Condensates", Phys. Rev. Lett. **93**, 180403 (2004). p. 15

[188] A. J. Leggett, "Bose-Einstein condensation in the alkali gases: Some fundamental concepts", Rev. Mod. Phys. **73**, 307 (2001). pp. 16, 18

[189] A. Leggett, *Quantum Liquids: Bose Condensation and Cooper Pairing in Condensed-matter Systems*, Oxford graduate texts in mathematics (OUP Oxford, 2006). p. 16

[190] Y. Castin, *Bose-Einstein condensates in atomic gases: simple theoretical results*, edited by R. Kaiser, C. Westbrook, and F. David (Springer Berlin Heidelberg, Berlin, Heidelberg, 2000), pp. 1–136. pp. 16, 19

[191] B. Svistunov, E. Babaev, and N. Prokof'ev, *Superfluid States of Matter* (Taylor & Francis, 2015). pp. 16, 25

[192] J. Harms, J. P. Toennies, and F. Dalfovo, "Density of superfluid helium droplets", Phys. Rev. B **58**, 3341 (1998). pp. 17, 38

[193] C. Foot, *Atomic physics*, Oxford master series in physics (Oxford University Press, 2005). pp. 17, 18, 134, 135

[194] L. Landau and E. Lifshitz, *Quantum Mechanics: Non-Relativistic Theory* (Elsevier Science, 1981). p. 17

[195] S. Müller, "Stability and Collapse Dynamics of Dipolar Bose-Einstein Condensates in One-Dimensional Optical Lattices", PhD Thesis (University of Stuttgart, 2013). p. 17

[196] Ferrier-Barbut, Igor, "Mixtures of Bose and Fermi Superfluids", PhD thesis (Ecole normale supérieure, 2014). pp. 17, 18

[197] M. Wenzel, "Macroscopic states of dipolar quantum gases", PhD thesis (University of Stuttgart, 2019), pp. 1–138. pp. 17, 19, 20, 22, 30, 33, 36, 37, 39, 40, 65, 116, 125, 141, 142, 155

[198] S. Inouye, M. R. Andrews, J. Stenger, H. J. Mlesner, D. M. Stamper-Kurn, and W. Ketterle, "Observation of Feshbach resonances in a Bose-Einstein condensate", Nature (London) **392**, 151 (1998). p. 18

[199] S. Yi and L. You, "Trapped atomic condensates with anisotropic interactions", Phys. Rev. A **61**, 041604 (2000). p. 19

[200] T. Lahaye, C. Menotti, L. Santos, M. Lewenstein, and T. Pfau, "The physics of dipolar bosonic quantum gases", Rep. Prog. Phys. **72**, 126401 (2009). pp. 19, 20, 22, 33, 38, 40

[201] S. Yi and L. You, "Trapped condensates of atoms with dipole interactions", Phys. Rev. A **63**, 053607 (2001). pp. 19, 35

[202] C. Ticknor, "Collisional Control of Ground State Polar Molecules and Universal Dipolar Scattering", Phys. Rev. Lett. **100**, 133202 (2008). p. 19

[203] J. L. Bohn, M. Cavagnero, and C. Ticknor, "Quasi-universal dipolar scattering in cold and ultracold gases", New J. Phys. **11**, 055039 (2009). p. 19

[204] K. Góral and L. Santos, "Ground state and elementary excitations of single and binary Bose-Einstein condensates of trapped dipolar gases", Phys. Rev. A **66**, 023613 (2002). p. 20

[205] J. Hertkorn, "Numerical investigation of a trapped dipolar supersolid", Master's thesis (University of Stuttgart, 2019). pp. 20, 28, 29, 39, 48–50, 53, 55, 116, 155–158

[206] F. Schwabl, R. Hilton, and A. Lahee, *Advanced Quantum Mechanics*, Advanced texts in physics (Springer, 2005). pp. 21, 22

[207] F. Dalfovo, S. Giorgini, L. P. Pitaevskii, and S. Stringari, "Theory of Bose-Einstein condensation in trapped gases", Rev. Mod. Phys. **71**, 463 (1999). pp. 21, 25, 58

[208] F. Wächtler and L. Santos, "Quantum filaments in dipolar Bose-Einstein condensates", Phys. Rev. A **93**, 061603 (2016). p. 22

[209] F. Wächtler and L. Santos, "Ground-state properties and elementary excitations of quantum droplets in dipolar Bose-Einstein condensates", Phys. Rev. A **94**, 043618 (2016). p. 22

[210] C. Sulem and P. Sulem, *The Nonlinear Schrödinger Equation: Self-Focusing and Wave Collapse*, Applied Mathematical Sciences (Springer New York, 1999). p. 22

[211] T. Tao, *Terence Tao's research blog "What's new"*, https://terrytao.wordpress.com/2009/11/26/from-bose-einstein-condensates-to-the-nonlinear-schrodinger-equation/#more-3135 (visited on 05/26/2024). p. 22

[212] M.-w. Xiao, "Theory of transformation for the diagonalization of quadratic Hamiltonians", arXiv:0908.0787 (2009). p. 22

[213] P. Nozieres, *Theory Of Quantum Liquids: Superfluid Bose Liquids* (CRC Press, 2018). p. 22

[214] A. Abrikosov, L. Gorkov, I. Dzyaloshinski, and R. Silverman, *Methods of Quantum Field Theory in Statistical Physics*, Dover Books on Physics (Dover Publications, 2012). p. 22

[215] T. D. Lee, K. Huang, and C. N. Yang, "Eigenvalues and Eigenfunctions of a Bose System of Hard Spheres and Its Low-Temperature Properties", Phys. Rev. **106**, 1135 (1957). p. 23

[216] T. T. Wu, "Ground State of a Bose System of Hard Spheres", Phys. Rev. **115**, 1390 (1959). p. 23

[217] R. Lopes, C. Eigen, N. Navon, D. Clément, R. P. Smith, and Z. Hadzibabic, "Quantum Depletion of a Homogeneous Bose-Einstein Condensate", Phys. Rev. Lett. **119**, 190404 (2017). p. 23

[218] S. Moroni and M. Boninsegni, "Condensate Fraction in Liquid 4He", J. Low Temp. Phys. **136**, 129 (2004). p. 23

[219] H. R. Glyde, S. O. Diallo, R. T. Azuah, O. Kirichek, and J. W. Taylor, "Atomic momentum distribution and Bose-Einstein condensation in liquid ^{4}He under pressure", Phys. Rev. B **84**, 184506 (2011). p. 23

[220] D. Ceperley and B. Alder, "Quantum Monte Carlo", Science **231**, 555 (1986). p. 23

[221] A. Y. Cherny, "Low-density expansions for the homogeneous dipolar Bose gas at zero temperature", Phys. Rev. A **100**, 063631 (2019). p. 24

[222] Ilg, T., "Quantum Fluctuations and Appearance of Supersolidity in Confined Ultracold Atomic Gases", PhD thesis (University of Stuttgart, 2023). pp. 24, 33

[223] D. Baillie, R. M. Wilson, and P. B. Blakie, "Collective Excitations of Self-Bound Droplets of a Dipolar Quantum Fluid", Phys. Rev. Lett. **119**, 255302 (2017). pp. 24, 28, 108

[224] H. Saito, "Path-Integral Monte Carlo Study on a Droplet of a Dipolar Bose–Einstein Condensate Stabilized by Quantum Fluctuation", J. Phys. Soc. Jpn **85**, 053001 (2016). p. 24

[225] T. Ilg, J. Kumlin, L. Santos, D. S. Petrov, and H. P. Büchler, "Dimensional crossover for the beyond-mean-field correction in bose gases", Phys. Rev. A **98**, 051604 (2018). p. 24

[226] C. Bühler, T. Ilg, and H. P. Büchler, "Quantum fluctuations in one-dimensional supersolids", Phys. Rev. Res. **5**, 033092 (2023). pp. 24, 51

[227] R. Bombín, V. Cikojević, F. Mazzanti, and J. Boronat, "Quantum-Monte-Carlo–based functional for dysprosium dipolar systems", Phys. Rev. A **109**, 033312 (2024). pp. 24, 42, 57, 117, 153

[228] P. B. Blakie, "Optical Manipulation of Bose-Einstein Condensates", PhD Thesis (University of Otago, 2001). p. 25

[229] R. M. Martin, *Electronic Structure: Basic Theory and Practical Methods* (Cambridge University Press, 2004). p. 25

[230] E. Engel and R. Dreizler, *Density Functional Theory: An Advanced Course*, Theoretical and Mathematical Physics (Springer Berlin Heidelberg, 2011). p. 25

[231] A. Triay, "Existence of minimizers in generalized Gross-Pitaevskii theory with the Lee-Huang-Yang correction", arXiv:1904.10672 (2019). p. 25

[232] S. Stringari, "Collective Excitations of a Trapped Bose-Condensed Gas", Phys. Rev. Lett. **77**, 2360 (1996). pp. 25, 157

[233] A.-C. Lee, D. Baillie, and P. B. Blakie, "Numerical calculation of dipolar-quantum-droplet stationary states", Phys. Rev. Res. **3**, 013283 (2021). pp. 25, 27, 40, 44, 108

[234] W. Bao, Y. Cai, and H. Wang, "Efficient numerical methods for computing ground states and dynamics of dipolar Bose–Einstein condensates", J. Comp. Phys. **229**, 7874 (2010). pp. 25, 40

[235] X. Antoine, W. Bao, and C. Besse, "Computational methods for the dynamics of the nonlinear Schrödinger/Gross–Pitaevskii equations", Comput. Phys. Comm. **184**, 2621 (2013). pp. 25, 39–41

[236] W. Bao and Y. Cai, "Mathematical theory and numerical methods for Bose-Einstein condensation", Kinetic and Related Models **6**, 1 (2013). pp. 25, 26, 39, 40, 100

[237] H.-Y. Lu, H. Lu, J.-N. Zhang, R.-Z. Qiu, H. Pu, and S. Yi, "Spatial density oscillations in trapped dipolar condensates", Phys. Rev. A **82**, 023622 (2010). pp. 26, 27, 69, 87, 97

[238] Y.-C. Zhang, F. Maucher, and T. Pohl, "Supersolidity around a critical point in dipolar Bose-Einstein condensates", Phys. Rev. Lett. **123**, 15301 (2019). pp. 26, 51, 53, 95, 104, 106–108, 116, 152

[239] K. Góral, K. Rzążewski, and T. Pfau, "Bose-Einstein condensation with magnetic dipole-dipole forces", Phys. Rev. A **61**, 051601 (2000). p. 27

[240] S. Ronen, D. C. Bortolotti, and J. L. Bohn, "Bogoliubov modes of a dipolar condensate in a cylindrical trap", Phys. Rev. A **74**, 013623 (2006). pp. 27–29, 40–42, 44, 58, 71, 83, 85, 87, 97, 100

[241] P. B. Blakie, D. Baillie, and R. N. Bisset, "Roton spectroscopy in a harmonically trapped dipolar Bose-Einstein condensate", Phys. Rev. A **86**, 021604 (2012). pp. 27, 33, 71, 86–88, 97, 100

[242] D. O'Dell, S. Giovanazzi, G. Kurizki, and V. M. Akulin, "Bose-Einstein Condensates with $1/r$ Interatomic Attraction: Electromagnetically Induced "Gravity"", Phys. Rev. Lett. **84**, 5687 (2000). p. 27

[243] I. Papadopoulos, P. Wagner, G. Wunner, and J. Main, "Bose-Einstein condensates with attractive $1/r$ interaction: The case of self-trapping", Phys. Rev. A **76**, 053604 (2007). p. 27

[244] G. E. Astrakharchik and B. A. Malomed, "Dynamics of one-dimensional quantum droplets", Phys. Rev. A **98**, 013631 (2018). p. 27

[245] M. Tylutki, G. E. Astrakharchik, B. A. Malomed, and D. S. Petrov, "Collective excitations of a one-dimensional quantum droplet", Phys. Rev. A **101**, 051601 (2020). p. 27

[246] Schmidt, M. and Lassablière, L. and Quéméner, G. and Langen, T., "Self-bound dipolar droplets and supersolids in molecular Bose-Einstein condensates", Phys. Rev. Res. **4**, 013235 (2022). pp. 27, 37–39, 104, 108, 114, 118, 121, 124, 147, 153, 154

[247] N. Bigagli, W. Yuan, S. Zhang, B. Bulatovic, T. Karman, I. Stevenson, and S. Will, "Observation of Bose–Einstein condensation of dipolar molecules", Nature (London), 10.1038/s41586-024-07492-z (2024). pp. 27, 104, 118, 121, 153

[248] S. A. Morgan, S. Choi, K. Burnett, and M. Edwards, "Nonlinear mixing of quasiparticles in an inhomogeneous Bose condensate", Phys. Rev. A **57**, 3818 (1998). pp. 27–29

[249] S. Choi, L. O. Baksmaty, S. J. Woo, and N. P. Bigelow, "Excitation spectrum of vortex lattices in rotating Bose-Einstein condensates", Phys. Rev. A **68**, 031605 (2003). p. 28

[250] L. Jia, A.-B. Wang, and S. Yi, "Low-lying excitations of vortex lattices in condensates with anisotropic dipole-dipole interaction", Phys. Rev. A **97**, 043614 (2018). p. 28

[251] C. W. Gardiner, "Particle-number-conserving Bogoliubov method which demonstrates the validity of the time-dependent Gross-Pitaevskii equation for a highly condensed Bose gas", Phys. Rev. A **56**, 1414 (1997). p. 29

[252] P. B. Blakie, R. J. Ballagh, and C. W. Gardiner, "Theory of coherent Bragg spectroscopy of a trapped Bose-Einstein condensate", Phys. Rev. A **65**, 033602 (2002). pp. 29, 30

[253] W.-C. Wu and A. Griffin, "Quantized hydrodynamic model and the dynamic structure factor for a trapped Bose gas", Phys. Rev. A **54**, 4204 (1996). p. 29

[254] A. R. P. Lima, "Hydrodynamic studies of dipolar quantum gases" (Freie Universität Berlin, 2011). p. 29

[255] F. Zambelli, L. Pitaevskii, D. M. Stamper-Kurn, and S. Stringari, "Dynamic structure factor and momentum distribution of a trapped Bose gas", Phys. Rev. A **61**, 063608 (2000). pp. 30, 63

[256] S. Stringari, "Sum rules for density and particle excitations in Bose superfluids", Phys. Rev. B **46**, 2974 (1992). p. 30

[257] S. M. Roccuzzo, A. Gallemí, A. Recati, and S. Stringari, "Rotating a Supersolid Dipolar Gas", Phys. Rev. Lett. **124**, 045702 (2020). pp. 30, 51, 95

[258] I. Ferrier-Barbut, M. Wenzel, F. Böttcher, T. Langen, M. Isoard, S. Stringari, and T. Pfau, "Scissors Mode of Dipolar Quantum Droplets of Dysprosium Atoms", Phys. Rev. Lett. **120**, 160402 (2018). p. 30

[259] J. Tao, M. Zhao, and I. B. Spielman, "Observation of anisotropic superfluid density in an artificial crystal", Phys. Rev. Lett. **131**, 163401 (2023). pp. 30, 50, 51

[260] C.-L. Hung, X. Zhang, L.-C. Ha, S.-K. Tung, N. Gemelke, and C. Chin, "Extracting density-density correlations from *in situ* images of atomic quantum gases", New J. Phys. **13**, 075019 (2011). pp. 30, 63, 89

[261] C.-L. Hung, X. Zhang, N. Gemelke, and C. Chin, "Observation of scale invariance and universality in two-dimensional Bose gases", Nature (London) **470**, 236 (2011). p. 30

[262] C.-L. Hung, V. Gurarie, and C. Chin, "From Cosmology to Cold Atoms: Observation of Sakharov Oscillations in a Quenched Atomic Superfluid", Science **341**, 1213 (2013). pp. 30, 63, 89

[263] M. Naraschewski and R. J. Glauber, "Spatial coherence and density correlations of trapped bose gases", Phys. Rev. A **59**, 4595 (1999). pp. 30, 63

[264] S. Fölling, F. Gerbier, A. Widera, O. Mandel, T. Gericke, and I. Bloch, "Spatial quantum noise interferometry in expanding ultracold atom clouds", Nature (London) **434**, 481 (2005). p. 30

[265] J. Javanainen, "Spectrum of Light Scattered from a Degenerate Bose Gas", Phys. Rev. Lett. **75**, 1927 (1995). p. 30

[266] Bisset, R., "Theoretical Study of the Trapped Dipolar Bose Gas in the Ultra-Cold Regime", PhD thesis (University of Otago, 2013). pp. 31, 40, 121

[267] M. Klawunn, A. Recati, L. P. Pitaevskii, and S. Stringari, "Local atom-number fluctuations in quantum gases at finite temperature", Phys. Rev. A **84**, 033612 (2011). pp. 31, 35

[268] J. Hofmann and W. Zwerger, "Universal relations for dipolar quantum gases", Phys. Rev. Res. **3**, 013088 (2021). p. 31

[269] J. Hofmann and W. Zwerger, "Deep Inelastic Scattering on Ultracold Gases", Phys. Rev. X **7**, 011022 (2017). p. 31

[270] R. J. Donnelly, J. A. Donnelly, and R. N. Hills, "Specific heat and dispersion curve for helium II", J. Low Temp. Phys. **44**, 471 (1981). p. 31

[271] Q. Zhou and T.-L. Ho, "Universal Thermometry for Quantum Simulation", Phys. Rev. Lett. **106**, 225301 (2011). p. 31

[272] T. Hartke, B. Oreg, N. Jia, and M. Zwierlein, "Doublon-Hole Correlations and Fluctuation Thermometry in a Fermi-Hubbard Gas", Phys. Rev. Lett. **125**, 113601 (2020). p. 31

[273] J. Dunkel, "Nonlinear Dynamics II: Continuum Systems", MIT OpenCourseWare (2015). pp. 32, 35

[274] J. E. Pearson, "Complex patterns in a simple system", Science **261**, 189 (1993). pp. 32, 153

[275] J. Swift and P. C. Hohenberg, "Hydrodynamic fluctuations at the convective instability", Phys. Rev. A **15**, 319 (1977). p. 32

[276] J. Dunkel, S. Heidenreich, M. Bär, and R. E. Goldstein, "Minimal continuum theories of structure formation in dense active fluids", New J. Phys. **15**, 045016 (2013). pp. 32, 103, 153

[277] Z.-Q. Yu, "Landau criterion for an anisotropic Bose-Einstein condensate", Phys. Rev. A **95**, 033618 (2017). p. 33

[278] M. Wenzel, F. Böttcher, J.-N. Schmidt, M. Eisenmann, T. Langen, T. Pfau, and I. Ferrier-Barbut, "Anisotropic Superfluid Behavior of a Dipolar Bose-Einstein Condensate", Phys. Rev. Lett. **121**, 030401 (2018). p. 33

[279] M. Klawunn and L. Santos, "Hybrid multisite excitations in dipolar condensates in optical lattices", Phys. Rev. A **80**, 013611 (2009). p. 33

[280] U. R. Fischer, "Stability of quasi-two-dimensional Bose-Einstein condensates with dominant dipole-dipole interactions", Phys. Rev. A **73**, 031602 (2006). p. 33

[281] P. Nozières, "Is the Roton in Superfluid ^{4}He the Ghost of a Bragg Spot?", J. Low Temp. Phys. **137**, 45 (2004). p. 34

[282] I. Ferrier-Barbut, M. Wenzel, M. Schmitt, F. Böttcher, and T. Pfau, "Onset of a modulational instability in trapped dipolar Bose-Einstein condensates", Phys. Rev. A **97**, 011604 (2018). pp. 35, 110, 156

[283] R. M. Wilson, S. Ronen, and J. L. Bohn, "Stability and excitations of a dipolar Bose-Einstein condensate with a vortex", Phys. Rev. A **79**, 013621 (2009). pp. 35, 71, 87, 97

[284] V. Heinonen, K. J. Burns, and J. Dunkel, "Quantum hydrodynamics for supersolid crystals and quasicrystals", Phys. Rev. A **99**, 063621 (2019). pp. 35, 103, 113, 153

[285] M. D. Cowley and R. E. Rosensweig, "The interfacial stability of a ferromagnetic fluid", J. Fluid Mech. **30**, 671 (1967). p. 35

[286] J. V. I. Timonen, M. Latikka, L. Leibler, R. H. A. Ras, and O. Ikkala, "Switchable Static and Dynamic Self-Assembly of Magnetic Droplets on Superhydrophobic Surfaces", Science **341**, 253 (2013). p. 35

[287] G. Baym and C. J. Pethick, "Ground-State Properties of Magnetically Trapped Bose-Condensed Rubidium Gas", Phys. Rev. Lett. **76**, 6 (1996). p. 35

[288] V. M. Pérez-García, H. Michinel, J. I. Cirac, M. Lewenstein, and P. Zoller, "Low Energy Excitations of a Bose-Einstein Condensate: A Time-Dependent Variational Analysis", Phys. Rev. Lett. **77**, 5320 (1996). p. 35

[289] S. Giovanazzi, A. Görlitz, and T. Pfau, "Ballistic expansion of a dipolar condensate", J. Opt. B **5**, S208 (2003). p. 35

[290] R. M. W. van Bijnen, N. G. Parker, S. J. J. M. F. Kokkelmans, A. M. Martin, and D. H. J. O'Dell, "Collective excitation frequencies and stationary states of trapped dipolar Bose-Einstein condensates in the Thomas-Fermi regime", Phys. Rev. A **82**, 033612 (2010). p. 35

[291] J. Stuhler, A. Griesmaier, T. Koch, M. Fattori, T. Pfau, S. Giovanazzi, P. Pedri, and L. Santos, "Observation of Dipole-Dipole Interaction in a Degenerate Quantum Gas", Phys. Rev. Lett. **95**, 150406 (2005). p. 36

[292] T. Lahaye, T. Koch, B. Fröhlich, M. Fattori, J. Metz, A. Griesmaier, S. Giovanazzi, and T. Pfau, "Strong dipolar effects in a quantum ferrofluid", Nature (London) **448**, 672 (2007). pp. 36, 38

[293] E. Poli, T. Bland, C. Politi, L. Klaus, M. A. Norcia, F. Ferlaino, R. N. Bisset, and L. Santos, "Maintaining supersolidity in one and two dimensions", Phys. Rev. A **104**, 063307 (2021). pp. 37, 97, 116

[294] L. Lavoine and T. Bourdel, "Beyond-mean-field crossover from one dimension to three dimensions in quantum droplets of binary mixtures", Phys. Rev. A **103**, 033312 (2021). p. 37

[295] C. Eberlein, S. Giovanazzi, and D. H. J. O'Dell, "Exact solution of the Thomas-Fermi equation for a trapped Bose-Einstein condensate with dipole-dipole interactions", Phys. Rev. A **71**, 033618 (2005). pp. 38, 87

[296] A. Bulgac, "Dilute Quantum Droplets", Phys. Rev. Lett. **89**, 050402 (2002). pp. 38, 103, 106

[297] M. Schmitt, "A Self-bound Dilute Quantum Liquid of Dysprosium Atoms", PhD thesis (University of Stuttgart, 2017). p. 38

[298] S. Stringari and J. Treiner, "Surface properties of liquid ^{3}He and ^{4}He: A density-functional approach", Phys. Rev. B **36**, 8369 (1987). p. 38

[299] F. Dalfovo, A. Lastri, L. Pricaupenko, S. Stringari, and J. Treiner, "Structural and dynamical properties of superfluid helium: A density-functional approach", Phys. Rev. B **52**, 1193 (1995). p. 38

[300] M. Schmidt, "Numerical studies of dipolar supersolids in two dimensions", Master's thesis (University of Stuttgart, 2020). pp. 39, 90, 99, 116

[301] N. Adhvaryu, "Dipolar Quantum Gases under Rotation", Master's thesis (University of Stuttgart, 2023). p. 39

[302] Y.-C. Zhang, T. Pohl, and F. Maucher, "Phases of supersolids in confined dipolar Bose-Einstein condensates", Phys. Rev. A **104**, 013310 (2021). pp. 39, 104, 106, 108, 110, 114–117, 147, 152

[303] MathWorks, *MATLAB documentation*, `https://www.mathworks.com/help/matlab/` (visited on 06/04/2024). p. 39

[304] S. M. Roccuzzo, "Supersolidity in a dipolar quantum gas", PhD thesis (University of Trento, 2021). pp. 40, 75

[305] W. Bao, Q. Du, and Y. Zhang, "Dynamics of Rotating Bose–Einstein Condensates and its Efficient and Accurate Numerical Computation", SIAM J. Appl. Math. **66**, 758 (2006). p. 40

[306] B. Xiong, J. Gong, H. Pu, W. Bao, and B. Li, "Symmetry breaking and self-trapping of a dipolar bose-einstein condensate in a double-well potential", Phys. Rev. A **79**, 013626 (2009). p. 40

[307] C. F. Barenghi and N. G. Parker, *A primer on quantum fluids* (SpringerBriefs in Physics, 2016). pp. 40, 41

[308] W. Bao, D. Jaksch, and P. A. Markowich, "Numerical solution of the Gross-Pitaevskii equation for Bose-Einstein condensation", J. Comp. Phys. **187**, 318 (2003). p. 40

[309] S. MacNamara and G. Strang, "Operator splitting", edited by R. Glowinski, S. J. Osher, and W. Yin, 95 (2016). p. 40

[310] M. Modugno, L. Pricoupenko, and Y. Castin, "Bose-Einstein condensates with a bent vortex in rotating traps", Eur. Phys. J. D **22**, 235 (2003). p. 41

[311] D. Baillie and P. B. Blakie, "Droplet Crystal Ground States of a Dipolar Bose Gas", Phys. Rev. Lett. **121**, 195301 (2018). pp. 41, 96, 116

[312] Wilson, R. M., "Manifestations of the Roton in Dipolar Bose-Einstein Condensates", PhD thesis (University of Colorado, 2011). pp. 41–43, 121

[313] X. Antoine, A. Levitt, and Q. Tang, "Efficient spectral computation of the stationary states of rotating Bose–Einstein condensates by preconditioned nonlinear conjugate gradient methods", J. Comp. Phys. **343**, 92 (2017). pp. 41–43

[314] X. Antoine, Q. Tang, and Y. Zhang, "A Preconditioned Conjugated Gradient Method for Computing Ground States of Rotating Dipolar Bose-Einstein Condensates via Kernel Truncation Method for Dipole-Dipole Interaction Evaluation", Comm. Comp. Phys. **24**, 966 (2018). pp. 41–43

[315] E. Aybar and M. Ö. Oktel, "Temperature-dependent density profiles of dipolar droplets", Phys. Rev. A **99**, 013620 (2019). pp. 42, 65, 82, 153

[316] J. Sánchez-Baena, C. Politi, F. Maucher, F. Ferlaino, and T. Pohl, "Heating a dipolar quantum fluid into a solid", Nature Commun. **14**, 1868 (2023). pp. 42, 57, 65, 82, 153

[317] J. Sánchez-Baena, T. Pohl, and F. Maucher, "Superfluid-supersolid phase transition of elongated dipolar Bose-Einstein condensates at finite temperatures", Phys. Rev. Res. **6**, 023183 (2024). pp. 42, 57, 65, 82, 153

[318] A. Edelman, T. A. Arias, and S. T. Smith, "The Geometry of Algorithms with Orthogonality Constraints", SIAM J. on Matrix Analysis and Applications **20**, 303 (1998). p. 43

[319] J.-F. Mennemann, D. Matthes, R.-M. Weishäupl, and T. Langen, "Optimal control of Bose–Einstein condensates in three dimensions", New J. Phys. **17**, 113027 (2015). p. 44

[320] J.-F. Mennemann, T. Langen, L. Exl, and N. Mauser, "Optimal control of the self-bound dipolar droplet formation process", Comp. Phys. Comm. **244**, 205 (2019). pp. 44, 99

[321] A. G. Baydin, B. A. Pearlmutter, A. A. Radul, and J. M. Siskind, "Automatic Differentiation in Machine Learning: a Survey", J. of Machine Learning Res. **18**, 1 (2018). p. 44

[322] A. D. Martin and P. B. Blakie, "Stability and structure of an anisotropically trapped dipolar Bose-Einstein condensate: Angular and linear rotons", Phys. Rev. A **86**, 053623 (2012). pp. 44, 87, 97

[323] G. W. Stewart, "A Krylov–Schur Algorithm for Large Eigenproblems", SIAM J. on Matrix Analysis and Applications **23**, 601 (2002). p. 44

[324] K. Góral, L. Santos, and M. Lewenstein, "Quantum phases of dipolar bosons in optical lattices", Phys. Rev. Lett. **88**, 170406 (2002). p. 47

[325] S. Yi, T. Li, and C. P. Sun, "Novel Quantum Phases of Dipolar Bose Gases in Optical Lattices", Phys. Rev. Lett. **98**, 260405 (2007). p. 48

[326] O. Dutta, M. Gajda, P. Hauke, M. Lewenstein, D.-S. Lühmann, B. A. Malomed, T. Sowiński, and J. Zakrzewski, "Non-standard Hubbard models in optical lattices: a review", Rep. Prog. Phys. **78**, 066001 (2015). pp. 48, 154

[327] J. Zhang, C. Zhang, J. Yang, and B. Capogrosso-Sansone, "Supersolid phases of lattice dipoles tilted in three dimensions", Phys. Rev. A **105**, 063302 (2022). p. 48

[328] A. J. Leggett, "Can a Solid Be "Superfluid"?", Phys. Rev. Lett. **25**, 1543 (1970). pp. 49–51, 84

[329] A. J. Leggett, "On the Superfluid Fraction of an Arbitrary Many-Body System at $T = 0$", J. Stat. Phys. **93**, 927 (1998). pp. 49–51

[330] L. Chomaz, "Probing the supersolid order via high-energy scattering: Analytical relations among the response, density modulation, and superfluid fraction", Phys. Rev. A **102**, 023333 (2020). pp. 50, 51

[331] J. C. Smith, D. Baillie, and P. B. Blakie, "Supersolidity and crystallization of a dipolar Bose gas in an infinite tube", Phys. Rev. A **107**, 033301 (2023). pp. 50, 51, 53

[332] A. Smerzi, S. Fantoni, S. Giovanazzi, and S. R. Shenoy, "Quantum Coherent Atomic Tunneling between Two Trapped Bose-Einstein Condensates", Phys. Rev. Lett. **79**, 4950 (1997). p. 50

[333] R. Gati and M. K. Oberthaler, "A bosonic Josephson junction", J. Phys. B: At. Mol. Opt. Phys. **40**, R61 (2007). p. 50

[334] S. Giovanazzi, J. Esteve, and M. K. Oberthaler, "Effective parameters for weakly coupled Bose–Einstein condensates", New J. Phys. **10**, 045009 (2008). p. 50

[335] A. Aftalion, X. Blanc, and R. L. Jerrard, "Nonclassical Rotational Inertia of a Supersolid", Phys. Rev. Lett. **99**, 135301 (2007). pp. 50, 51

[336] B. T. E. Ripley, D. Baillie, and P. B. Blakie, "Two-dimensional supersolidity in a planar dipolar bose gas", Phys. Rev. A **108**, 053321 (2023). pp. 50, 104, 106–108, 110, 114, 116, 117

[337] P. B. Blakie, "Superfluid fraction tensor of a two-dimensional supersolid", J. Phys. B. **57**, 115301 (2024). pp. 50, 51, 104

[338] P. B. Blakie, L. Chomaz, D. Baillie, and F. Ferlaino, "Compressibility and speeds of sound across the superfluid-to-supersolid phase transition of an elongated dipolar gas", Phys. Rev. Res. **5**, 033161 (2023). pp. 50, 53, 69, 72, 74, 75, 77, 81, 163

[339] G. Chauveau, C. Maury, F. Rabec, C. Heintze, G. Brochier, S. Nascimbene, J. Dalibard, J. Beugnon, S. M. Roccuzzo, and S. Stringari, "Superfluid Fraction in an Interacting Spatially Modulated Bose-Einstein Condensate", Phys. Rev. Lett. **130**, 226003 (2023). pp. 50, 51

[340] A. Gallemí, S. M. Roccuzzo, S. Stringari, and A. Recati, "Quantized vortices in dipolar supersolid Bose-Einstein-condensed gases", Phys. Rev. A **102**, 023322 (2020). pp. 51, 85

[341] Tengstrand, M Nilsson and Boholm, David and Sachdeva, Rashi and Bengtsson, Jakob and Reimann, SM, "Persistent currents in toroidal dipolar supersolids", Phys. Rev. A **103**, 013313 (2021). pp. 51, 69

[342] N. Sepúlveda, C. Josserand, and S. Rica, "Nonclassical rotational inertia fraction in a one-dimensional model of a supersolid", Phys. Rev. B **77**, 054513 (2008). p. 51

[343] Sepúlveda, N., Josserand, C., and Rica, S., "Superfluid density in a two-dimensional model of supersolid", Eur. Phys. J. B **78**, 439 (2010). p. 51

[344] F. Ancilotto, M. Rossi, and F. Toigo, "Supersolid structure and excitation spectrum of soft-core bosons in three dimensions", Phys. Rev. A **88**, 033618 (2013). pp. 51, 53

[345] G. Biagioni, "Can a superfluid be solid? A study of the supersolid phase in a dipolar quantum gas", PhD thesis (University of Florence, 2023). pp. 51, 81, 148, 152

[346] N. Preti, N. Antolini, G. Biagioni, A. Fioretti, G. Modugno, L. Tanzi, and C. Gabbanini, "A blue repulsive potential for dysprosium Bose-Einstein condensates", arXiv:2403.18677 (2024). pp. 51, 81, 152

[347] M. Šindik, T. Zawi ślak, A. Recati, and S. Stringari, "Sound, superfluidity, and layer compressibility in a ring dipolar supersolid", Phys. Rev. Lett. **132**, 146001 (2024). pp. 51, 68, 71, 72, 74, 78, 80, 81

[348] J. C. Smith, D. Baillie, and P. B. Blakie, "Quantum Droplet States of a Binary Magnetic Gas", Phys. Rev. Lett. **126**, 025302 (2021). pp. 51, 97

[349] Y. Pomeau and S. Rica, "Dynamics of a model of supersolid", Phys. Rev. Lett. **72**, 2426 (1994). p. 53

[350] S. Saccani, S. Moroni, and M. Boninsegni, "Excitation Spectrum of a Supersolid", Phys. Rev. Lett. **108**, 175301 (2012). pp. 53, 69, 95, 114

[351] Cinti, F. and Macrì, T. and Lechner, W. and Pupillo, G. and Pohl, T., "Defect-induced supersolidity with soft-core bosons", Nature Commun. **5**, 3235 (2014). pp. 53, 69, 114

[352] G. Biagioni, N. Antolini, A. Alaña, M. Modugno, A. Fioretti, C. Gabbanini, L. Tanzi, and G. Modugno, "Dimensional crossover in the superfluid-supersolid quantum phase transition", Phys. Rev. X **12**, 021019 (2022). p. 53

[353] Y.-C. Zhang, V. Walther, and T. Pohl, "Self-bound droplet clusters in laser-driven Bose-Einstein condensates", Phys. Rev. A **103**, 023308 (2021). pp. 53, 103, 113

[354] P. B. Blakie, D. Baillie, L. Chomaz, and F. Ferlaino, "Supersolidity in an elongated dipolar condensate", Phys. Rev. Res. **2**, 043318 (2020). p. 53

[355] C. R. Cabrera, L. Tanzi, J. Sanz, B. Naylor, P. Thomas, P. Cheiney, and L. Tarruell, "Quantum liquid droplets in a mixture of Bose-Einstein condensates", Science **359**, 301 (2018). p. 56

[356] W. Kohn, "Cyclotron resonance and de Haas-van Alphen oscillations of an interacting electron gas", Phys. Rev. **123**, 1242 (1961). pp. 58, 87

[357] J. F. Dobson, "Harmonic-Potential Theorem: Implications for Approximate Many-Body Theories", Phys. Rev. Lett. **73**, 2244 (1994). p. 58

[358] S. Pal, D. Baillie, and P. B. Blakie, "Excitations and number fluctuations in an elongated dipolar Bose-Einstein condensate", Phys. Rev. A **102**, 043306 (2020). pp. 62, 64

[359] J. Steinhauer, R. Ozeri, N. Katz, and N. Davidson, "Peak in the static structure factor of a Bose-Einstein condensate", Phys. Rev. A **72**, 023608 (2005). p. 63

[360] M. Schemmer, A. Johnson, and I. Bouchoule, "Monitoring squeezed collective modes of a one-dimensional Bose gas after an interaction quench using density-ripple analysis", Phys. Rev. A **98**, 043604 (2018). pp. 63, 89

[361] J. Esteve, J.-B. Trebbia, T. Schumm, A. Aspect, C. I. Westbrook, and I. Bouchoule, "Observations of Density Fluctuations in an Elongated Bose Gas: Ideal Gas and Quasicondensate Regimes", Phys. Rev. Lett. **96**, 130403 (2006). pp. 63, 89

[362] A. Imambekov, I. E. Mazets, D. S. Petrov, V. Gritsev, S. Manz, S. Hofferberth, T. Schumm, E. Demler, and J. Schmiedmayer, "Density ripples in expanding low-dimensional gases as a probe of correlations", Phys. Rev. A **80**, 033604 (2009). pp. 63, 89

[363] J. Armijo, T. Jacqmin, K. V. Kheruntsyan, and I. Bouchoule, "Probing three-body correlations in a quantum gas using the measurement of the third moment of density fluctuations", Phys. Rev. Lett. **105**, 230402 (2010). pp. 63, 89

[364] T. Jacqmin, J. Armijo, T. Berrada, K. V. Kheruntsyan, and I. Bouchoule, "Sub-Poissonian Fluctuations in a 1D Bose Gas: From the Quantum Quasicondensate to the Strongly Interacting Regime", Phys. Rev. Lett. **106**, 230405 (2011). pp. 63, 89

[365] A. Blumkin, S. Rinott, R. Schley, A. Berkovitz, I. Shammass, and J. Steinhauer, "Observing Atom Bunching by the Fourier Slice Theorem", Phys. Rev. Lett. **110**, 265301 (2013). p. 63

[366] B. Efron, "Bootstrap methods: another look at the jackknife", Ann. Statist. **7**, 1 (1979). pp. 64, 91

[367] B. Efron and R. J. Tibshirani, *An introduction to the bootstrap*, Monographs on Statistics and Applied Probability 57 (Chapman & Hall, New York, 1993). p. 64

[368] D. N. Politis and J. P. Romano, "Large Sample Confidence Regions Based on Subsamples under Minimal Assumptions", Ann. Stat. **22**, 2031 (1994). p. 64

[369] D. N. Politis, J. P. Romano, and M. Wolf, *Subsampling* (Springer, New York, 1999). p. 64

[370] P. B. Blakie, D. Baillie, and S. Pal, "Variational theory for the ground state and collective excitations of an elongated dipolar condensate", Comm. Theor. Phys. **72**, 085501 (2020). p. 64

[371] D. Petter, A. Patscheider, G. Natale, M. J. Mark, M. A. Baranov, R. van Bijnen, S. M. Roccuzzo, A. Recati, B. Blakie, D. Baillie, L. Chomaz, and F. Ferlaino, "Bragg scattering of an ultracold dipolar gas across the phase transition from Bose-Einstein condensate to supersolid in the free-particle regime", Phys. Rev. A **104**, L011302 (2021). pp. 65, 96, 152

[372] R. Dubessy, C. De Rossi, T. Badr, L. Longchambon, and H. Perrin, "Imaging the collective excitations of an ultracold gas using statistical correlations", New J. Phys. **16**, 122001 (2014). pp. 65, 156, 157

[373] S. Balibar, "The enigma of supersolidity", Nature (London) **464**, 176 (2010). pp. 68, 84

[374] Schmitt, Andreas, "Introduction to superfluidity", Lect. Notes Phys **888** (2015). p. 68

[375] K. R. Atkins, "Third and Fourth Sound in Liquid Helium II", Phys. Rev. **113**, 962 (1959). p. 68

[376] Donnelly, Russell J., "The two-fluid theory and second sound in liquid helium", Phys. Today **62**, 34 (2009). pp. 68, 78

[377] L. Tanzi, S. M. Roccuzzo, E. Lucioni, F. Famà, A. Fioretti, C. Gabbanini, G. Modugno, A. Recati, and S. Stringari, "Supersolid symmetry breaking from compressional oscillations in a dipolar quantum gas", Nature (London) **574**, 382 (2019). p. 68

[378] L. Tanzi, J. G. Maloberti, G. Biagioni, A. Fioretti, C. Gabbanini, and G. Modugno, "Evidence of superfluidity in a dipolar supersolid from nonclassical rotational inertia", Science **371**, 1162 (2021). pp. 68, 83, 96

[379] Mukherjee, K. and Reimann, S. M., "Classical-linear-chain behavior from dipolar droplets to supersolids", Phys. Rev. A **107**, 043319 (2023). p. 68

[380] G. Biagioni, N. Antolini, B. Donelli, L. Pezzè, A. Smerzi, M. Fattori, A. Fioretti, C. Gabbanini, M. Inguscio, L. Tanzi, and G. Modugno, "Measurement of the superfluid fraction of a supersolid by josephson effect", Nature (London), 10.1038/s41586-024-07361-9 (2024). p. 68

[381] Yoo C.-D. and Dorsey A. T., "Hydrodynamic theory of supersolids: Variational principle, effective Lagrangian, and density-density correlation function", Phys. Rev. B **81**, 134518 (2010). p. 68

[382] J. Hofmann and W. Zwerger, "Hydrodynamics of a superfluid smectic", J. Stat. Mech.: Theory and Experiment **2021**, 033104 (2021). pp. 68, 72, 74

[383] L. M. Platt, D. Baillie, and P. Blakie, "Sounds waves and fluctuations in one-dimensional supersolids", arXiv:2403.19151 (2024). pp. 68, 69, 74, 81

[384] N. Navon, R. P. Smith, and Z. Hadzibabic, "Quantum gases in optical boxes", Nat. Phys. **17**, 1334 (2021). pp. 68, 71

[385] T. A. Hilker, L. H. Dogra, C. Eigen, J. A. P. Glidden, R. P. Smith, and Z. Hadzibabic, "First and Second Sound in a Compressible 3D Bose Fluid", Phys. Rev. Lett. **128**, 223601 (2022). p. 69

[386] Z. Yan, P. B. Patel, B. Mukherjee, C. J. Vale, R. J. Fletcher, and M. W. Zwierlein, "Thermography of the superfluid transition in a strongly interacting Fermi gas", Science **383**, 629 (2024). pp. 69, 78

[387] S. M. Roccuzzo, S. Stringari, and A. Recati, "Supersolid edge and bulk phases of a dipolar quantum gas in a box", Phys. Rev. Res. **4**, 013086 (2022). pp. 69, 81, 117

[388] P. Juhász, M. Krstaji ć, D. Strachan, E. Gandar, and R. P. Smith, "How to realize a homogeneous dipolar Bose gas in the roton regime", Phys. Rev. A **105**, L061301 (2022). pp. 69, 81, 117

[389] L. Amico et al., "Roadmap on Atomtronics: State of the art and perspective", AVS Quantum Science **3**, 039201 (2021). p. 69

[390] T. Bland, I. V. Yatsuta, M. Edwards, Y. O. Nikolaieva, A. O. Oliinyk, A. I. Yakimenko, and N. P. Proukakis, "Persistent current oscillations in a double-ring quantum gas", Phys. Rev. Res. **4**, 043171 (2022). p. 69

[391] T. Bland and Q. Marolleau and P. Comaron and B. A. Malomed and N. P. Proukakis, "Persistent current formation in double-ring geometries", J. Phys. B: At. Mol. Opt. Phys. **53**, 115301 (2020). p. 69

[392] Nilsson Tengstrand, M. and Stürmer, P. and Ribbing, J. and Reimann, S. M., "Toroidal dipolar supersolid with a rotating weak link", Phys. Rev. A **107**, 063316 (2023). p. 69

[393] R. M. Wilson, S. Ronen, J. L. Bohn, and H. Pu, "Manifestations of the roton mode in dipolar bose-einstein condensates", Phys. Rev. Lett. **100**, 245302 (2008). pp. 71, 83, 85, 87, 97

[394] R. M. Wilson, S. Ronen, and J. L. Bohn, "Angular collapse of dipolar Bose-Einstein condensates", Phys. Rev. A **80**, 023614 (2009). pp. 71, 83, 87, 97, 110

[395] R. M. Wilson, C. Ticknor, J. L. Bohn, and E. Timmermans, "Roton immiscibility in a two-component dipolar Bose gas", Phys. Rev. A **86**, 033606 (2012). pp. 71, 104

[396] M. Šindik, T. Zawi ślak, A. Recati, and S. Stringari, "Sound, superfluidity and layer compressibility in a ring dipolar supersolid", arXiv:2308.05981v1, 2024. pp. 74, 78, 80

[397] G. Biagioni, "Evidence of superfluidity in a dipolar supersolid through non-classical rotational inertia." Master's thesis (University of Florence, 2019). p. 75

[398] E. Taylor, H. Hu, X.-J. Liu, L. P. Pitaevskii, A. Griffin, and S. Stringari, "First and second sound in a strongly interacting Fermi gas", Phys. Rev. A **80**, 053601 (2009). p. 78

[399] L. A. Sidorenkov, M. K. Tey, R. Grimm, Y.-H. Hou, L. Pitaevskii, and S. Stringari, "Second sound and the superfluid fraction in a Fermi gas with resonant interactions", Nature (London) **498**, 78 (2013). p. 78

[400] H. Li, E. Halperin, S. Ronen, and J. L. Bohn, "Merging dipolar supersolids in a double-well potential", Phys. Rev. A **109**, 013307 (2024). pp. 78, 104

[401] L. Klaus, T. Bland, E. Poli, C. Politi, G. Lamporesi, E. Casotti, R. N. Bisset, M. J. Mark, and F. Ferlaino, "Observation of vortices and vortex stripes in a dipolar condensate", Nat. Phys. **18**, 1453 (2022). p. 81

[402] M. A. Norcia, C. Politi, L. Klaus, E. Poli, M. Sohmen, M. J. Mark, R. N. Bisset, L. Santos, and F. Ferlaino, "Two-dimensional supersolidity in a dipolar quantum gas", Nature (London) **596**, 357 (2021). pp. 84, 97, 99, 102, 153

[403] T. Bland, E. Poli, C. Politi, L. Klaus, M. A. Norcia, F. Ferlaino, L. Santos, and R. N. Bisset, "Two-dimensional supersolid formation in dipolar condensates", Phys. Rev. Lett. **128**, 195302 (2022). pp. 84, 99, 102, 151, 153

[404] A. S. Arkhipov, G. E. Astrakharchik, A. V. Belikov, and Y. E. Lozovik, "Ground-state properties of a one-dimensional system of dipoles", J. Exp. Theor. Phys. Lett. **82**, 39 (2005). pp. 86, 88

[405] G. E. Astrakharchik, J. Boronat, I. L. Kurbakov, and Y. E. Lozovik, "Quantum Phase Transition in a Two-Dimensional System of Dipoles", Phys. Rev. Lett. **98**, 060405 (2007). pp. 86, 88

[406] P. B. Blakie, D. Baillie, and R. N. Bisset, "Depletion and fluctuations of a trapped dipolar Bose-Einstein condensate in the roton regime", Phys. Rev. A **88**, 013638 (2013). pp. 86, 88

[407] O. Dutta and P. Meystre, "Ground-state structure and stability of dipolar condensates in anisotropic traps", Phys. Rev. A **75**, 053604 (2007). pp. 87, 97

[408] T. Macrì, F. Maucher, F. Cinti, and T. Pohl, "Elementary excitations of ultracold soft-core bosons across the superfluid-supersolid phase transition", Phys. Rev. A **87**, 061602 (2013). pp. 95, 114

[409] Z.-K. Lu, Y. Li, D. S. Petrov, and G. V. Shlyapnikov, "Stable Dilute Supersolid of Two-Dimensional Dipolar Bosons", Phys. Rev. Lett. **115**, 075303 (2015). pp. 95, 103, 104, 106, 107

[410] M. A. Norcia, E. Poli, C. Politi, L. Klaus, T. Bland, M. J. Mark, L. Santos, R. N. Bisset, and F. Ferlaino, "Can Angular Oscillations Probe Superfluidity in Dipolar Supersolids?", Phys. Rev. Lett. **129**, 040403 (2022). pp. 96, 99, 151, 156

[411] M. S. Dresselhaus, G. Dresselhaus, and A. Jorio, *Group Theory, Applications to the Physics of Condensed Matter* (Springer-Verlag Berlin Heidelberg, 2008). pp. 96, 158

[412] S. Fishman, G. De Chiara, T. Calarco, and G. Morigi, "Structural phase transitions in low-dimensional ion crystals", Phys. Rev. B **77**, 064111 (2008). p. 96

[413] K. Pyka, J. Keller, H. L. Partner, R. Nigmatullin, T. Burgermeister, D. M. Meier, K. Kuhlmann, A. Retzker, M. B. Plenio, W. H. Zurek, A. del Campo, and T. E. Mehlstäubler, "Topological defect formation and spontaneous symmetry breaking in ion Coulomb crystals", Nat. Comm. **4**, 2291 (2013). p. 96

[414] P. B. Blakie, A. S. Bradley, M. J. Davis, R. J. Ballagh, and C. W. Gardiner, "Dynamics and statistical mechanics of ultra-cold Bose gases using c-field techniques", Adv. Phys. **57**, 363 (2008). p. 97

[415] S. R. Jammalamadaka and A. SenGupta, *Topics in Circular Statistics* (World Scientific, 2001). p. 99

[416] P. Ilzhöfer, M. Sohmen, G. Durastante, C. Politi, A. Trautmann, G. Natale, G. Morpurgo, T. Giamarchi, L. Chomaz, M. J. Mark, and F. Ferlaino, "Phase coherence in out-of-equilibrium supersolid states of ultracold dipolar atoms", Nat. Phys. **17**, 356 (2021). p. 99

[417] A. Alaña, N. Antolini, G. Biagioni, I. L. Egusquiza, and M. Modugno, "Crossing the superfluid-supersolid transition of an elongated dipolar condensate", Phys. Rev. A **106**, 043313 (2022). p. 99

[418] A. Alaña, I. L. Egusquiza, and M. Modugno, "Supersolid formation in a dipolar condensate by roton instability", Phys. Rev. A **108**, 033316 (2023). p. 99

[419] A. Alaña, "Supersolid-formation-time shortcut and excitation reduction by manipulating the dynamical instability", Phys. Rev. A **109**, 023308 (2024). p. 99

[420] E. Casotti, E. Poli, L. Klaus, A. Litvinov, C. Ulm, C. Politi, M. J. Mark, T. Bland, and F. Ferlaino, "Observation of vortices in a dipolar supersolid", arXiv:2403.18510 (2024). p. 102

[421] R. E. Rosensweig, M. Zahn, and R. Shumovich, "Labyrinthine instability in magnetic and dielectric fluids", J. Magnetism and Magnetic Materials **39**, 127 (1983). pp. 103, 107, 109, 110, 112

[422] A. J. Dickstein, S. Erramilli, R. E. Goldstein, D. P. Jackson, and S. A. Langer, "Labyrinthine Pattern Formation in Magnetic Fluids", Science **261**, 1012 (1993). pp. 103, 107, 109–112

[423] D. P. Jackson, R. E. Goldstein, and A. O. Cebers, "Hydrodynamics of fingering instabilities in dipolar fluids", Phys. Rev. E **50**, 298 (1994). pp. 103, 109–111

[424] E. Florence, F. Cyrille, J.-C. Bacri, and S. Neveu, "Macro-Organized Patterns in Ferrofluid Layer: Experimental Studies", J. Phys. I France **7**, 711 (1997). pp. 103, 107, 111

[425] J. A. Miranda and E. Alvarez-Lacalle, "Viscosity contrast effects on fingering formation in rotating hele-shaw flows", Phys. Rev. E **72**, 026306 (2005). pp. 103, 109, 110

[426] A. Zakinyan, E. Beketova, and Y. Dikansky, "Flows and instabilities of ferrofluids at the microscale", Microfluidics and Nanofluidics **21**, 88 (2017). pp. 103, 109, 110

[427] S. Grebenev, J. P. Toennies, and A. F. Vilesov, "Superfluidity Within a Small Helium-4 Cluster: The Microscopic Andronikashvili Experiment", Science **279**, 2083 (1998). p. 103

[428] F. Dalfovo and S. Stringari, "Helium nanodroplets and trapped Bose–Einstein condensates as prototypes of finite quantum fluids", J. Chem. Phys. **115**, 10078 (2001). p. 103

[429] J. P. Toennies, A. F. Vilesov, and K. B. Whaley, "Superfluid Helium Droplets: An Ultracold Nanolaboratory", Phys. Today **54**, 31 (2001). p. 103

[430] R. P. Huebener and J. R. Clem, "Magnetic flux structures in superconductors—a conference summary", Rev. Mod. Phys. **46**, 409 (1974). p. 103

[431] A. Cēbers, C. Gourdon, V. Jeudy, and T. Okada, "Normal-state bubbles and lamellae in type-I superconductors", Phys. Rev. B **72**, 014513 (2005). p. 103

[432] R. Prozorov, "Equilibrium Topology of the Intermediate State in Type-I Superconductors of Different Shapes", Phys. Rev. Lett. **98**, 257001 (2007). p. 103

[433] R. Prozorov, A. F. Fidler, J. R. Hoberg, and P. C. Canfield, "Suprafroth in type-I superconductors", Nat. Phys. **4**, 327 (2008). p. 103

[434] E. Ciaramella, M. Tamburrini, and E. Santamato, "Talbot assisted hexagonal beam patterning in a thin liquid crystal film with a single feedback mirror at negative distance", Appl. Phys. Lett. **63**, 1604 (1993). p. 103

[435] W. S. Edwards and S. Fauve, "Patterns and quasi-patterns in the Faraday experiment", J. Fluid Mech. **278**, 123 (1994). p. 103

[436] T. Ackemann, Y. A. Logvin, A. Heuer, and W. Lange, "Transition between positive and negative hexagons in optical pattern formation", Phys. Rev. Lett. **75**, 3450 (1995). p. 103

[437] F. Arecchi, S. Boccaletti, and P. Ramazza, "Pattern formation and competition in nonlinear optics", Phys. Rep. **318**, 1 (1999). p. 103

[438] K. B. W. Buckley, M. A. Metlitski, and A. R. Zhitnitsky, "Neutron Stars as Type-I Superconductors", Phys. Rev. Lett. **92**, 151102 (2004). p. 103

[439] G. Labeyrie, E. Tesio, P. M. Gomes, G.-L. Oppo, W. J. Firth, G. R. M. Robb, A. S. Arnold, R. Kaiser, and T. Ackemann, "Optomechanical self-structuring in a cold atomic gas", Nat. Phot. **8**, 321 (2014). pp. 103, 113

[440] F. Maucher, T. Pohl, S. Skupin, and W. Krolikowski, "Self-organization of light in optical media with competing nonlinearities", Phys. Rev. Lett. **116**, 163902 (2016). pp. 103, 113

[441] F. Maucher, T. Pohl, W. Krolikowski, and S. Skupin, "Pattern formation in the nonlinear Schrödinger equation with competing nonlocal nonlinearities", Optical Data Processing and Storage **3**, 13 (2017). p. 103

[442] Y.-C. Zhang, V. Walther, and T. Pohl, "Long-Range Interactions and Symmetry Breaking in Quantum Gases through Optical Feedback", Phys. Rev. Lett. **121**, 073604 (2018). pp. 103, 106, 113

[443] G. Baio, G. R. M. Robb, A. M. Yao, and G.-L. Oppo, "Optomechanical transport of cold atoms induced by structured light", Phys. Rev. Res. **2**, 023126 (2020). pp. 103, 113

[444] G. Baio, G. R. M. Robb, A. M. Yao, G.-L. Oppo, and T. Ackemann, "Multiple self-organized phases and spatial solitons in cold atoms mediated by optical feedback", Phys. Rev. Lett. **126**, 203201 (2021). p. 103

[445] S. Ostermann, F. Piazza, and H. Ritsch, "Spontaneous Crystallization of Light and Ultracold Atoms", Phys. Rev. X **6**, 021026 (2016). p. 103

[446] S. Ostermann, V. Walther, and S. F. Yelin, "Superglass formation in an atomic BEC with competing long-range interactions", Phys. Rev. Res. **4**, 023074 (2022). p. 103

[447] A. Bartolo, N. Vigne, M. Marconi, G. Beaudoin, K. Pantzas, I. Sagnes, G. Huyet, F. Maucher, S. V. Gurevich, J. Javaloyes, A. Garnache, and M. Giudici, "Temporal localized turing patterns in mode-locked semiconductor lasers", Optica **9**, 1386 (2022). p. 103

[448] K. Nelissen, B. Partoens, and F. M. Peeters, "Bubble, stripe, and ring phases in a two-dimensional cluster with competing interactions", Phys. Rev. E **71**, 066204 (2005). p. 103

[449] Y. H. Liu, L. Y. Chew, and M. Y. Yu, "Self-assembly of complex structures in a two-dimensional system with competing interaction forces", Phys. Rev. E **78**, 066405 (2008). pp. 103, 118

[450] A. J. Archer, C. Ionescu, D. Pini, and L. Reatto, "Theory for the phase behaviour of a colloidal fluid with competing interactions", J. Phys. Cond. Mat. **20**, 415106 (2008). pp. 103, 113, 118

[451] J. von Hardenberg, E. Meron, M. Shachak, and Y. Zarmi, "Diversity of Vegetation Patterns and Desertification", Phys. Rev. Lett. **87**, 198101 (2001). p. 103

[452] I. H. Riedel, K. Kruse, and J. Howard, "A Self-Organized Vortex Array of Hydrodynamically Entrained Sperm Cells", Science **309**, 300 (2005). p. 103

[453] Q.-X. Liu, P. M. J. Herman, W. M. Mooij, J. Huisman, M. Scheffer, H. Olff, and J. van de Koppel, "Pattern formation at multiple spatial scales drives the resilience of mussel bed ecosystems", Nat. Comm. **5**, 5234 (2014). p. 103

[454] D. G. Ravenhall, C. J. Pethick, and J. R. Wilson, "Structure of Matter below Nuclear Saturation Density", Phys. Rev. Lett. **50**, 2066 (1983). pp. 103, 109

[455] N. Chamel and P. Haensel, "Physics of Neutron Star Crusts", Living Rev. Rel. **11**, 10 (2008). pp. 103, 109

[456] M. E. Caplan and C. J. Horowitz, "Colloquium: Astromaterial science and nuclear pasta", Rev. Mod. Phys. **89**, 041002 (2017). pp. 103, 109

[457] G. Ahlers, L. I. Berge, and D. S. Cannell, "Thermal convection in the presence of a first-order phase change", Phys. Rev. Lett. **70**, 2399 (1993). p. 103

[458] S. W. Morris, E. Bodenschatz, D. S. Cannell, and G. Ahlers, "Spiral defect chaos in large aspect ratio Rayleigh-Bénard convection", Phys. Rev. Lett. **71**, 2026 (1993). p. 103

[459] G. Ahlers, S. Grossmann, and D. Lohse, "Heat transfer and large scale dynamics in turbulent Rayleigh-Bénard convection", Rev. Mod. Phys. **81**, 503 (2009). p. 103

[460] H. Saito, Y. Kawaguchi, and M. Ueda, "Ferrofluidity in a Two-Component Dipolar Bose-Einstein Condensate", Phys. Rev. Lett. **102**, 230403 (2009). pp. 104, 107

[461] Y. Kawaguchi and M. Ueda, "Spinor Bose–Einstein condensates", Phys. Rep. **520**, 253 (2012). pp. 104, 107

[462] K.-T. Xi, T. Byrnes, and H. Saito, "Fingering instabilities and pattern formation in a two-component dipolar Bose-Einstein condensate", Phys. Rev. A **97**, 023625 (2018). pp. 104, 107

[463] K. Sasaki, N. Suzuki, D. Akamatsu, and H. Saito, "Rayleigh-Taylor instability and mushroom-pattern formation in a two-component Bose-Einstein condensate", Phys. Rev. A **80**, 063611 (2009). p. 104

[464] S. Gautam and D. Angom, "Rayleigh-Taylor instability in binary condensates", Phys. Rev. A **81**, 053616 (2010). p. 104

[465] T. Kadokura, T. Aioi, K. Sasaki, T. Kishimoto, and H. Saito, "Rayleigh-Taylor instability in a two-component Bose-Einstein condensate with rotational symmetry", Phys. Rev. A **85**, 013602 (2012). p. 104

[466] A. Gallemí and L. Santos, "Superfluid properties of a honeycomb dipolar supersolid", Phys. Rev. A **106**, 063301 (2022). pp. 104, 106, 151

[467] A. B. Steinberg, F. Maucher, S. V. Gurevich, and U. Thiele, "Exploring bifurcations in Bose–Einstein condensates via phase field crystal models", Chaos: An Interdisciplinary Journal of Nonlinear Science **32**, 113112 (2022). p. 104

[468] E. J. Halperin, S. Ronen, and J. L. Bohn, "Frustration in a dipolar bose-einstein condensate introduced by an optical lattice", Phys. Rev. A **107**, L041301 (2023). p. 104

[469] Y.-C. Zhang, T. Pohl, and F. Maucher, "Metastable patterns in one- and two-component dipolar bose-einstein condensates", Phys. Rev. Res. **6**, 023023 (2024). pp. 104, 107, 116, 117

[470] D. Baillie and P. B. Blakie, "A general theory of flattened dipolar condensates", New J. Phys. **17**, 033028 (2015). pp. 104, 112, 114

[471] Y.-C. Zhang and F. Maucher, "Variational Approaches to Two-Dimensionally Symmetry-Broken Dipolar Bose–Einstein Condensates", Atoms **11**, 10.3390/atoms11070102 (2023). pp. 104, 106, 107, 110, 114, 116

[472] M. Arazo, A. Gallemí, M. Guilleumas, R. Mayol, and L. Santos, "Self-bound crystals of antiparallel dipolar mixtures", Phys. Rev. Res. **5**, 043038 (2023). p. 104

[473] A.-C. Lee, D. Baillie, and P. B. Blakie, "Excitations and phase ordering of the spin-stripe phase of a binary dipolar condensate", Phys. Rev. A **109**, 023323 (2024). p. 104

[474] O. Goulko and A. Kent, "The grasshopper problem", Proc. R. Soc. A: Math. Phys. Eng. Sci. **473**, 20170494 (2017). p. 104

[475] D. Llamas, J. Kent-Dobias, K. Chen, A. Kent, and O. Goulko, "Origin of symmetry breaking in the grasshopper model", Phys. Rev. Res. **6**, 023235 (2024). p. 104

[476] E. Poli, T. Bland, S. J. M. White, M. J. Mark, F. Ferlaino, S. Trabucco, and M. Mannarelli, "Glitches in rotating supersolids", Phys. Rev. Lett. **131**, 223401 (2023). p. 104

[477] K. Perlin, "An Image Synthesizer", SIGGRAPH Comp. Graph. **19**, 287 (1985). p. 105

[478] Y. Kora and M. Boninsegni, "Patterned Supersolids in Dipolar Bose Systems", J. Low Temp. Phys. **197**, 337 (2019). p. 106

[479] H. A. Barnes, "The yield stress—a review or 'παντα ρει'—everything flows?", Journal of Non-Newtonian Fluid Mechanics **81**, 133 (1999). p. 107

[480] G. Biroli, C. Chamon, and F. Zamponi, "Theory of the superglass phase", Phys. Rev. B **78**, 224306 (2008). pp. 107, 151

[481] H. Hu and X.-J. Liu, "Collective excitations of a spherical ultradilute quantum droplet", Phys. Rev. A **102**, 053303 (2020). p. 108

[482] Z.-H. Luo, W. Pang, B. Liu, Y.-Y. Li, and B. A. Malomed, "A new form of liquid matter: Quantum droplets", Front. Phys. **16**, 32201 (2020). p. 108

[483] M. Le Berre, E. Ressayre, A. Tallet, Y. Pomeau, and L. Di Menza, "Example of a chaotic crystal: The labyrinth", Phys. Rev. E **66**, 026203 (2002). p. 111

[484] S. Echeverría-Alar and M. G. Clerc, "Labyrinthine patterns transitions", Phys. Rev. Res. **2**, 042036 (2020). p. 111

[485] E. C. McGarrigle, K. T. Delaney, L. Balents, and G. H. Fredrickson, "Emergence of a Spin Microemulsion in Spin-Orbit Coupled Bose-Einstein Condensates", Phys. Rev. Lett. **131**, 173403 (2023). p. 111

[486] M. Jona-Lasinio, K. Łakomy, and L. Santos, "Roton confinement in trapped dipolar Bose-Einstein condensates", Phys. Rev. A **88**, 013619 (2013). pp. 112, 114

[487] T. Macrì, S. Saccani, and F. Cinti, "Ground State and Excitation Properties of Soft-Core Bosons", J. Low Temp. Phys. **177**, 59 (2014). p. 114

[488] Y.-C. Zhang, T. Pohl, and F. Maucher, "Phases of supersolids in confined dipolar bose-einstein condensates", 2021. p. 115

[489] S. Jin, J. Gao, K. Chandrashekara, C. Gölzhäuser, J. Schöner, and L. Chomaz, "Two-dimensional magneto-optical trap of dysprosium atoms as a compact source for efficient loading of a narrow-line three-dimensional magneto-optical trap", Phys. Rev. A **108**, 023719 (2023). pp. 117, 137

[490] G. Anich, R. Grimm, and E. Kirilov, "Comprehensive Characterization of a State-of-the-Art Apparatus for Cold Electromagnetic Dysprosium Dipoles", arXiv:2304.12844 (2023). pp. 117, 139

[491] S. Sachdev, "Kagomé- and triangular-lattice Heisenberg antiferromagnets: Ordering from quantum fluctuations and quantum-disordered ground states with unconfined bosonic spinons", Phys. Rev. B **45**, 12377 (1992). p. 118

[492] M. Kunimi and Y. Kato, "Mean-field and stability analyses of two-dimensional flowing soft-core bosons modeling a supersolid", Phys. Rev. B **86**, 060510 (2012). pp. 118, 151

[493] G. Valtolina, K. Matsuda, W. G. Tobias, J.-R. Li, L. De Marco, and J. Ye, "Dipolar evaporation of reactive molecules to below the Fermi temperature", Nature (London) **588**, 239 (2020). p. 118

[494] N. Bigagli, C. Warner, W. Yuan, S. Zhang, I. Stevenson, T. Karman, and S. Will, "Collisionally stable gas of bosonic dipolar ground-state molecules", Nat. Phys. **19**, 1579 (2023). pp. 118, 121

[495] M. Wenzel, "A dysprosium quantum gas in highly controllable optical traps", Master's thesis (University of Stuttgart, 2015). pp. 120, 125, 140, 141

[496] I. Segal, L. Halicz, and I. T. Platzner, "Isotope ratio measurements of dysprosium by multiple collection inductively coupled plasma mass spectrometry", Int. J. Mass Spectrometry **216**, 177 (2002). p. 120

[497] Ilzhöfer, Philipp, "Creation of Dipolar Quantum Mixtures of Erbium and Dysprosium", PhD thesis (University of Innsbruck, 2014). pp. 120–122, 124, 126, 134, 135, 137, 138

[498] D. A. Steck, "Rubidium 87 D Line Data", available online at `http://steck.us/alkalidata` (revision 2.3.2, 10 September 2023). p. 121

[499] A. R. Griesmaier, "Dipole-dipole interaction in a degenerate quantum gas Bose-Einstein condensation of chromium atoms", PhD thesis (University of Stuttgart, 2007). p. 121

[500] C. W. Martin, R. Zalubas, L. Hagan, and I. for Basic Standards (U.S.), *Atomic Energy Levels - The Rare-Earth Elements* (NSRDS-NBS, 1978). pp. 120, 121

[501] M. Schmitt, "High Resolution Laser Spectroscopy of Dysprosium", Master's thesis (University of Stuttgart, 2012). p. 121

[502] J. Ferch, W. Dankwort, and H. Gebauer, "Hyperfine structure investigations in DyI with the atomic beam magnetic resonance method", Phys. Lett. A **49**, 287 (1974). p. 120

[503] M. Lu, S. H. Youn, and B. L. Lev, "Spectroscopy of a narrow-line laser-cooling transition in atomic dysprosium", Phys. Rev. A **83**, 012510 (2011). pp. 122, 136

[504] V. A. Dzuba, V. V. Flambaum, and Y. V. Stadnik, "Probing Low-Mass Vector Bosons with Parity Nonconservation and Nuclear Anapole Moment Measurements in Atoms and Molecules", Phys. Rev. Lett. **119**, 223201 (2017). p. 122

[505] N. Petersen, M. Trümper, and P. Windpassinger, "Spectroscopy of the 1001-nm transition in atomic dysprosium", Phys. Rev. A **101**, 042502 (2020). p. 122

[506] A. Frisch, K. Aikawa, M. Mark, A. Rietzler, J. Schindler, E. Zupanič, R. Grimm, and F. Ferlaino, "Narrow-line magneto-optical trap for erbium", Phys. Rev. A **85**, 051401 (2012). pp. 122, 135

[507] A. Patscheider, B. Yang, G. Natale, D. Petter, L. Chomaz, M. J. Mark, G. Hovhannesyan, M. Lepers, and F. Ferlaino, "Observation of a narrow inner-shell orbital transition in atomic erbium at 1299 nm", Phys. Rev. Res. **3**, 033256 (2021). p. 122

[508] K. Baumann, N. Q. Burdick, M. Lu, and B. L. Lev, "Observation of low-field Fano-Feshbach resonances in ultracold gases of dysprosium", Phys. Rev. A **89**, 020701 (2014). pp. 122, 142

[509] T. Maier, I. Ferrier-Barbut, H. Kadau, M. Schmitt, M. Wenzel, C. Wink, T. Pfau, K. Jachymski, and P. S. Julienne, "Broad universal feshbach resonances in the chaotic spectrum of dysprosium atoms", Phys. Rev. A **92**, 060702 (2015). p. 122

[510] Y. Tang, A. Sykes, N. Q. Burdick, J. L. Bohn, and B. L. Lev, "s-wave scattering lengths of the strongly dipolar bosons ^{162}Dy and ^{164}Dy", Phys. Rev. A **92**, 022703 (2015). p. 122

[511] Y. Tang, A. G. Sykes, N. Q. Burdick, J. M. DiSciacca, D. S. Petrov, and B. L. Lev, "Anisotropic Expansion of a Thermal Dipolar Bose Gas", Phys. Rev. Lett. **117**, 155301 (2016). p. 122

[512] Y. Tang, W. Kao, K.-Y. Li, S. Seo, K. Mallayya, M. Rigol, S. Gopalakrishnan, and B. L. Lev, "Thermalization near Integrability in a Dipolar Quantum Newton's Cradle", Phys. Rev. X **8**, 021030 (2018). p. 122

[513] J. Kluge, "Design of a Zeeman slower for a second generation experimental setup on quantum degenerate Dysprosium gas", Master's thesis (University of Stuttgart, 2019). pp. 122–124, 133, 134

[514] P. Uerlings, "A novel Quantum Gas Microscope for Dysprosium Atoms: Magnetic-Field Control and Oven Characterization", Master's thesis (University of Stuttgart, 2021). pp. 122–125, 134, 142

[515] W. Lunden, L. Du, M. Cantara, P. Barral, A. O. Jamison, and W. Ketterle, "Enhancing the capture velocity of a dy magneto-optical trap with two-stage slowing", Phys. Rev. A **101**, 063403 (2020). p. 124

[516] G. Casale, "Optischer Transport ultrakalter Dysprosium Atome", Bachelor's thesis (University of Stuttgart, 2023). p. 124

[517] M. E. M. Kob, "High intensity absorption imaging scheme for a Dysprosium quantum gas", Bachelor's thesis (University of Stuttgart, 2023). p. 125

[518] P. Ilzhöfer, G. Durastante, A. Patscheider, A. Trautmann, M. J. Mark, and F. Ferlaino, "Two-species five-beam magneto-optical trap for erbium and dysprosium", Phys. Rev. A **97**, 023633 (2018). pp. 125, 136–139, 152

[519] Baier, S., "An optical dipole trap for Erbium with tunable geometry", Master's thesis (University of Innsbruck, 2012). p. 126

[520] Holzenkamp, P., "An Optical Dipole Trap with Tunable Geometry for Dysprosium", Bachelor's thesis (Heidelberg University, 2022). p. 126

[521] P. Schmidt, "Scattering properties of ultra-cold chromium atoms", PhD thesis (University of Stuttgart, 2003). p. 127

[522] J. Werner, "Observation of Feshbach resonances in an ultracold gas of ^{52}Cr", PhD thesis (University of Stuttgart, 2006). p. 127

[523] Cold Physics Organization, *CPECS, GitHub repository*, `https://github.com/coldphysics/experiment-control` (visited on 05/11/2024). p. 127

[524] P. T. Starkey, C. J. Billington, S. P. Johnstone, M. Jasperse, K. Helmerson, L. D. Turner, and R. P. Anderson, "A scripted control system for autonomous hardware-timed experiments", Rev. Sci. Instrum. **84**, 085111 (2013). pp. 127, 128, 152

[525] C. Billington, "State-dependent forces in cold quantum gases", PhD thesis (Monash University, 2018). pp. 127, 128

[526] S. P. Johnstone, "Quantum Turbulence in a Planar Bose–Einstein Condensate", PhD thesis (Monash University, 2018). pp. 127, 128

[527] P. T. Starkey, "A software framework for control and automation of precisely timed experiments", PhD thesis (Monash University, 2019). pp. 127, 128

[528] Z. Vendeiro, J. Ramette, A. Rudelis, M. Chong, J. Sinclair, L. Stewart, A. Urvoy, and V. Vuletić, "Machine-learning-accelerated Bose-Einstein condensation", Phys. Rev. Res. **4**, 043216 (2022). pp. 127, 132, 142, 147

[529] F. S. Cárcoba, "Experiment control for quantum simulation with non-local interactions", en, PhD thesis (Joint Quantum Institute, National Institute of Standards and Technology and the University of Maryland College Park, 2020). p. 127

[530] A. Sitaram, G. K. Campbell, and A. Restelli, "Programmable system on chip for controlling an atomic physics experiment", Rev. Sci. Instrum. **92**, 055107 (2021). p. 127

[531] J. Kilinc, "A New Setup for Scaling Up Microlens-Based Individual-Atom Quantum Processors", Master's thesis (Heidelberg University, 2019). p. 127

[532] J. Schabbauer, "Experiment control for quantum simulation with non-local interactions", en, Diploma thesis (Vienna University of Technology, 2023). pp. 127, 128, 130, 131, 152

[533] L. Pause, T. Preuschoff, D. Schäffner, M. Schlosser, and G. Birkl, "Reservoir-based deterministic loading of single-atom tweezer arrays", Phys. Rev. Res. **5**, L032009 (2023). p. 127

[534] L. Pause, "A New Setup for Scaling Up Microlens-Based Individual-Atom Quantum Processors", PhD thesis (Darmstadt University of Technology, Sept. 2023). p. 127

[535] T. Simula, "Droplet time crystals", Phys. Scr. **98**, 035004 (2023). p. 127

[536] Google Groups, *labscript discussions*, `https://groups.google.com/g/labscriptsuite` (visited on 05/12/2024). p. 128

[537] Léonard lab team, *Experiment Control, GitLab repository*, (2024) `https://gitlab.tuwien.ac.at/quantuminfo/experiment-control` (visited on 05/11/2024). p. 128

[538] A. Keshet and W. Ketterle, "A distributed, graphical user interface based, computer control system for atomic physics experiments", Rev. Sci. Instrum. **84**, 015105 (2013). p. 128

[539] The HDF Group, *HDF5 data format*, (2024) `https://www.hdfgroup.org/` (visited on 05/28/2024). p. 128

[540] ZeroMQ community, *ZeroMQ website*, `https://zeromq.org/` (visited on 05/12/2024). p. 130

[541] J. Bechhoefer, "Feedback for physicists: a tutorial essay on control", Rev. Mod. Phys. **77**, 783 (2005). p. 130

[542] F. Seidler, "Digital high bandwidth feedback controller", Master's thesis (University of Bonn, 2015). p. 130

[543] MOGLabs, *Application Notes AN001: PID intensity-stabilisation with the ARF*, `https://www.moglabs.com/support/appnotes` (visited on 03/13/2024). pp. 130, 131

[544] L. Li, W. Huie, N. Chen, B. DeMarco, and J. P. Covey, "Active cancellation of servo-induced noise on stabilized lasers via feedforward", Phys. Rev. Appl. **18**, 064005 (2022). p. 131

[545] A. Rose, *PandasGUI, GitHub repository*, `https://github.com/fonsecajr/pandasgui` (visited on 05/11/2024). p. 131

[546] R. P. Anderson, *analysislib-mloop, GitHub repository*, `https://github.com/rpanderson/analysislib-mloop` (visited on 05/11/2024). pp. 131, 132, 152

[547] P. B. Wigley, P. J. Everitt, A. van den Hengel, J. W. Bastian, M. A. Sooriyabandara, G. D. McDonald, K. S. Hardman, C. D. Quinlivan, P. Manju, C. C. N. Kuhn, I. R. Petersen, A. N. Luiten, J. J. Hope, N. P. Robins, and M. R. Hush, "Fast machine-learning online optimization of ultra-cold-atom experiments", Sci. Rep. **6**, 25890 (2016). pp. 131, 132, 145, 152

[548] M. R. Hush, *M-LOOP website*, `https://m-loop.readthedocs.io/en/stable/index.html` (visited on 05/11/2024). pp. 131, 152

[549] R. S. Judson and H. Rabitz, "Teaching lasers to control molecules", Phys. Rev. Lett. **68**, 1500 (1992). p. 132

[550] A. Bohrdt, C. S. Chiu, G. Ji, M. Xu, D. Greif, M. Greiner, E. Demler, F. Grusdt, and M. Knap, "Classifying snapshots of the doped Hubbard model with machine learning", Nat. Phys. **15**, 921 (2019). p. 132

[551] M. Reinschmidt, J. Fortágh, A. Günther, and V. Volchkov, "Reinforcement Learning in Ultracold Atom Experiments", (2023). p. 132

[552] E. T. Davletov, V. V. Tsyganok, V. A. Khlebnikov, D. A. Pershin, D. V. Shaykin, and A. V. Akimov, "Machine learning for achieving Bose-Einstein condensation of thulium atoms", Phys. Rev. A **102**, 011302 (2020). p. 132

[553] A. J. Barker, H. Style, K. Luksch, S. Sunami, D. Garrick, F. Hill, C. J. Foot, and E. Bentine, "Applying machine learning optimization methods to the production of a quantum gas", Machine Learning: Science and Technology **1**, 015007 (2020). p. 132

[554] H. J. Metcalf and P. Straten, *Laser Cooling and Trapping* (Springer New York, NY, 1999). p. 134

[555] F. Mühlbauer, N. Petersen, C. Baumgärtner, L. Maske, and P. Windpassinger, "Systematic optimization of laser cooling of dysprosium", Appl. Phys. B **124**, 120 (2018). pp. 134, 136, 138, 139

[556] T. H. Loftus, T. Ido, M. M. Boyd, A. D. Ludlow, and J. Ye, "Narrow line cooling and momentum-space crystals", Phys. Rev. A **70**, 063413 (2004). pp. 134, 135, 137, 138

[557] Phelps, G. A., "A dipolar quantum gas microscope", PhD thesis (Harvard University, 2019). pp. 134, 135, 137

[558] D. Dreon, L. A. Sidorenkov, C. Bouazza, W. Maineult, J. Dalibard, and S. Nascimbene, "Optical cooling and trapping of highly magnetic atoms: the benefits of a spontaneous spin polarization", J. Phys. B: At. Mol. Opt. Phys. **50**, 065005 (2017). pp. 135–137, 139

[559] T. Maier, H. Kadau, M. Schmitt, A. Griesmaier, and T. Pfau, "Narrow-line magneto-optical trap for dysprosium atoms", Opt. Lett. **39**, 3138 (2014). pp. 136, 138, 139

[560] M. Barbiero, M. G. Tarallo, D. Calonico, F. Levi, G. Lamporesi, and G. Ferrari, "Sideband-enhanced cold atomic source for optical clocks", Phys. Rev. Appl. **13**, 014013 (2020). p. 137

[561] J. Gao, "A First Two-Dimensional Magneto-Optical Trap for Dysprosium", PhD admission thesis (Heidelberg University, 2022). p. 137

[562] S. Stellmer, "Degenerate quantum gases of strontium", PhD thesis (University of Innsbruck, 2013). p. 137

[563] T. Arpornthip, C. A. Sackett, and K. J. Hughes, "Vacuum-pressure measurement using a magneto-optical trap", Phys. Rev. A **85**, 033420 (2012). p. 138

[564] A. D. Tranter, H. J. Slatyer, M. R. Hush, A. C. Leung, J. L. Everett, K. V. Paul, P. Vernaz-Gris, P. K. Lam, B. C. Buchler, and G. T. Campbell, "Multiparameter optimisation of a magneto-optical trap using deep learning", Nature Commun. **9**, 4360 (2018). p. 139

[565] C. G. Townsend, N. H. Edwards, C. J. Cooper, K. P. Zetie, C. J. Foot, A. M. Steane, P. Szriftgiser, H. Perrin, and J. Dalibard, "Phase-space density in the magneto-optical trap", Phys. Rev. A **52**, 1423 (1995). p. 139

[566] C. C. Bradley, C. A. Sackett, and R. G. Hulet, "Bose-Einstein Condensation of Lithium: Observation of Limited Condensate Number", Phys. Rev. Lett. **78**, 985 (1997). p. 140

[567] C. Bouazza, "Ultracold dysprosium gas in optical dipole traps: control of interactions between highly magnetic atoms", PhD thesis (Paris Sciences et Lettres University, 2018). pp. 141, 142

[568] K. M. O'Hara, M. E. Gehm, S. R. Granade, and J. E. Thomas, "Scaling laws for evaporative cooling in time-dependent optical traps", Phys. Rev. A **64**, 051403 (2001). pp. 141, 142

[569] A. J. Olson, R. J. Niffenegger, and Y. P. Chen, "Optimizing the efficiency of evaporative cooling in optical dipole traps", Phys. Rev. A **87**, 053613 (2013). p. 141

[570] R. Hobson, W. Bowden, A. Vianello, I. R. Hill, and P. Gill, "Midinfrared magneto-optical trap of metastable strontium for an optical lattice clock", Phys. Rev. A **101**, 013420 (2020). p. 143

[571] Z. Vendeiro, "Raman Cooling to High Phase Space Density", PhD thesis (Massachusetts Institute of Technology, 2021). p. 143

[572] M. Naraschewski and D. M. Stamper-Kurn, "Analytical description of a trapped semi-ideal Bose gas at finite temperature", Phys. Rev. A **58**, 2423 (1998). p. 144

[573] C. E. Rasmussen and C. K. I. Williams, *Gaussian Processes for Machine Learning* (The MIT Press, Massachusetts Institute of Technology, Cambridge, Massachusetts, 2006). p. 145

[574] B. Shahriari, K. Swersky, Z. Wang, R. P. Adams, and N. de Freitas, "Taking the Human Out of the Loop: A Review of Bayesian Optimization", Proc. IEEE **104**, 148 (2016). p. 145

[575] M. Boninsegni, N. Prokof'ev, and B. Svistunov, "Superglass Phase of ^{4}He", Phys. Rev. Lett. **96**, 105301 (2006). p. 151

[576] L. Tanzi, S. Roccuzzo, E. Lucioni, F. Famà, A. Fioretti, C. Gabbanini, G. Modugno, A. Recati, and S. Stringari, "Supersolid symmetry breaking from compressional oscillations in a dipolar quantum gas", Nature (London) **574**, 382 (2019). p. 152

[577] S. D. Huber and G. Blatter, "Mesoscopic aspects of strongly interacting cold atoms", Phys. Rev. B **79**, 174504 (2009). p. 152

[578] J. Léonard, A. Morales, P. Zupancic, T. Esslinger, and T. Donner, "Supersolid formation in a quantum gas breaking a continuous translational symmetry", Nature (London) **543**, 87 (2017). p. 152

[579] P. Muruganandam and S. Adhikari, "Fortran programs for the time-dependent Gross–Pitaevskii equation in a fully anisotropic trap", Comp. Phys. Commun. **180**, 1888 (2009). p. 155

[580] Y. Qiu, *Spectra website*, `https://spectralib.org/index.html` (visited on 06/04/2024). p. 155

[581] G. Gaël and J. Benoît et al., *eigen website*, `http://eigen.tuxfamily.org` (visited on 06/04/2024). p. 155

[582] J. Bezanson, A. Edelman, S. Karpinski, and V. B. Shah, "Julia: A fresh approach to numerical computing", SIAM review **59**, 65 (2017). p. 155

[583] I. T. Jolliffe, *Principal component analysis*, Springer Series in Statistics (Springer, New York, 2002). p. 156

[584] K. Pearson, "On lines and planes of closest fit to systems of points in space", Phil. Mag. **2**, 559 (1901). p. 156

[585] H. Hotelling, "Analysis of a complex of statistical variables into principal components", J. Educ. Psychol. **24**, 417 (1933). p. 156

[586] S. R. Segal, Q. Diot, E. A. Cornell, A. A. Zozulya, and D. Z. Anderson, "Revealing buried information: Statistical processing techniques for ultracold-gas image analysis", Phys. Rev. A **81**, 053601 (2010). pp. 156, 157

[587] D. M. Farkas, E. A. Salim, and J. Ramirez-Serrano, "Production of Rubidium Bose-Einstein Condensates at a 1 Hz Rate", arXiv: 1403.4641 (2014). p. 156

[588] Mathematica, *Wolfram Language & System Documentation Center*, `https://reference.wolfram.com/language/` (visited on 06/08/2024). p. 158

[589] Mathematica, *Mathematica's KarhunenLoeveDecomposition*, `https://reference.wolfram.com/language/ref/KarhunenLoeveDecomposition.html` (visited on 06/08/2024). p. 158

[590] Mathematica, *Mathematica's PrincipalComponents*, `https://reference.wolfram.com/language/ref/PrincipalComponents.html` (visited on 06/08/2024). p. 158

[591] J. L. Rodgers and W. A. Nicewander, "Thirteen Ways to Look at the Correlation Coefficient", The American Statistician **42**, 59 (1988). pp. 162, 163